Spring 2024

Damage Control Measures in Composites: Focus on Damage Tolerance of Aerospace Structures

Kais Jribi
Embry-Riddle Aeronautical University, jribik@my.erau.edu

DAMAGE CONTROL MEASURES IN COMPOSITES:

FOCUS ON DAMAGE TOLERANCE OF AEROSPACE STRUCTURES

By

Kais Jribi

A Dissertation Submitted to the Faculty of Embry-Riddle Aeronautical University

In Partial Fulfillment of the Requirements for the Degree of

Doctor of Philosophy in Aerospace Engineering

03/2024

Embry-Riddle Aeronautical University

Daytona Beach, Florida

To my beloved wife, who journeyed from Poland to the United States to stand beside me. Your love, support, and encouragement have been the pillars of my strength throughout this journey towards my PhD. You are not just my partner but my greatest ally in every step of this path.

To my dear son, whose laughter and joy have filled our home and hearts, providing the much-needed light during the most rigorous days of my academic pursuit. Your innocence and happiness have been the source of my daily motivation.

To my parents, whose unwavering support and belief in my capabilities have never faltered. You instilled in me the values of hard work and perseverance that have led me to this moment. Your sacrifices and love have shaped me in innumerable ways.

To each of you, this achievement is as much yours as it is mine. You have been my constant source of love and inspiration. This journey would have been incomplete without your presence and support.

This dissertation stands as a testament to our shared journey, sacrifices, and unconditional love.

Thank you.

ACKNOWLEDGEMENTS

I would like to express my profound gratitude to Dr. Alberto Walter Da Silva Mello Jr., whose guidance and support as my advisor have been invaluable throughout my PhD journey. His expertise and insights have greatly contributed to my research and personal growth.

I am also immensely grateful to Dr. Sirish Namilae, Dr. Habib Eslami, and Dr. Birce Dikici for their invaluable contributions as members of my committee. Their feedback and perspectives have significantly enriched my academic experience.

My sincere appreciation goes to the Aerospace Engineering Department for their financial support and unwavering belief in my research. Their assistance has been a cornerstone in my academic journey.

Special thanks to Jonathan H. Gosse and Douglas J. Neill from Computational Engineering Software for their mentorship and support. Their advice and encouragement have been instrumental in my research.

I am also thankful to Patz Materials and Technologies and Correlated Solutions for generously providing the prepreg and software, respectively. These resources have been crucial in the success of my research.

Last but certainly not least, I extend my heartfelt thanks to my wife, family, and friends for their unconditional support and assistance. Their constant encouragement and belief in me have been the backbone of my perseverance and success in reaching my goals.

ABSTRACT

Barely Visible Impact Damage (BVID) in composite materials presents a stealthy yet significant risk to structural integrity, particularly challenging due to its elusive nature. The approach adopted here diverges from traditional methodologies, focusing on the novel application of Digital Image Correlation (DIC) to map surface area changes during in-situ Compression After Impact (CAI) tests. This technique allows for an in-depth analysis of planar strains along the x and y axes, shedding light on the material's behavior under stress.

A pivotal advancement lies in developing a method for precisely identifying when BVID-induced delamination recommences. By meticulously analyzing strain pattern deviations along these axes, the onset of additional damage is accurately pinpointed, significantly improving predictive capabilities for delamination due to BVID. This approach enhances the structural integrity assessment of composite materials, bolstering safety measures.

The techniques and insights gained significantly contribute to advancing maintenance strategies and structural evaluation in aerospace composites by offering refined tools for early detection of BVID-induced damage.

TABLE OF CONTENTS

LIST OF FIGURES

LIST OF TABLES

NOMENCLATURE

AoI	Area of Interest
AS	Laminae Layups $[45/90/-45/0/-45/0/-45/0/45/90/45/90]_s$
ASTM	American Society for Testing and Materials
BVID	Barely Visible Impact Damage
CAI	Compression After Impact
CFRP	Carbon Fiber Reinforced Polymers
E	Elastic Moduli
J_2'	Invariant of the Deviatoric Strain Tensor
LL	Limit Loads
LVI	Low Velocity Impact
S	Laminae Layups $[45/0/-45/90]_{3s}$
SEM	Scanning Electron Microscope
UL	Ultimate Load
V	Volume Fraction
W	Out of Plane Displacement
ε	Strain Value

1 Introduction

Carbon Fiber Reinforced Polymers, or CFRP for short, are consolidated in the aerospace industry due to their superiority in terms of stiffness and strength-to-weight compared to conventional metal alloys. CFRPs are also a favored material to produce more complicated sections in airplane structures because they minimize the number of individual parts required to construct a structure, lowering the likelihood of component failure due to faulty machining or assembly. Furthermore, designers may optimize the structure to withstand loads in a particular direction based on the loading parameters, minimizing the requirement for reinforcement in non-critical loading modes and substantially decreasing the structure's weight.

CFRPs are ideal for applications requiring minimum weight with satisfactory strength. The practical application of composites has faced some drawbacks due to their unusual mechanical behavior. One typical problem composite structures face is the laminate's low impact and shear resistance in the transverse direction [1].

In addition, damage is unavoidable during all phases of manufacturing, in-service operation, and maintenance, whether due to human error or the operating environment. A careful inspection should be performed regularly to avoid any catastrophic damage that increases the operating cost.

1.1 Classifying Damage in Aerospace Composites

The most typically seen composite damages are delamination, matrix fracture, fiber breakage, porosity, and fiber-matrix debonding. Often, the impact of a foreign object, which could be hail damage, tool drops, bird strikes, runway debris, or ground equipment, causes 80% of the damage[2].

The level of damage discovered in the structure during a regular examination dictates the proper course of action. Figure 1.1 depicts impact damage tolerance and several damage types based on data from reference [3].

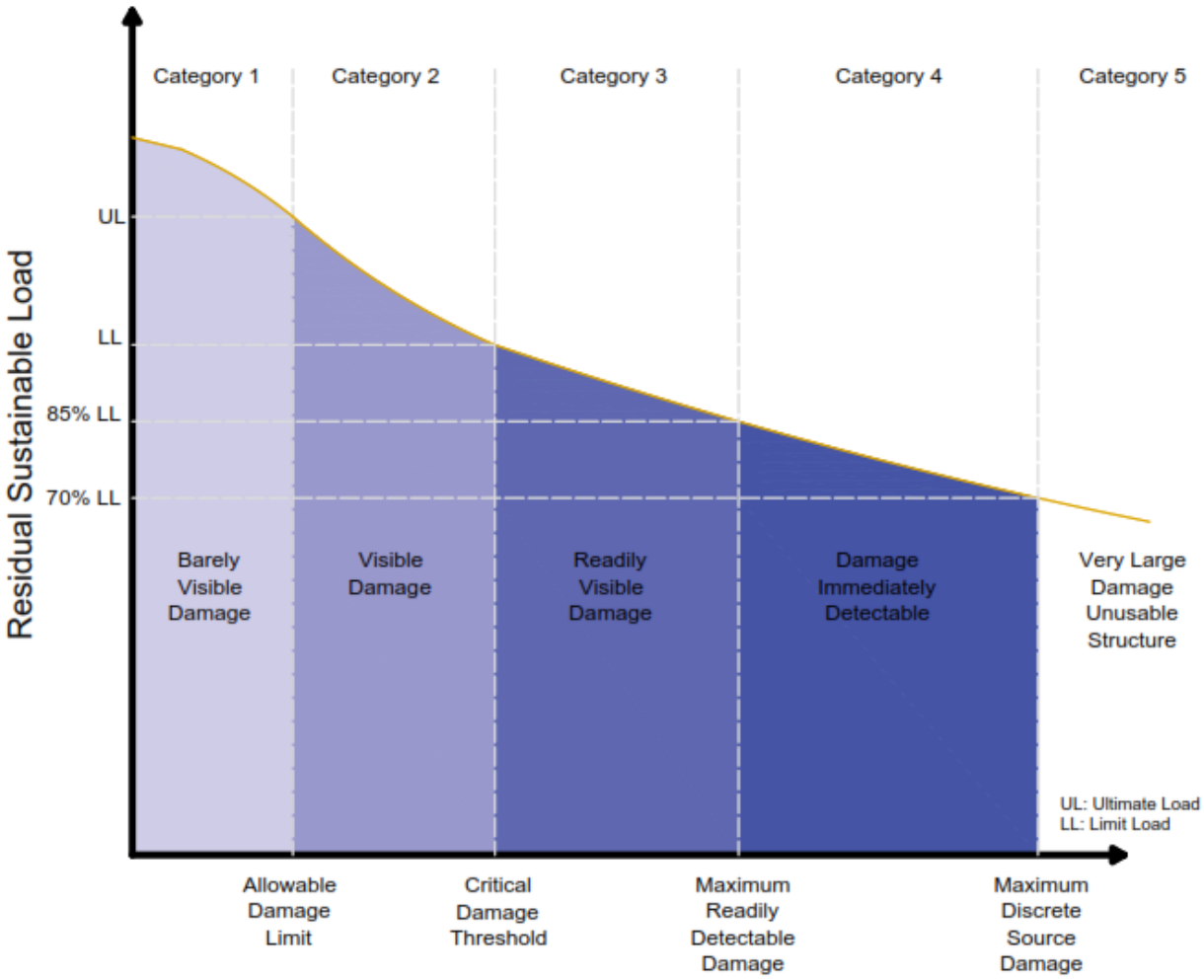

Figure 1.1 Impact damage tolerance and the different damage categories.

These categories are sorted according to their severity. The first type of damage is the most difficult one to detect and is frequently overlooked; in this category, the structure can often retain its integrity since it can still withstand ultimate design loads. Nevertheless, it has been demonstrated that this damage could be the beginning of a catastrophic failure and should be adequately addressed [3]. In the second category, the damage is detectable but can be tolerated; thus, the damage tolerance domain name is used. The structure would withstand limit loads in this category until it reaches the critical damage threshold. When the damage reaches the third stage,

repairs should be undertaken. Starting at this level, the residual sustainable loads range between 85% and 100% of the limit load, and the damage is readily observable. The fourth category is when the structure is at 70% to 85% of its design limit load, and the damage is instantly visible. The fifth and final category is where the structure falls outside the scope of structural safety and sustains significant damage, rendering it unexploitable.

According to Dubinskiy et al. [4], impact is responsible for about 80% of the structural damage in composite materials. This type of damage is frequently classified into high-velocity impacts that would cause considerable structural damage and requires quick remedial action and low-velocity impacts that may cause damage but would not generally result in a disastrous occurrence. Nonetheless, damage generated by a low-velocity impact should be inspected and recorded since it often induces Barely Visible Impact Damage (BVID), which can drastically diminish the residual strength of the component [5]. As a result, it should be continuously monitored to prevent further degeneration of the structure, which might lead to catastrophic failure.

1.2 Unveiling Barely Visible Impact Damage (BVID) in CFRPs

CFRPs are known for their higher permanent deformation resistance [6]. As a result, BVID-type damage is imperceptible to the human eye, making it a critical issue that must be addressed.

BVID failure mechanisms include delamination and cracks due to the shear and bending stresses (Figure 1.2). The composition of the damage would depend on the material properties, the type of impact and its severity, the specimen's boundary conditions, and the impactor's geometry [7].

The structural strength of a composite can be adversely affected by the introduction of BVIDs. Since the damage frequently goes undiagnosed and remains undiscovered for a substantial amount of time, it might subsequently expand to a critical magnitude, causing a devasting occurrence that would compromise the integrity of the structure. For example, research for the residual strength

assessment of a damaged composite sample due to low-velocity impacts under compressive stress revealed a drop of up to 60% of pre-damage strength as the delamination would cause local buckling of the laminae.[5,8–11]. Damage propagation would not occur under a tensile stress test, where the fiber would carry most of the load, and the delamination would not propagate according to the fracture mechanics approach [12].

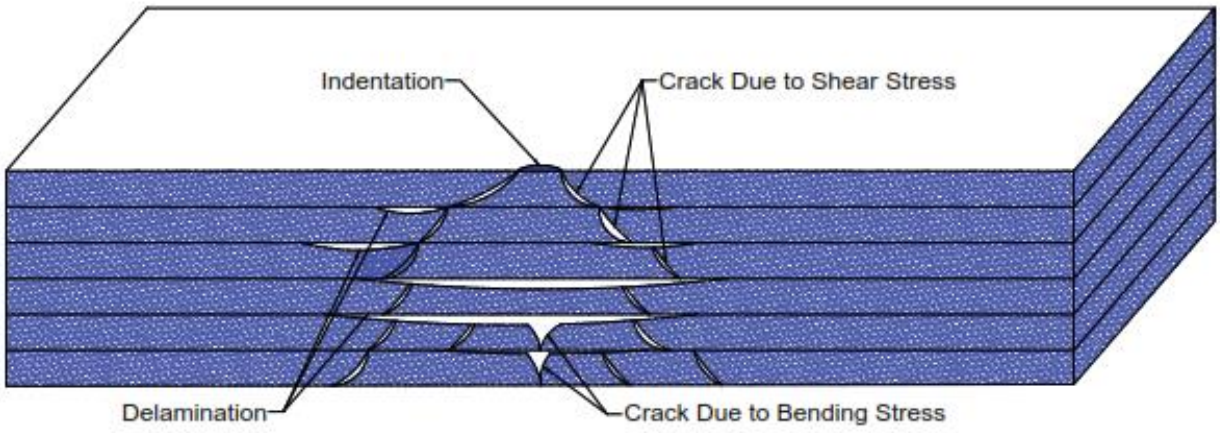

Figure 1.2 Basic anatomy of a BVID [13].

However, delamination spreads among plies with different fiber orientations when the laminate is subjected to compressive stress following a BVID. It is observed that fractures within the matrix material are contained within the confines of individual layers, prompting the onset of delamination. This situation arises as the matrix material redistributes the stresses from the compromised fibers to the remaining intact portions of the structure, thereby exacerbating the progression of delamination.

Damage propagation can occur if delamination is initiated and a compressive load is applied, as demonstrated in the introduction to BVIDs. As a result, numerous studies and models are being

developed to determine the behavior of the damage under various loads and to establish fracture control measures for composite structures.

1.3 Advancements in Composite Damage Tolerance Research

Extensive research has been conducted in composite damage tolerance, mainly focusing on the aftermath of BVID and the ensuing delamination under various load scenarios. Zhang et al. utilized a detailed three-dimensional finite element approach to monitor and quantify the strain energy release in real-time during delamination progression [14]. Yang delved into the specific post-impact behavior of laminated composites, utilizing ultrasonic scanning techniques to observe and quantify the stiffness reduction across delaminated areas, shedding light on the material's degradation pattern under continued stress [15].

Xu et al. examined how composites respond to cyclic compressive loads after an initial impact, revealing a notable decrease in the material's ability to bear loads - a drop to about 70-80% of its original capacity. They highlighted the critical relationship between initial damage and subsequent fatigue behavior [16]. In a similar research, Wang et al. predicted the buckling response and the potential pathways of delamination propagation, incorporating these factors into the comprehensive failure analysis of composites with specific focus on elliptical delamination [17]. Sun et al. adopted high-fidelity finite element numerical models alongside experimental quasi-static indentation tests to trace the evolution of damage from the moment of impact to subsequent loading scenarios [18].

Pascoe has broadly categorized the methodologies for predicting and analyzing delamination growth into four main streams (Figure 1.3): stress-strain based models, fracture mechanics based models, cohesive-zone models, and extended finite element-based models, each evolving over the decades to address specific aspects of composite behavior under stress. However, these methods have limitations, particularly in handling the intricate nature of damage progression, the ambiguity

in damage characterization, and the complexities introduced by the composite's heterogeneous structure [19].

As evidenced by presentations from Justusson et al. [20] at the Aircraft Structural Integrity Program and initiatives by Neill et al. [21], industry and academic pursuits continually push the boundaries in estimating service life and enhancing the safety margins of composite structures. Broader initiatives, such as the NAVY's SBIR program and the formation of NASA's Advanced Composite Consortium, underscore the ongoing need for advanced predictive capabilities, robustness, and efficient inspection methodologies in aerospace composites [13,20–23].

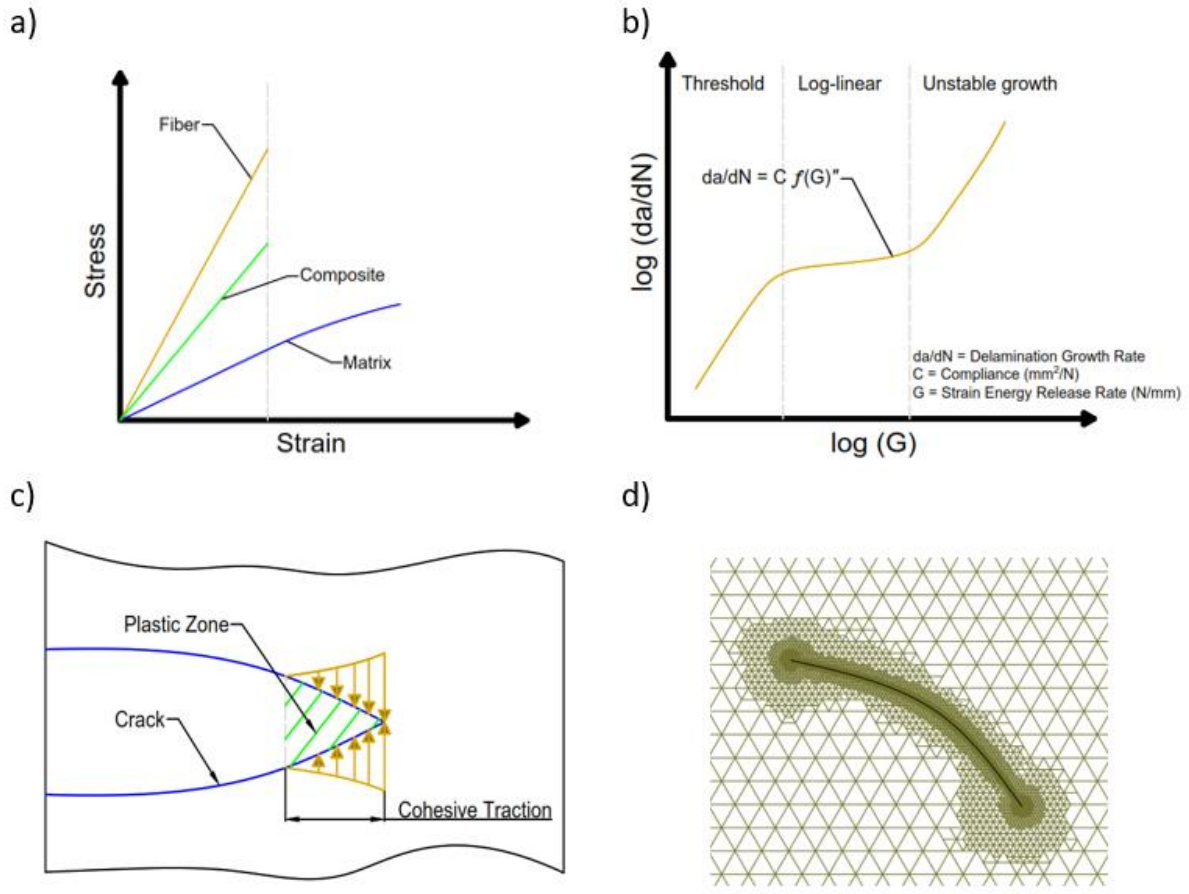

Figure 1.3 Prediction modules for the fatigue-driven delamination growth (a) stress/strain models (b) fracture mechanics models (c) cohesive-zone models (d) extended finite element models

1.4 Research Objective and Significance

The primary gap in this line of study is the focus on the initial damage size and applied load to determine the reinitiation of the delamination propagation, both of which are hard to acquire and determine during the operational phase of the composite structure. This research aims to deviate from the standard approach by experimentally investigating and finding a relationship between the surface strains and the out-of-plane displacements. Both can be easily acquired and provide a better approach to detecting the thresholds at which delamination commences after an initial impact or damage. The results are compared to the standard approach that would utilize stress, making it a reference point in this study to validate the results.

For statistical significance, two different layups are used in this research, along with five different LVI energy levels for each of the layups.

The present investigation also employs Digital Image Correlation (DIC) to accurately capture and assess surface strains to determine the thresholds at which delamination recommences after an initial impact or damage.

2 Material and Equipment Selection

This investigation required a comprehensive set of materials and equipment to facilitate manufacturing, testing, and the extraction of experimental values. The selection outlined here was strategically chosen to support each study phase based on the facilities available at Embry-Riddle Aeronautical University in Daytona Beach, Florida. When specific equipment or materials are unavailable within the university's laboratories, provisions were made to acquire them through the Aerospace Engineering Department or appropriate external vendors, ensuring a seamless and efficient research process.

2.1 Criteria for Material Selection in Composite Manufacturing

Prepreg was selected for this project to ensure consistency and reliability throughout the manufacturing process, offering distinct advantages over wet layup methods such as predictable curing, ease of laminae layup definition, and extended working time, collectively reducing the likelihood of inconsistencies [24].

The samples were manufactured with prepreg provided by Patz Materials and Technology, PMT-F7G/IM7 12K-145G5M/35 RC/12”/UDP. These materials comprise HexTow IM7-GP 12K carbon fibers combined with PMT-F7 epoxy resin, known for its high glass transition temperature and robust resin modulus due to its specific curing temperature of 350°F, as shown in Figure 2.1.

PMT-F7G/IM7 prepreg was stored in an airtight bag to maintain its quality and prevent moisture damage at temperatures of 10°F, where it retains its properties for one year. During the handling process, the prepreg can be used at a temperature equal to or below 70°F for thirty days.

For the vacuum bagging process, Stretchlon® 800 bagging film, which can withstand the 350°F curing temperature, was supplied by FIBERGLAST, along with the necessary yellow sealant tape. Additional materials, including mold release (#1153 FibRelease), peel ply, and

breather cloth, were procured from the Composite Lab at the Micaplex research park, ensuring a comprehensive set of high-quality materials for the prepreg layup process.

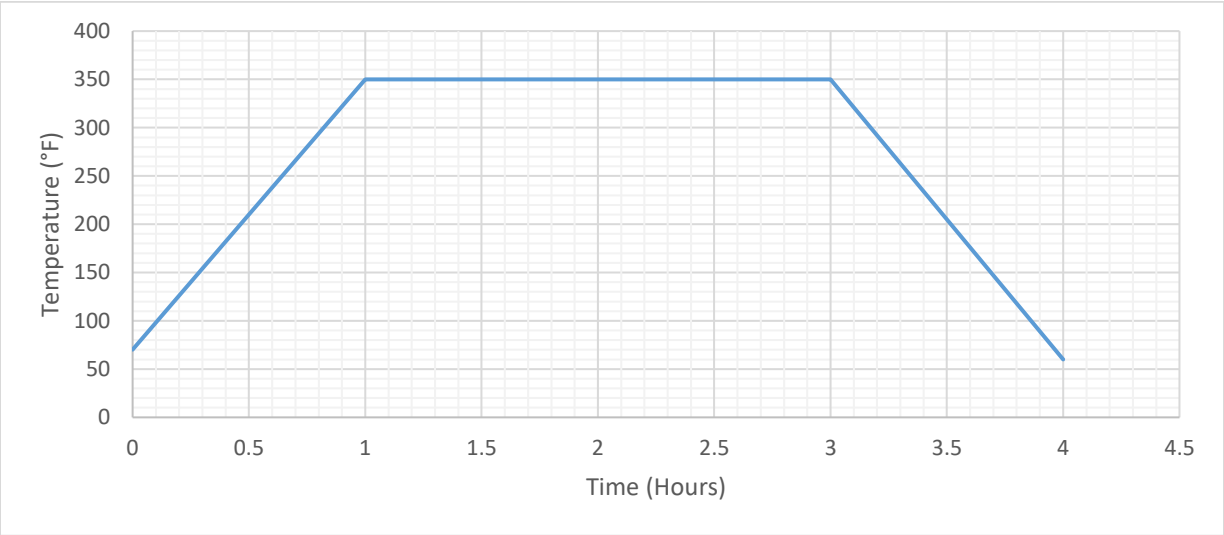

Figure 2.1 PMT-F7 min. cure profile

2.2 Essential Equipment for Composite Fabrication and Testing

In pursuit of conducting the research, an extensive variety of specialized apparatus and software were employed to guarantee accuracy in both fabrication and examination. The subsequent components were crucial to the undertaking:

2.2.1 Econoclave® Model: EC2X4

The Econoclave® EC2X4 (Figure 2.2) at the Micaplex Research Park's composite lab exemplifies the highest standard of aerospace-grade autoclaves that conserve energy while curing and bonding small composite parts. The standard models operate at temperatures of 450°F (232°C) and 800°F (427°C) at pressures of 150 psi and 200 psi, respectively. Complementing the autoclave's 48-inch length and 24-inch diameter are factory-tested, fully integrated components, including skid-mounted controls, a vacuum system, and cooling tanks.

The Econoclave® was constructed per ASME Division I, Section VIII standards. It features a secure locking mechanism and a quick-opening door, and it employs the industry-standard CPC system to cure composites and maintain temperature uniformity to reduce the odds of thermal stress and strains within the sample [25].

Figure 2.2 Autoclave EC2X4-200P800F

2.2.2 Tinius Olsen Load Frame

The Aerospace Engineering Materials Testing Lab houses the Tinius Olsen ST150 shown in Figure 2.3, an adaptable electromechanical testing apparatus specifically engineered to conduct extensive material tests. The apparatus has a sturdy 150kN (30,000lbf) load cell conforming to ASTM standards to guarantee precise and dependable measurements. The ST150 is coupled with the Horizon Materials Testing software, providing an advanced platform for data analysis,

supporting rigorous research and quality control with its customizable test routines and report generation capabilities.

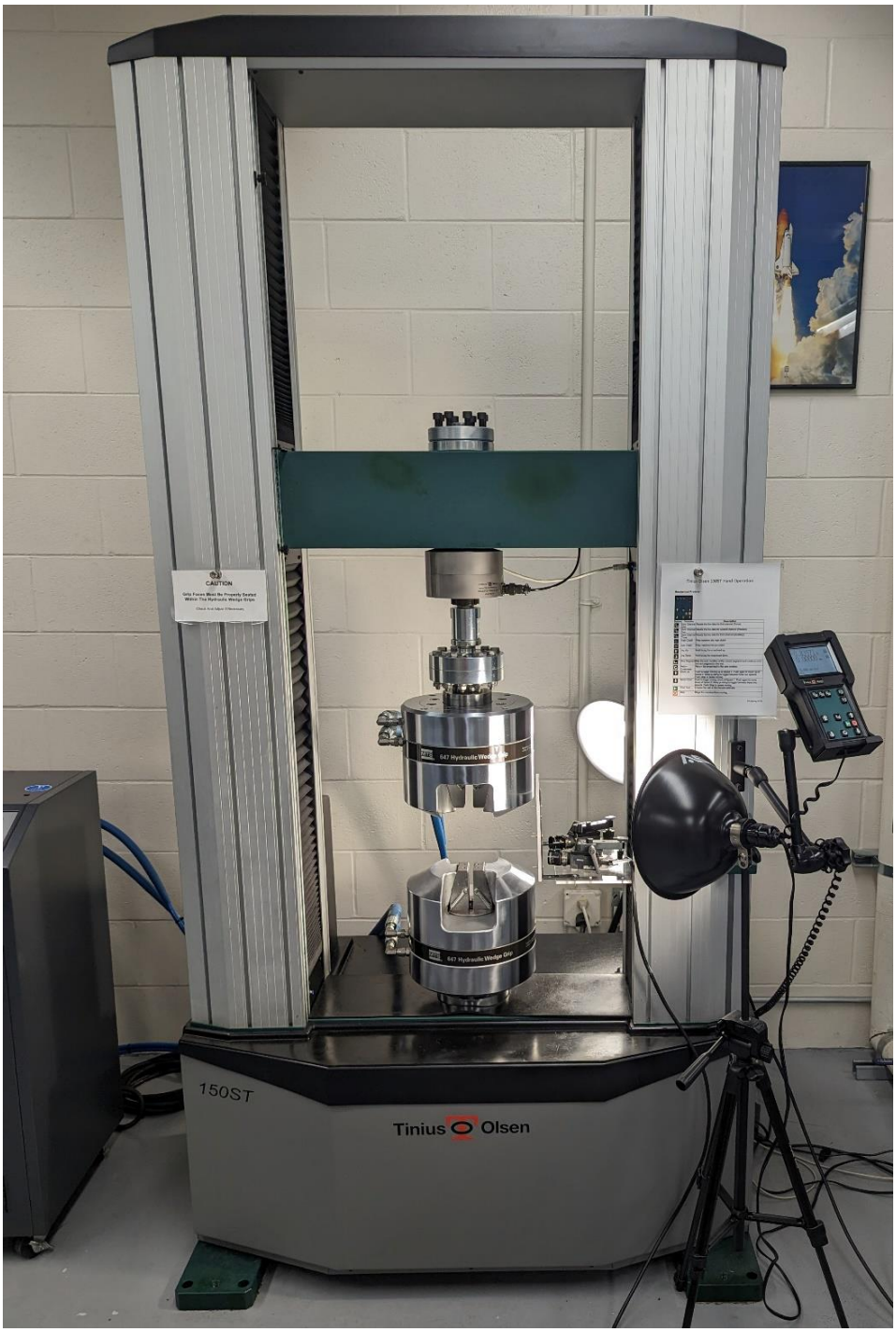

Figure 2.3 Tinius Olsen ST150 load frame.

2.2.3 Digital Image Correlation

Correlated Solutions' VIC-3D system is a digital image correlation tool that precisely measures 3D shapes, displacements, and strains. This advanced system boasts high-speed cameras with resolutions reaching up to 2448x2048 pixels, enabling the capture of dynamic events at record-breaking speeds. Further streamlining of the process is done through the VIC-Snap software integration. The software allows for simplifying image acquisition across various testing scenarios, solidifying its effectiveness as a versatile solution for all material testing and analysis requirements.

The VIC-2D system, also developed by Correlated Solutions, is a specialized two-dimensional Digital Image Correlation (DIC) system. It is adept at measuring in-plane displacements and stresses on planar surfaces. This system utilizes high-resolution cameras to capture and analyze the behavior of planar or near-planar objects as they deform under load. While the VIC-3D system measures three-dimensional shapes, displacements, and strains, the VIC-2D is tailored exclusively for two-dimensional surface measurements.

The system works by comparing images taken before and after the adjustment. Also, the system monitors the movement of the speckle pattern applied to the specimen surface to calculate field displacement and strain data. This approach allows detailed analysis of material behavior, including local strain rates, essential for detecting physical faults or understanding complex deformation mechanics.

It is particularly beneficial in studies where the sample or structure of interest has negligible out-of-plane movement, making it an efficient choice for planar strain analysis.

2.2.4 Instron 9250HV Impact Frame

The Aerospace Engineering Materials Testing Lab houses the Instron 9250HV, as shown in Figure 2.4. This dynamic impact testing system is vital in studying Barely Visible Impact Damage

(BVID) in composite materials. By inflicting varying levels of impact, this specialized equipment replicates real-world scenarios and allows researchers to detect and analyze delamination. The capability to adjust impact energy levels offers a wealth of data for comprehending the material's behavior and durability in diverse stress environments. This knowledge is essential in aerospace, where materials must endure diverse impacts regularly.

Figure 2.4 Instron Dynatup 9250HV impactor

2.2.5 Bruker SkyScan 1275

The Bruker SkyScan 1275 shown in Figure 2.5 is an advanced 3D X-ray microtomography device developed for high-resolution scanning at a high speed. Its features include GPU-

accelerated reconstruction, 2D/3D morphological analysis, and sophisticated surface and volume rendering display. This technology excels at detecting internal structures, flaws, and micro-level damage in composite materials such as CFRP. The SkyScan 1275 employs X-ray sources and efficient flat-panel detectors to achieve the best possible mix of image quality and scanning speed. Its usage in detecting delamination and manufacturing damage in CFRP samples was crucial, as it provided precise internal and external geometric reconstructions and material contrasts for comprehensive analysis.

Figure 2.5 Bruker SkyScan 1275

2.2.6 SEM Quanta 650

The SEM Quanta 650 shown in Figure 2.6 is a Scanning Electron Microscope for thorough material analysis. A standout feature is its seamless integration with Bruker's QUANTAX EDS system, complete with the impressive XFlash® 7 detector series known for its wide solid angle

and exceptional X-ray collection efficiency. This enables improved elemental analysis, offering semi-quantitative data with remarkable detection capabilities. The versatile SEM Quantax 650 is often coupled with various detectors, such as the top-of-the-line Oxford Instruments X-MaxN 150 mm energy dispersive x-ray detector, and excels in high-resolution imaging and variable pressure scanning electron microscopy. It is the ideal tool for comprehensive investigations into surface characteristics, making it a valuable asset for various applications.

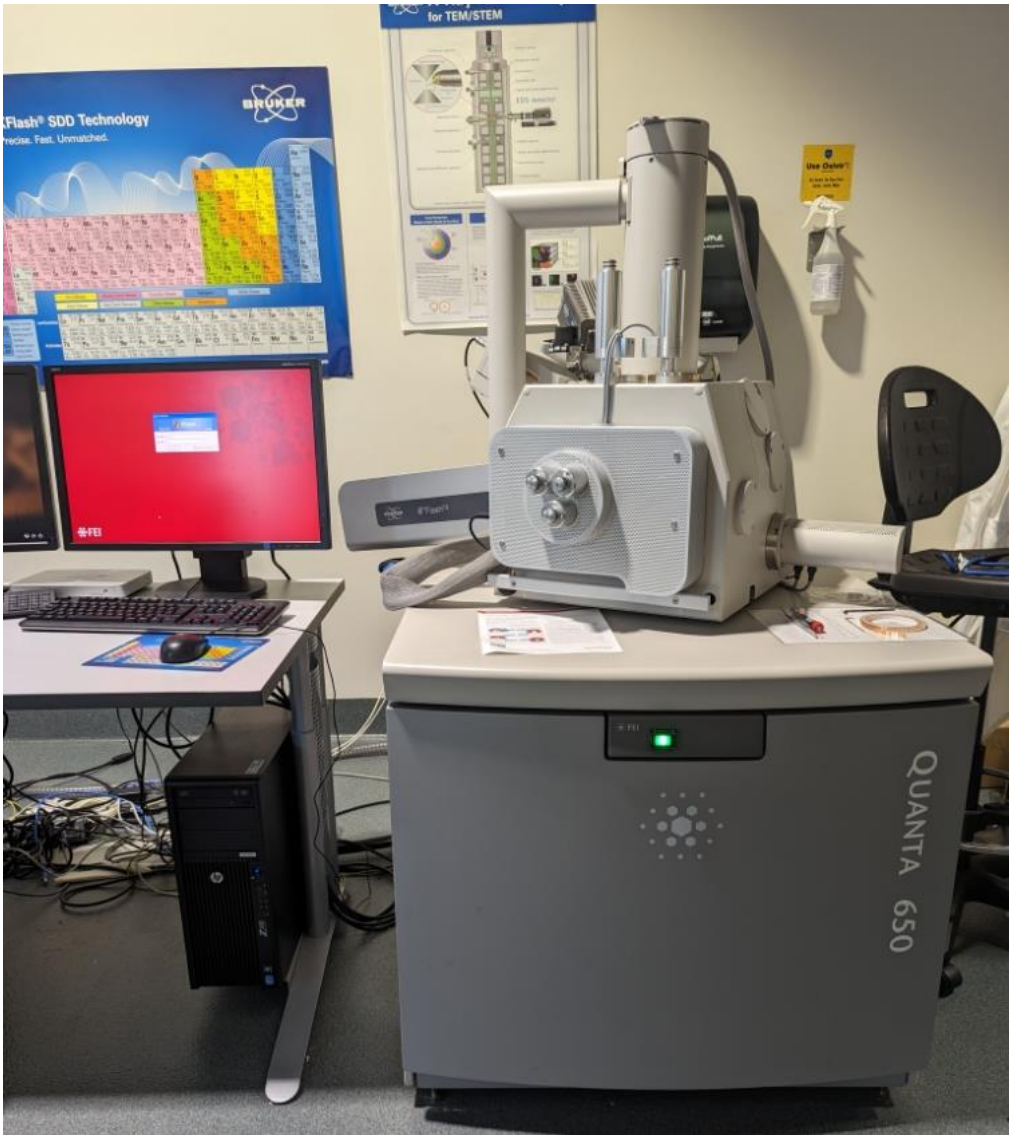

Figure 2.6 SEM Quanta 650

3 Experimental Setup and Methodology

This chapter extensively examines the experimental configuration and methods and the complexities involved in data acquisition, testing, and analysis. This chapter thoroughly examines and discusses the tools and equipment outlined in Chapter 2 and the strategies and tactics employed to refine and enhance the outcomes. The principal objective of this section is to explain the experimental procedure, focusing on ensuring the reproducibility and accuracy of the results.

3.1 Sample Preparation and Standard Compliance

3.1.1 Coupons for Mechanical Property Determination

A uniform process is adopted here to streamline the preparation of coupons to determine material properties and perform the compression after impact test, ensuring adherence to ASTM standards and precision in material preparation.

The coupons that are used to determine material properties complied with the standards ASTM D3039 for tensile experiments and ASTM D6641 for compressive tests. An Amazon basics paper trimmer cut the prepreg into the proper dimensions.

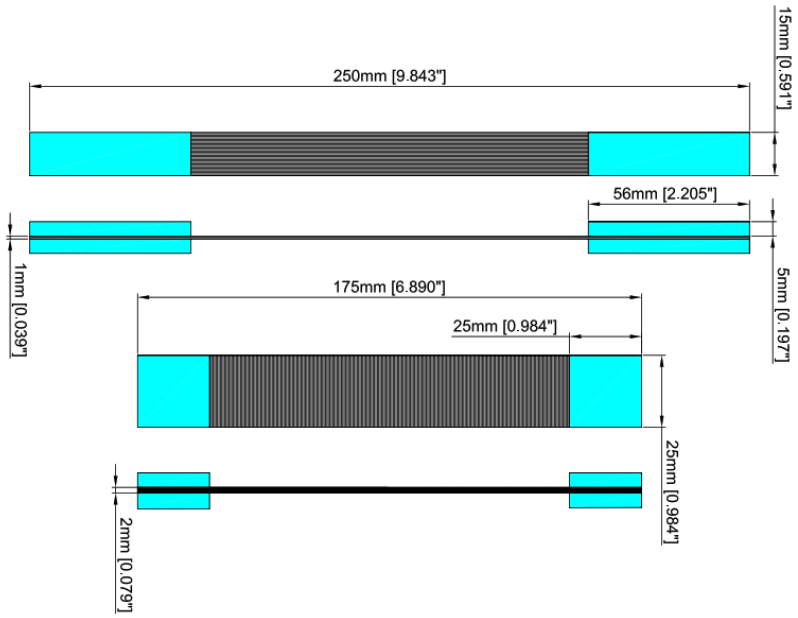

Figure 3.1 ASTM D3039 samples for tensile tests (Top: 0, Bottom: 90)

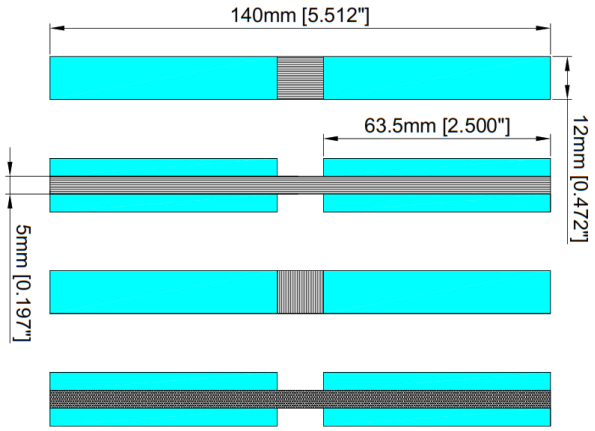

Figure 3.2 ASTM D6641 samples for compressive tests (Top: 0, Bottom: 90)

3.1.2 Coupons for BVID and Onset of Failure Determination

The prepreg was also cut into (4 x 6 in) coupons with fiber orientation at 0°, 90°, -45°, and 45° angles following the ASTM D7136 standard (Figure 3.3). The laminae were then returned to the freezer and held at 10°F (-12.22°C) to prevent the epoxy from curing prematurely.

A flat aluminum plate acting as a mold was sanded using 800-grid sanding paper to remove any imperfections or remnants from earlier prepreg curing processes. Then, acetone was applied to the surface and cleaned away with paper towels until there was no sign of aluminum dust. As soon as the remaining acetone evaporates, utilizing a clean paper towel, a thin layer of the releasing agent 1153 is applied in an even manner to ensure that it dries up rapidly. Later, the sealant tape is placed along the borders of the aluminum plate to maximize the surface area available to produce coupons.

Several plate sizes were employed depending on the availability and amount of samples to be made. The precut coupons are then removed from the freezer and placed on the plate, ensuring that the samples are aligned to minimize the inaccuracy caused by fiber misalignment.

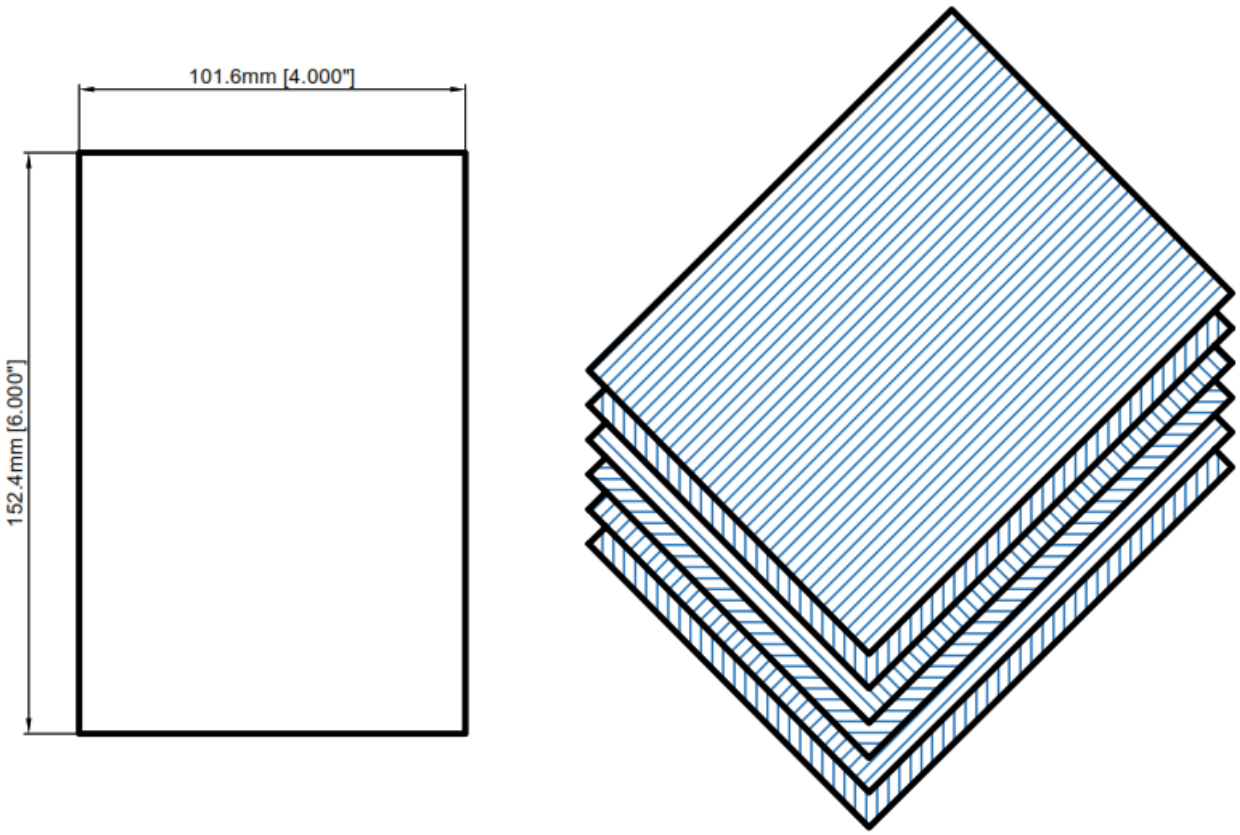

Figure 3.3 Coupon dimensions and laminae stacking orientation

Based on post measurements and due to the resin and fiber migration during the curing process [26], the number of prepreg plies required to create a 0.039 in (1mm) thickness was found to be 8; hence, 16 laminae were used for the sample requiring a 0.079 in (2mm) thickness within a margin of error of ±0.001" (±0.0254mm).

As for the coupons used for the testing, the laminae are removed from the freezer and positioned to achieve two layups of 24 layers each. A $[45/0/-45/90]_{3s}$ and a $[45/90/-45/0/-45/0/-45/0/45/90/45/90]_{s}$ with the 0° fiber orientation directed along the 6" dimension. Both layups were marked with red and blue nail polish for further identification.

Sixty coupons were prepared to ensure a comprehensive and reliable data set for analysis. These coupons were then divided into two groups of 30, representing two different laminate layup configurations.

A peel ply and a breather are cut and layered on top of the laminae, covering the whole surface area of the samples. Next, two 2×2 in breathers were cut and positioned in the gap left on the aluminum plate to function as a filter on which the vacuum probes' bases are positioned. The next stage in preparation was to cut a vacuum bagging film with dimensions greater than the aluminum plate to cover the entire surface area, adhere it to the sealant tape, and seal the cast. Finally, using a sharp cutting knife, the vacuum bagging film is pierced, and the upper sections of the vacuum probes are attached to the base so that the gasket creates a flawless seal.

3.2 Autoclave Process for Sample Curing

Preparing and curing a composite sample in the MicaPlex Composite Lab's autoclave involves several critical steps and settings. Initially, users log in via the "Security Login" screen, which leads to the "Run Operations" interface. The vacuum of -350 torr is established to match the prepreg's curing requirement. This vacuum setting ensures the integrity of the vacuum bagging process. Upon setting the vacuum, the system is returned to automatic mode for operation.

A new batch is created for each experiment, where users input specific part numbers and names and select appropriate attachments, thermocouples, vacuum probes, and source ports. The curing formula is then developed, consisting of a temperature increase at 3°C/min up to 160°C, then automatically adjusting to a curing temperature of 175°C for 2 hours, following Patz Materials & Technologies' specifications. After curing, the sample is cooled at -3°C/min to room temperature.

A trend view screen, illustrated in Figure 3.4, displays the progression of the curing steps to monitor the curing process, ensuring adherence to the specifications set by the prepreg manufacturer.

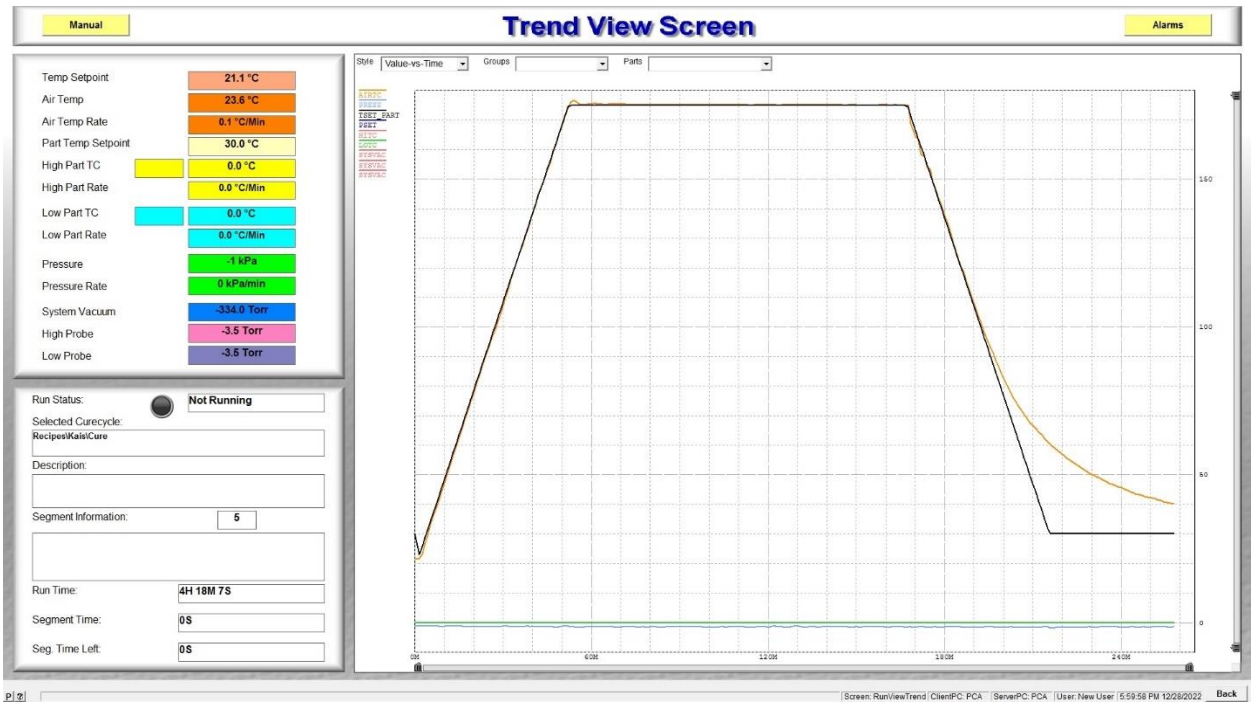

Figure 3.4 Trend view screen [13]

3.3 Post-Cure Handling and Sample Preparation

The samples are unbagged by removing the upper section of the vacuum probes and then pulling out the bagging film, which typically gets affixed to the sealant tape and breather. Next, the peel ply is removed, and the composite sample is released from the mold.

3.3.1 Tensile and Compressive Coupon Tab Attachment

For the coupons used to determine material properties, composite fiberglass with a 45/-45 degree layup and a total thickness of 0.197” (5 mm) is used for the tabs; the tabs are dimensioned using the sawing machine at the composite lab’s workshop at the Micaplex research facility. The

tabs are then sanded with 400-grid sandpaper to generate micro scratches that would aid in bonding them to the testing sample using a combination of PR2032 epoxy resin and PH3665 activation agent. Spring-loaded metal clamps are then used to secure the tabs so the resin can cure at room temperature for at least 24 hours.

3.3.2 Coupon Inspection

The coupons must be inspected for any manufacturing imperfection. Typical damage could be in the form of voids between layers. Three methods of inspection could be applied in this process: X-ray radiography [27–29], IR thermography [27,30,31], and ultrasonic scanning [32–35].

The department previously utilized an UltraPac II imaging system for ultrasonic scanning tasks. However, the available equipment was outdated and uncalibrated, which was unsuitable for the precision requested in this research. Subsequently, acting on recommendations from NDTSupply, the department procured a DFX-8 ultrasonic system. Despite adhering to the prescribed procedures, this system proved ineffective in detecting damage within the coupons to be used for the CAI testing for the present work. Therefore, the Bruker Skyscan 1275 was proposed as an alternative for this study. However, this approach is not without limitations, most importantly, the size limitation imposed by the X-ray scanner.

To ensure complete compatibility with the Bruker SkyScan 1275 micro-CT system, the samples used for testing underwent a resizing process from their original dimensions of 6" x 4" (101.6 mm x 152.4 mm) to 3 15/16" x 3 5/32" (100 mm x 80 mm). This adjustment allowed the samples to fit neatly into the scanner's chamber, limited to samples with diameters up to 96 mm.

This unexpected size change presented an opportunity to speed up the scanning process for damage identification. Compared to standard ultrasonic scanning, X-ray scanning has the distinct benefit of penetrating several samples without compromising outcome quality. This is due primarily to the lesser susceptibility of X-ray imaging to shadowing effects, especially when the

material's density remains relatively constant. This is a considerable advantage over ultrasonic scanning, which can be prone to shadowing issues, potentially masking vital damage indicators [36]. Because of the versatility of X-ray technology, a unique 3D-printed support capable of holding up to seven samples was created (Figure 3.5), effectively reducing the scanning time of all samples by a factor of six as one of the slots was used for a reference sample. This advancement streamlined the inspection process and improved subsequent scanning procedures, particularly after implementing Barely Visible Impact Damage (BVID) and conducting Compression After Impact (CAI) testing.

Scanning with the SkyScan 1275 involves initializing the control software, adjusting sample positioning using the interface icons, and selecting the appropriate X-ray settings for CFRP samples, as seen in Table 3.1. Users then configure scanning parameters such as voltage, current, and scan resolution, culminating in specifying file storage details. This workflow enables multiple samples to be scanned within approximately 3 hours.

Following the end of the scan, a total of 1833 X-ray images were acquired. The next step is to run the NRecon software along with the server used for the reconstruction. The number of threads plays a significant role in speeding up the process. Therefore, a laptop with a high-end GPU with 16 threads was used (Figure 3.6).

Upon loading the images into the system, a mid-sample cut projection is visualized, serving as an initial reference for potential optimization or adjustments before data reconstruction. This preview feature automatically engages algorithms to calculate and suggest corrections for ring artifacts and adjust for beam hardening, aiming to counteract misalignments and enhance image quality.

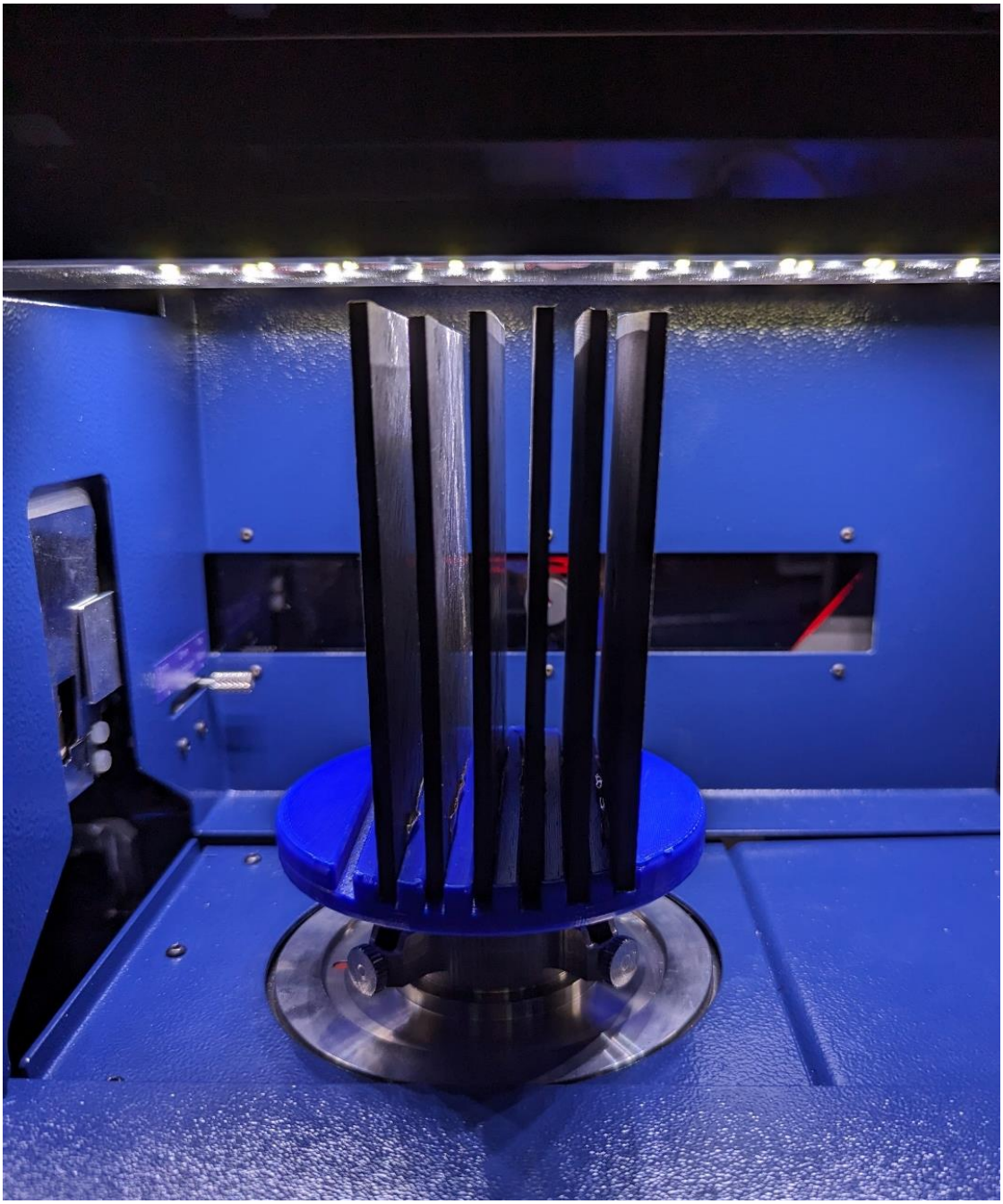

Figure 3.5 3D printed support used for multiple sample scan in the specimen chamber

Table 3.1 Scanning parameters for BVID detection in CFRP

Parameter	Pixel size	Voltage	Current	Rotation increment	Frames per rotation
Value	50.77um	50kV	200uA	0.2 degrees	30 frames

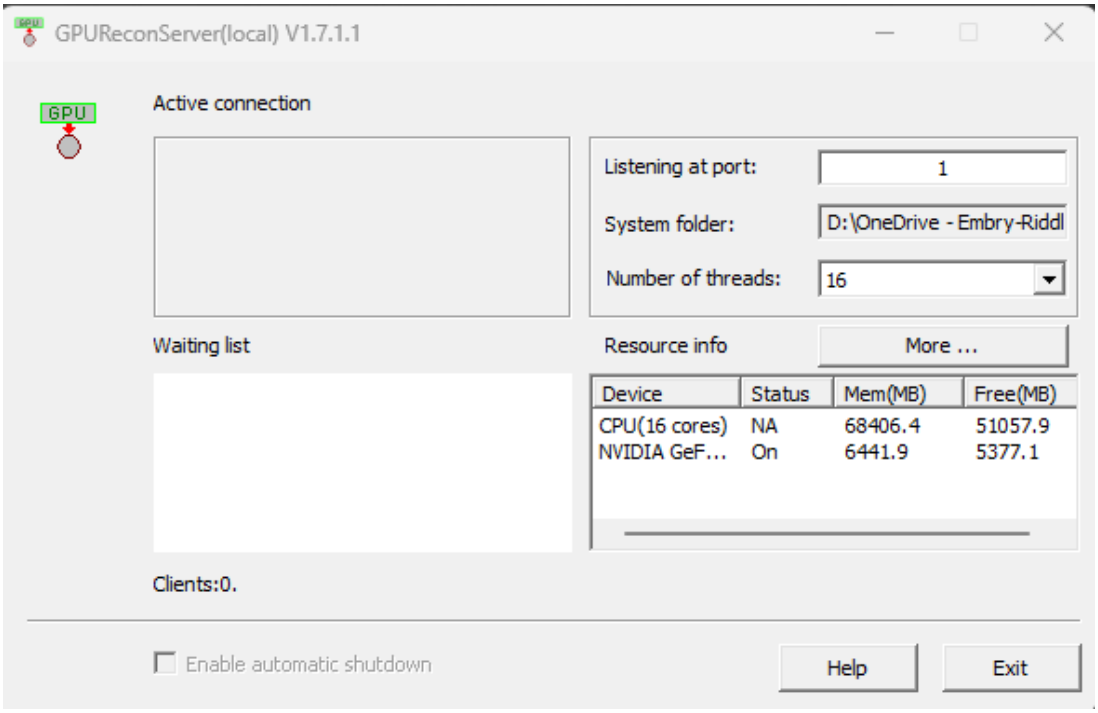

Figure 3.6 GPUReconServer

Figure 3.7 illustrates the preview output, indicating that the samples exhibit a minus 2-degree tilt, which can be rectified by adjusting the CS rotation. In some scenarios, manual intervention is necessary to fine-tune the beam hardening profile and eliminate the rings caused by overexposure to the X-ray beam. In this instance, the predefined variables proved sufficient, as evidenced by the histogram analysis displayed beneath the output (Figure 3.8), negating the need for additional alterations other than selecting that the object is larger than the field of view.

In sequence, the system starts the reconstruction phase of the analysis, utilizing the optimized parameters established in the preview stage.

Following the reconstruction process, an in-house MATLAB code (APPENDIX - A) was used to separate the samples for the next step. This process is a tradeoff for reducing the time required for the scanning with the help of the 3D printed support and reconstruction process of all the samples to around 90 hours compared to the projected 594 hours.

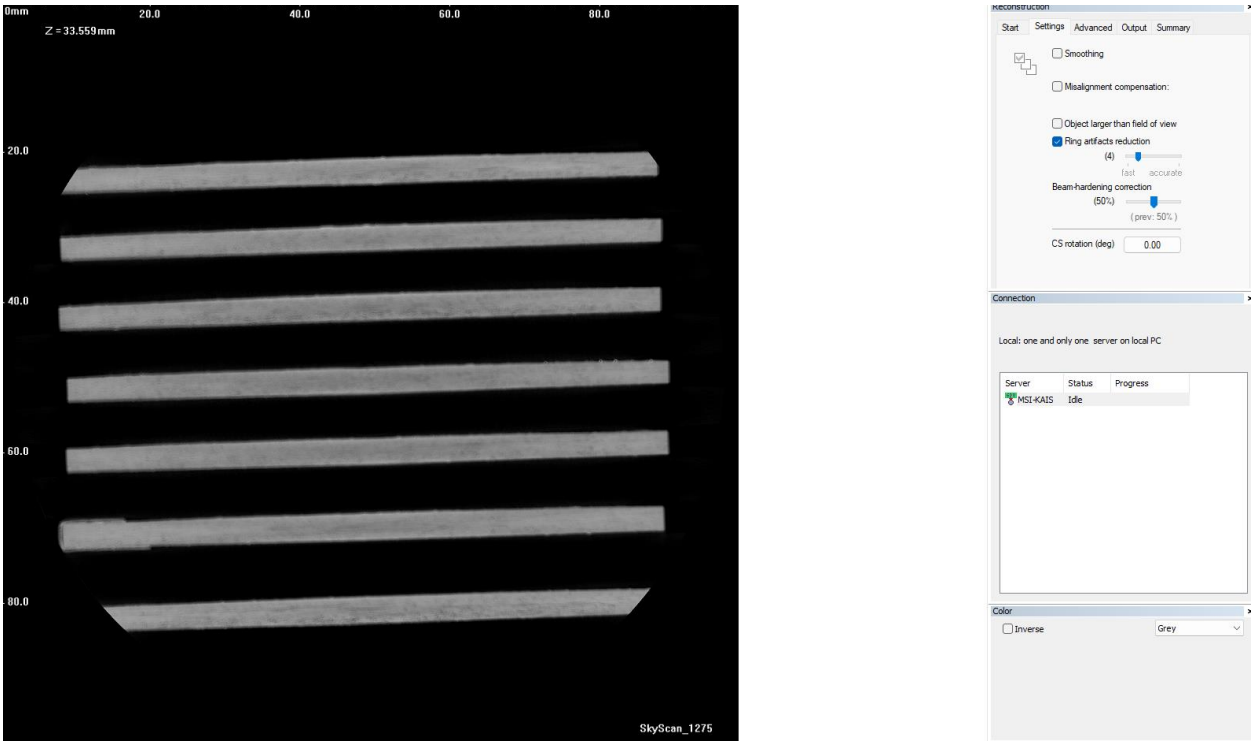

Figure 3.7 Preview output

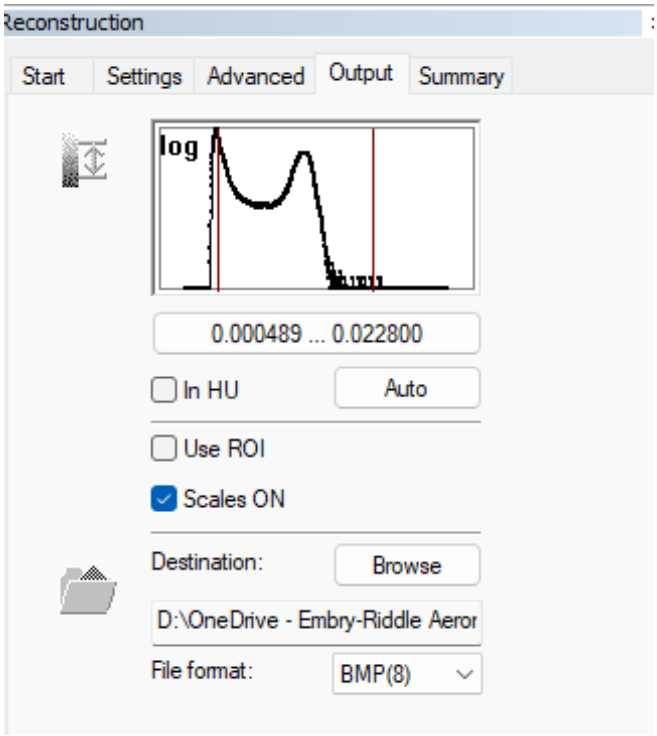

Figure 3.8 Histogram profile

The Matlab script automates the process, and the reconstructed images are saved in the order they are processed and numbered in sequence.

The subfolders' names followed the sample's pattern, where the initials "AS" were used for the $[45/90/-45/0/-45/0/-45/0/45/90/45/90]_s$ samples, and the "S" was used for the $[45/0/-45/90]_{3s}$ ones.

The top crop values for each of the separate samples are then determined with the help of the imaging process tool. Then, the travel distance is calculated and integrated into the sample height variable.

Two software instances are opened simultaneously (Figure 3.9), where the first image is from the bottom of the sample and the second is from the top. This approach accommodates the slight tilt in the samples, ensuring accurate cropping as the top crop and the height values were extracted in a way that would work for both.

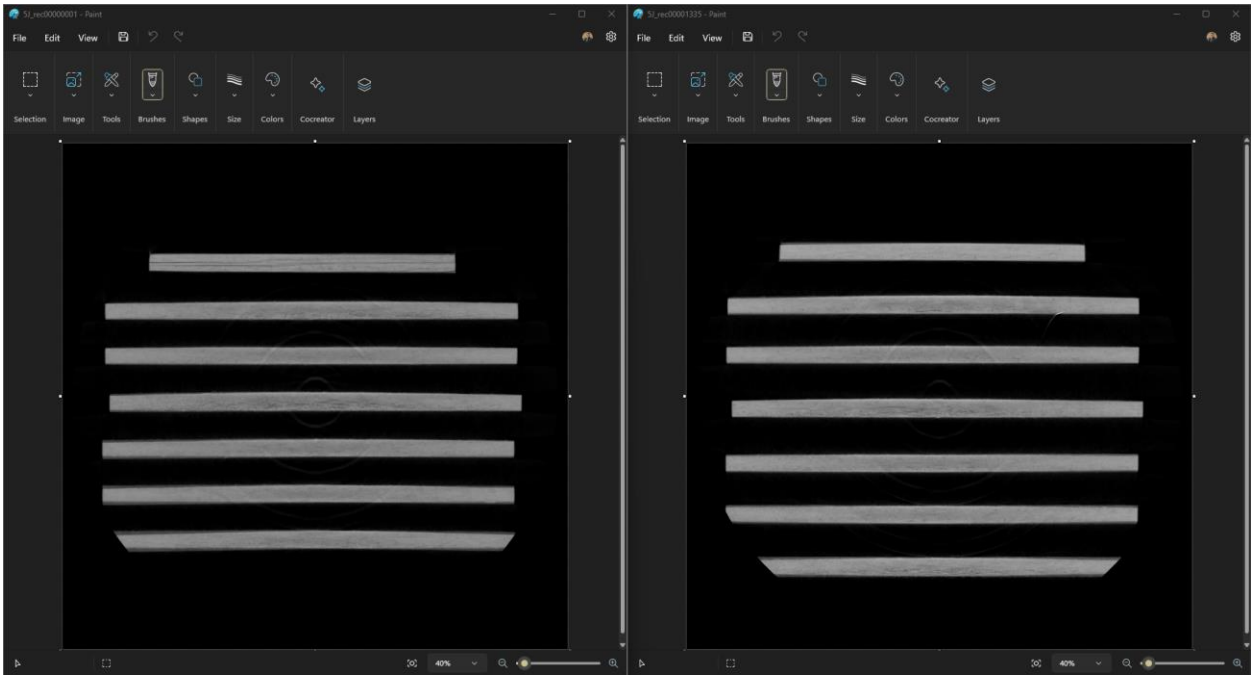

Figure 3.9 Crop values determination using Microsoft Paint

The log file and shadow image are then copied to each subfolder before the cropping tool initiates and starts reading each file, determining the height and width, and cropping the images based on the primary input. The next step is to pad the cropped images by adding a black mask to restore them to the initial image size of 1944x1944 pixels. Then, it would save each image in the appropriate folder while maintaining the sequence and naming profile. The outcome is a set of folders containing the X-ray imaging of exactly one sample (Figure 3.10).

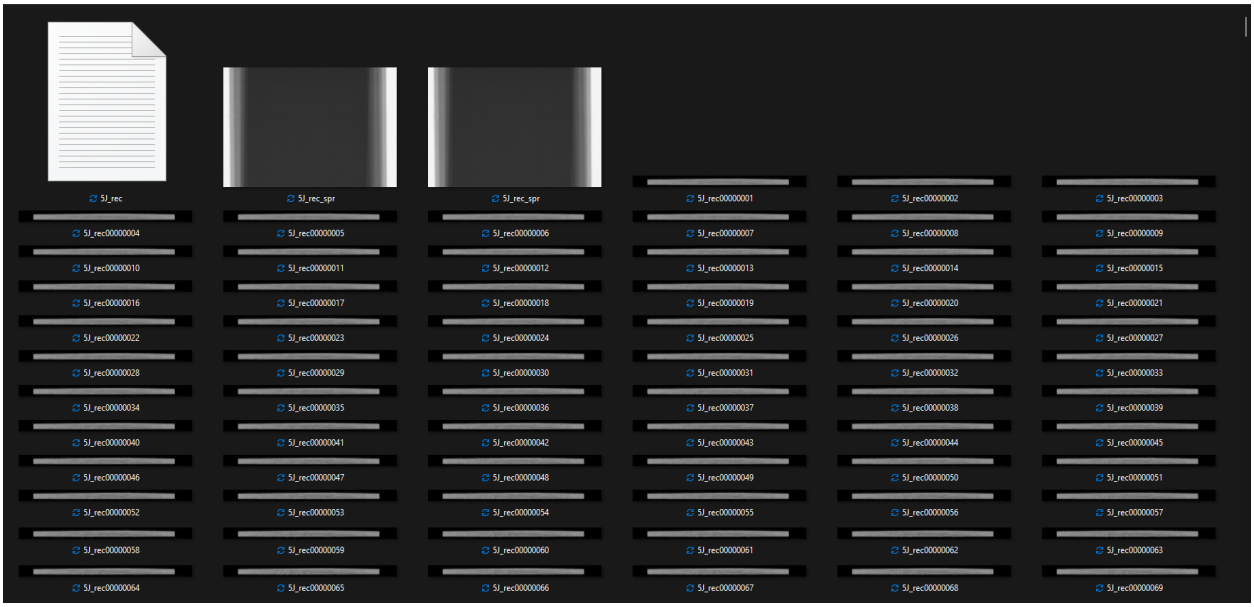

Figure 3.10 Sample output

CTVox software is essential in inspecting manufactured samples to detect any damages before moving on to the next stage. Images from the sample output are first imported into the software, creating a detailed 3D model (Figure 3.11). Users can alter the Opacity curve to reduce noise introduced by the scanning process, improving the visibility of critical information. A color map is manually constructed for a more refined examination (Figure 3.12), assigning unique hues to different portions of the sample, making identifying changes or defects within the medium easier.

Once the inspection and adjustments are complete, the final color profile is saved in the CTVox folder under “ColorProfileCompositeDelamination.tf," ensuring that the precise parameters used in the inspection are documented and retrievable for future analysis or comparison.

The consistent blue/green hue signifies no variation within the medium, thus confirming the sample's high quality by showing no signs of damage. Conversely, as depicted in Figure 3.13, a compromised sample is marked by a change in color at its center, signaling a variation in the medium or, in other words, delamination within the sample.

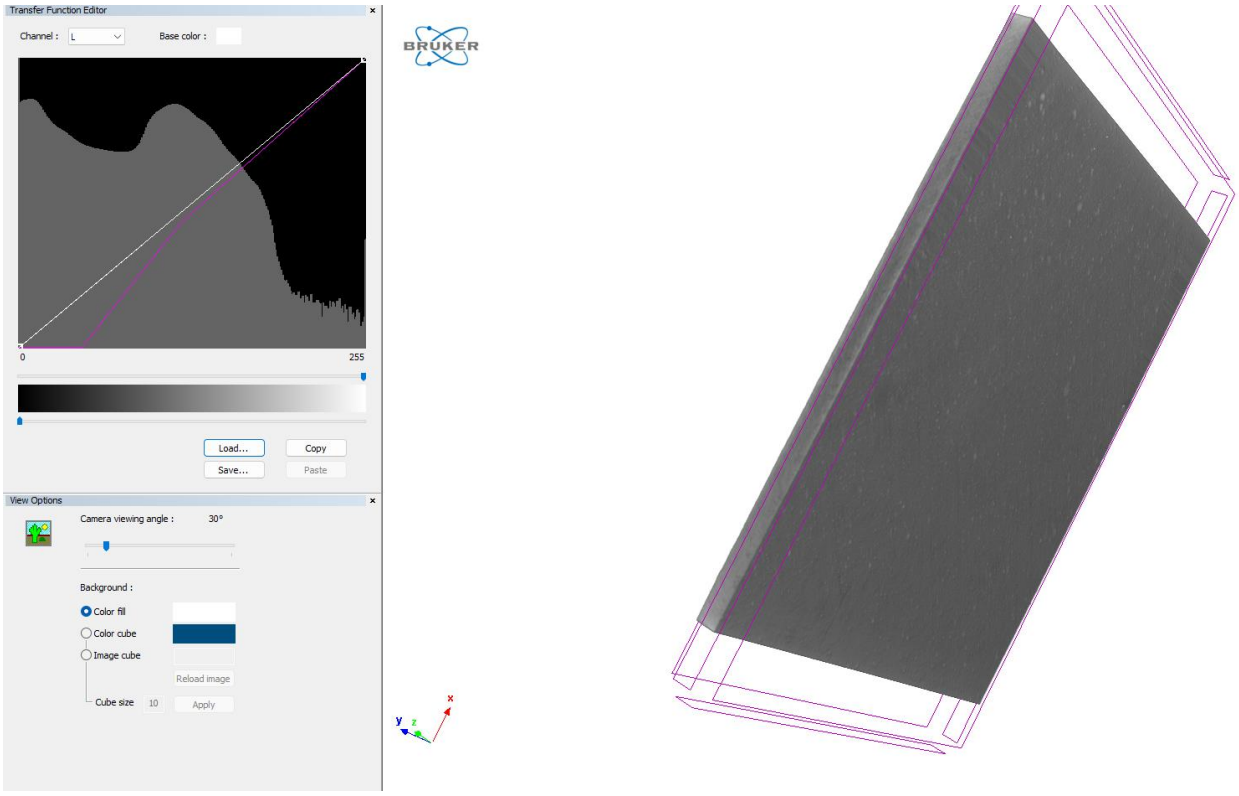

Figure 3.11 CTVox loading window with a grey scale sample

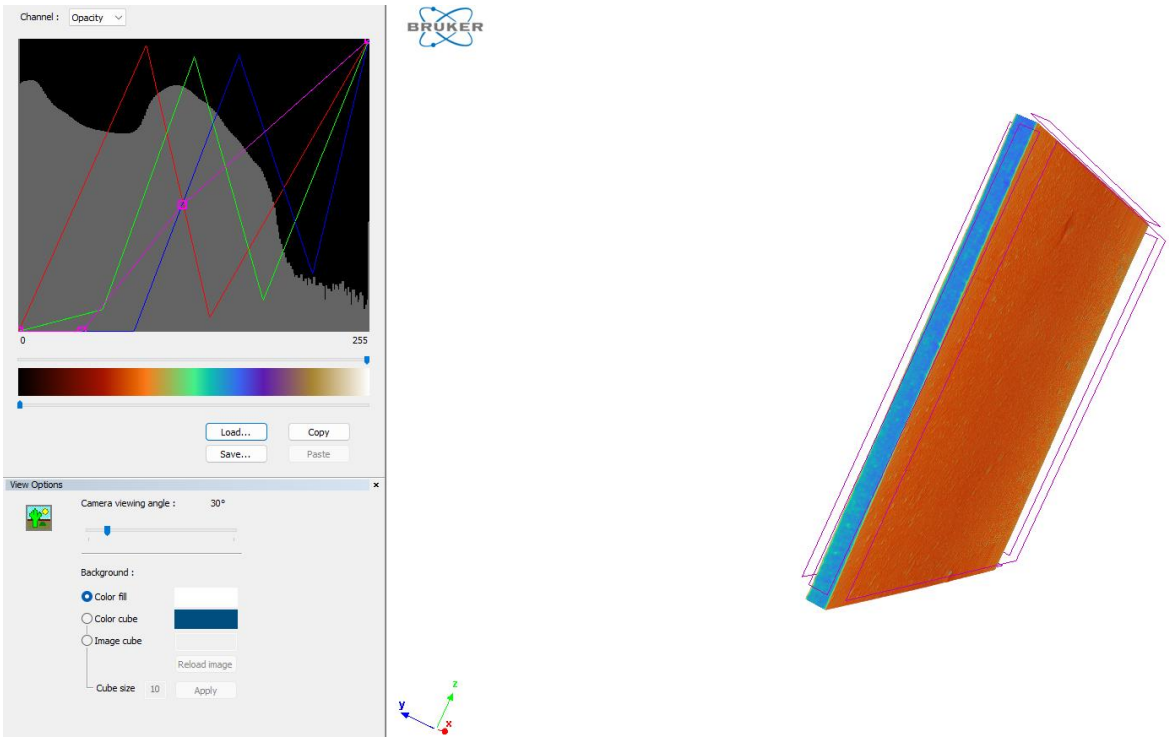

Figure 3.12 Sample with the color map applied.

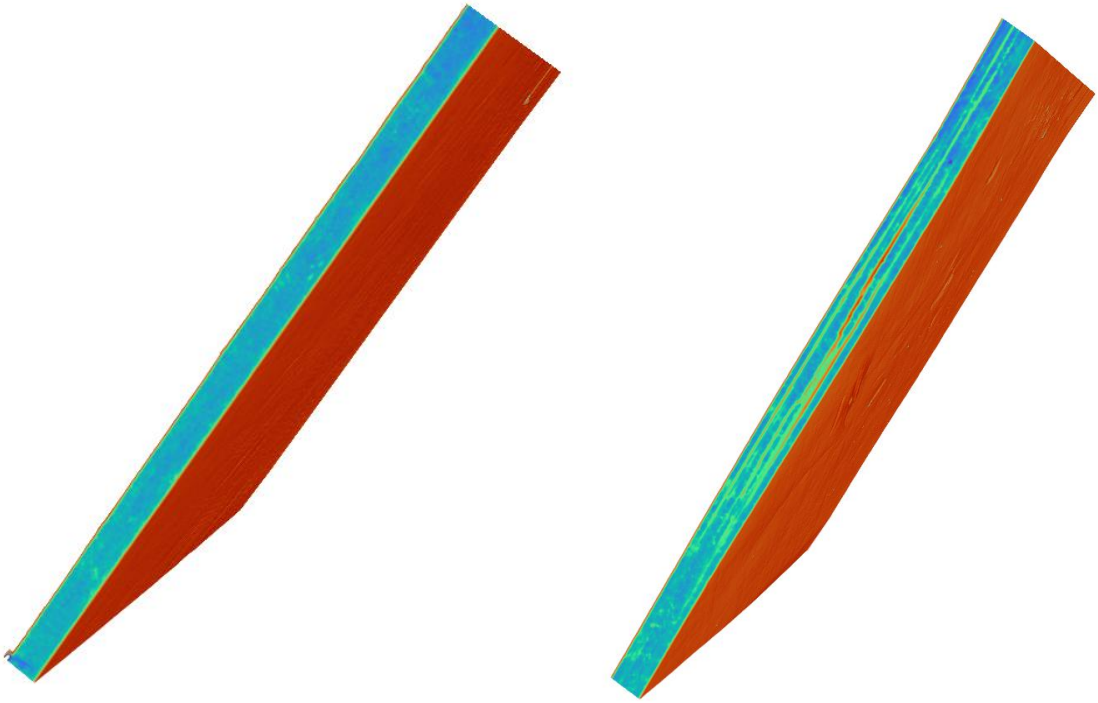

Figure 3.13 Side-by-side comparison of a pristine (left) vs damaged sample (right)

At the end of the inspection process, 50 coupons passed the initial inspection, whereas 5 of each layup failed. The samples that have failed the inspection process are repurposed as testing coupons based on the type of damage to optimize the speckling technique or approximate the energy levels required to generate a BVID.

3.3.3 Speckle Patterns Application

The Digital Image Correlation (DIC) technique is selected to measure strain and displacement in ASTM D3039, ASTM D664, and ASTM D7136 samples under the applicable testing standard. The DIC would reduce the inaccuracy of measuring strain using bonded strain gages with a linear variable differential transformer [37].

Speckling for Digital Image Correlation (DIC) is a necessary preparation step that ensures accurate and dependable measurements by capturing and analyzing a specimen's surface images. At the same time, it deforms, thereby estimating surface displacements and strains. For the software to accurately track and correlate the images, the quality and pattern of the speckles are crucial. A random, high-contrast pattern is typically applied to the sample's surface through painting, spraying, or adhesive stickers. The material and observation scale determines the specific pattern used. Ensuring the highest quality of the speckle pattern is critical; it must be generated at random, possess sufficient contrast and size regarding the region of interest and the camera's resolution, and maintain stability during the testing process.

As seen in Figure 3.14, a randomized speckle pattern was deposited using spray paint on the surface of the coupons for the ASTM D3039 and ASTM D6641 samples. Afterward, the samples are brushed to remove stray specks that may otherwise fall during testing, disrupting the quality of reference points for the DIC to function correctly.

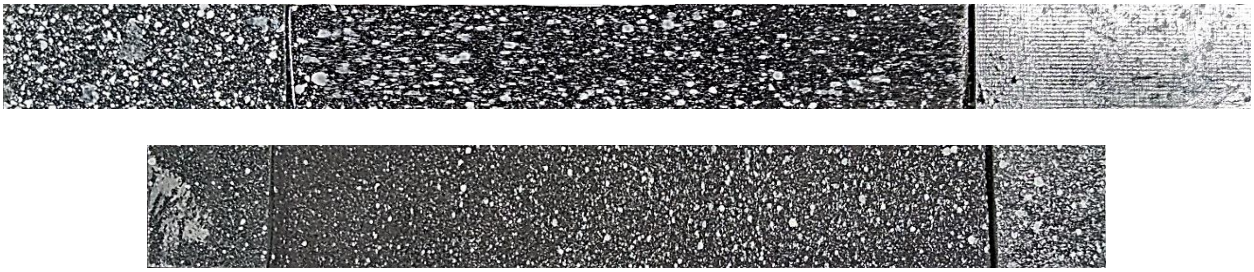

Figure 3.14 Speckle patterns on ASTM D3039 samples (Top: 0, Bottom: 90) [13]

The exact process was used to apply the speckle patterns on the testing coupons with a more refined distribution of the speckles, as localized strain value determination is crucial for the following research step.

3.4 Mechanical Testing of CFRP Samples

This segment examines standard experiments of composite coupons cured following the steps provided by the prepreg manufacturer to determine the exact material properties of the samples used to investigate the delamination propagation for a comprehensive BVID study [13]. This effort focuses on defining the elastic moduli E. The unidirectional fiber-reinforced composites' strength and stiffness characteristics are assessed using samples with 0° and 90° fiber orientations under tensile and compressive loads.

The load is applied using the Tinius Olsen, and the appropriate dimensions and loading parameters are entered into the Horizon program, including a timestep of 3mm/min (0.1181in/min) for compressive and tensile loading. The DIC assembly is then positioned facing the sample (Figure 3.15), and the cameras are manually focused on the calibration specimen by adjusting the illumination and zoom range with Vic-Snap software's help.

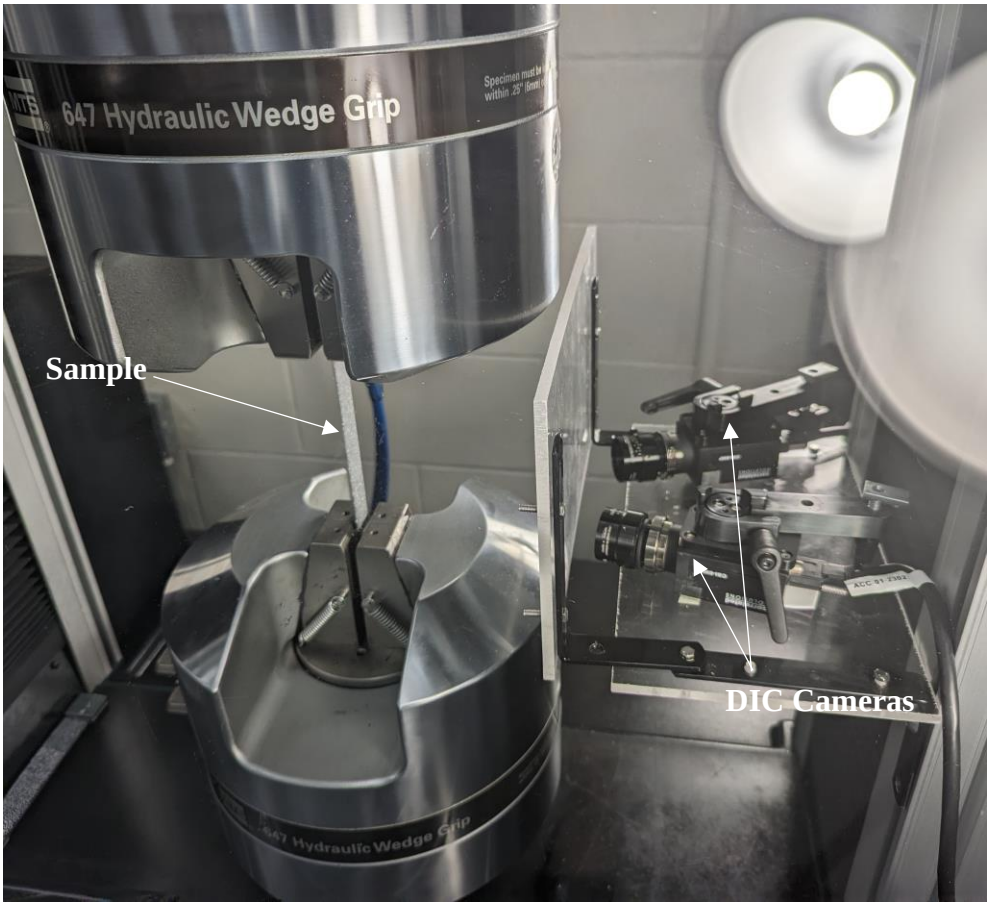

Figure 3.15 Sample fixture and DIC setup positioning

A two-camera setup is not strictly necessary for the 2D analysis of surface strain; however, it was employed to acquire two distinct data sets, allowing for comparative analysis and validation in the event of uncertainties or discrepancies. The samples were carefully mounted and secured using a hydraulic grip, ensuring stability and consistent load application throughout the testing. Horizon and Vic-Snap software systems were synchronized to facilitate seamless data acquisition, enabling simultaneous capture and recording of the specimen's behavior. The testing protocol was executed through the complete failure of the samples, providing a complete dataset encompassing the entire deformation and failure process.

The subsequent step involves the Vic-2D software to analyze the speckle images for a particular specimen. Once these images are loaded, the Area of Interest (AoI) tools are exploited

to delineate the specific region for detailed analysis. In addition, a reference point is selected to verify the autocorrelation of the reference point (Figure 3.17).

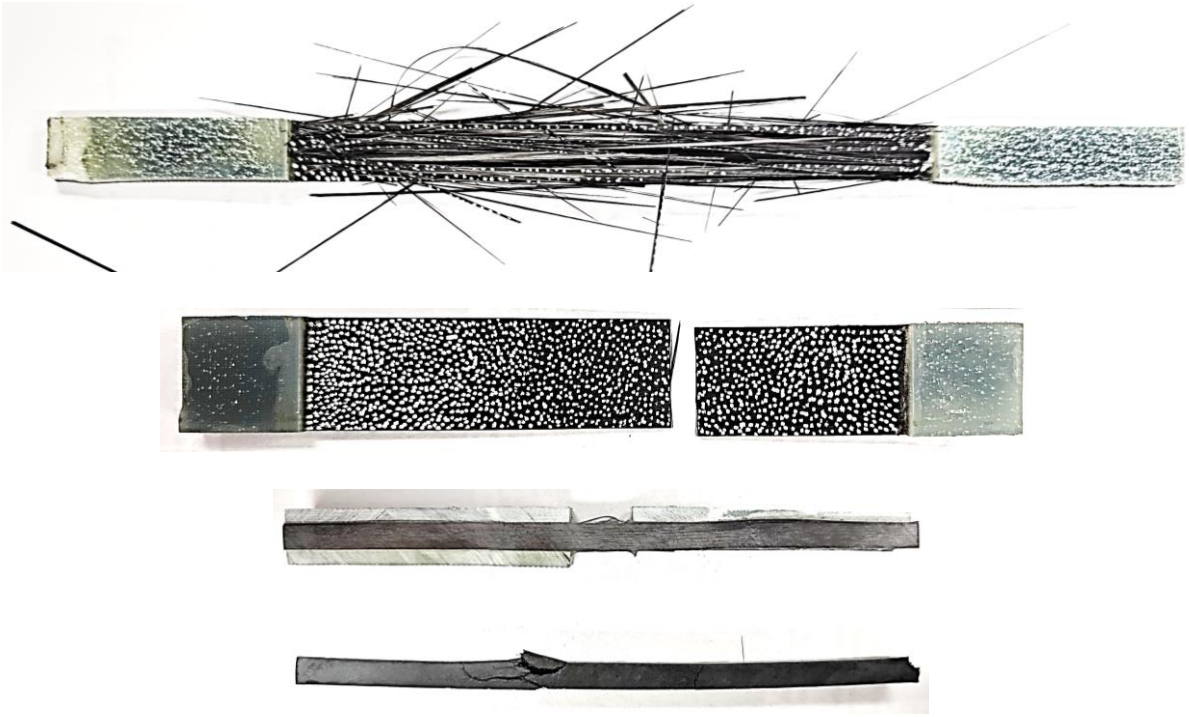

Figure 3.16 Aftermath of the testing procedure (from the top: 0° tensile, 90° tensile, 0° compression, 90° compression)

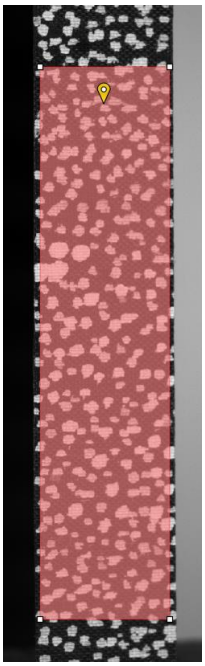

Figure 3.17 Area of interest and reference point selection

Following the definition of the reference point and the AoI and clicking on the question mark, a subset size suggestion is automatically generated, as seen in Figure 3.18.

The step size is then selected, determining the strain's resolution. In the case of the determination of material properties, localized strain is not of significant use. Therefore, a step size of 7 was selected to reduce the computational load while maintaining the quality of the results.

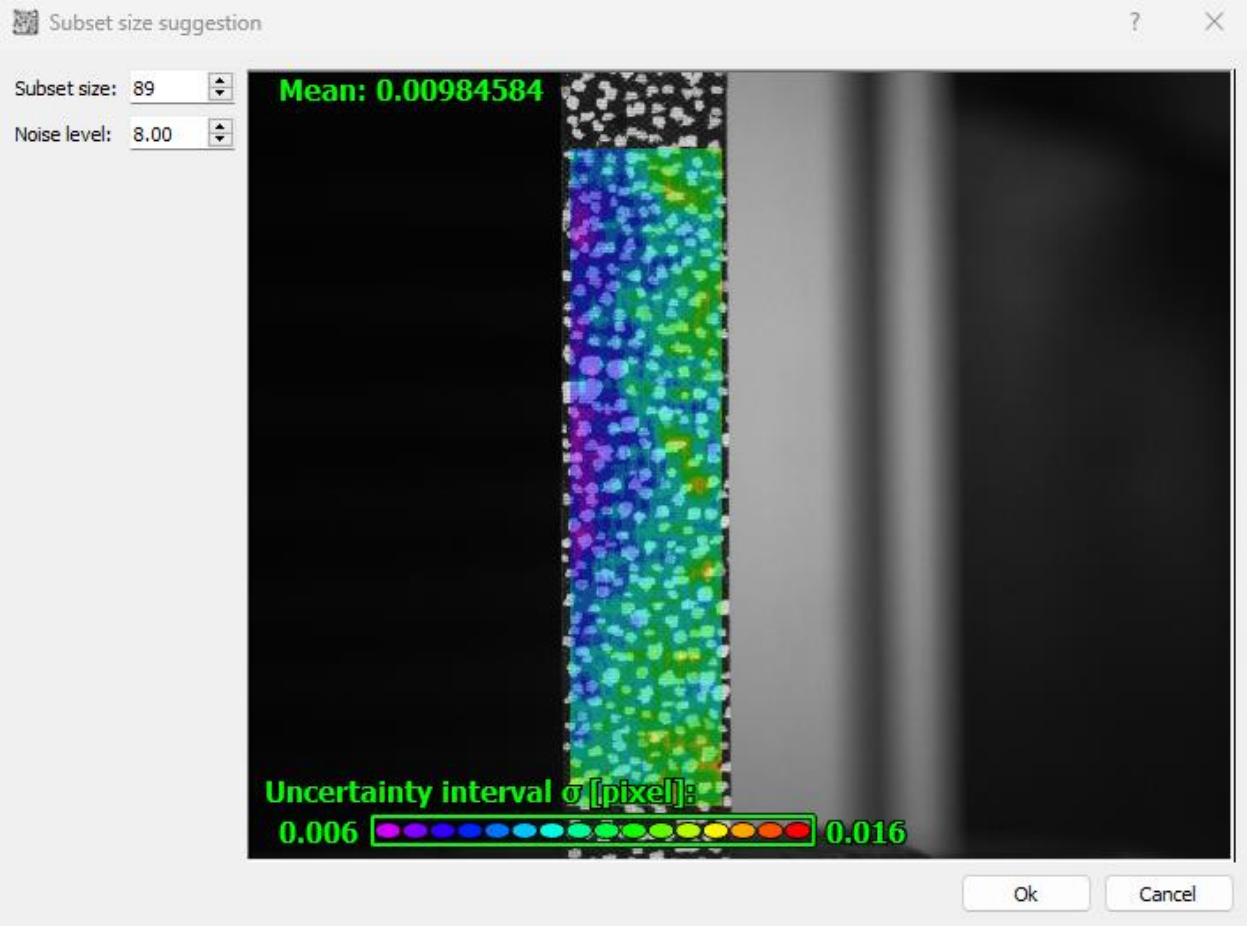

Figure 3.18 Subset size suggestion

In Vic-2D, The default options for the subset were kept where they were weighted according to the Gaussian weight. The system processed 901 photos for the first sample, finishing the operation in 6 min and 30 seconds. The analysis produced accurate results, with error levels as low

as 0.002. This minimal error margin attests to the quality of the recorded images and Vic-2D's ability to extract accurate data.

Trailing the analysis, the post-processing part consists of calculating the strain values. The strain could be determined using a variation of tensor types and variables; for this research, a Lagrange tensor type is selected.

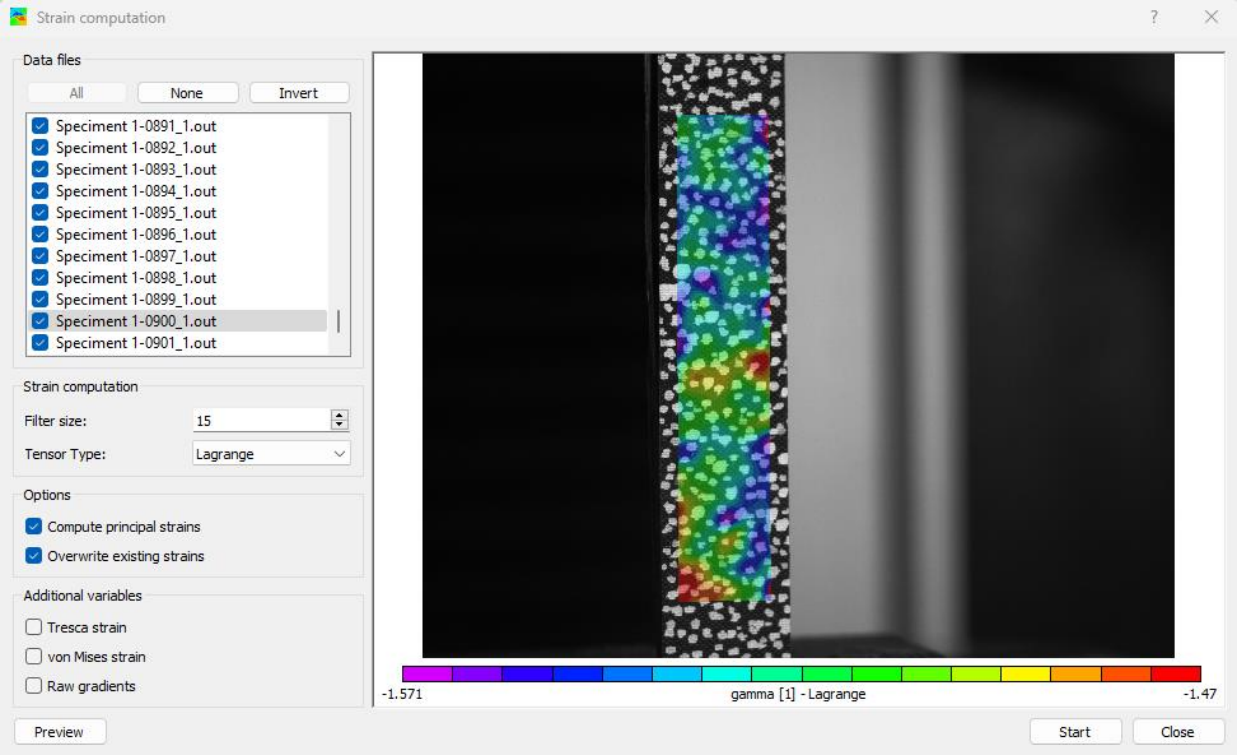

Figure 3.19 Strain computation

From there, only the mean values of 'ε_{yy}', known as the strain value in the y-axis direction, are extracted and saved for further analysis.

The process is repeated for all five samples for every testing method. The strains were later plotted against the stress values automatically generated by the Horizon software to extract the elastic moduli of each sample.

3.5 Comparative Analysis of CFRP Mechanical Properties

Conducting a comparative analysis of experimental findings and manufacturer-supplied specifications is crucial for verifying the precision and dependability of material claims. This section analyzes the data provided by the manufacturers, followed by a comparison with the observed results obtained from the trials.

3.5.1 Manufacturer's Material Specifications and Preliminary Analysis

Manufacturers of prepreg materials customize the properties and details supplied according to particular applications and the prepreg's components. They provide various data, including the reinforcement fiber type, resin type, recommended curing temperatures and methods, and physical attributes such as thickness and weight. They also include critical mechanical properties like tensile and flexural strength, helping users choose the suitable material for their applications.

The prepreg used for this research was provided by Patz Materials and Technologies (PMT). It comprises their proprietary PMT-F7 epoxy resin with mechanical properties shown in Table 3.2, accompanied by Hexcel® HexTow® IM7 12K., the latter having a modulus of 276GPa [38].

Table 3.2 Mechanical properties of PMT-F7 resin

Tensile strength (N/m^2)	**Tensile modulus E_m (GPa)**	**Maximum strain (%)**
71.829	2.99	4.14

Table 3.3 Mechanical properties for laminate: PMT-F7 / IM7 12K unidirectional fiber

	Strength (N/m^2)	**Modulus (GPa)**	**Test method**
0° Tension	2748.250	159.270	ASTM D3039
0° Compression	1968.453	151.685	ASTM D6641

It is worth noting that crucial details, such as the fiber volume fraction in the prepreg and the elastic modulus of the laminate at 90° for both tension and compression, are frequently overlooked by manufacturers. In addition, critical parameters such as the Poisson Ratio and Shear Modulus, which are essential for the computation of characteristics of multilayer composites, are sometimes omitted from the specifications provided.

The Voigt model, often called the rule of mixtures, is a straightforward approach for initial estimates of composite material properties. It simplifies analysis by assuming that fibers and the surrounding matrix are aligned parallelly, providing a maximum estimate of the material's characteristics. This method is beneficial for early analysis or when detailed microstructure information is unavailable[39]. By applying this model longitudinally, and with known values for the fiber and matrix's modulus, it is possible to calculate the fiber volume fraction V_f of the composite.

$$E_c = E_f \cdot V_f + E_m \cdot (1 - V_f) \tag{3.1}$$

Where E_c , E_f , and E_m are the composite, the fiber and the matrix moduli respectively.

$$V_f = \frac{E_m - E_c}{E_m - E_f} = \frac{2.99 - 159.270}{2.99 - 276} \approx 0.57 \tag{3.2}$$

Consequently, the fiber volume fraction is determined to be roughly 57.2%.

After establishing the fiber volume fraction, the transverse modulus $E_\perp$ can be calculated employing the inverse rule of mixtures [40,41].

$$\frac{1}{E_\perp} = \frac{E_f}{V_f} + \frac{E_m}{1 - V_f} \tag{3.3}$$

$$E_{\perp} = \frac{1}{\frac{0.572}{276} + \frac{1-0.572}{2.99}} \approx 6.89GPa \tag{3.4}$$

3.5.2 Empirical Evaluation and Manufacturer Data Comparison

The accuracy of Digital Image Correlation (DIC) measurements is significantly influenced by the quality of the speckle pattern and the close correlation between analyzed images [42,43]. As the samples reached their maximum load capacity, the sudden shift in speckle pattern positioning compromises the quality of results, notably if post-processing included images past the proportional limit. Thus, the analysis will focus solely on the elastic zone for comparison.

Subsequent figures will present the data from five specimens for each test method, set against the manufacturer's data for each test.

Along with the comparison, the standard deviation for each test method is defined by calculating the mean of the experimental values "x_i" and determining the standard deviation by square rooting the sum of the squared deviation divided by the number of samples "*N*". The percentage error can then be calculated using the (3.7) equation, where "*M*" is the value provided by the manufacturer.

$$Mean = \frac{\sum x_i}{N} \tag{3.5}$$

$$Standard\ \ Deviation = \sqrt{\frac{\sum (x_i - Mean)^2}{N}} \tag{3.6}$$

$$\%error = \frac{Mean - M}{M} \times 100 \tag{3.7}$$

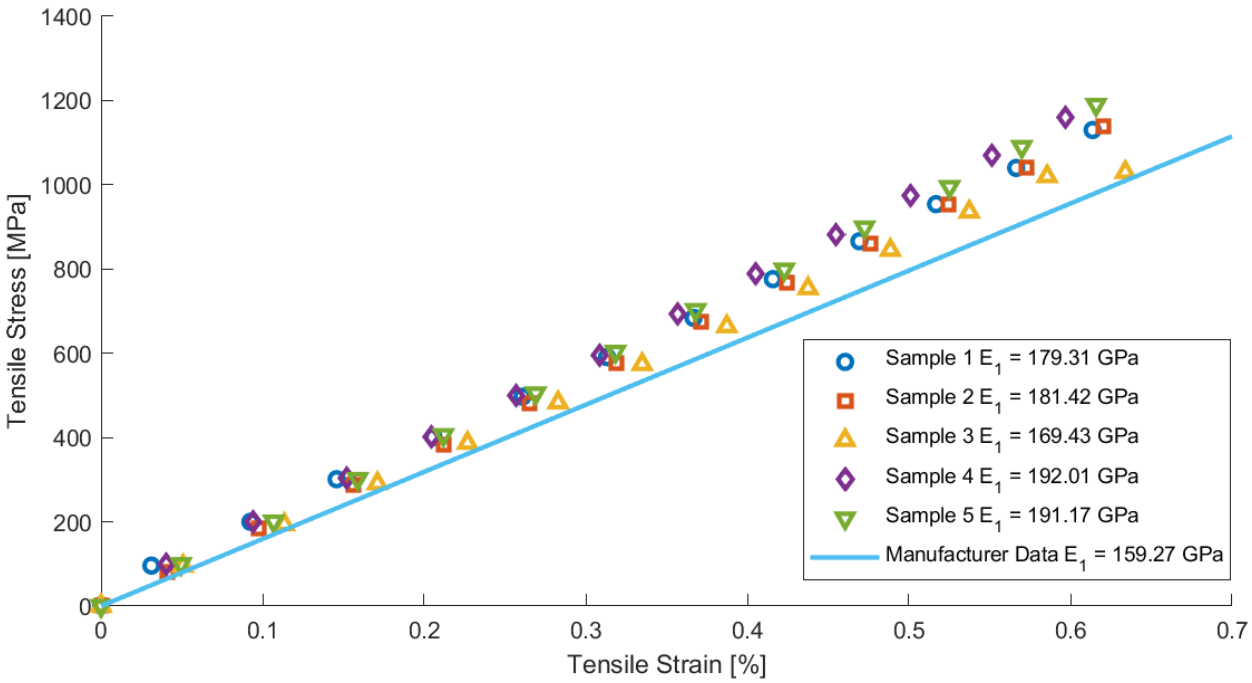

Figure 3.20 Tensile testing results in the 0° angle vs. the provided manufacturer's data

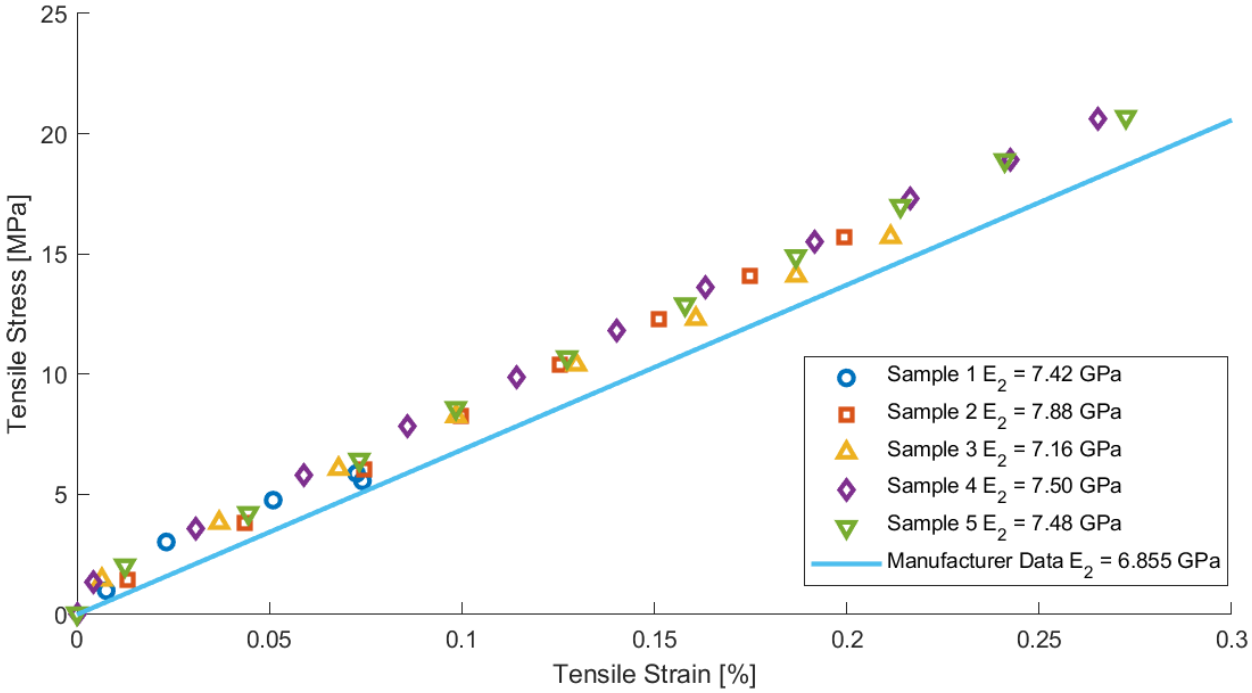

Figure 3.21 Tensile testing results in the 90° angle vs. the provided manufacturer's data

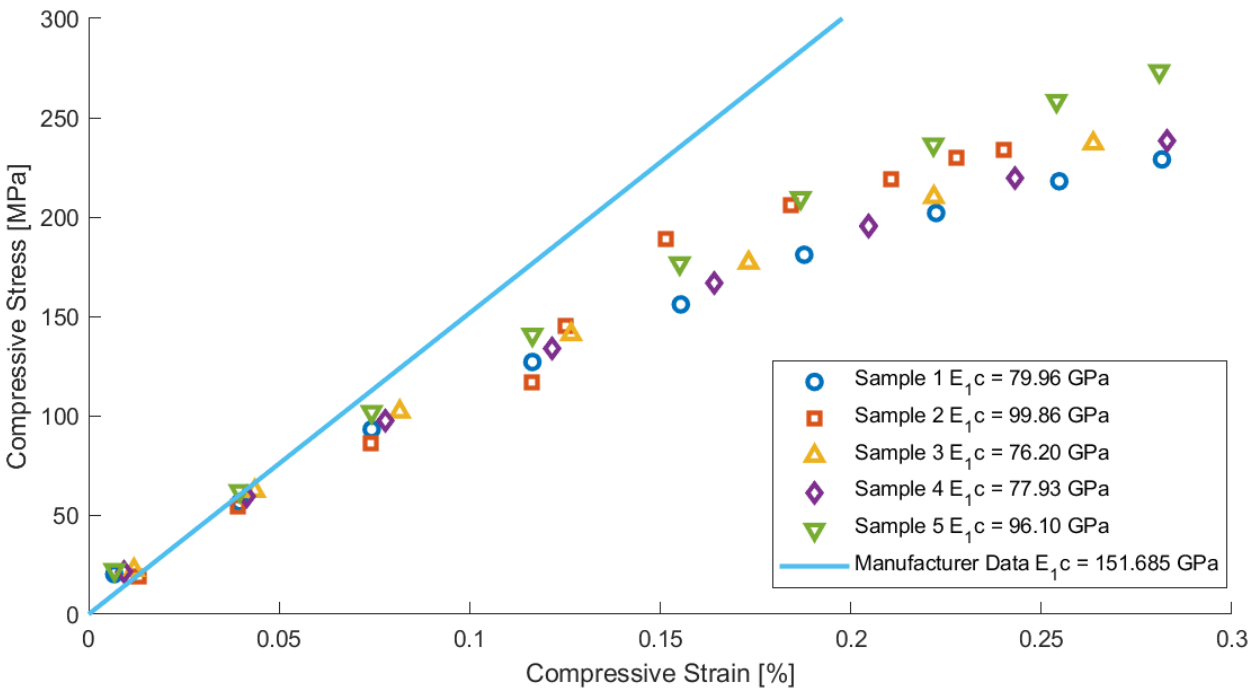

Figure 3.22 Compressive testing results in the 0° angle vs. the provided manufacturer's data

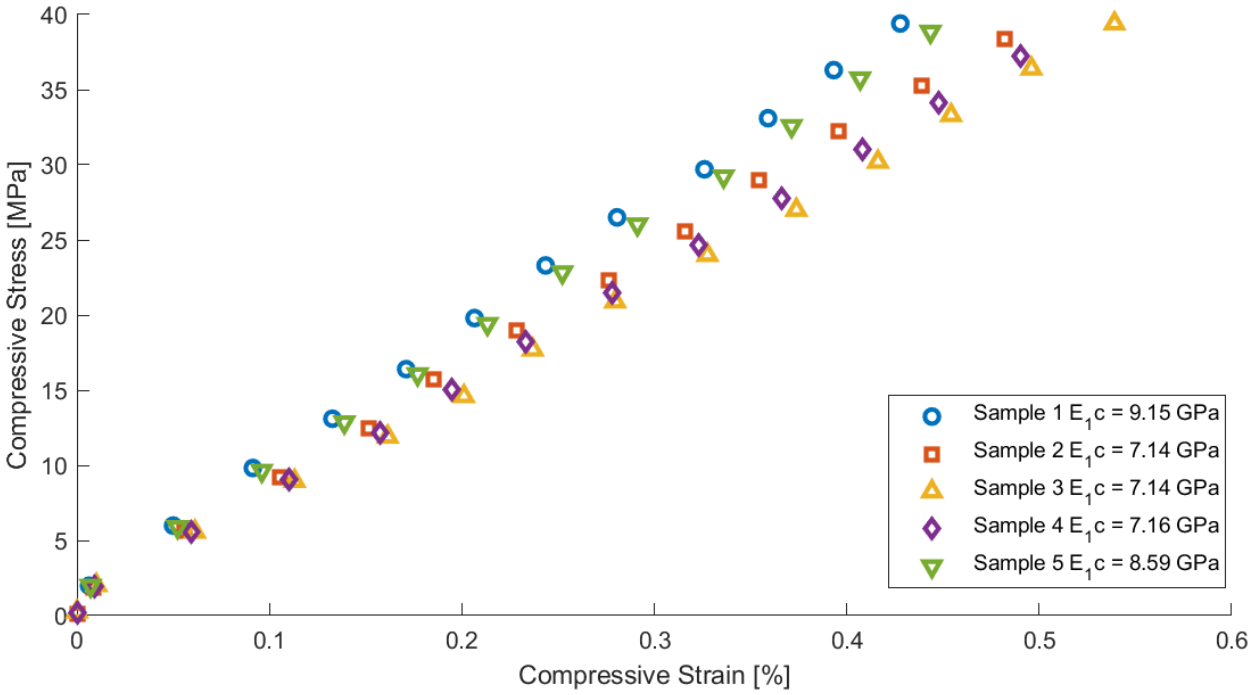

Figure 3.23 Compressive testing results in the 90° angle

Concerning the tensile tests performed in a 0° orientation, the experimental values exhibit a standard deviation of around 8.34 GPa. Moreover, across all samples, the mean percentage inaccuracy to the data provided by the manufacturer is around 14.69%. The degree of inconsistency seen is significant and requires further investigation, which will be further expounded upon in the following section.

The calculated standard deviation for the 90° samples subjected to tensile testing is approximately 0.23 GPa, indicating a narrow data spread around the mean value. This low standard deviation implies a consistent material behavior within the specific testing environment. Furthermore, an average percentage error of 9.23% has been noted to the manufacturer's data. This figure falls below the often-accepted maximum error threshold of 10% for composite structures, a benchmark reflecting the tolerance for variability and unpredictability inherent in such materials[44].

The standard deviation in compressive testing along the fiber orientation was 9.92 GPa, indicating significant variability in compressive strength outcomes. The average percentage error of 43.30% compared to the manufacturer's expectations markedly surpasses common standards, indicating significant inconsistent material behavior. This discrepancy and its reasoning are discussed in the following section, with methods to improve the findings.

As for the 90° compressive testing, where manufacturer specifications are absent for the compressive modulus, the calculated standard deviation of 0.58 GPa and an average percentage error of 6.21% relative to the mean underscore the results' consistency. This level of precision in the data points, particularly in the absence of a manufacturer benchmark, indicates a notable degree of reliability and uniformity in the material's compressive behavior at a 90-degree orientation.

3.5.3 In-depth Analysis of Discrepancies in Results

The CFRP samples showed significant differences in elastic modulus values when compared to the specifications provided by the prepreg manufacturer. Such differences point to possible changes in the composite's composition or processing parameters during manufacturing. The elastic modulus rose in the 0° orientation, reaching up to 192 GPa. The Voigt modulus equation was used to investigate the causes of these variations, with the goal of quantifying changes in fiber volume fraction, an essential metric in defining the mechanical properties of composite materials.

$$V_f = \frac{E_m - E_{cx}}{E_m - E_f} = \frac{2.99 - 169.43}{2.99 - 276} \approx 0.6096 \tag{3.8}$$

The fiber volume fraction was recalculated using this method, demonstrating an increase from 57% to 60.9%. This increase indicates that the matrix volume in the composite has decreased, mainly due to absorption processes during manufacturing processes.

The recalculated fiber volume fraction was then used to approximate the experimental elastic modulus in the 90° direction.

$$E_{\perp} = \frac{1}{\frac{0.6096}{276} + \frac{1 - 0.6096}{2.99}} \approx 7.53 GPa \tag{3.9}$$

In this instance, the recalculated value using the adjusted fiber volume fraction aligns closely with the mean experimental value of 7.49 GPa derived from the 90° tensile tests. This adjustment significantly narrows the percentage error from 9.23% to 0.534%, leading to a more accurate representation of the material's properties.

An SEM image analysis of the 0° tensile test sample (Figure 3.24) validated the fiber volume percentage. The fiber count was calculated using an in-house built MATLAB image processing technique (APPENDIX - B), which verified a fiber volume fraction of around 60.86%.

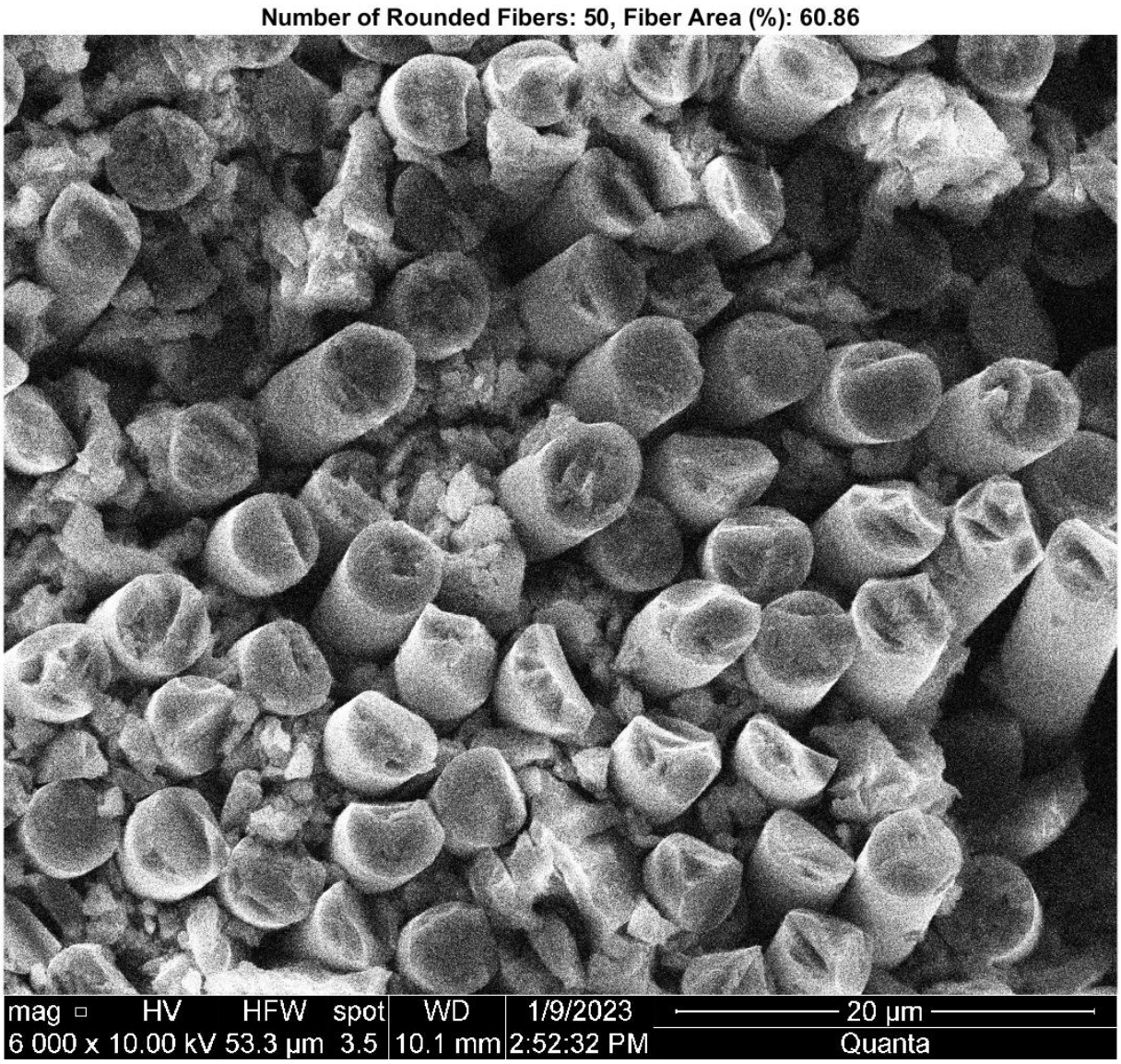

Figure 3.24 Fiber distribution image taken using SEM along the 0°

In the compression tests conducted along the fiber orientation orientation, the significant variation observed in elastic modulus values is believed to be primarily due to sample buckling. This phenomenon is attributed to the compromised effectiveness of the matrix component, which is crucial for distributing the load evenly across the fibers. To refine the accuracy of the results, data points beyond the 0.03% compressive strain, as illustrated in Figure 3.25, were excluded from the analysis. This methodological adjustment reduced the average percentage error compared to

the manufacturer's specified modulus of 151.685 GPa, settling at approximately 6.87%. Furthermore, the standard deviation was recalculated to be around 3.54 GPa.

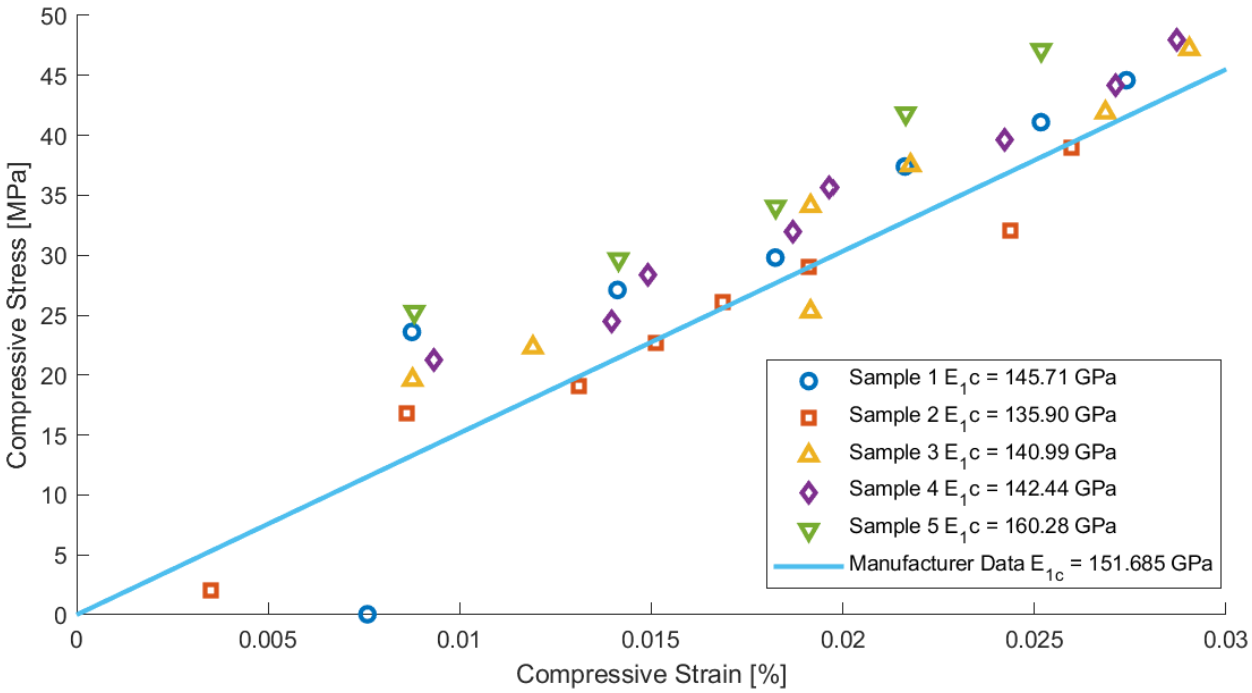

Figure 3.25 Adjusted compressive testing results in the 0° angle vs. the provided manufacturer's data

Table 3.4 Measured vs. manufacturer's elastic modulus

	Measured Modulus (GPa)	**Manufacturer Modulus (GPa)**	**Standard Deviation (GPa)**	**% Error**
0° Tension	182.668	159.27	8.34	14.69
0° Compression	86.010	151.685	9.92	43.30
0° Compression Adjusted	145.064	151.685	3.54	6.87
90° Tension	7.488	6.855	0.23	9.23
90° Compression	7.836	N/A	0.58	N/A

3.6 Inducing BVID for Damage Analysis

Before conducting the impact tests on the Carbon Fiber Reinforced Polymer (CFRP) sample, it is essential to consider the material's specific properties and the anticipated responses at different energy levels. The CFRP with a fiber volume fraction of 60.96%, exhibits varying elastic moduli in different orientations: in the 0° direction, it has a high tensile modulus of 182.668 GPa and a compressive modulus of 145.064 GPa, indicating significant stiffness and resistance to deformation along the fiber direction. Conversely, the 90° orientation shows a lower tensile modulus of 7.488 GPa and a compressive modulus of 7.836 GPa, suggesting more compliance and energy absorption capacity perpendicular to the fiber direction.

Given these properties, different reactions are expected at varying impact energies. At lower energies (2.5, 5, 7.5 Joules), the CFRP will likely exhibit minor surface damage and delamination, especially along the interfaces of different fiber orientations. This is due to the material's balance between stiffness and compliance, where the energy absorption is not uniform across the orientations. Intermediate energies (10, 12.5 Joules) may induce more significant delamination and interlaminar damages, potentially affecting the CFRP's critical layers depending on the impact point.

At the highest tested energy (15 Joules), it is expected to observe extensive delamination and matrix cracking due to the high stiffness in the 0° orientation, which could lead to energy being transmitted more forcefully to the less stiff areas, risking damage to the core structural layers of the CFRP. This analysis sets the stage for a comprehensive understanding of how the CFRP will respond under the impact tests, with the elastic moduli playing a crucial role in defining the material's behavior under different impact scenarios.

Equipped with the results from determining material properties, low-velocity impacts (LVI) were performed using the Instron 9250HV to generate BVIDs. These BVIDs mimic the damage caused by tool dropping, runway debris, or any small impact factor on the composite surface.

The first step is to determine the support conditions. To prevent the sample from dislodging, it was clamped along all four edges instead of simply supporting it, which would have resulted in more damage than anticipated if it had been simply supported [45]. It also allowed for more realistic damage initiation compared to the back-face support. The current 9250HV system has a pneumatic clamping fixture (Figure 3.26) that secures the coupon with 65psi±5psi of pressure to ensure the clammed support conditions and a rebound stopper that inhibits the drop sled from re-hitting the sample.

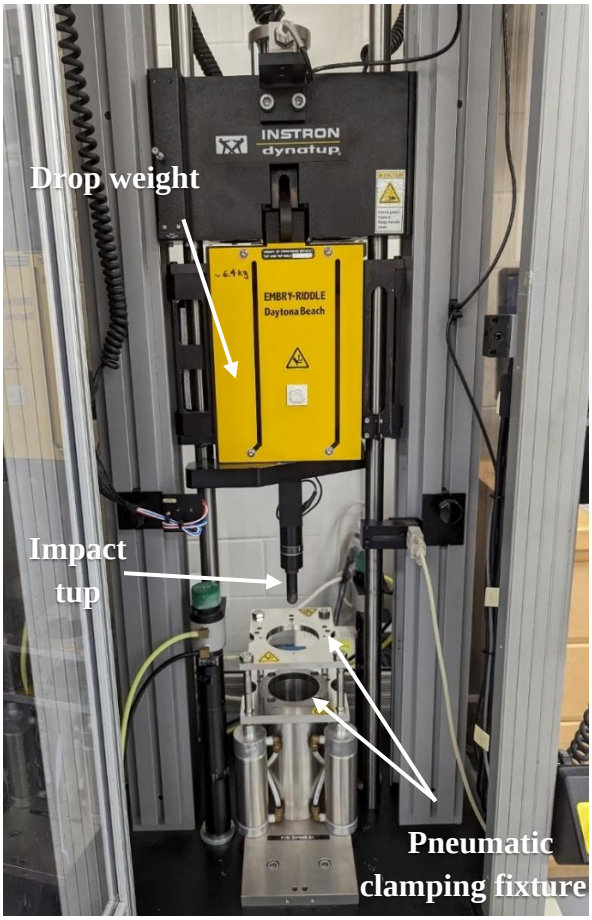

Figure 3.26 9250HV system parts

The selection of the tup diameter and the energy levels for the impact is crucial as the research aims to generate various BVID outer damage diameters without reaching the visible range. For this purpose, samples that failed the inspection are selected and subjected to impact energy levels ranging between 2.5 and 15 Joules (1.84-11.06 ft-lb) with the help of a blunt 0.5-inch diameter hemispherical tup. These levels are selected to generate matrix crack and delamination while preventing fiber breakage and perforation[46] (Figure 3.27).

Calibrating the drop weight value was necessary to attain the desired energy levels; however, the software could not accurately register the weight due to a malfunctioning sensor. Attempts to resolve this issue with Instron were unsuccessful since the system had entered phase 4 (Out of production/reasonable efforts) [47]. Consequently, Instron advised a workaround by suggesting the manual entry of 6.4 kg as the drop weight and bypassing the calibration process altogether.

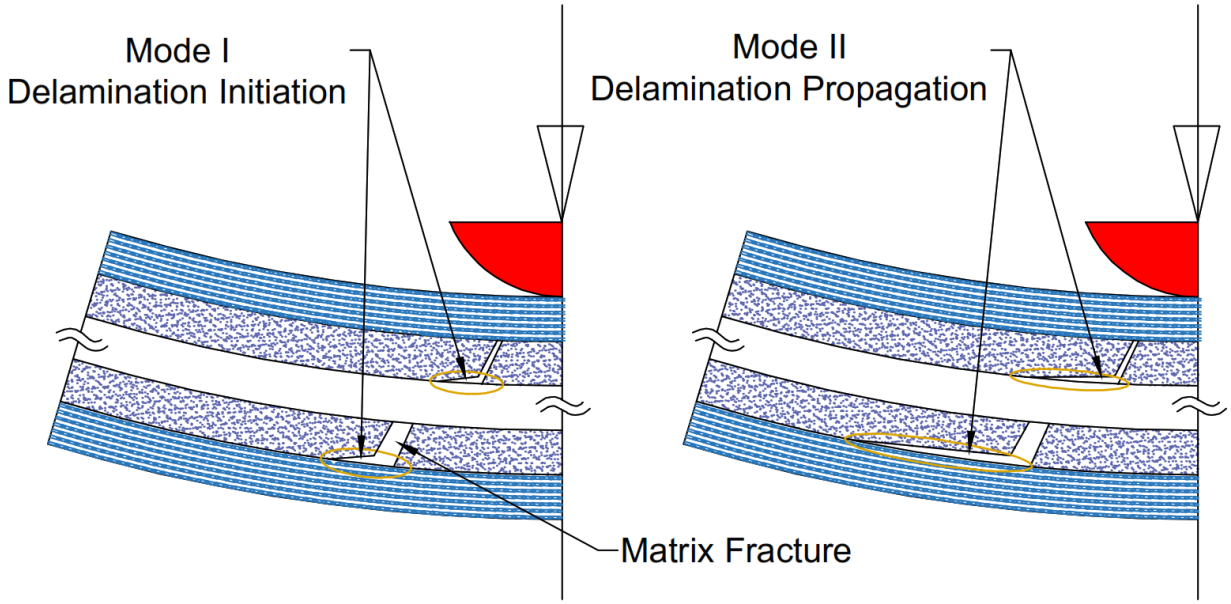

Figure 3.27 Delamination initiation (mode I) and propagation (mode II) [13].

Additionally, two channels for recording impulse data from the tup and the dynamic load were coupled to the data acquisition system.

The final parameter to be assigned would be the data acquisition frequency. Considering that the tangible impulses would last between 5 and 10 milliseconds, the recording range was set to 100 milliseconds to prevent the premature termination of the recording and to provide approximately 32,000 data points. The collected data consists of load, velocity, impact energy, and time, enabling the consistency of impact parameters.

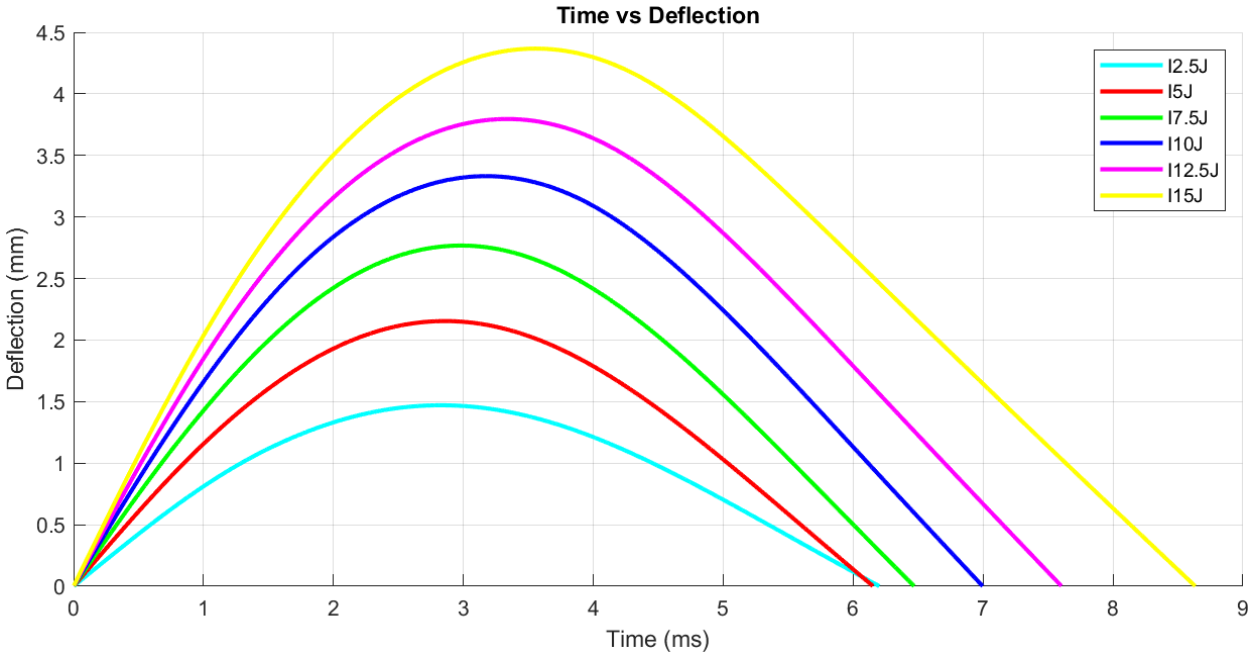

Figure 3.28 Time (ms) vs. deflection (mm) curve at varying energy levels

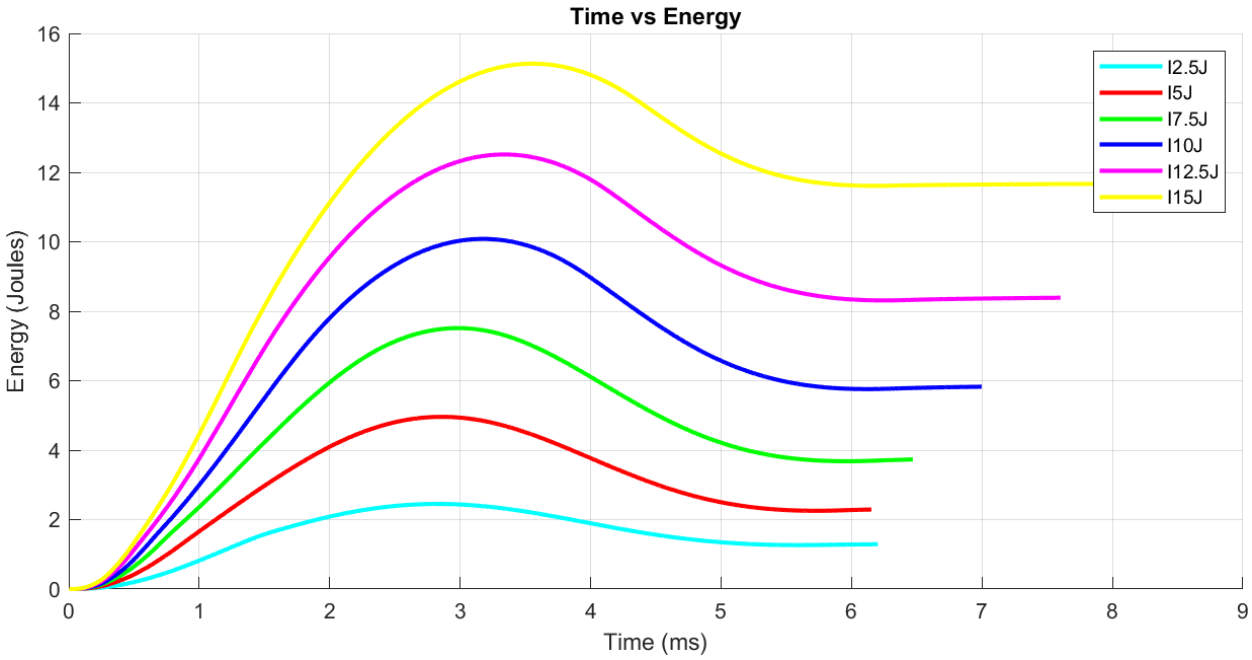

Figure 3.29 Time (ms) vs. Energy (J) curve at varying energy levels

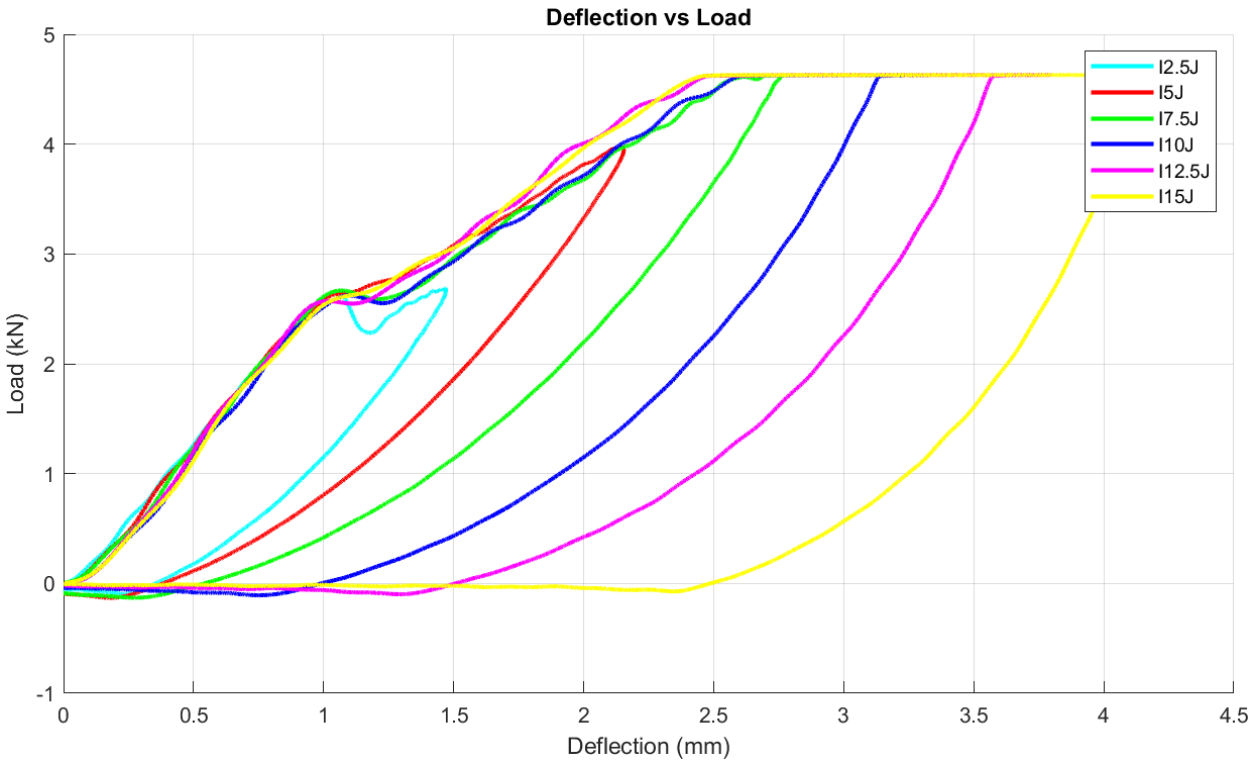

Figure 3.30 Deflection (mm) vs. load (kN) curve at varying energy levels.

3.7 Mapping and Analysis of BVID in CFRP Samples

Following the introduction of a BVID in the samples with the help of the 9250HV system, the samples are rescanned using X-ray following the same procedures detailed in Coupon Inspection.

CTVox, the software used for the 3D inspection, allows for a general view of the damage perimeter. However, for a more detailed analysis and to obtain accurate measurements of the damage, the DataViewer app is used.

However, an issue arises during the segregation of the specimens into distinct files with the help of the Matlab code. The default setting in DataViewer reverts to 1µm per pixel, diverging from the intended 50.769µm per pixel, thereby affecting the built-in scaling accuracy. This issue is rectified by manually entering the accurate dimension value to reinstate the correct scale, as demonstrated in Figure 3.31.

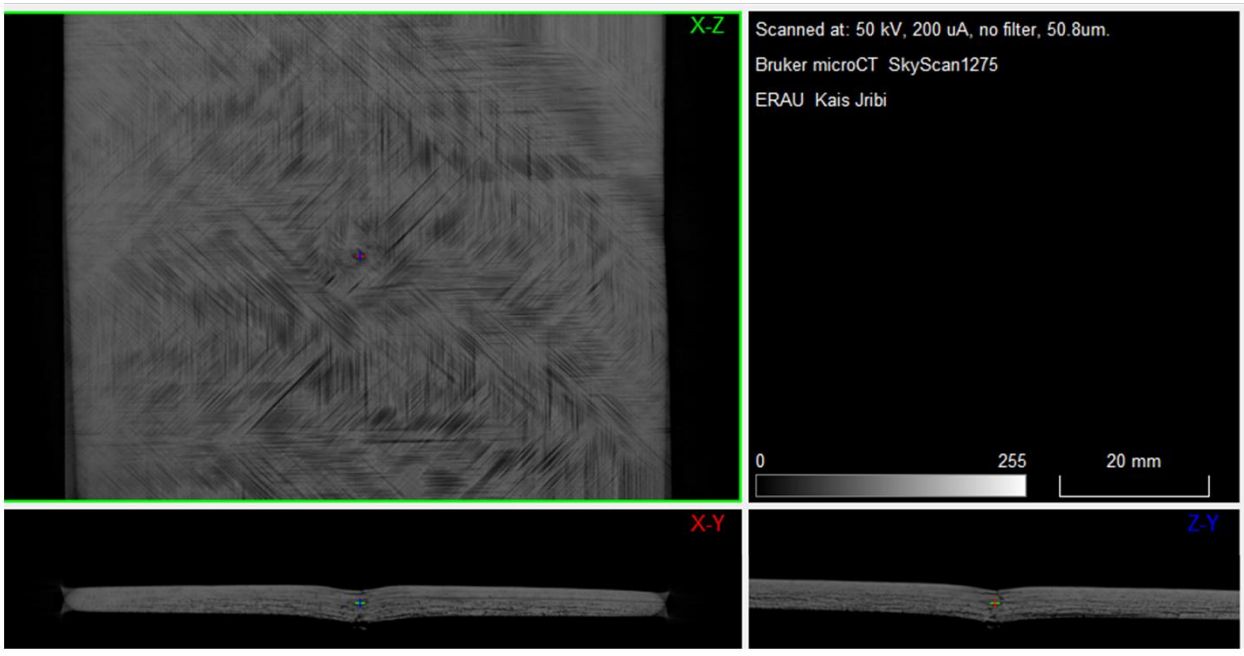

Figure 3.31 General view of a sample in DataViewer

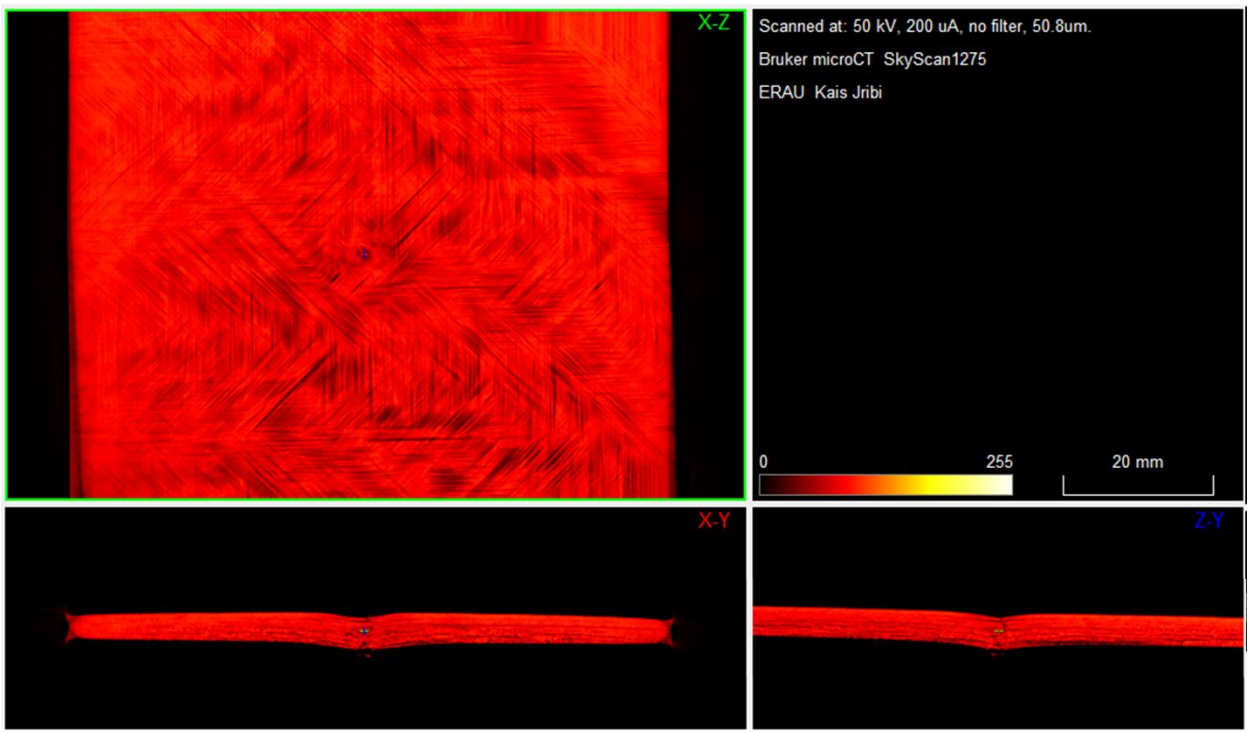

Figure 3.32 General view of a sample with a black body color profile

The results of the impact damage, as detailed in Figure 3.33, exhibit the expected damage profiles corresponding to the different energy levels applied. These observations, however, acknowledge inherent challenges in precisely measuring the extent of damage in a controlled environment. First, the heterogeneous nature of composite materials leads to varying responses under impact, resulting in non-uniform damage patterns that are difficult to quantify accurately [48]. Second, the resolution limitations of imaging technology may not capture the minutest of damages, especially when they are within the material's subsurface or in the case of micro-cracking and delamination. Third, the environmental factors and the condition of the specimen at the time of impact, such as temperature and material aging, can significantly influence the damage morphology.

While sophisticated imaging and color profiling techniques substantially assist in the visual assessment and analysis of impact damage in composite structures, it is critical to recognize and accommodate the inherent constraints in reaching perfect precision in damage dimension depiction.

Figure 3.33 Damage profiles from LVI with different energy levels (from the top: 2.5J, 5J, 7.5J, 10J, 12.5J, 15J and 20J)

A Scanning Electron Microscope (SEM) Quanta 650 was employed to closely examine a specimen subjected to a Low-Velocity Impact (LVI) at 2.5J for more detailed visualization of the damage perimeter. Before the SEM analysis, the sample was bisected using a diamond saw to expose the damaged interior region. It was then cleaned to remove dust or debris using a Branson 2510-DTH ultrasonic cleaner (Figure 3.34), ensuring the surface was free from contaminants. Finally, the specimen was dried using compressed air to prepare it for the high-resolution imaging required to discern the intricate details of the damage.

Figure 3.34 Branson 2510-DTH ultrasonic cleaner

While handling the samples, the user must wear cleanroom gloves as the grease generated by the human skin can adversely affect the image quality and deteriorate the vacuum performance. After the sample has been thoroughly cleaned, the xT Microscope server is activated, bringing up the main control interface.

Users should ensure the beam is inactive from this interface before selecting the vent button. This action gradually diminishes the vacuum, allowing the chamber door to be manually opened. The software's chamber status icon on the bottom right will turn grey to indicate that proceeding with the door opening is safe. The sample is then placed onto the holder and secured. The door is carefully shut while monitoring the sample using the live feed camera to prevent it from touching the pole piece or any surrounding sensors. With the door in place, the pump button is engaged to recommend vacuuming, changing the status icon to orange.

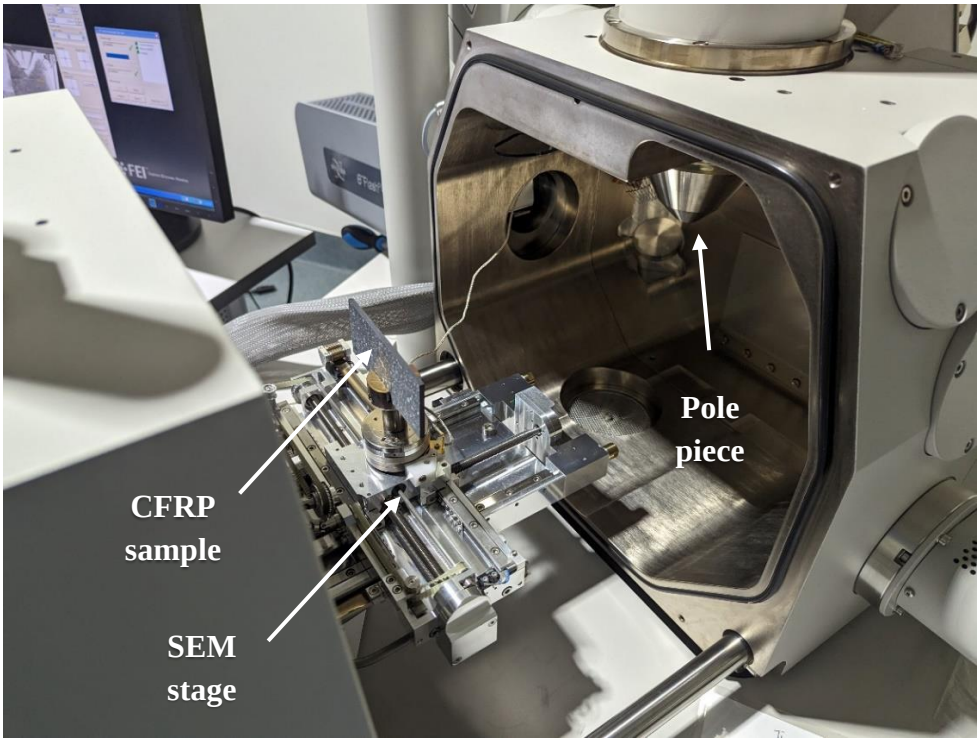

Figure 3.35 Anatomy of the SEM chamber and a fixed sample

Adjustments can be made to the sample's height during the pumping down process to achieve the optimal 10mm working distance. The status indicator turns green once the chamber attains the necessary vacuum level. This green signal denotes that the testing environment is stabilized, and activating the beam for imaging is appropriate.

Once the beam is activated, the user maneuvers around the sample to identify distinct features worth capturing. The user refines the focus and enhances the image quality by utilizing the' reduced area' icon. To save the high-quality image, the user pauses the imaging process and then navigates to the designated shared folder for secure storage.

After the scanning process, the procedure is reversed. The sample is carefully extracted from the chamber, and the pressure is returned to a vacuum. The server is shut down, and the user logs out from the PC.

The outcome of the scan can be seen in Figure 3.36, where the damage can be seen between the 16^{th} and 18^{th} layers and again between the 22^{nd} and $23^{rd,}$ confirming the properties expected from an LVI of 2.5J of energy.

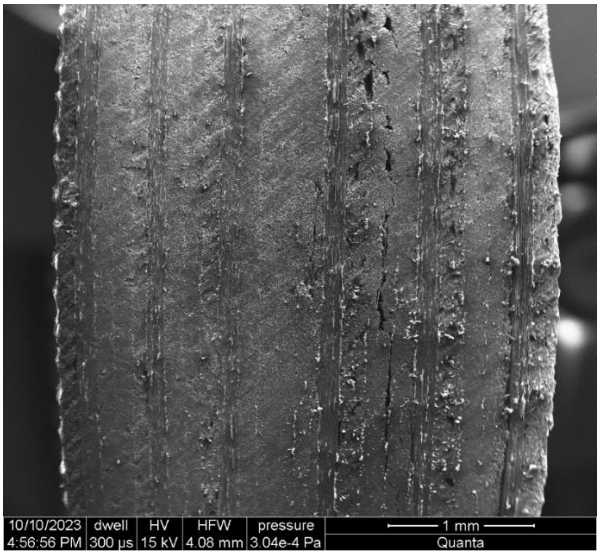

Figure 3.36 A SEM scan of a sample after getting damaged by a LVI

3.8 Evaluating CFRP Samples Under Compression After Impact (CAI)

Compression After Impact (CAI) is a vital test performed on composite materials, primarily in the aerospace sector, to evaluate a composite structure's residual strength and performance following an impact event. This test is critical for understanding the behavior of composite materials such as Carbon Fiber Reinforced Polymers (CFRP) under real-world operational loads.

The standard protocol calls for applying compressive force to the impacted specimen until it fails. As a result, the CAI strength is defined as the maximum compressive force the specimen can withstand per unit cross-sectional area before failure.

This work aims to determine the point at which delamination, produced initially by Low-Velocity Impact (LVI), reinitiates. The task is accomplished by carefully monitoring the displacement and strain values on the specimen's surface for any abnormalities that may indicate the widening of delamination within the sample.

The compression after impact (CAI) test adapts to ASTM D7137/D7137M specifications. Initially, a Boing BSS-7260 CAI fixture that permits edgewise compression while retaining constrained boundaries was proposed. Alas, with the changes in the samples' dimensions to fit within the X-ray chamber, a new, bespoke fixture is manufactured to accommodate the specimens adequately.

The newly engineered fixture was crafted from a 7075 aluminum alloy, known for its superior strength-to-weight ratio and essential for precision in testing equipment. The fixture's surface was treated with a matte black finish to enhance the data acquisition process for Digital Image Correlation (DIC), effectively minimizing any glare that could interfere with the accuracy of the measurements.

The specimens' side edges were thickened with the help of masking tape and carefully positioned in the fixture to limit z-axis displacement and avoid buckling-induced failure. A layer

of grease was also appended to the sides to reduce the friction between the fixture and the sample, ensuring smooth loading and preventing any unwanted friction that could contribute to inaccuracies in the test results.

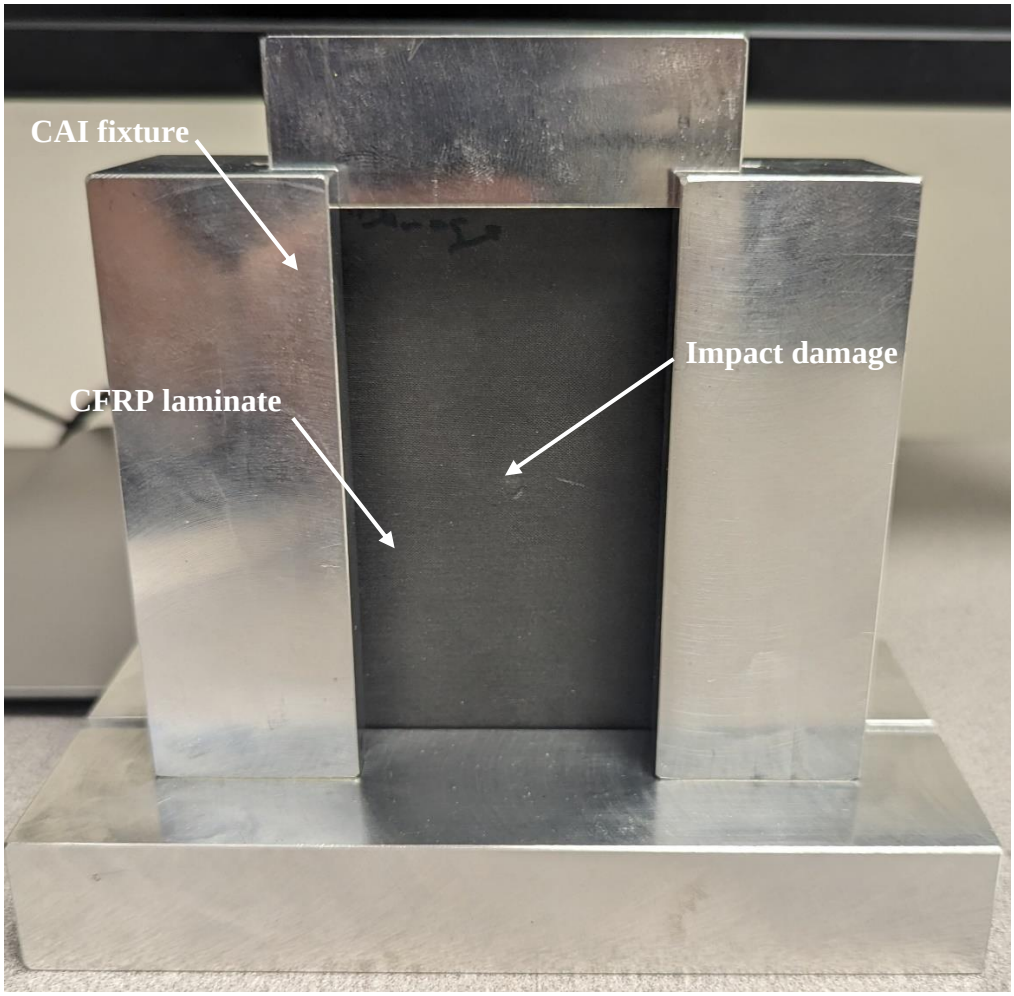

Figure 3.37 Compression after impact testing fixture with a damaged sample

The fixture was then mounted on the Tinius Olsen testing machine, and the DIC setup was positioned facing the sample, as shown in Figure 3.38.

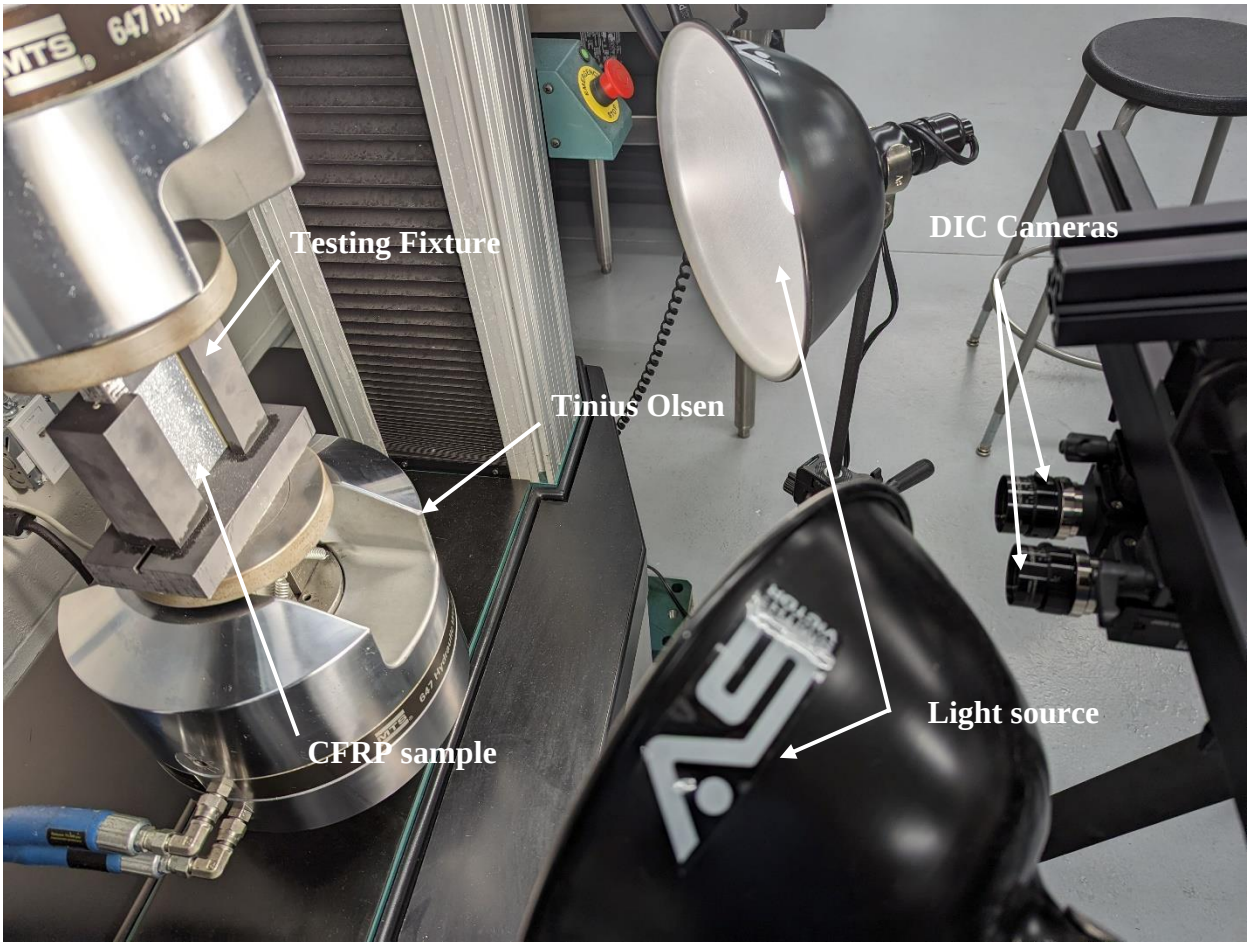

Figure 3.38 DIC setup facing a CAI testing fixture mounted on the Tinius Olsen testing machine

The next step is to acquire the images needed for the DIC calibration by taking images of the 3mm grid calibration tile using the Vic-Snap software while rotating and tilting the tile sidewise to capture all the angles.

The Vic-3D software is started after gathering at least 50 images. The calibration images option is later selected, and the procured images are loaded. The caliber icon is selected, which commands the software to extract the points from images taken with both cameras and try correlating them. In this case study, the calibration score ended up being 0.012, as seen in Figure 3.39, which falls

below the threshold of 0.1. Otherwise, gathering a different set of images and restarting the calibration process is necessary before starting the CAI testing.

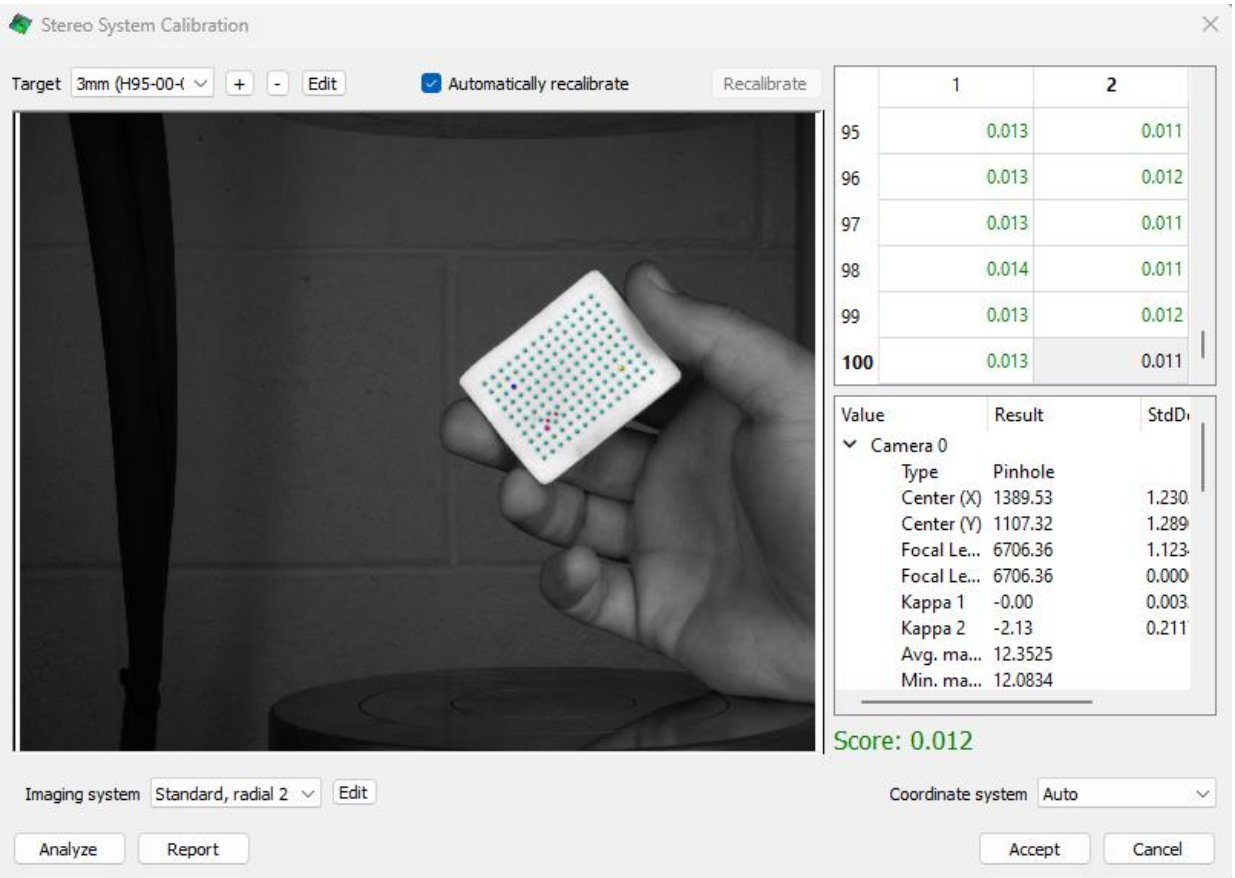

Figure 3.39 Calibration results using Vic-3D

A table with the calibration parameters and magnification is generated based on the calibration results, showcasing the coordinate system's location, focal length, and magnification parameters (Table 3.5).

Once calibration was completed, the test sequence commenced adhering to the established protocol for testing the material properties of Carbon Fiber Reinforced Polymers (CFRP). The Horizon and Vic-Snap software systems were employed in tandem. The configuration for Horizon, however, was specifically tailored to execute a semi-static compressive loading regimen, applying

a load at a gradual rate of 0.00208% strain per second, equivalent to a displacement of 0.125mm per minute.

Table 3.5 Camera calibration parameters and magnification

	Camera 1	**Camera 2**
Center x [pixel]	1389.53	1391.86
Center y [pixel]	1107.32	1112
Focal length x [pixel]	6706.36	6711.74
Focal length y [pixel]	6706.36	6711.74
Skew	0	0
Kappa1	-0.00288777	-0.0058589
Kappa2	-2.1343	-1.62553
Kappa3	0	0
Average magnification [pixel/mm]	12.3525	12.2806
Minimum magnification [pixel/mm]	12.0834	12.0447
Maximum magnification [pixel/mm]	12.7584	12.6744

Once calibration was completed, the appropriate loading parameters had to be determined and programmed using the Horizon software. To achieve this goal, a series of damaged samples underwent preliminary testing to gauge the maximum displacement the CFRP could withstand before complete failure. This exploratory phase revealed that the average threshold of displacement was 1.2mm. Consequently, Horizon was programmed to halt the test upon reaching 0.75mm of displacement, anticipating that delamination would resume propagation by this juncture.

The configuration for Horizon was explicitly tailored to execute a semi-static compressive loading regimen, applying a load at a gradual rate of 0.00208% strain per second, equivalent to a

displacement of 0.125mm per minute in tandem with the image acquisition process performed by Vic-Snap software.

To verify the reliability of the results and prevent the possibility of under-testing, control samples from each designated BVID energy level were tested beyond the 0.75mm threshold, extending up to a maximum displacement of 1.5mm. This approach ensured a comprehensive assessment of the sample's integrity and the precise identification of the onset of delamination propagation.

For each sample evaluated, the Horizon software collects a complete dataset that includes time, force, positional displacement, and stress. A MATLAB script, available in APPENDIX - C, has been designed to separate and manage this data for individual investigation properly. This script rigorously separates the aggregate data, ensuring that the findings of each sample are extracted and structured systematically.

3.9 Assessment of Displacement and Strain in CAI Testing

The subsequent step involves revisiting the Vic-3D software to select the speckle images for a particular specimen. Once these images are loaded, the Area of Interest (AoI) tools are utilized to delineate the specific region for detailed analysis. In addition, a reference point is selected to verify the autocorrelation of the reference point between both sets of images taken by different cameras (Figure 3.40).

While analyzing specific samples, the Digital Image Correlation (DIC) software occasionally encounters difficulty in tracking the speckle patterns from one image to the next. This challenge typically arises when the software's initial prediction fails to identify the reference speckles in subsequent frames correctly. The root causes are often twofold: either the speckles are obscured due to material dislocation or an abrupt displacement resulting from the sample failure.

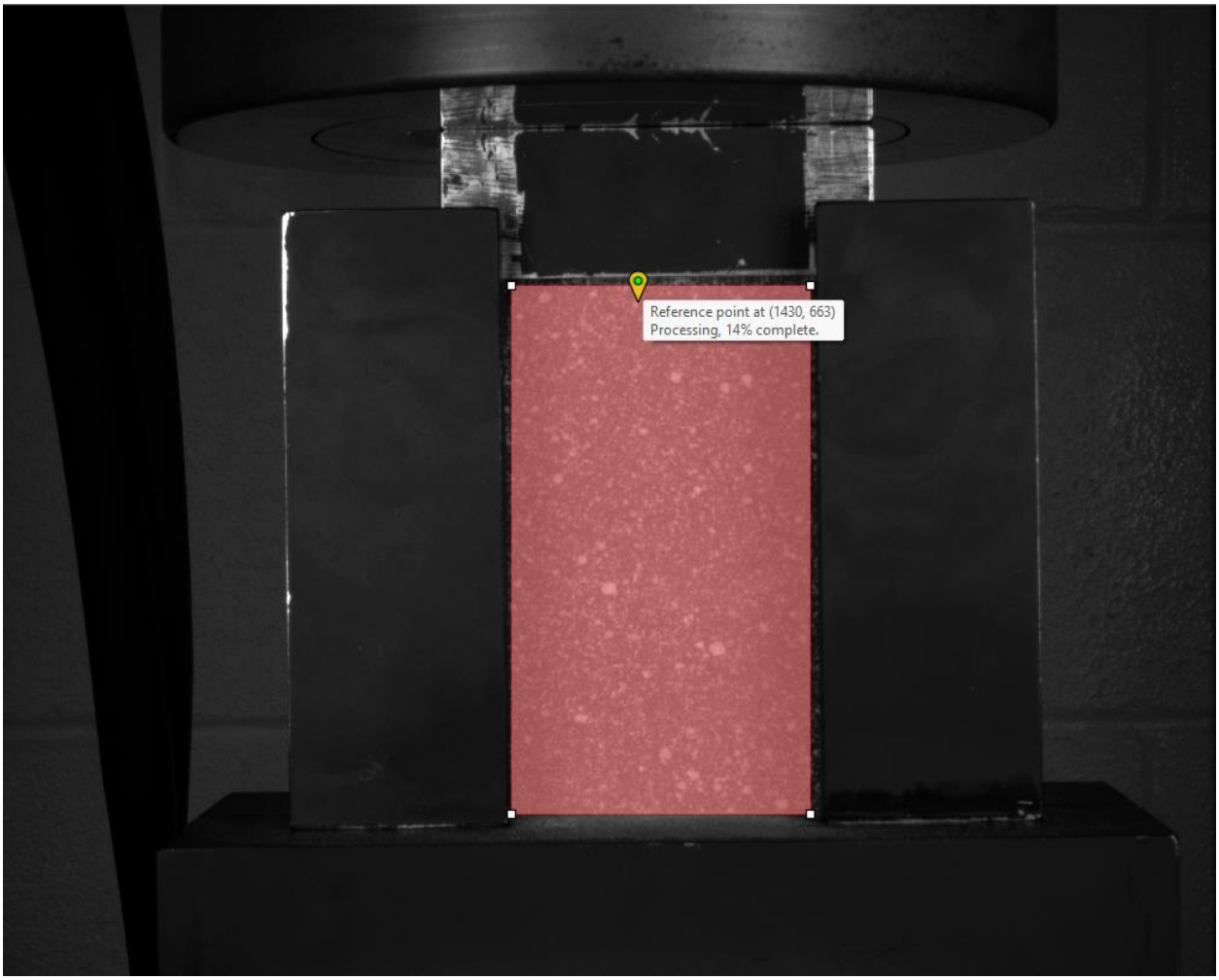

Figure 3.40 Area of interest and reference point selection

This issue was predominantly observed in control samples that were allowed to bypass the threshold set to 0.75mm. Two ways have been presented to address this. The first method is selecting and evaluating only images acquired before the sample's failure, avoiding frames with unpredictable speckle displacement. The second solution necessitates a manual adjustment in the initial guess editor window (Figure 3.41): the user can relocate the guess box to the correct position and secure the selection with a right-click. This action must be performed twice to affirm the reference point.

Subsequently, the down arrow key is used to fine-tune all initial guesses for the following images. While effective, this manual adjustment method is labor-intensive and time-consuming, necessitating careful attention to detail to ensure the accuracy of the speckle tracking process.

Upon establishing the reference point and the AoI and clicking the question mark icon, the software offers an automated subset size recommendation, as depicted in Figure 3.42. This subset size is crucial as it influences the granularity of the displacement and strain measurement across the specimen's surface.

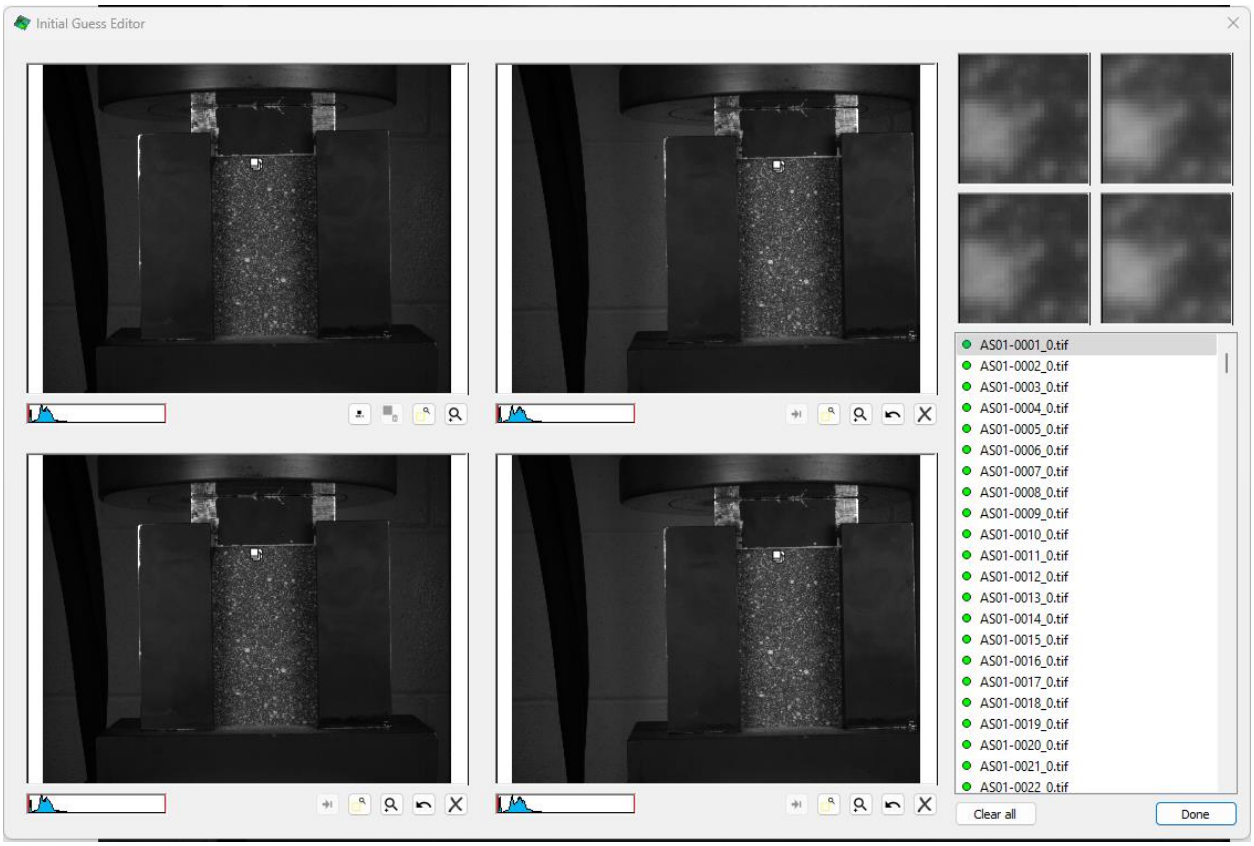

Figure 3.41 Initial guess editor

Subsequently, selecting the step size is critical in defining the resolution of the displacement and strain data captured. When precision in tracking localized strain distribution is paramount, a

step size of 1 was initially adopted to ensure a comprehensive and detailed analysis of localized strain variations. However, this high level of detail comes with the trade-off of a substantially increased computational burden. For instance, processing with a step size of 1 would require approximately 2713 minutes, equating to nearly two days of continuous computation.

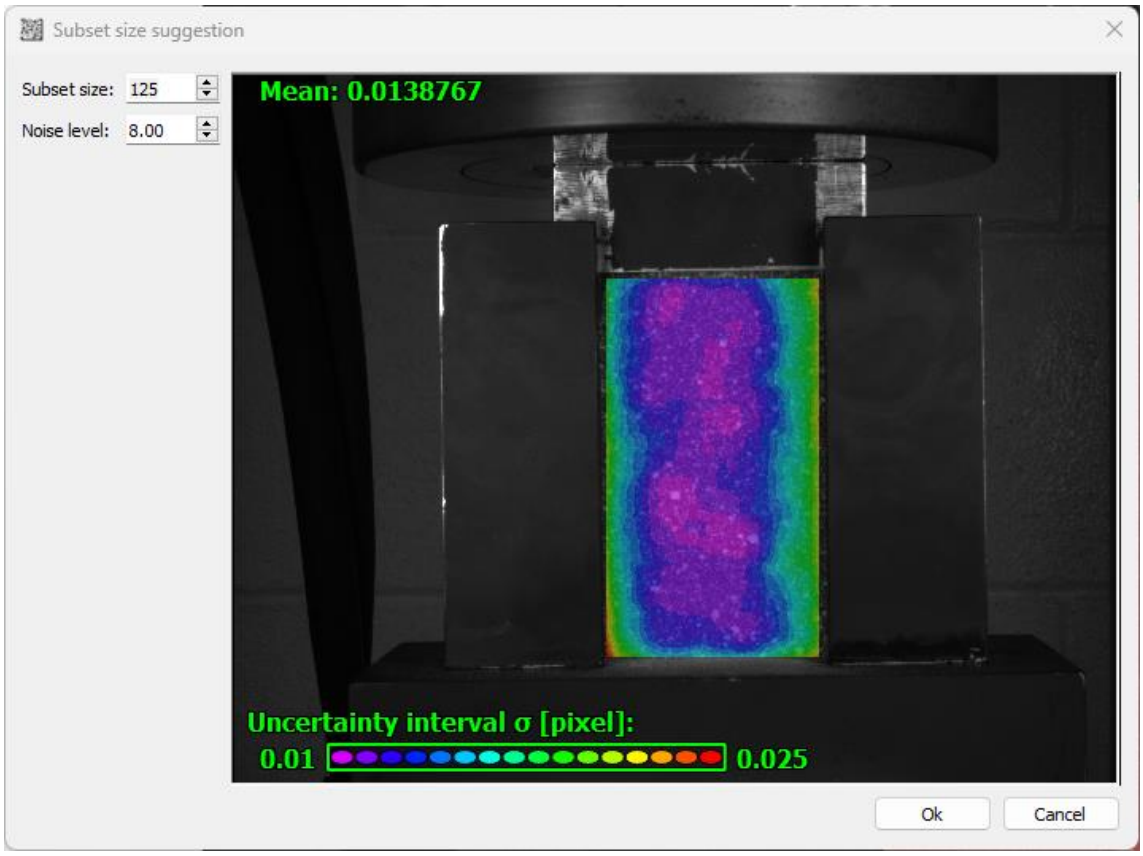

Figure 3.42 Subset size suggestion.

Given the prolonged processing time, a pragmatic decision was made to adjust the step size to 4. While reducing the resolution slightly, this modification ensures adequate quality in the resulting displacement and strain maps. The adjustment significantly expedites the analysis, reducing the computational time to 136 minutes per sample.

After the Vic-3D analysis is completed, the shift to strain computation is initiated by clicking the 'ε' icon, which displays the strain computation interface. The filter size and tensor type are chosen, adapting the calculation to the analysis's needs.

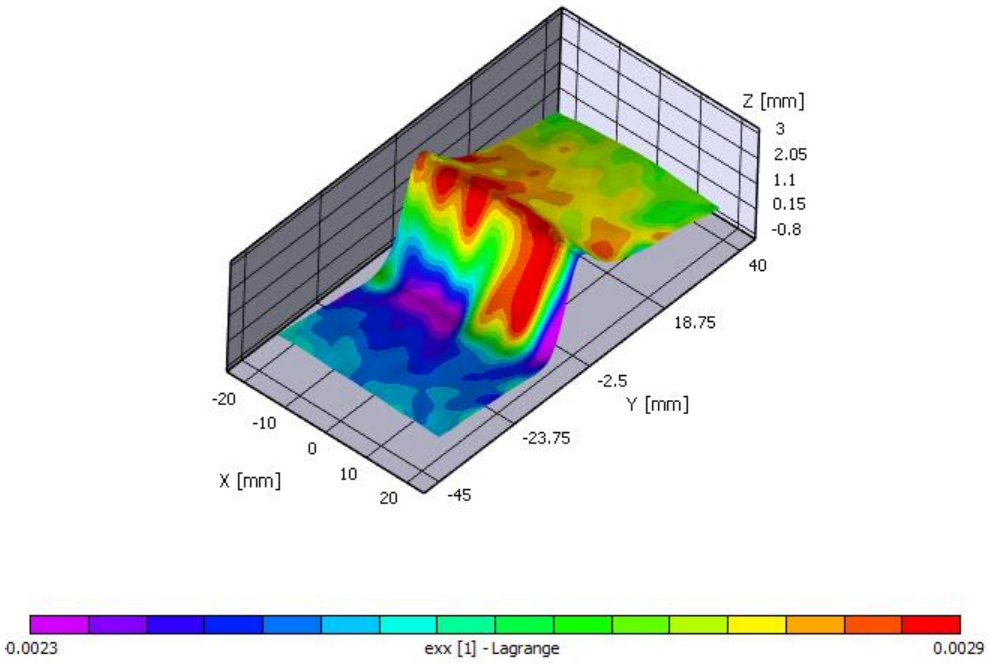

Figure 3.43 Strain computation screen.

Once the computation is complete, the next phase involves removing the rigid motion. Removing rigid motion refers to the movement of an object where the distance between any two points of the object remains constant throughout the motion. Understanding and accounting for rigid body motions is crucial in Digital Image Correlation (DIC) and material testing. During testing, objects or samples may undergo rigid motions that must be differentiated from the deformation patterns of primary interest. Accurate DIC analysis involves separating these rigid motions to focus on the displacement and stress patterns that indicate material behavior under load.

After excluding rigid motion effects, the results can be observed with the help of the plot function in the Vic-3D software. However, all the data is exported in a MATLAB format to correlate observed displacements with stress measurements recorded via the Horizon software.

3.10 Post-CAI Damage Examination and Mapping

The final step in the experimental sequence involves assessing the extent of damage from the CAI tests. The specimens are rescanned using the X-ray machine, adhering to the protocols outlined in the Mapping and Analysis of BVID in CFRP Samples section. Figure 3.44 exemplifies a sample loaded to complete failure, illustrating significant damage. In contrast, for specimens halted at 0.75mm displacement, the delamination is relatively minor. The extent of the delamination propagation is depicted in Figure 3.45, where the top image shows the sample pre-CAI and the bottom image post-CAI

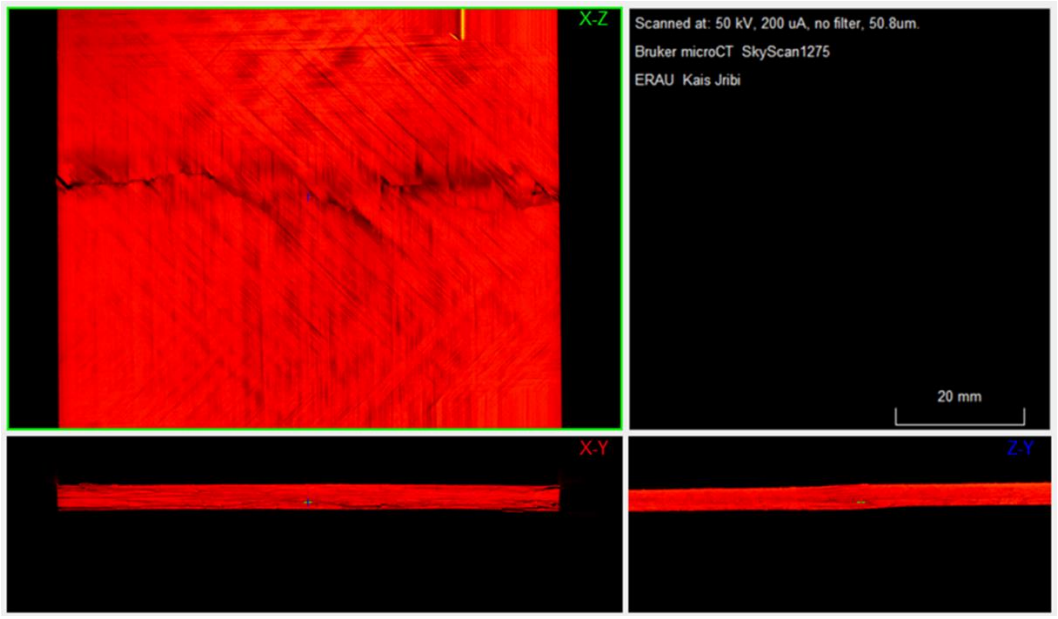

Figure 3.44 3D projection of the final damage topology.

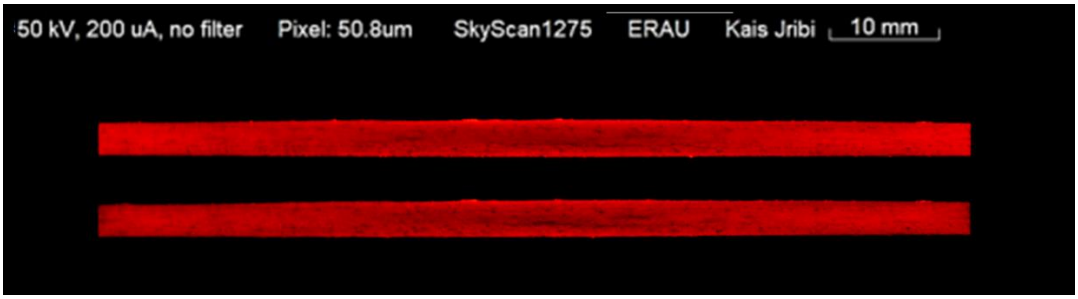

Figure 3.45 Sample before and after CAI (top: pre-CAI, bottom: post-CAI).

4 Post-BVID Delamination Reoccurrence: Analysis and Modeling

This chapter digs into the study of delamination reinitiation in composite structures following Barely Visible Impact Damage (BVID). It focuses on analyzing the relationship between surface strain variations and displacement W along the Z-axis with the onset and progression of delamination. The section will discuss how these critical parameters are quantitatively evaluated and interpreted to understand the implications of BVID on the structural integrity of CFRP materials. Emphasis will be placed on determining a model that would serve as a reference profile to estimate the critical out of plane displacement $W_{cr.}$.

4.1 Synchronization and Integration of DIC and Mechanical Testing Data

Data integration and synchronization from various sources are paramount in studying delamination reinitiation in CFRP structures following Barely Visible Impact Damage (BVID). This task is handled using MATLAB scripts, which form the backbone of the data processing methodology.

The initial stage involves a MATLAB code (APPENDIX - D) developed explicitly for merging critical datasets from the VIC-3D system, used in Digital Image Correlation (DIC) and Horizon software. This code streamlines the directory selection and file verification process, ensuring all necessary data files are accounted for. Once the files are identified, the script merges and interpolates the data, creating a synchronized dataset linking the stresses recorded by the Horizon software with the frames acquired with the help of the Vic-snap software based on their time stamp.

Building on this foundation, a secondary MATLAB script comes into play (APPENDIX - E), focusing on refining data handling further. This script is tasked with loading and organizing DIC data from '.mat' files. It allows that for selecting a specific data folder and proceeds to load all relevant '.mat' files. One of the critical features of this script is its ability to identify regions of

interest by analyzing displacement fields. By applying cropping to these areas, the analysis is concentrated on regions most affected by the impact damage, ensuring that the study remains focused on the most pertinent data.

Moreover, this script organizes the cropped data into a structured format, neatly compiling displacement and strain components for each frame. This organization is crucial for ease of access and analysis. The script then integrates this structured DIC data with corresponding experimental data from the combined data file. This results in a comprehensive dataset combining mechanical properties and surface strain measurements.

4.2 Visualization of Displacement Patterns in BVID-Affected CFRP

A MATLAB function (APPENDIX - F) generates a three-dimensional W displacement map to visualize displacement patterns within CFRP structures affected by Barely Visible Impact Damage (BVID). The operation begins by creating an interactive figure featuring a slider control, which enables the examination of displacement data across several frames.

The methodology combines W displacement information obtained from DIC measurements across multiple frames. Determining this data's minimum and highest values establishes the range for all subsequent 3D visualizations. The initial plot illustrates the displacement at a given frame and can update in response to interactions with the sliders; this effectively captures the dynamic nature of displacement over time.

One noteworthy feature of this visualization technique is its ability to employ a circle marker to emphasize regions exhibiting the most significant displacement, which emphasizes crucial sections of the material, establishing a central focus for subsequent examination. Additionally, strain values are integrated and correlated with the discovered regions of maximum displacement by providing a holistic perspective on the interplay between stress, strain, and displacement at critical junctures.

By including color mapping in this visualization tool, the perception of displacement variations over the composite surface becomes more detailed, improving interpretability. By incorporating a color bar and a uniform climatic range throughout all frames, a benchmark is set for comparative study.

The adjusted MATLAB visualization code was adapted to showcase the displacement patterns in CFRP structures during the CAI testing procedure. The resultant code, which effectively generates sixteen frames from the dataset with identical spacing, is depicted in Figure 4.1. The depicted picture provides valuable insights during the early phases, as the displacement values in the upper four frames primarily fall within the range of -0.01 to 0.01 mm, indicating a limited variance in initial displacement, which can be attributed to noise levels. As the analysis progresses through the dataset, the displacement pattern transforms into an inverted parabolic form. This transition marks the consistency of the W displacement and signifies the initial stages of damage development. One aspect worth mentioning is the W displacement of 0.05 mm recorded in the third row. This particular frame serves a crucial purpose in identifying the location of the BVID impact damage and demarcates the core area of the delamination perimeter. Following this, as the delamination undergoes further expansion, the displacement W further emphasizes the precise site of the damage. However, although the 3D images in Figure 4.1 provide an indication of when the damage begins to propagate again, this observation is not definitive. The presence of visual indicators that imply additional damage spreading may be ascribed to noise in the data, thus requiring a prudent approach to interpretation.

An analogous behavior trend is illustrated in Figure 4.2, with the fundamental distinction being that the compressive load applied to this specific specimen exceeded the 0.75mm displacement threshold. The sample ultimately crashes due to this access stress, as illustrated in Figure 4.3.

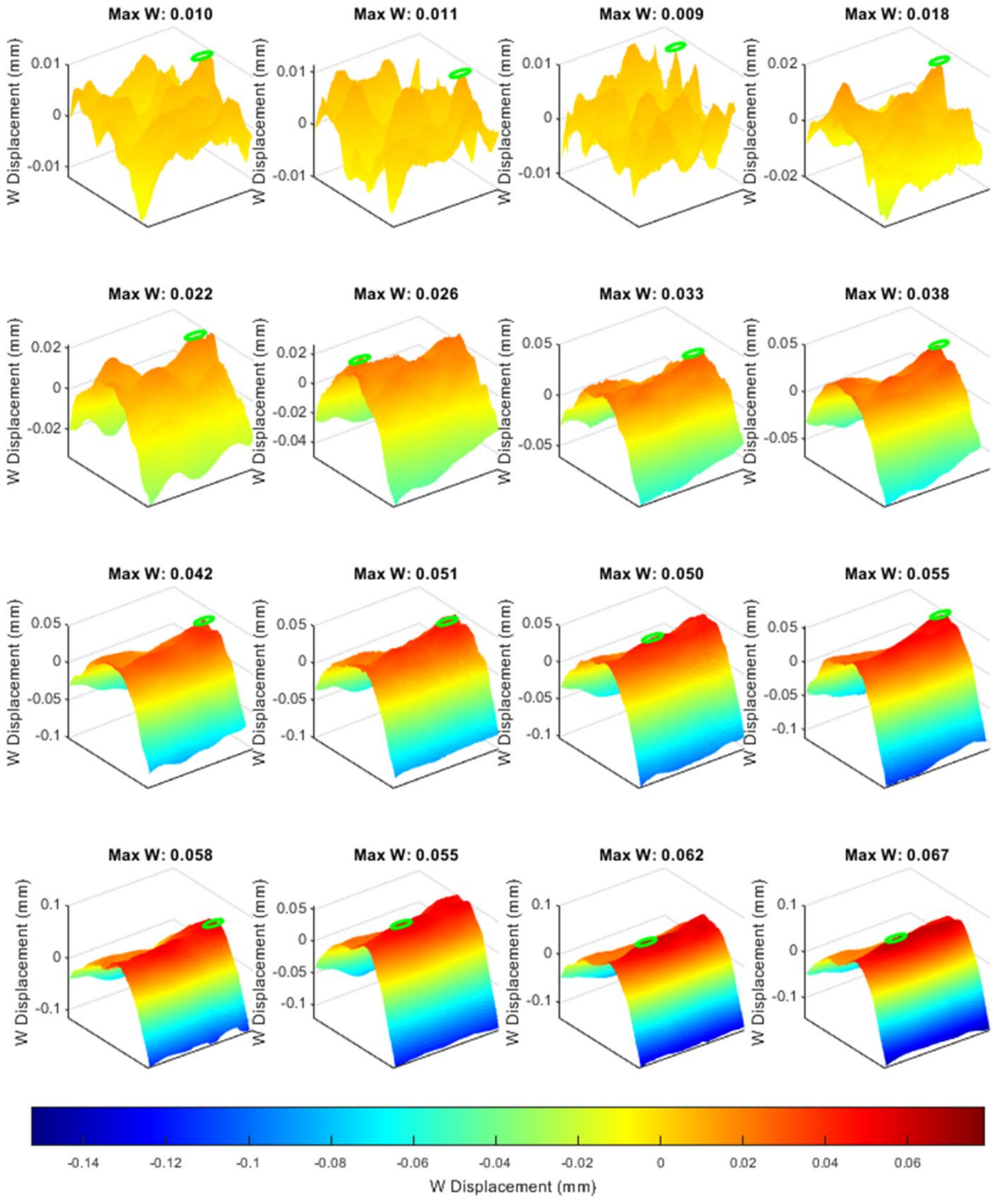

Figure 4.1 Identifying delamination reinitiation points via W displacement in CFRP.

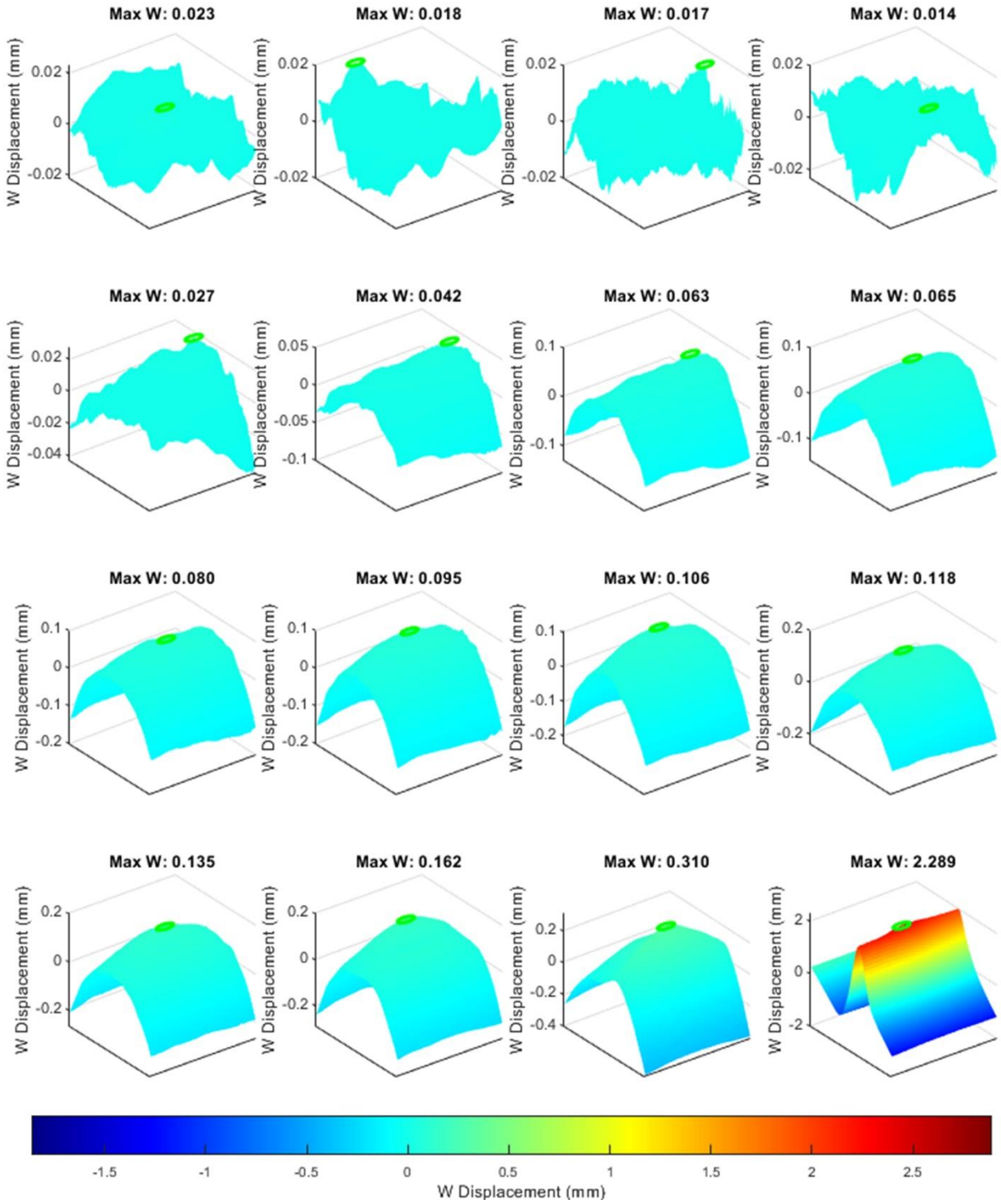

Figure 4.2 Evaluating CFRP response beyond 0.75mm compressive threshold.

Figure 4.3 Structural failure in CFRP due to excessive compressive loads.

4.3 Correlation Between Stress Shifts and Impact Energy

The correlation between maximum out-of-plane displacement and stress is a fundamental approach to detecting the beginning of delamination caused by Barely Visible Impact Damage (BVID) in composite materials. During data analysis, a distinct change in stress values indicates the start of delamination at the impact site, as illustrated in Figure 4.4. This change is readily noticeable in specimens suffering from BVID after being subjected to impact energies ranging from 5J to 10J. This shift, Marked with a red rectangle for better visibility in the images, does not specify an exact stress level but instead points out a critical range of stress where delamination is prone to restart, aligning with findings reported by Sun et al. [49].

It is important to note that damage from lower impact energies, specifically 2.5J, is too small for detection via changes in stress values. On the other hand, damages from higher impact energies, like 12.5J, are more challenging to identify as the extensive damage masks the shift in stress. This limitation underlines the sensitivity range of the method, highlighting its optimal use for detecting damages caused by impact energies that are neither too low nor too high.

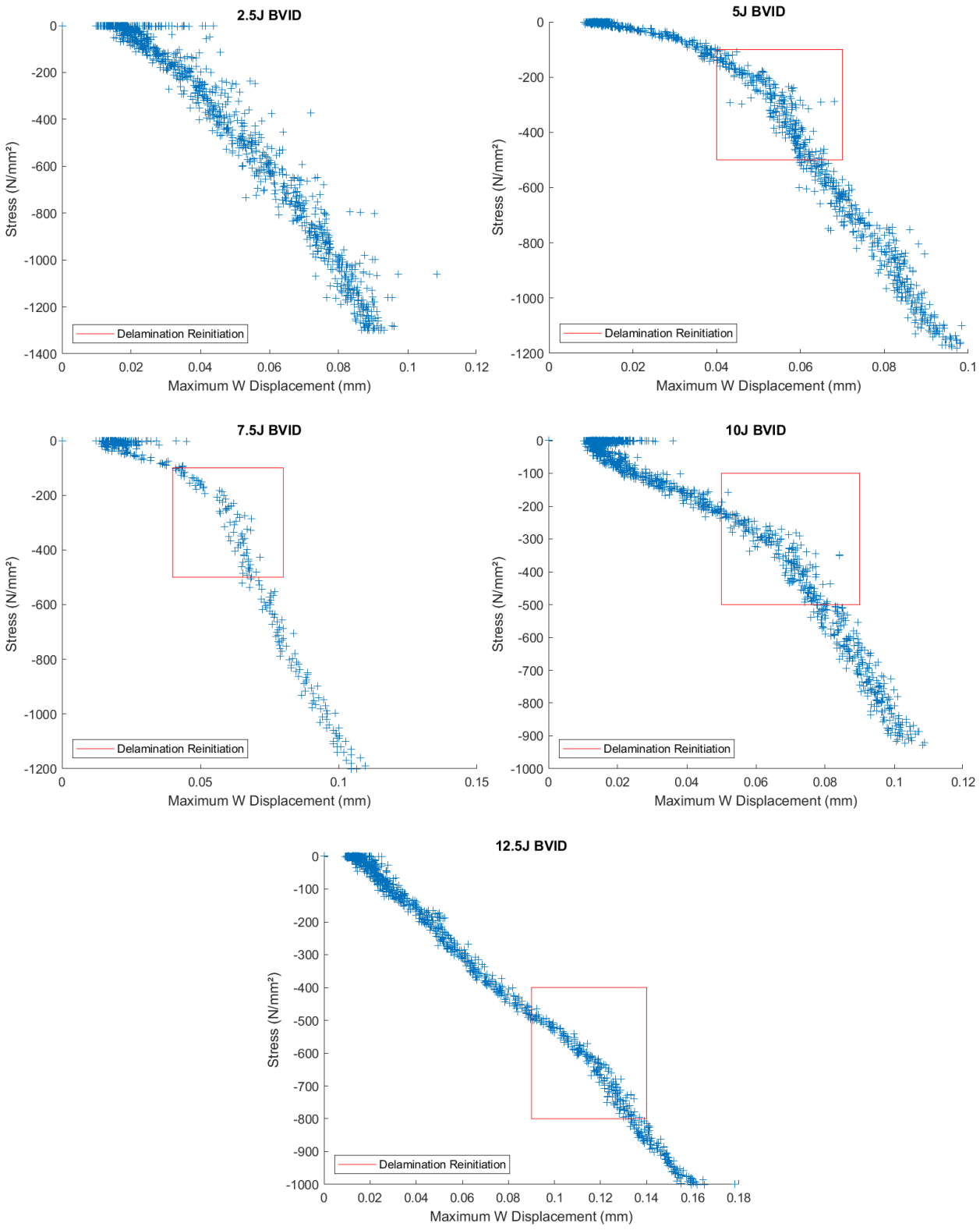

Figure 4.4 Correlation of peak displacement with stress across various BVID boundaries for 'AS'.

4.4 Integrating Surface Strain and Stress Analysis

This section introduces an alternative method that focuses on analyzing the surface strain measurements to precisely detect the onset of delamination. This technique emphasizes the close examination of surface strain patterns, offering a refined approach to identifying the initial moments of delamination with greater accuracy. By establishing a connection between these observed strain patterns and stress metrics, this approach facilitates the identification of the critical stress threshold at which the integrity of the material begins to deteriorate. The analysis incorporates the plotting of longitudinal ε_{xx}, transverse ε_{yy}, and shear strains ε_{xy} together on a single graph, improving the visualization of delamination initiation.

Figure 4.5 illustrates how displacement and strain relationships are mapped, with stress values plotted on an additional axis to highlight the stress levels corresponding to these measurements. A notable pattern emerges when longitudinal and transverse strains diverge from the shear strain and each other, signaling the beginning of damage progression from the point of Barely Visible Impact Damage (BVID). This divergence serves as a vital clue for the onset of damage, which is further corroborated by analysis of the saddle charts. These charts document the peak displacements at the BVID site, illustrating the variance in the highest displacement (W) point due to data inconsistencies. The graphical representation eventually converges on the central part of the sample where the BVID was implemented, pinpointing the exact spot of displacement escalation.

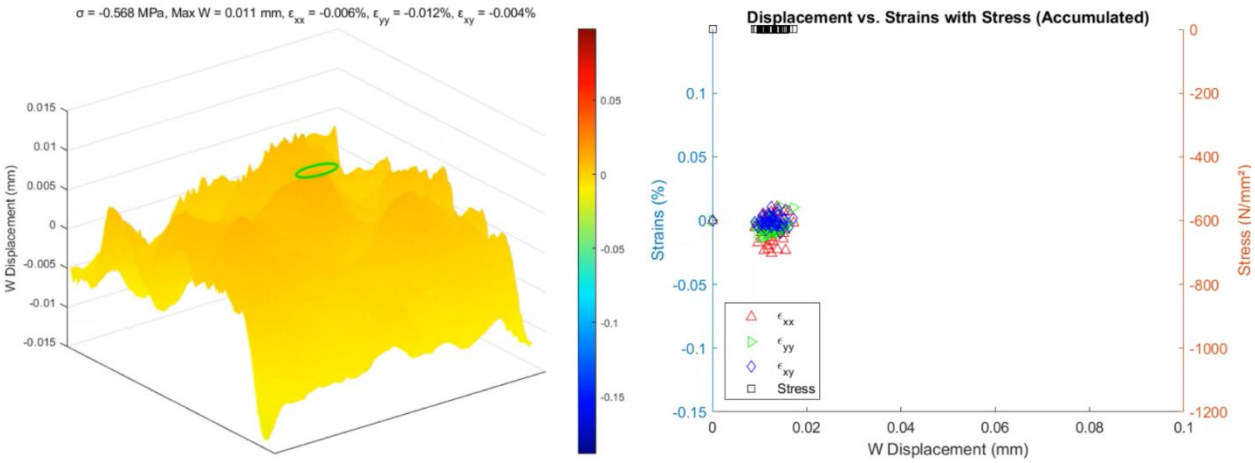
σ = -0.568 MPa, Max W = 0.011 mm, ε_xx = -0.006%, ε_yy = -0.012%, ε_xy = -0.004%
W Displacement (mm)
Displacement vs. Strains with Stress (Accumulated)
Strains (%)
Stress (N/mm²)
W Displacement (mm)
ϵxx
ϵyy
ϵxy
Stress

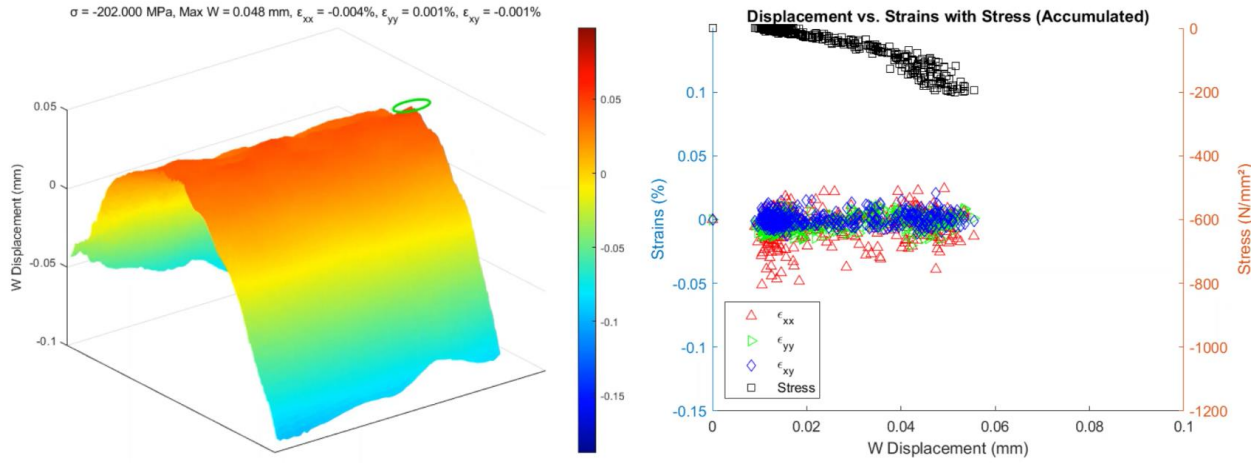
σ = -202.000 MPa, Max W = 0.048 mm, ε_xx = -0.004%, ε_yy = 0.001%, ε_xy = -0.001%
W Displacement (mm)
Displacement vs. Strains with Stress (Accumulated)
Strains (%)
Stress (N/mm²)
W Displacement (mm)
ϵxx
ϵyy
ϵxy
Stress

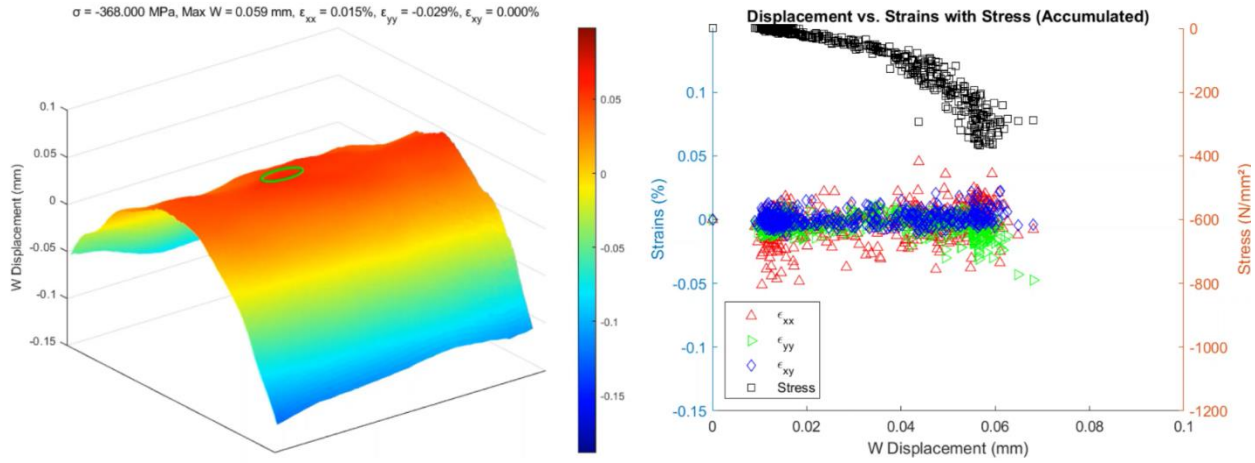
σ = -368.000 MPa, Max W = 0.059 mm, ε_xx = 0.015%, ε_yy = -0.029%, ε_xy = 0.000%
W Displacement (mm)
Displacement vs. Strains with Stress (Accumulated)
Strains (%)
Stress (N/mm²)
W Displacement (mm)
ϵxx
ϵyy
ϵxy
Stress

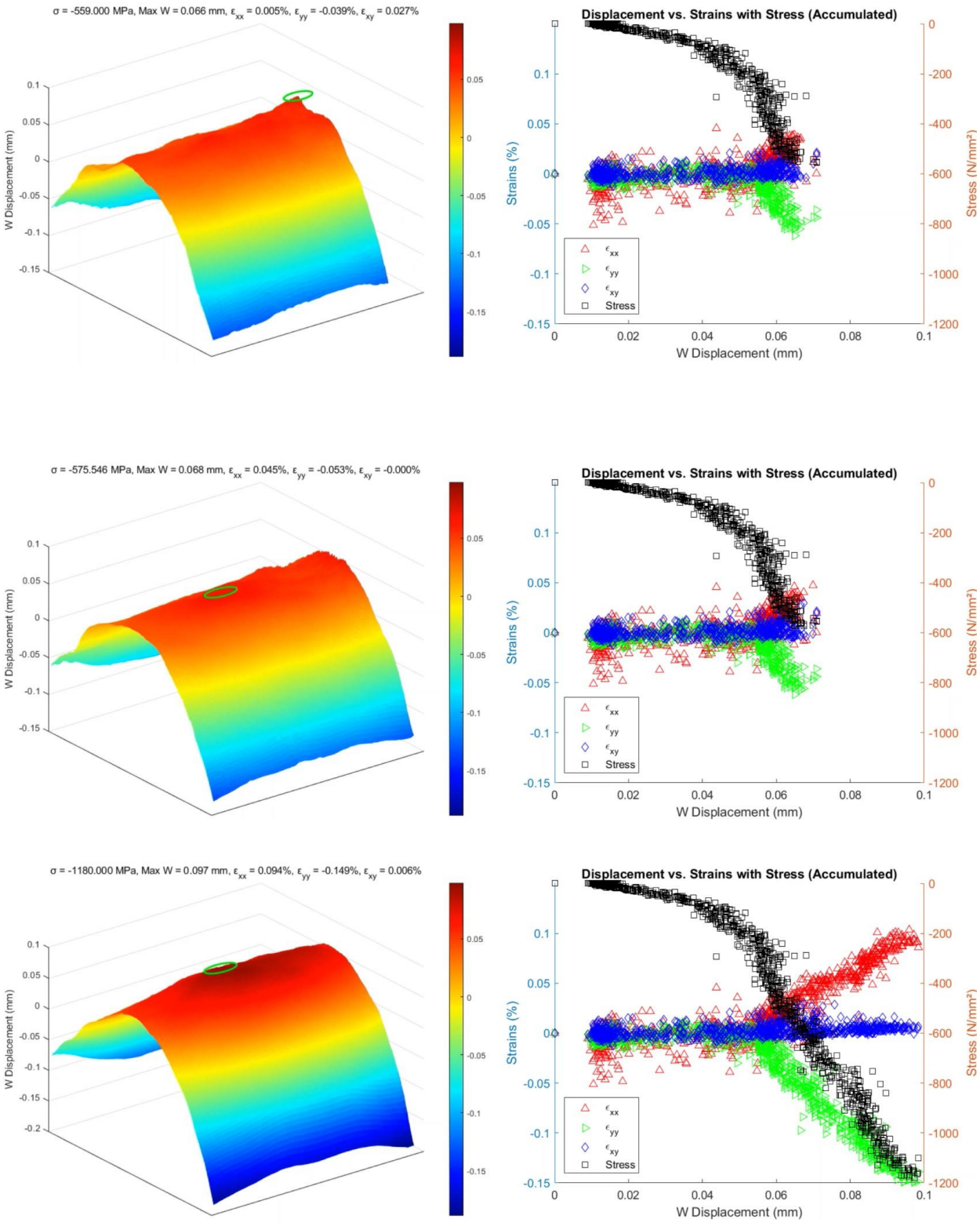

Figure 4.5. Step-by-step comparative analysis of CFRP response under CAI (5J impact damage from 'AS').

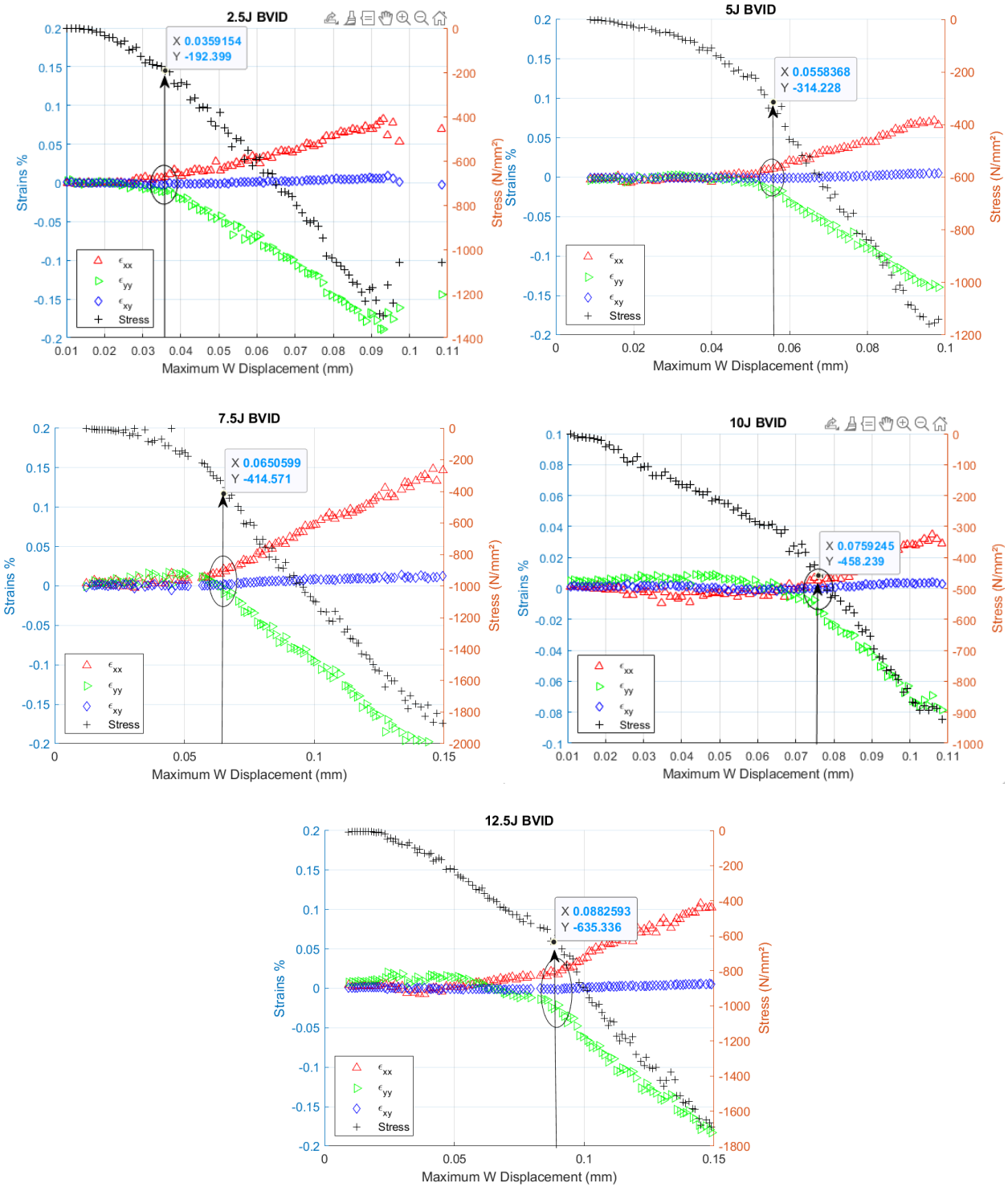

Figure 4.6. Comparative analysis of CFRP response under CAI testing for varying BVID damage perimeters (northwest to southeast: 2.5J, 5J, 7.5J, 10J, and 12.5J from 'AS').

Figure 4.6 presents a comprehensive analysis of the effects of varying impact energy levels on material behavior through detailed experimental data. At a lower impact energy of 2.5 J, the material exhibits the initial signs of strain divergence “defined as a significant change in the material's reaction to applied stress” at a displacement of 3.59×10^{-2} mm and a stress level of -192.4 MPa. As the impact energy is increased to 5 J, the divergence point moves to a higher displacement of 5.58×10^{-2} mm and a stress level of -314.2 MPa, indicating a shift in material behavior under increased stress. The trend continues with a 7.5 J impact, where the strain begins to diverge at a displacement of 6.51×10^{-2} mm, and the stress escalates to -414.6 MPa, further showcasing the material's response to escalating impact energies.

The pattern of behavior extends to higher impact energies, such as 10 J and 12.5 J. For a 10 J impact, the material reaches a strain divergence point at a displacement of 7.59×10^{-2} mm and a stress level of -458.2 MPa. At an even higher impact energy of 12.5 J, the material's displacement increases significantly to 8.83×10^{-2} mm, with the stress level intensifying to -635.3 MPa. This data effectively illustrates how incremental increases in impact energy influence the point of strain divergence, displacement, and stress within the material, offering valuable insights into the dynamic response of CFRP materials to different levels of BVID impacts during CAI testing.

Table 4.1 Stress levels for delamination reinitiation

Energy Levels	**Stress (MPa)**	**Displacement (mm)**
2.5 J	-192.4	3.59×10^{-2}
5 J	-314.2	5.58×10^{-2}
7.5 J	-414.6	6.51×10^{-2}
10 J	-458.2	7.59×10^{-2}
12.5 J	-635.3	8.83×10^{-2}

5 Interpreting Results: Insights into BVID Dynamics

5.1 Analysis of Equivalent Strain and Critical Displacement

The findings reveal a consistent pattern relating strains and out-of-plane displacements to the threshold where delamination starts to reinitiate from a BVID generated under different LVIs. A novel method for understanding this relationship is introduced in this section. This technique employs a comprehensive analysis of global strains by utilizing the square of the equivalent strain $\varepsilon_{eq.}$, as defined by the invariant of the deviatoric strain tensor J_2' [50], and correlates it with out-of-plane displacement W, as illustrated in Figure 5.1.

$$\varepsilon_{eq.}^2 = \frac{1}{2}\left[\left(\varepsilon_{xx} - \varepsilon_{yy}\right)^2 + \left(\varepsilon_{xx} - \frac{2W}{2t}\right)^2 + \left(\varepsilon_{yy} - \frac{2W}{2t}\right)^2\right] \tag{5.1}$$

Equation (5.1) delineates the foundational principle behind this analysis. The study examines two distinct laminate configurations: the AS $[45/90/-45/0/-45/0/-45/0/45/90/45/90]_s$ and the S $[45/0/-45/90]_{3s}$. A discernible pattern emerges across both configurations, illustrating a transition of data points from one linear trajectory to another. This transition matches the behavior experienced by a plate under buckling. Which, in this case, indicates the buckling of the delaminated area. The points of intersection between these linear paths have been determined and documented, highlighting the specific displacement at which a critical displacement $W_{cr.}$ is reached for varying levels of impact energy. Figure 5.2 further elaborates on this concept by plotting the measured values of the equivalent strain $\varepsilon_{eq.}$ against their corresponding critical displacements $W_{cr.}$. This graphical representation facilitates the identification of a linear trendline for both the 'AS' and 'S' laminate configurations.

Consequently, the analysis culminates in deriving two predictive equations, denoted as (5.2) and (5.3). These equations serve as a mathematical model to estimate the threshold for the reoccurrence of delamination.

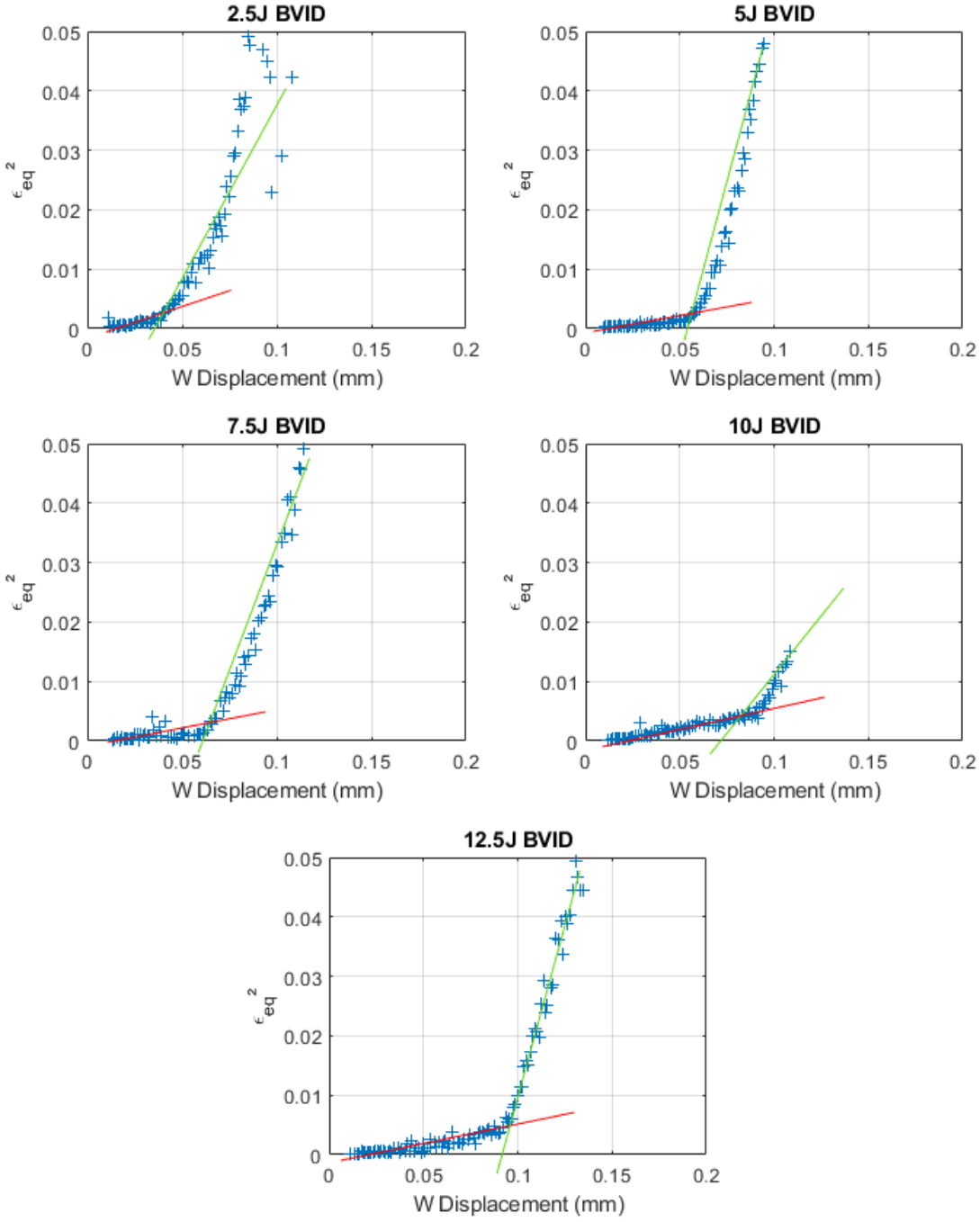

Figure 5.1. Peak displacement versus the square of equivalent strain across various BVID boundaries for 'AS'.

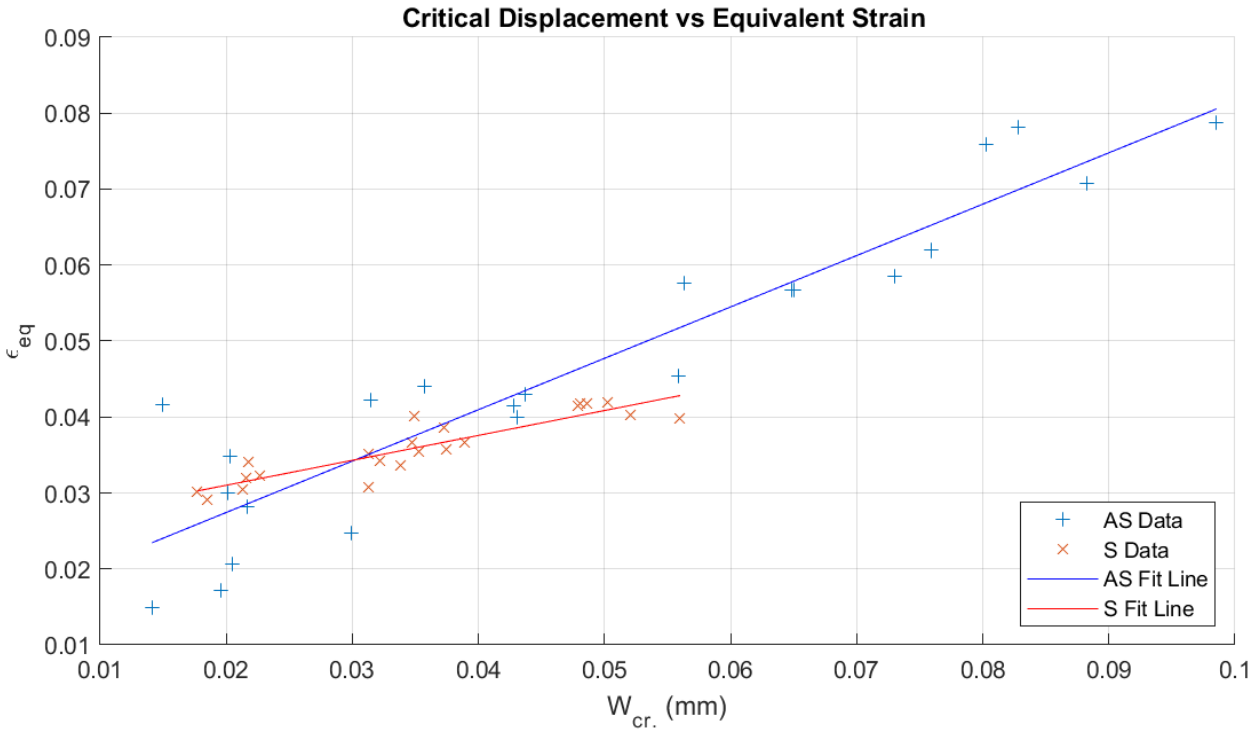

Figure 5.2. Critical displacement vs. equivalent strain for 'AS' and 'S'

$$AS \rightarrow \varepsilon_{eq.cr.} = 0.6765 \times W_{cr.} + 0.0139 \tag{5.2}$$

$$S \rightarrow \varepsilon_{eq.cr.} = 0.3280 \times W_{cr.} + 0.0245 \tag{5.3}$$

A definite relationship between the sample properties, critical displacement $W_{cr.}$, and surface strains is defined after determining the linear trendline. The relationship provides a clear indication in situations where the focus is on the reinitiation of damage propagation only without prior knowledge of the initial damage perimeters, particularly in BVIDs. The model simplifies to the bellow equation with α, and β as constants.

$$\sqrt{\frac{1}{2}\left[\left(\varepsilon_{xx}-\varepsilon_{yy}\right)^2+\left(\varepsilon_{xx}-\frac{2W_{cr.}}{t}\right)^2+\left(\varepsilon_{yy}-\frac{2W_{cr.}}{t}\right)^2\right]} = \alpha W_{cr.} + \beta \tag{5.3}$$

Where ε represents the strain components (ε_{xx}, and ε_{yy}), $W_{cr.}$ represents the critical displacement, t indicates the thickness of the sample, α , and β are modulating factors that adjust the impact of displacement based on the laminate layup.

The observation from Figure 5.2 underscores a crucial aspect of the model's applicability concerning preventing delamination reinitiation in composite materials subjected to an LVI. It outlines that delamination will not reoccur as long as the observed data presents a point where the displacement W, alongside the equivalent strain $\varepsilon_{eq.}$, remains beneath the defined threshold.

5.2 Uncertainty Analysis

The quantitative assessment of the delamination initiation thresholds under low-velocity impacts on composite materials, specifically focusing on 'AS' and 'S' laminate configurations, has revealed a linear relationship between the critical displacement and the equivalent strain.

Using linear regression analysis yielded linear models with slopes and intercepts, encapsulating the linear trend observed in the datasets.

The regression analysis demonstrated a strong positive linear relationship for both configurations, summarized in the Table 5.1.

Table 5.1 Regression coefficients and statistics

Configuration	**Slope (α)**	**Intercept (β)**	**R-value**	**P-value**	**Standard Error**
AS	0.6765	0.0139	0.9345	6.98×10^{-11}	0.0562
S	0.3280	0.0245	0.8992	1.28×10^{-8}	0.0357

Where the R-value reflects the strength of the linear relationship, with values closer to 1 indicating a stronger correlation. Both configurations exhibit high R-values, indicating strong linear relationships.

Table 5.2 Error metrics and confidence intervals

Config.	**Slope Error (%)**	**Intercept Error (%)**	**Slope CI (95%)**	**Intercept CI (95%)**
AS	8.31	404.44	(0.5595, 0.7934)	(-0.1031, 0.1309)
S	10.88	145.86	(0.2535, 0.4024)	(-0.0500, 0.0989)

Table 5.2 showcases the error metrics and confidence intervals where the slope error percentage indicates the precision of the slope value, while the intercept error percentage reflects the relative accuracy of the intercept. The confidence intervals provide a range of values within which the true slope and intercept lie with a 95% accuracy.

The linear relationships described by the regression equations for the 'AS' and 'S' configurations underline the predictive power of the model to determine the critical displacement and the equivalent strain at which the delamination propagation would reinitiate from a BVID in composite laminates. The addition of error metrics and confidence intervals enriches the analysis, offering a nuanced view of the models' reliability. This comprehensive analysis paves the way for designing more resilient composite structures by predicting and understanding the impact damage behavior.

6 Conclusion and Future Perspectives

The investigation explored the quantification of parameters essential for understanding damage propagation in composite materials subjected to Compression After Impact (CAI) testing following the introduction of Barely Visible Impact Damage (BVID) under various Low Velocity Impacts (LVI). Significant insights into the dynamic response of the delamination reinitiation from a BVID site have been interpreted through experimental analysis and comparative studies using two different laminate layups.

The investigation leverages advanced techniques, including Digital Image Correlation (DIC), X-ray microtomography, and scanning electron microscopy, to analyze and map the extent and progression of damage within CFRP samples subjected to low-velocity impacts. Furthermore, this research has underscored a critical aspect often overlooked in composite material studies: the disparity between manufacturer-stated values and actual experimental results. The findings notably highlight variations in material properties, such as elastic moduli, which have profound implications for the structural analysis and application of CFRPs.

A cornerstone of this investigation was integrating DIC results with mechanical testing data, a methodology that unveiled the elaborate relationship between surface strains, out-of-plane displacements, and the re-initiation and propagation of delamination. By employing advanced visualization techniques and synchronized datasets, the study successfully mapped displacement patterns and stress shifts indicative of delamination from a BVID.

The research findings reveal a consistent pattern of strain divergence and out-of-plane displacements correlating with the onset of delamination reinitiation. Using the equivalent strain derived from the invariant of the deviatoric strain tensor, a novel approach has been introduced to predict the threshold for delamination reoccurrence.

While the current study marks a significant step forward in understanding and predicting the reoccurrence of delamination in CFRP materials post-BVID, the path forward calls for an expanded research framework. By incorporating ex-situ analyses, diversifying material and structural parameters, and broadening the material scope, future studies can build upon this foundation to develop a more encompassing and accurate predictive model that can be used to determine the delamination reinitiation in more complex and challenging environments.

7 REFERENCES

[1] Reid, S. R., and Zhou, G., Eds., "Impact Behaviour of Fibre-Reinforced Composite Materials and Structures," CRC Press ; Woodhead Pub, Boca Raton : Cambridge, England, 2000.

[2] Cook, L., Boulic, A., Harris, D., Bellamy, P., and Irving, P. E., "Reliability of Damage Detection in Advanced Composite Aircraft Structures: Prepared for CAA By," TSO, Norwich, 2013.

[3] Polimeno, U., and Meo, M., "Detecting Barely Visible Impact Damage Detection on Aircraft Composites Structures," *Composite Structures*, Vol. 91, No. 4, 2009, pp. 398–402. https://doi.org/10.1016/j.compstruct.2009.04.014

[4] Dubinskii, S., Feygenbaum, Y., Senik, V., and Metelkin, E., "A Study of Accidental Impact Scenarios for Composite Wing Damage Tolerance Evaluation," *The Aeronautical Journal*, Vol. 123, No. 1268, 2019, pp. 1724–1739. https://doi.org/10.1017/aer.2018.152

[5] Dobyns, A. L., and Porter, T. R., "A Study of the Structural Integrity of Graphite Composite Structure Subjected to Low Velocity Impact," *Polymer Engineering and Science*, Vol. 21, No. 8, 1981, pp. 493–498. https://doi.org/10.1002/pen.760210809

[6] Zhang, C., Zhang, X., Duan, Y., Xia, Y., Ming, Y., and Zhu, Y., "Deformation Resistance Performance of Carbon Fiber-Reinforced Plastic Machined by Controlling Drilling Area Temperature below the Glass Transition Temperature," *Materials*, Vol. 14, No. 6, 2021, p. 1394. https://doi.org/10.3390/ma14061394

[7] Liu, D., "Impact-Induced Delamination—A View of Bending Stiffness Mismatching," *Journal of Composite Materials*, Vol. 22, No. 7, 1988, pp. 674–692. https://doi.org/10.1177/002199838802200706

[8] Fedulov, B. N., Fedorenko, A. N., and Lomakin, E. V., "Evaluation of the Residual Strength of Structures Made of Composite Materials Based on a Conservative Distribution of Damage Parameters," *IOP Conference Series: Materials Science and Engineering*, Vol. 581, No. 1, 2019, p. 012023. https://doi.org/10.1088/1757-899X/581/1/012023

[9] Poe, C. C., "Residual Strength of Composite Aircraft Structures with Damage," *Fatigue and Fracture*, ASM International, 1996, pp. 920–935. https://doi.org/10.31399/asm.hb.v19.a0002416

[10] Fedulov, B. N., and Fedorenko, A. N., "Residual Strength Estimation of a Laminated Composite with Barely Visible Impact Damage Based on Topology Optimization," *Structural and Multidisciplinary Optimization*, Vol. 62, No. 2, 2020, pp. 815–833. https://doi.org/10.1007/s00158-020-02538-y

[11] Davies, G. A. O., and Zhang, X., “Impact Damage Prediction in Carbon Composite Structures,” *International Journal of Impact Engineering*, Vol. 16, No. 1, 1995, pp. 149–170. https://doi.org/10.1016/0734-743X(94)00039-Y

[12] Wang, A., and Slomiana, M., “Fracture Mechanics of Delamination. Initiation and Growth.,” 1982.

[13] Jribi, K., Gosse, J. H., Neill, D. J., and Mello, A. W., “Damage Control Measures in Composites: BVID Damage Progression,” presented at the ASME 2023 Aerospace Structures, Structural Dynamics, and Materials Conference, San Diego, California, USA, 2023. https://doi.org/10.1115/SSDM2023-100771

[14] Zhang, L., Wang, R., Liu, W., Chen, C., and He, X., “Delamination Growth Behavior in Carbon Fiber Reinforced Plastic Angle Ply Laminates under Compressive Fatigue Loads,” *Journal of Reinforced Plastics and Composites*, Vol. 31, No. 4, 2012, pp. 259–267. https://doi.org/10.1177/0731684412436707

[15] Yang, Y., “A Numerical Study of Damage Mechanisms in the CAI of Laminated Composites for Aerospace Applications,” Jul2016.

[16] Xu, F., Liu, W., and Irving, P. E., “FATIGUE LIFE AND FAILURE OF IMPACT-DAMAGED CARBON FIBRE COMPOSITES UNDER COMPRESSIVE CYCLIC LOADS,” presented at the 21st International Conference on Composite Material, Xi’an, China, 2017.

[17] Wang, K., Zhao, L., Hong, H., Zhang, J., and Hu, N., “An Extended Analytical Model for Predicting the Compressive Failure Behaviors of Composite Laminate with an Arbitrary Elliptical Delamination,” *International Journal of Solids and Structures*, Vols. 185–186, 2020, pp. 439–447. https://doi.org/10.1016/j.ijsolstr.2019.09.002

[18] Sun, X. C., and Hallett, S. R., “Failure Mechanisms and Damage Evolution of Laminated Composites under Compression after Impact (CAI): Experimental and Numerical Study,” *Composites Part A: Applied Science and Manufacturing*, Vol. 104, 2018, pp. 41–59. https://doi.org/10.1016/j.compositesa.2017.10.026

[19] Pascoe, J. A., Alderliesten, R. C., and Benedictus, R., “Methods for the Prediction of Fatigue Delamination Growth in Composites and Adhesive Bonds – A Critical Review,” *Engineering Fracture Mechanics*, Vols. 112–113, 2013, pp. 72–96. https://doi.org/10.1016/j.engfracmech.2013.10.003

[20] Justusson, B., Liguore, S., and Schaefer, J., “Methods for Composite Structures Service Life Extension – CALE Demonstration,” San Antonio, TX, Dec 02 2019.

[21] Neill, D. J., Gosse, J., and Kanthasamy, K., “Margin of Safety Assessment for Composite StructureS Using the Onset Method,” presented at the AIAA Scitech 2021 Forum,

VIRTUAL EVENT, 2021. https://doi.org/10.2514/6.2021-0699

[22] "Aging Prediction of Airworthiness of Aircraft Composite Components Accounting for Flight and Environmental Conditions." Retrieved 19 December 2022. https://www.navysbir.com/n21_1/N211-019.htm

[23] "NASA's Advanced Composites Consortium." Retrieved 19 December 2022. https://www.nianet.org/research-centers/advanced-composite-consortium/

[24] Banks-Sills, L., Simon, I., and Chocron, T., "Multi-Directional Composite Laminates: Fatigue Delamination Propagation in Mode I—a Comparison," *International Journal of Fracture*, Vol. 219, No. 2, 2019, pp. 175–185. https://doi.org/10.1007/s10704-019-00388-4

[25] Potter, K., "Manufacturing Defects as a Cause of Failure in Polymer Matrix Composites," *Failure Mechanisms in Polymer Matrix Composites*, Elsevier, 2012, pp. 26–52. https://doi.org/10.1533/9780857095329.1.26

[26] Sacchetti, F., Grouve, W. J. B., Warnet, L. L., and Villegas, I. F., "Effect of Resin-Rich Bond Line Thickness and Fibre Migration on the Toughness of Unidirectional Carbon/PEEK Joints," *Composites Part A: Applied Science and Manufacturing*, Vol. 109, 2018, pp. 197–206. https://doi.org/10.1016/j.compositesa.2018.02.035

[27] Goidescu, C., Welemane, H., Garnier, C., Fazzini, M., Brault, R., Péronnet, E., and Mistou, S., "Damage Investigation in CFRP Composites Using Full-Field Measurement Techniques: Combination of Digital Image Stereo-Correlation, Infrared Thermography and X-Ray Tomography," *Composites Part B: Engineering*, Vol. 48, 2013, pp. 95–105. https://doi.org/10.1016/j.compositesb.2012.11.016

[28] Bull, D. J., Helfen, L., Sinclair, I., Spearing, S. M., and Baumbach, T., "A Comparison of Multi-Scale 3D X-Ray Tomographic Inspection Techniques for Assessing Carbon Fibre Composite Impact Damage," *Composites Science and Technology*, Vol. 75, 2013, pp. 55–61. https://doi.org/10.1016/j.compscitech.2012.12.006

[29] Lau, S. H., Chiu, W. K. S., Garzon, F., Chang, H., Tkachuk, A., Feser, M., and Yun, W., "Non Invasive, Multiscale 3D X-Ray Characterization of Porous Functional Composites and Membranes, with Resolution from MM to Sub 50 NM," *Journal of Physics: Conference Series*, Vol. 152, 2009, p. 012059. https://doi.org/10.1088/1742-6596/152/1/012059

[30] Meola, C., and Carlomagno, G. M., "Impact Damage in GFRP: New Insights with Infrared Thermography," *Composites Part A: Applied Science and Manufacturing*, Vol. 41, No. 12, 2010, pp. 1839–1847. https://doi.org/10.1016/j.compositesa.2010.09.002

[31] Lomov, S. V., Ivanov, D. S., Verpoest, I., Zako, M., Kurashiki, T., Nakai, H., Molimard, J., and Vautrin, A., "Full-Field Strain Measurements for Validation of Meso-FE Analysis of Textile Composites," *Composites Part A: Applied Science and Manufacturing*, Vol. 39,

No. 8, 2008, pp. 1218–1231. https://doi.org/10.1016/j.compositesa.2007.09.011

[32] Guinard, S., Allix, O., Guedradegeorges, D., and Vinet, A., "A 3D Damage Analysis of Low-Velocity Impacts on Laminated Composites," *Composites Science and Technology*, Vol. 62, No. 4, 2002, pp. 585–589. https://doi.org/10.1016/S0266-3538(01)00153-1

[33] Sarasini, F., Tirillò, J., Ferrante, L., Valente, M., Valente, T., Lampani, L., Gaudenzi, P., Cioffi, S., Iannace, S., and Sorrentino, L., "Drop-Weight Impact Behaviour of Woven Hybrid Basalt–Carbon/Epoxy Composites," *Composites Part B: Engineering*, Vol. 59, 2014, pp. 204–220. https://doi.org/10.1016/j.compositesb.2013.12.006

[34] Polimeno, U., Meo, M., Almond, D. P., and Angioni, S. L., "Detecting Low Velocity Impact Damage in Composite Plate Using Nonlinear Acoustic/Ultrasound Methods," *Applied Composite Materials*, Vol. 17, No. 5, 2010, pp. 481–488. https://doi.org/10.1007/s10443-010-9168-5

[35] Ambu, R., Aymerich, F., Ginesu, F., and Priolo, P., "Assessment of NDT Interferometric Techniques for Impact Damage Detection in Composite Laminates," *Composites Science and Technology*, Vol. 66, No. 2, 2006, pp. 199–205. https://doi.org/10.1016/j.compscitech.2005.04.027

[36] Ellison, A., and Kim, H., "Shadowed Delamination Area Estimation in Ultrasonic C-Scans of Impacted Composites Validated by X-Ray CT," *Journal of Composite Materials*, Vol. 54, No. 4, 2020, pp. 549–561. https://doi.org/10.1177/0021998319865311

[37] Shadmehri, F., and Hoa, S. V., "Digital Image Correlation Applications in Composite Automated Manufacturing, Inspection, and Testing," *Applied Sciences*, Vol. 9, No. 13, 2019, p. 2719. https://doi.org/10.3390/app9132719

[38] Patz Materials & Technologies, "PMT-F7," 2023.

[39] Carrera, E., and Associazione italiana di aeronautica e astronautica, Eds., "Composite Materials and Structures in Aerospace Engineering: Selected Plenary Lectures and Key-Note Contributions of the Two Events FULLCOMP - Meeting FULLy Integrated Analysis, Design, Manufacturing and Health-Monitoring of COMPosite Structures and 23rd Congress of AIDAA, Associazione Italiana Di Aeronautica Ed Astronautica, November 17-21, 2015, Torino, Italy," TTP, Trans Tech Publications Ltd, Pfaffikon, Switzerland, 2016.

[40] Li, Y., Xian, X. J., Choy, C. L., Guo, M., and Zhang, Z., "Compressive and Flexural Behavior of Ultra-High-Modulus Polyethylene Fiber and Carbon Fiber Hybrid Composites," *Composites Science and Technology*, Vol. 59, No. 1, 1999, pp. 13–18. https://doi.org/10.1016/S0266-3538(98)00056-6

[41] Wu, W., Wang, Q., and Li, W., "Comparison of Tensile and Compressive Properties of Carbon/Glass Interlayer and Intralayer Hybrid Composites," *Materials*, Vol. 11, No. 7,

2018, p. 1105. https://doi.org/10.3390/ma11071105

[42] Dong, Y. L., and Pan, B., "A Review of Speckle Pattern Fabrication and Assessment for Digital Image Correlation," *Experimental Mechanics*, Vol. 57, No. 8, 2017, pp. 1161–1181. https://doi.org/10.1007/s11340-017-0283-1

[43] Blaysat, B., Grédiac, M., and Sur, F., "Effect of Interpolation on Noise Propagation from Images to DIC Displacement Maps," *International Journal for Numerical Methods in Engineering*, Vol. 108, No. 3, 2016, pp. 213–232. https://doi.org/10.1002/nme.5212

[44] Franz, M., Schleich, B., and Wartzack, S., "Tolerance Management during the Design of Composite Structures Considering Variations in Design Parameters," *The International Journal of Advanced Manufacturing Technology*, Vol. 113, Nos. 5–6, 2021, pp. 1753–1770. https://doi.org/10.1007/s00170-020-06555-5

[45] Kaware, K. R., and Kotambkar, M. S., "Effect of Impactor Velocity and Boundary Condition on Low Velocity Impact Finite Element Modelling of CFRP Composite Laminates," *IOP Conference Series: Materials Science and Engineering*, Vol. 1004, No. 1, 2020, p. 012018. https://doi.org/10.1088/1757-899X/1004/1/012018

[46] Sun, X. C., Wisnom, M. R., and Hallett, S. R., "Interaction of Inter- and Intralaminar Damage in Scaled Quasi-Static Indentation Tests: Part 2 – Numerical Simulation," *Composite Structures*, Vol. 136, 2016, pp. 727–742. https://doi.org/10.1016/j.compstruct.2015.09.062

[47] Instron, "Life Cycle Notice Letter: Instron® Dynatup 9200 Series in Phase 4 – Discontinued Product," 2022.

[48] Xu, L. R., and Rosakis, A. J., "Impact Damage Visualization of Heterogeneous Two-Layer Materials Subjected to Low-Speed Impact," *International Journal of Damage Mechanics*, Vol. 14, No. 3, 2005, pp. 215–233. https://doi.org/10.1177/1056789505048604

[49] Sun, X. C., and Hallett, S. R., "Failure Mechanisms and Damage Evolution of Laminated Composites under Compression after Impact (CAI): Experimental and Numerical Study," *Composites Part A: Applied Science and Manufacturing*, Vol. 104, 2018, pp. 41–59. https://doi.org/10.1016/j.compositesa.2017.10.026

[50] Hearn, E. J., "Introduction to Advanced Elasticity Theory," *Mechanics of Materials 2*, Elsevier, 1997, pp. 220–299. https://doi.org/10.1016/B978-075063266-9/50009-3

8 PUBLICATIONS

Jribi, K., Gosse, J. H., Neill, D. J., and Mello, A. W., “Damage Control Measures in Composites: BVID Damage Progression,” presented at the ASME 2023 Aerospace Structures, Structural Dynamics, and Materials Conference, San Diego, California, USA, 2023. https://doi.org/10.1115/SSDM2023-100771

Jribi, K., Azizi B., and Mello, A. W., “In-Situ Detection of Delamination Reinitiation in Carbon Fiber Reinforced Polymers Post Barely Visible Impact Damage” Submitted to Composites Part B: Engineering

Jribi, K., Azizi B., and Mello, A. W., "CRFP Mechanical Properties - Stated Values vs. Experimental Data." Submitted to the ASME Journal of Engineering Materials and Technology. Manuscript ID: MATS-23-1238.

9 CONFERENCES

Jribi, K., Gosse, J. H., Neill, D. J., and Mello, A. W., “Barely Visible Impact Damage in Composites: Progression and Control Measures” 47th International Conference and Expo on Advanced Ceramics and Composites, (ICACC-S1-049-2023), Daytona Beach, FL, Jan. 2023

Jribi, K., Gosse, J. H., Neill, D. J., and Mello, A. W., “Damage Control Measures in Composites: BVID Damage Progression” ASME Aerospace Structures, Structural Dynamics and Materials Conference. SSDM 2023., Technical paper, San Diego, CA, Jun. 2023

Jribi, K., Mello, A. W., and Azizi, B., “Delamination Re-Initiation From a BVID in CFRP” ASME 2023 International Mechanical Engineering Congress and Exposition, (IMECE2023-119994), New Orleans, LA, Oct. – Nov. 2023

Jribi, K., Azizi, B., and Mello, A. W., “Characterization of Barely Visible Impact Damage” CAMX – the Composites and Advanced Materials Expo, (PS23-0000000026), Atlanta, GA, Oct. – Nov. 2023

Jribi, K., Azizi, B., and Mello, A. W., “Delamination in CFRP: Experimental Approach” 48th International Conference and Expo on Advanced Ceramics and Composites, (ICACC-S1-024-2024), Daytona Beach, FL, Jan. – Feb. 2024

10 APPENDIX - A

```
% This code is meant to crop the images taken by the x-ray into separate samples and later on, padd the
resultant images to the prior dimensions by adding black fillers to the upper and lower part resulting in a
1944x1944 pixel image.
clear all
% Prompt user to select folder
folderPath = uigetdir('Select a folder containing images');
if folderPath == 0
    disp('User selected Cancel');
    return;
end


% Get a list of all files in the folder
filePattern = fullfile(folderPath, '*rec0*.jpg');
theFiles = dir(filePattern);


% Initialize subfolder names and corresponding crop values
subFolderNames = {'Ref','AS19','AS20','AS21','AS22','AS23','AS24'};
topCropValues = [310,560,740,930,1100,1290,1460];
SampleHeight = [190,120,140,140,180,160,200];


% Check and create subfolders if they do not exist
for i = 1:length(subFolderNames)
    subFolderPath = fullfile(folderPath, subFolderNames{i});
    if ~exist(subFolderPath, 'dir')
        mkdir(subFolderPath); % Create the subfolder if it does not exist
    end
end


% Get all .log files and *rec_spr.* files in the main folder
logFiles = dir(fullfile(folderPath, '*.log'));
recSprFiles = dir(fullfile(folderPath, '*rec_spr.*'));


% Combine the lists of files to copy
filesToCopy = [logFiles; recSprFiles];


% Loop through each file to copy it into each subfolder
for idx = 1:length(filesToCopy)
    for k = 1:length(subFolderNames)
        subFolderPath = fullfile(folderPath, subFolderNames{k});
        sourceFile = fullfile(folderPath, filesToCopy(idx).name);
```

```
        destinationFile = fullfile(subFolderPath, filesToCopy(idx).name);
        copyfile(sourceFile, destinationFile);
    end
end


% Define the target size
targetSize = [1944 1944];


% Loop through all files
for j = 1:length(theFiles)
    baseFileName = theFiles(j).name;
    fullFileName = fullfile(folderPath, baseFileName);
    fprintf(1, 'Now reading %s\n', fullFileName);


    % Read the image
    imageArray = imread(fullFileName);


    % Get the original image size
    [height, width, ~] = size(imageArray);


    % Loop through each subfolder to crop, resize, and save the image
    for k = 1:length(subFolderNames)
        % Crop the image
        croppedImage = imcrop(imageArray, [0, topCropValues(k), width, SampleHeight(k)]);


        % Calculate the size for padding
        [cHeight, cWidth, ~] = size(croppedImage);
        padHeight = (targetSize(1) - cHeight)/2;
        padWidth = (targetSize(2) - cWidth)/2;

        % Pad the image to make it 1944x1944 and place the cropped image in the center
        paddedImage = padarray(croppedImage, [floor(padHeight), floor(padWidth)], 0, 'pre');
        paddedImage = padarray(paddedImage, [ceil(padHeight), ceil(padWidth)], 0, 'post');


        % Construct the new filename and path to save in subfolder
        newFileName = sprintf(baseFileName);
        newFullFileName = fullfile(folderPath, subFolderNames{k}, newFileName);


        % Save the resized and padded image
        imwrite(paddedImage, newFullFileName);
        fprintf(1, 'Saved cropped and resized image to: %s\n', newFullFileName);
```

```
  end
end
```

11 APPENDIX - B

```
% This code recognizes the percentage of fibers located within the image.

clear all;

% Open file selection dialog box
[filename, pathname] = uigetfile( ...
   {'*.jpg;*.tif;*.png;*.gif', 'All Image Files'; ...
   '*.*', 'All Files' }, 'Select an image');

% Construct the full path and load the image
fullFileName = fullfile(pathname, filename);
img = imread(fullFileName);

% Check if the image is RGB and convert to grayscale if it is
if size(img, 3) == 3
   grayImg = rgb2gray(img); % Convert to grayscale if it's RGB
else
   grayImg = img; % It's already grayscale or has a single channel
end
binaryImg = imbinarize(grayImg, 'adaptive');
binaryImg = bwareaopen(binaryImg, 100); % Remove small noise regions

% Perform morphological operations to enhance fiber regions
se = strel('disk', 5);
dilatedImg = imdilate(binaryImg, se);
filledImg = imfill(dilatedImg, 'holes');
erodedImg = imerode(filledImg, se);

% Find connected components (fibers)
cc = bwconncomp(erodedImg);
numFibers = cc.NumObjects;

% Calculate the total area of fibers as a percentage of the image area
imageArea = numel(binaryImg);
fiberArea = sum(erodedImg(:));
percentFiberArea = (fiberArea / imageArea) * 100;

% Display the original image with detected fibers and the percent area
figure;
imshow(img);
title(['Number of Rounded Fibers: ', num2str(numFibers), ', Fiber Area (%): ', num2str(percentFiberArea,
'%.2f')]);
```

12 APPENDIX - C

```
% This code is meant separate the results recorded using the Horizon software into separate Excel files and
save each sample to the appropriate folder.
Clear all


% Prompt the user to select the file
[filename, filepath] = uigetfile({'*.xlsx'}, 'Select the Excel file with test data');
if isequal(filename,0)
   disp('User selected Cancel');
   return;
else
   disp(['User selected ', fullfile(filepath, filename)]);
end


% Define the original file path
originalFile = fullfile(filepath, filename);


% Read the data from the Excel file with original column headers
data = readtable(originalFile, 'VariableNamingRule', 'preserve');


% Find the indices where the first column has a value of 0.1, indicating the start of a new sample
sampleStarts = find(data.('Time (sec)') == 0.1);


% Add the first row as the start of the first sample if it's not already 0.1
if data.('Time (sec)')(1) ~= 0.1
   sampleStarts = [1; sampleStarts];
end


% Add an end index for the last segment
sampleStarts(end+1) = size(data, 1) + 1;


% Base directory for saving files
baseSaveDir = filepath; % This will save in the same directory as the source file, change as necessary


% Iterate through each segment and write to a new Excel file in its own directory
for i = 1:length(sampleStarts)-1
   % Define the segment of data for this test
   segment = data(sampleStarts(i):sampleStarts(i+1)-1, :);

   % Determine file name and directory
```

```
    if i <= 25
        fileName = sprintf('S%02d.xlsx', 26-i); % S25 to S01
    else
        fileName = sprintf('AS%02d.xlsx', 51-i); % AS25 to AS01
    end
    dirName = fullfile(baseSaveDir, fileName(1:end-5)); % Remove .xlsx to get folder name


    % Create directory if it doesn't exist
    if ~exist(dirName, 'dir')
       mkdir(dirName);
    end

    % Define full file path
    fullFilePath = fullfile(dirName, fileName);


    % Write the segment to a new Excel file in its own directory
    writetable(segment, fullFilePath);
end
```

13 APPENDIX - D

```
% This code reads the xlsx file generated by extracting the data from the Horizon xlsx file and would then campare it with the csv data from the DIC, then it would look for the matching times in each file and combine them together in one xlsx file.
clear all;


% Prompt user to select the main folder
mainFolder = uigetdir;
if isequal(mainFolder, 0)
    disp('User selected Cancel');
    return;
end


% List of subfolder names
subfolderNames = ["AS01", "AS02", "AS03", "AS04", "AS05", "AS06", "AS07", "AS08", "AS09", "AS10", "AS11", "AS12", "AS13", "AS14", "AS15", "AS16", "AS17", "AS18", "AS19", "AS20", "AS21", "AS22", "AS23", "AS24", "AS25", "S01", "S02", "S03", "S04", "S05", "S06", "S07", "S08", "S09", "S10", "S11", "S12", "S13", "S14", "S15", "S16", "S17", "S18", "S19", "S20", "S21", "S22", "S23", "S24", "S25"];


% Process each subfolder
for k = 1:length(subfolderNames)
    subfolder = fullfile(mainFolder, subfolderNames(k));
    folderName = subfolderNames(k);


    % Construct file paths
    excelFile = fullfile(subfolder, folderName + ".xlsx");
    csvFile = fullfile(subfolder, folderName + ".csv");


    % Check if files exist
    if ~isfile(excelFile) || ~isfile(csvFile)
        disp(['Missing files in ' folderName]);
        continue;
    end


    % Read the Excel file with 'PreserveVariableNames' set to true
    excelTable = readtable(excelFile, 'PreserveVariableNames', true);


    % Read the CSV file with 'PreserveVariableNames' set to true
    csvTable = readtable(csvFile, 'PreserveVariableNames', true);
```

```
% Check for required columns in CSV file
if ~any(strcmp(csvTable.Properties.VariableNames, 'Time_0'))
    disp(['Column "Time_0" not found in ' csvFile]);
    continue;
end


% Adjust 'Time_0' and 'Time_1'in CSV file
csvTable.Time_0 = csvTable.Time_0 - csvTable.Time_0(1);
csvTable.Time_1 = csvTable.Time_1 - csvTable.Time_1(1);


% Check for required column in Excel file
if ~any(strcmp(excelTable.Properties.VariableNames, 'Time (sec)'))
    disp(['Column "Time (sec)" not found in ' excelFile]);
    continue;
end


% Initialize a new column in csvTable for each column in excelTable (except Time (sec))
for i = 2:width(excelTable)
    columnName = excelTable.Properties.VariableNames{i};
    if height(csvTable) ~= height(excelTable)
        % Adjust the number of rows in the new column to match csvTable
        csvTable.(columnName) = NaN(height(csvTable), 1);
    else
        csvTable.(columnName) = excelTable.(columnName);
    end
end


% Copy and interpolate data as needed
timeExcelColumn = excelTable.('Time (sec)');
for i = 1:height(excelTable)
    timeExcel = timeExcelColumn(i);
    [minDiff, index] = min(abs(csvTable.Time_0 - timeExcel));
    for j = 2:width(excelTable)
        varName = excelTable.Properties.VariableNames{j};
        if isnan(csvTable.(varName)(index))
            csvTable.(varName)(index) = excelTable.(varName)(i);
        end
    end
end


% Interpolate missing values for each new column
for j = 2:width(excelTable)
    validIndices = ~isnan(csvTable.(excelTable.Properties.VariableNames{j}));
```

```
        if any(validIndices)
            csvTable.(excelTable.Properties.VariableNames{j}) = interp1(csvTable.Time_0(validIndices),
csvTable.(excelTable.Properties.VariableNames{j})(validIndices), csvTable.Time_0, 'linear', 'extrap');
        end
    end


    % Save the modified data to an Excel file
    newExcelFile = fullfile(subfolder, subfolderNames(k) + "_CombinedData.xlsx");
    writetable(csvTable, newExcelFile);
    disp(['Processed and saved data for ' subfolderNames(k)]);
end


disp('Processing complete for all subfolders.');
```

14 APPENDIX - E

```
% This script should be run before the functions plotting the data. It searches for the .mat files generated with the help of VIC-3D in the sample folders and loads all of them. It then detects the empty data values based on the last frame and crops them from every other frame. It later accounts for the ridged W displacement by normalizing the transition at the sample borders where the sample is fixed.
clear all;


% Load data
folder_path = uigetdir;
if folder_path == 0
    error('No folder was selected.');
else
    % Load .mat files
    files = dir(fullfile(folder_path, '*.mat'));
    DIC_Data = struct();
    minW = Inf;
    maxW = -Inf;


    % Determine cropping indices (assume last frame represents all frames)
    last_frame_data = load(fullfile(folder_path, files(end).name));
    [row_idx, col_idx] = find(last_frame_data.W ~= 0);
    min_row = min(row_idx);
    max_row = max(row_idx);
    min_col = min(col_idx);
    max_col = max(col_idx);


    % Load, crop frame data, and adjust edge values
    for i = 1:length(files)
        file_path = fullfile(folder_path, files(i).name);
        frame_data = load(file_path);
        cropped_W = frame_data.W(min_row:max_row, min_col:max_col);


        % Identify the lower and upper edges of the sample
        lower_edge = cropped_W(1, :);
        upper_edge = cropped_W(end, :);


        % Find the lowest value on the lower and upper edges
        min_edge_value = min([lower_edge, upper_edge]);


        % Raise the minimum edge value to 0 if it's negative
        if min_edge_value < 0
```

```
            cropped_W = cropped_W - min_edge_value;
        end


        DIC_Data.(sprintf('frame_%d', i-1)) = struct('W', cropped_W);
        minW = min(minW, min(cropped_W(:)));
        maxW = max(maxW, max(cropped_W(:)));
    end


    % Load XLSX file
    [~, folder_name] = fileparts(folder_path);
    xlsx_file_name = fullfile(folder_path, strcat(folder_name, '_CombinedData.xlsx'));
    if isfile(xlsx_file_name)
        CombinedData = readtable(xlsx_file_name, 'VariableNamingRule', 'preserve');
    else
        error('The XLSX file does not exist in the selected folder.');
    end
end
```

15 APPENDIX - F

```
% Initialize figure and slider
hFig = figure;
hAx = axes('Parent', hFig);
maxTime = height(CombinedData);
hSlider = uicontrol('Parent', hFig, 'Style', 'slider', 'Value', 2, 'Min', 2, 'Max', maxTime, ...
                    'SliderStep', [1/(maxTime-2) , 10/(maxTime-2) ], 'Units', 'normalized', 'Position', [0.1 0.02 0.8
0.05]);


% Get the minimum and maximum values of cropped W displacement
all_W_data = [];
for i = 2:length(files)
    frame_data = load(fullfile(folder_path, files(i).name));
    all_W_data = [all_W_data; frame_data.(displacement_field)(min_row:max_row, min_col:max_col)];
end
minW = min(all_W_data(:));
maxW = max(all_W_data(:));


% Initial plot
sliderValue = round(get(hSlider, 'Value'));
Displacement3DMap(sliderValue, DIC_Data, CombinedData, hAx, minW, maxW);


% Add listener for slider
addlistener(hSlider, 'ContinuousValueChange', @(src, evt) Displacement3DMap(round(get(src,'Value')),
DIC_Data, CombinedData, hAx, minW, maxW));


% Function to plot frame
function Displacement3DMap(frameNumber, DIC_Data, CombinedData, hAx, minW, maxW)
    frame_name = sprintf('frame_%d', frameNumber-1);
    if isfield(DIC_Data, frame_name)
        W_data = DIC_Data.(frame_name).W;
        exx_data = DIC_Data.(frame_name).exx;
        eyy_data = DIC_Data.(frame_name).eyy;
        exy_data = DIC_Data.(frame_name).exy;


        % Find the indices of the maximum W value
        [maxWValue, maxWIndex] = max(W_data(:));
        [row, col] = ind2sub(size(W_data), maxWIndex);


        % Get corresponding strains in percent
        maxW_exx = exx_data(row, col) * 100;
```

```
        maxW_eyy = eyy_data(row, col) * 100;
        maxW_exy = exy_data(row, col) * 100;


        stress = CombinedData.('Stress (N/mm²)')(frameNumber);
        % Plot W displacement
        axes(hAx);
        surf(W_data, 'EdgeColor', 'none');
        titleHandle = title(sprintf('σ = %.3f MPa, Max W = %.3f mm, ε_x_x = %.3f%%, ε_y_y = %.3f%%, ε_x_y
= %.3f%%', stress, maxWValue, maxW_exx, maxW_eyy, maxW_exy));
        set(titleHandle, 'FontWeight', 'normal');
        set(gca,'XTick',[], 'YTick', [])
        zlabel('W Displacement (mm)');
        colormap(jet); % Apply a colormap
        % Set the colorbar range to be consistent across all frames
        clim([minW maxW]);
        colorbar; % Show a colorbar


        % Draw a circle around the area with the highest W
        hold on;
        circleRadius = 5; % Define the radius of the circle
        theta = linspace(0, 2*pi, 100); % Parameter for the circle
        circleX = col + circleRadius * cos(theta); % X coordinates
        circleY = row + circleRadius * sin(theta); % Y coordinates
        circleZ = maxWValue * ones(size(circleX)); % Z coordinates at max W value
        plot3(circleX, circleY, circleZ, 'g-', 'LineWidth', 2); % Plot the circle
        hold off;
    else
    warning('No data available for frame %d.', frameNumber-1);
    end
end
```

16 APPENDIX - G

```
function DisplacementVsStrains(DIC_Data, CombinedData)
    figure;
    yyaxis left;
    hold on; % Hold on to add multiple plots


    % Initialize arrays to store strains and displacement for each frame
    displacements = [];
    strains_exx = [];
    strains_eyy = [];
    strains_exy = [];
    stresses = [];


    lastDisplacement = -Inf; % Initialize with an impossible value


    for i = 2:length(fields(DIC_Data))
        frame_name = sprintf('frame_%d', i - 1);
        if isfield(DIC_Data, frame_name)
            W_data = DIC_Data.(frame_name).W;
            exx_data = DIC_Data.(frame_name).exx * 100;
            eyy_data = DIC_Data.(frame_name).eyy * 100;
            exy_data = DIC_Data.(frame_name).exy * 100;


            [numRows, numCols] = size(W_data);


            % Extracting the specified column data for displacement and strains
            middleW = max(W_data(:, :), [], 'all');
            % Retrieve stress value
            stress = CombinedData.('Stress (N/mm²)')(i);
            % Find the corresponding strains for the maximum W value
            [~, idx] = max(W_data(:));
            [row, col] = ind2sub(size(W_data), idx);
            maxWStrains = [exx_data(row, col), eyy_data(row, col), exy_data(row, col)];


            % Calculate the percentage difference from the last displacement
            if lastDisplacement ~= -Inf
                percentDifference = abs((middleW - lastDisplacement) / lastDisplacement * 100);


                % Eliminate the noise
                if percentDifference < 1
                    displacements(end + 1) = middleW;
```

```
            strains_exx(end + 1) = maxWStrains(1);
            strains_eyy(end + 1) = maxWStrains(2);
            strains_exy(end + 1) = maxWStrains(3);
            stresses(end + 1) = stress;
        end
    end

    lastDisplacement = middleW; % Update the last displacement
  else
    warning('No data available for frame %d.', i - 1);
  end
end

% Determine the maximum absolute strain value
max_strain = max([abs(strains_exx), abs(strains_eyy), abs(strains_exy)]);

% Determine the maximum displacement
max_displacement = max(displacements);

% Plotting Displacement vs. Strains
yyaxis left;
plot(displacements, strains_exx, 'r^', 'DisplayName', '\epsilon_x_x');
plot(displacements, strains_eyy, 'g>', 'DisplayName', '\epsilon_y_y');
plot(displacements, strains_exy, 'bd', 'DisplayName', '\epsilon_x_y');

% Set Y-axis limits for strains such that 0 is in the middle
ylim([-max_strain, max_strain]);
ylabel('Strains %');

% Plotting stress on the right Y-axis
yyaxis right;
plot(displacements, stresses, 'ks', 'DisplayName', 'Stress')
ylabel('Stress (N/mm²)');

% Label X-axis
xlabel('W Displacement (mm)');

% Set X-axis limits conditionally
if max_displacement > 0.3
  xlim([0, 0.3]);
end
```

```
    % Label X-axis
    xlabel('W Displacement (mm)');


    title('Displacement vs. Strains with Stress');


    % Position the legend in the lower left corner
    legend('show', 'Location', 'southwest');

end


% Call the function with your data
DisplacementVsStrains(DIC_Data, CombinedData);
```

17 APPENDIX – H

Samples with the corresponding determinant plot for critical displacement "AS" [45/90/-45/0/-45/0/-45/0/45/90/45/90]$_s$
Impact Energy Level: 2.5 J

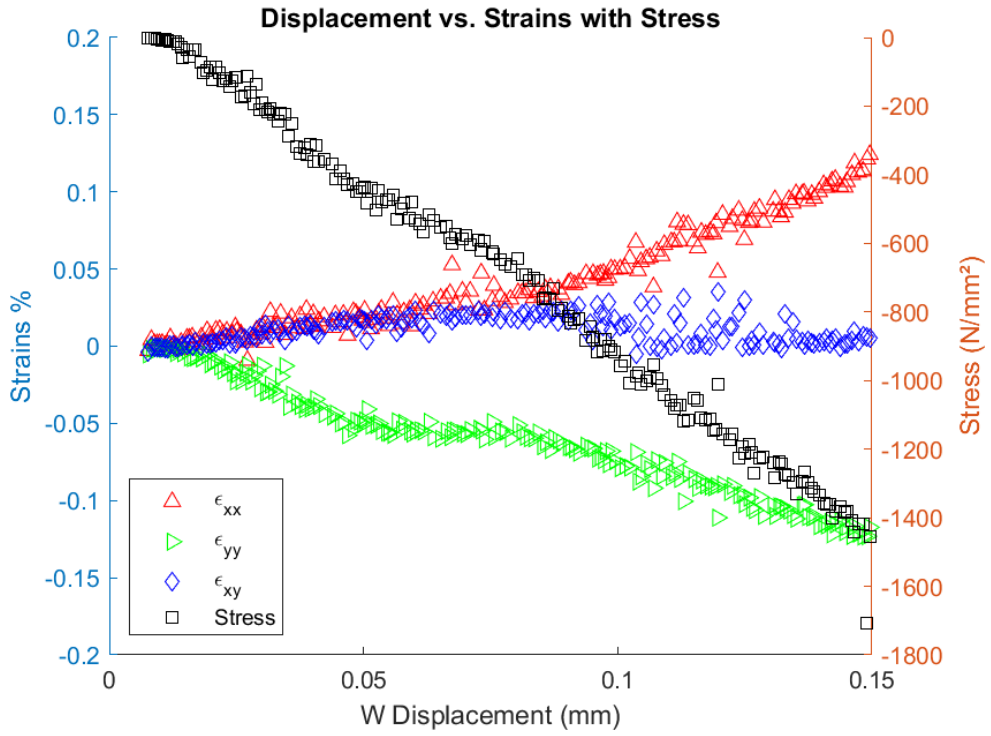

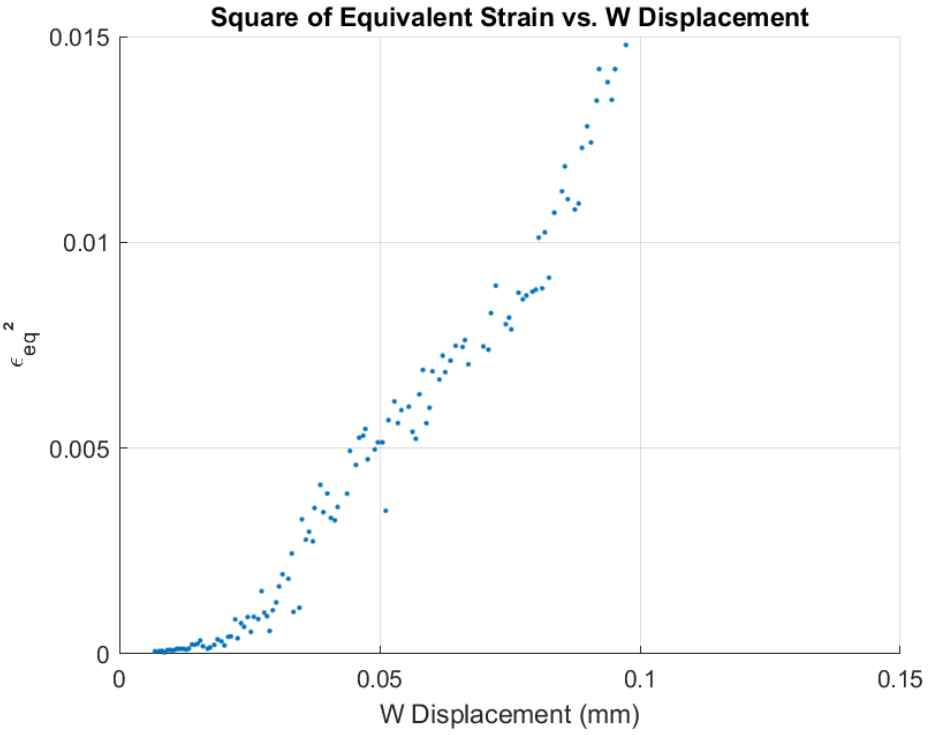

Impact Energy Level: 2.5 J

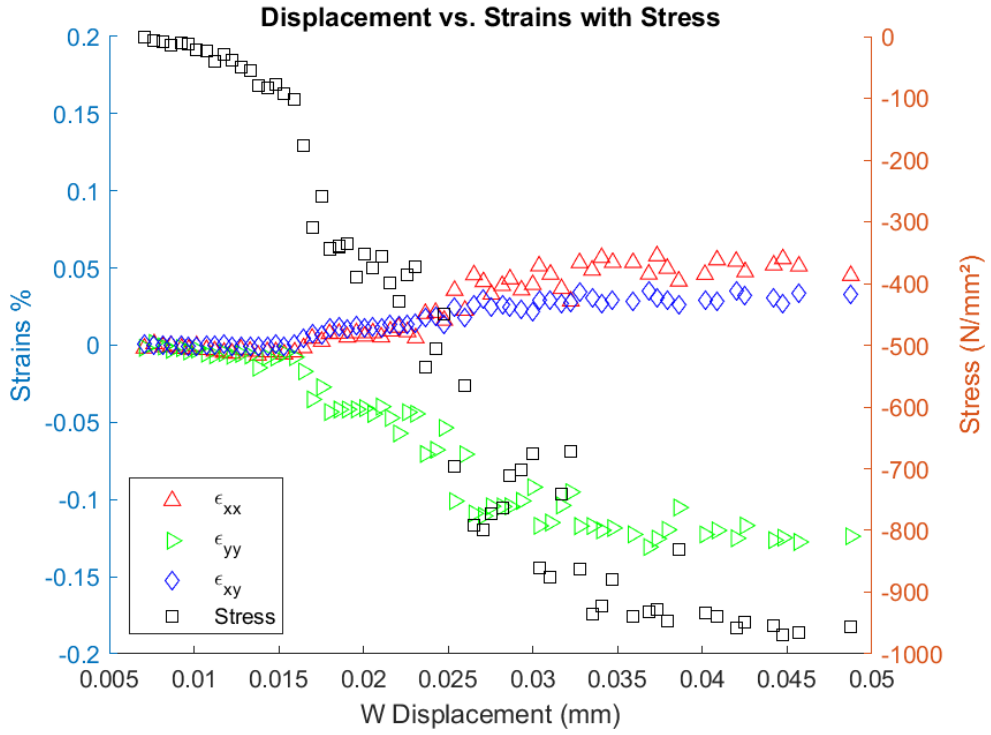

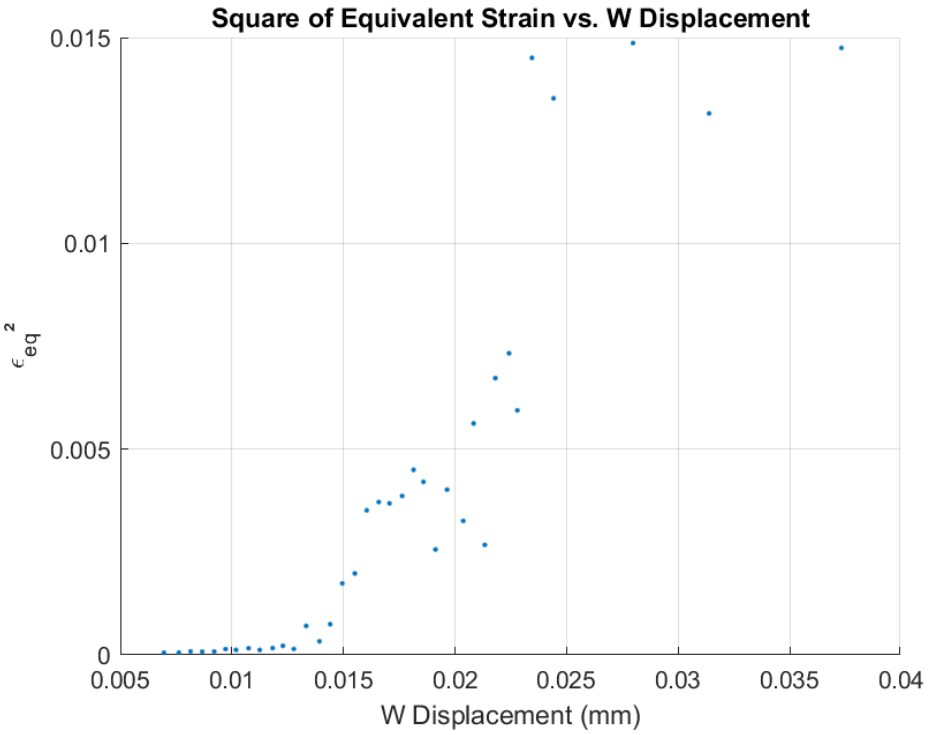

Impact Energy Level: 2.5 J

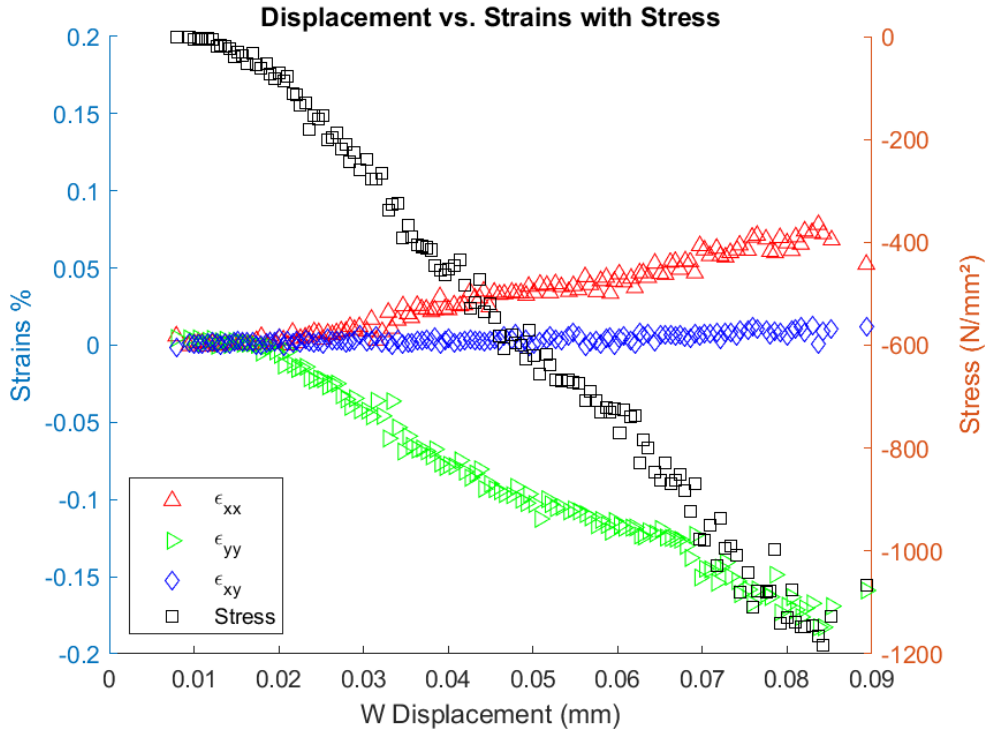

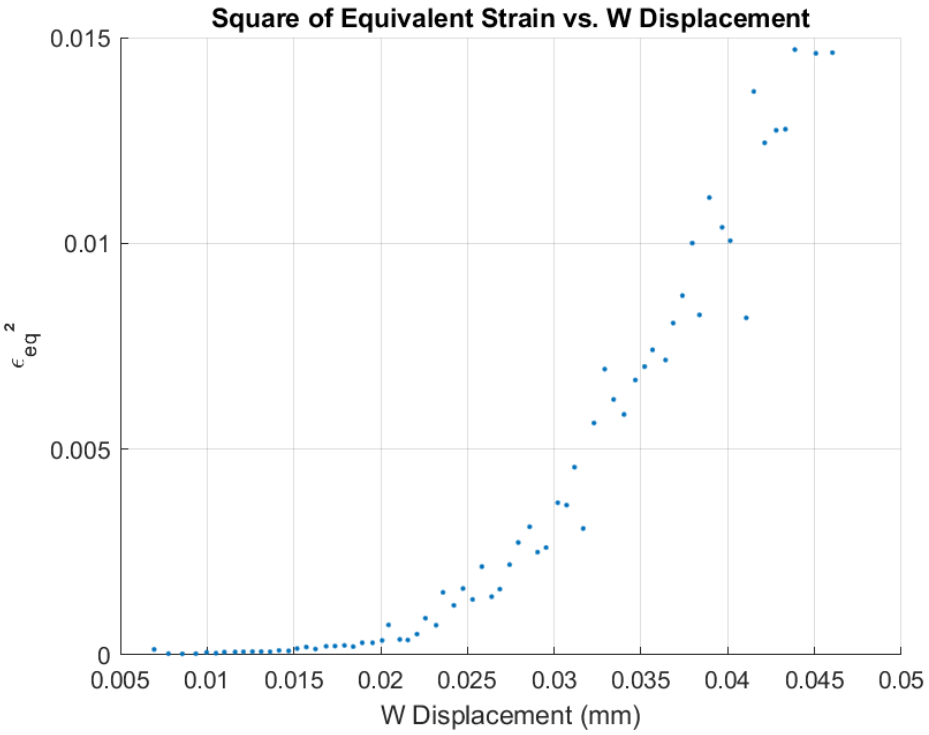

Impact Energy Level: 2.5 J

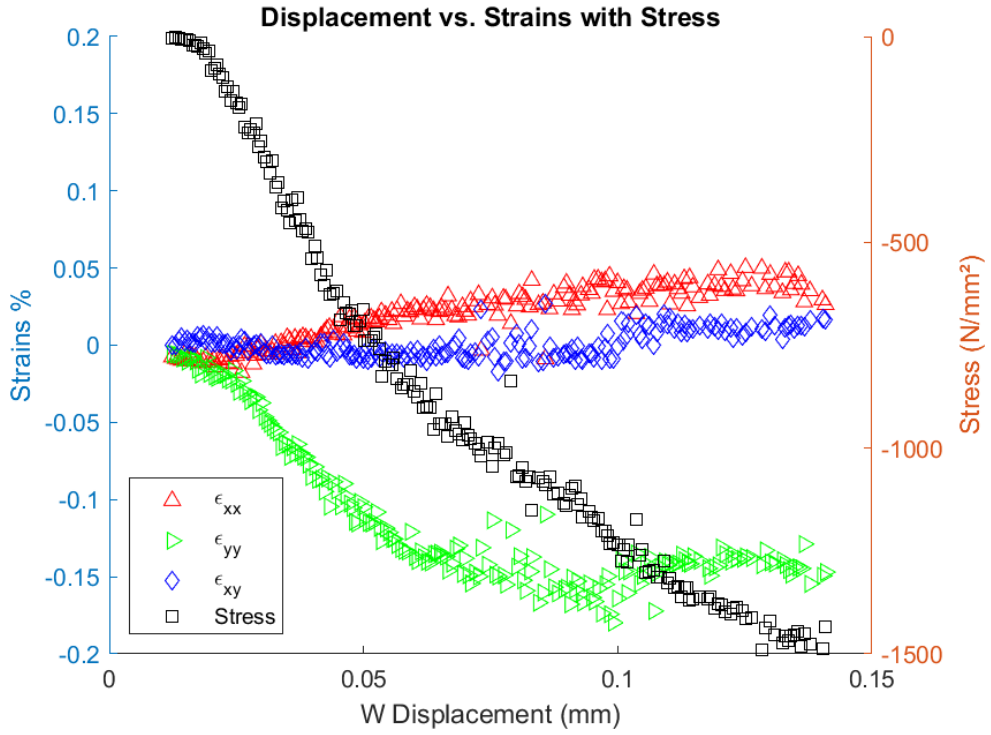

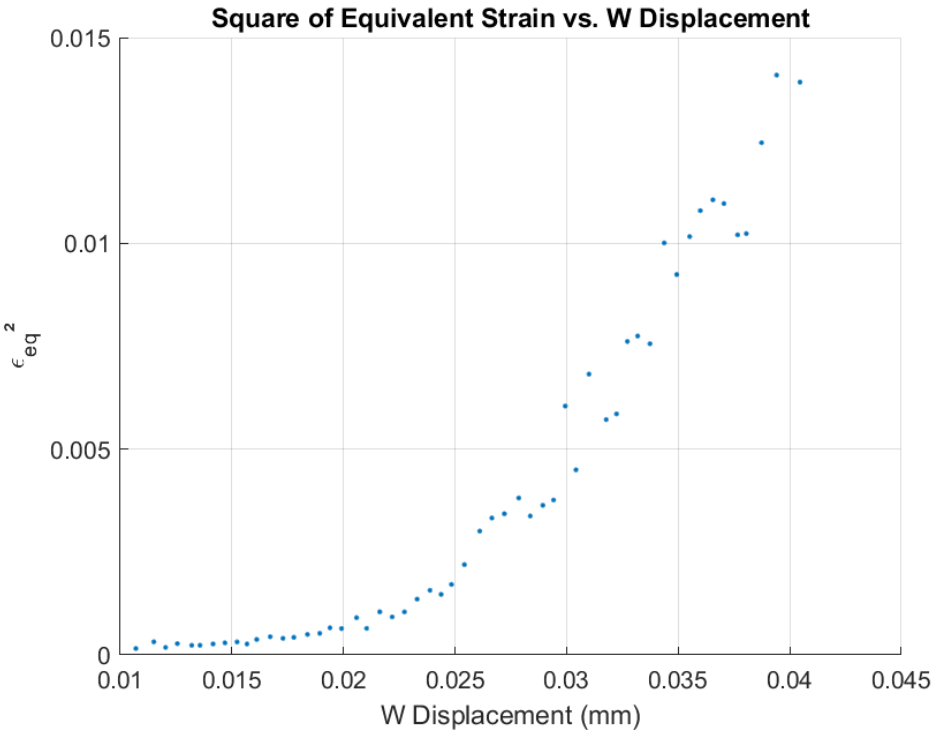

Impact Energy Level: 2.5 J

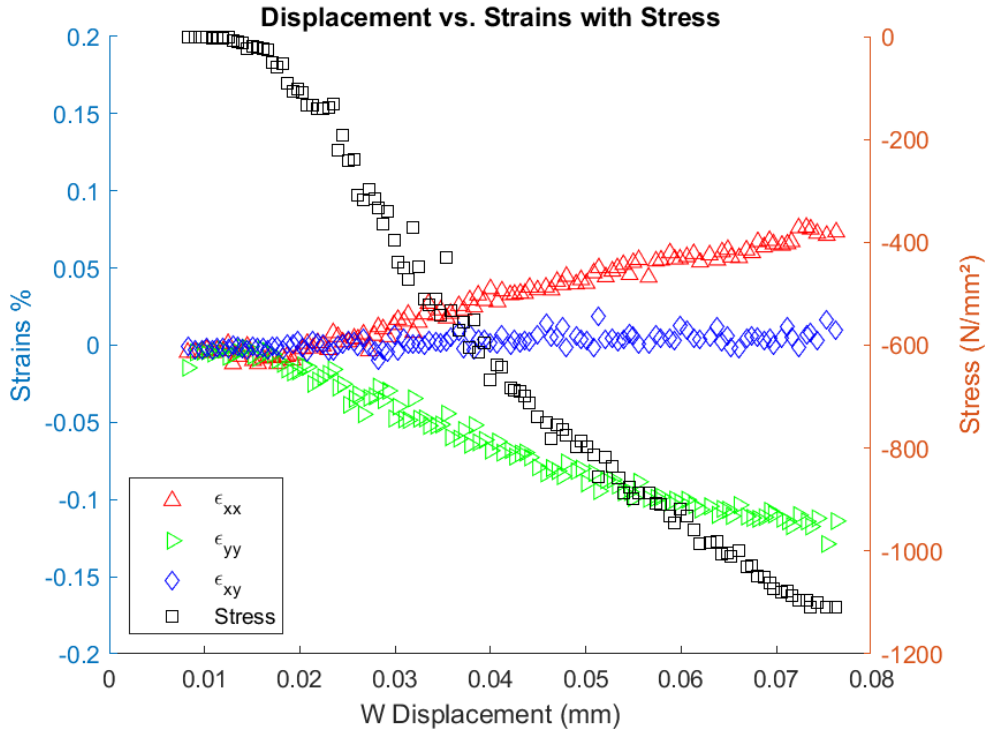

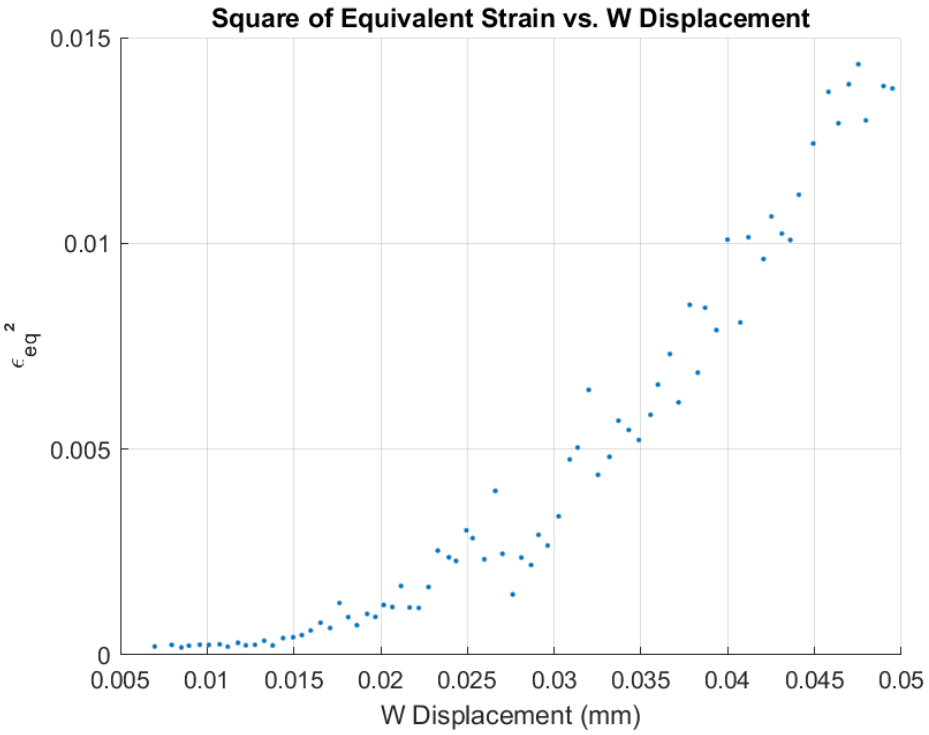

Impact Energy Level: 5 J

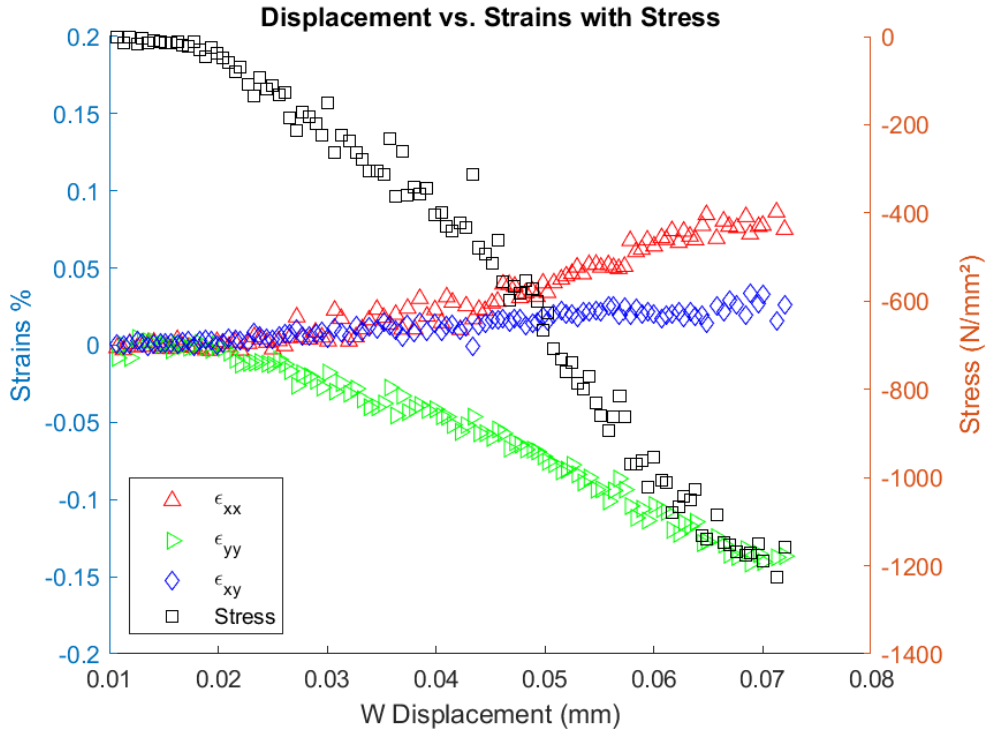

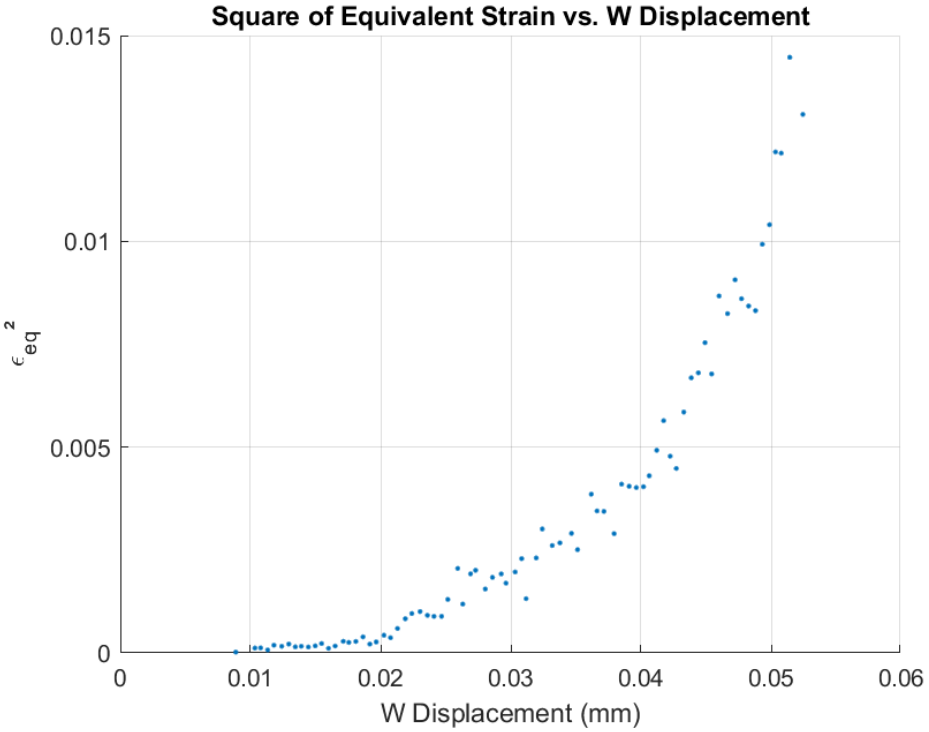

Impact Energy Level: 5 J

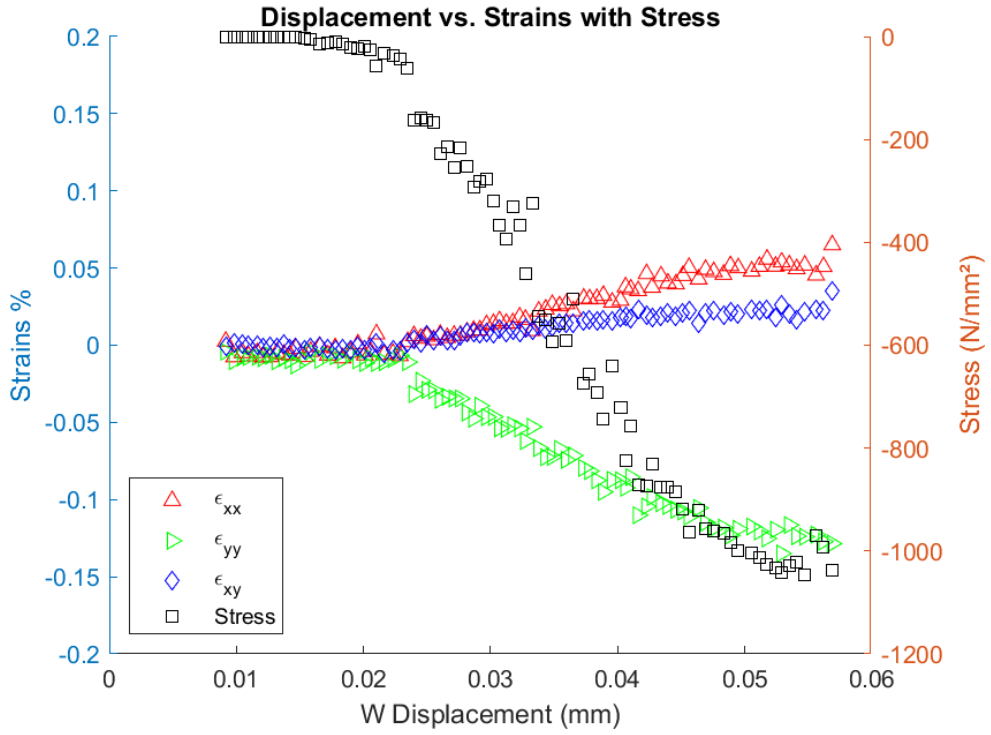

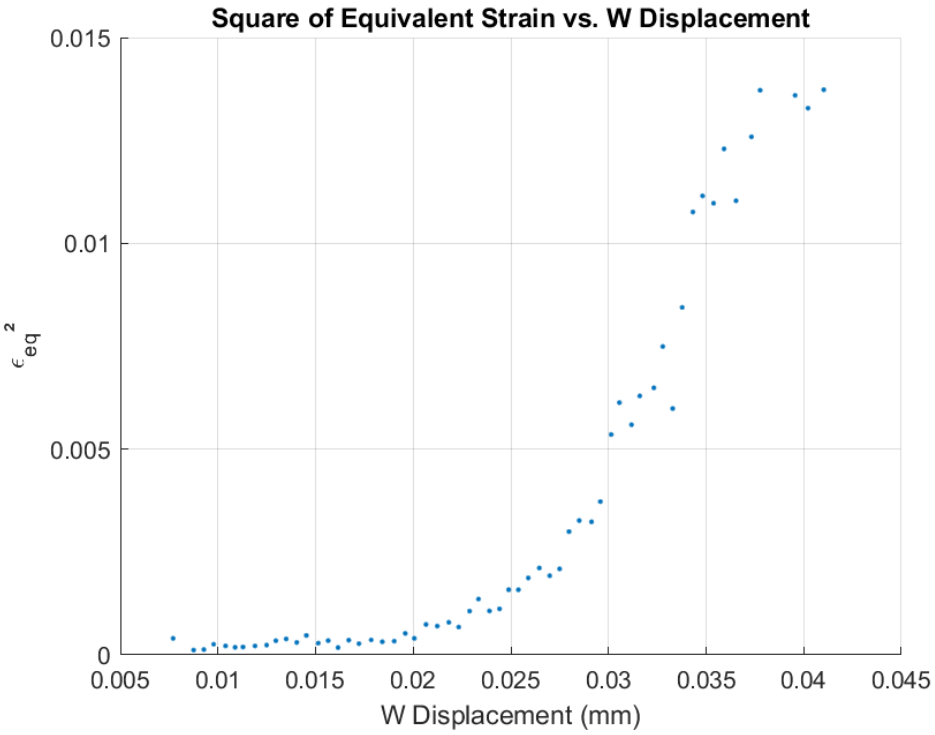

Impact Energy Level: 5 J

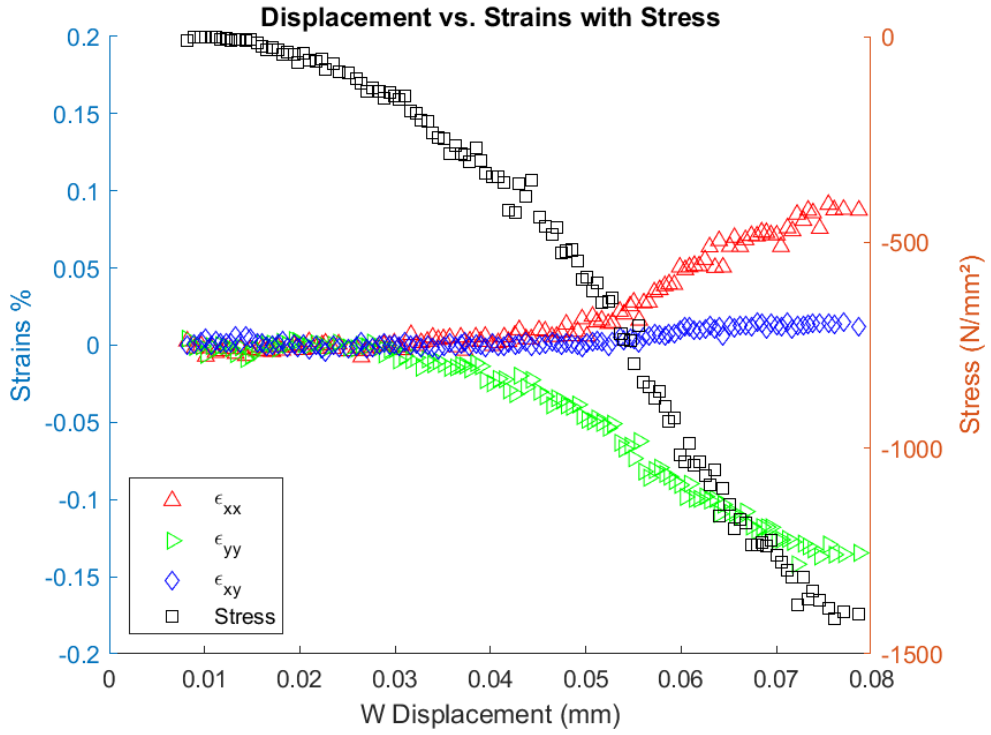

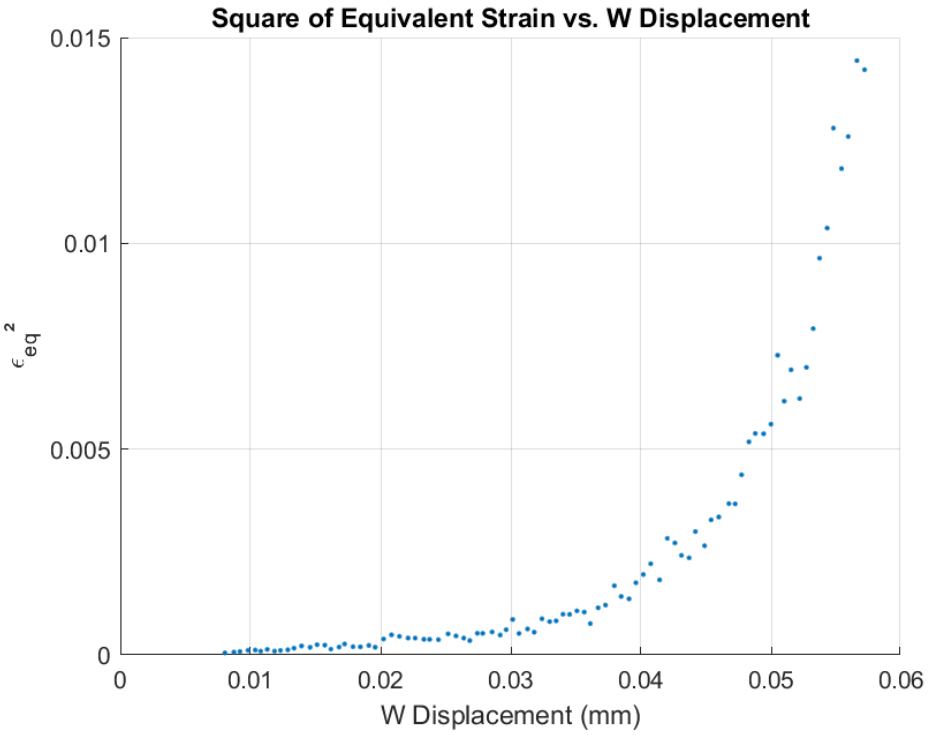

Impact Energy Level: 5 J

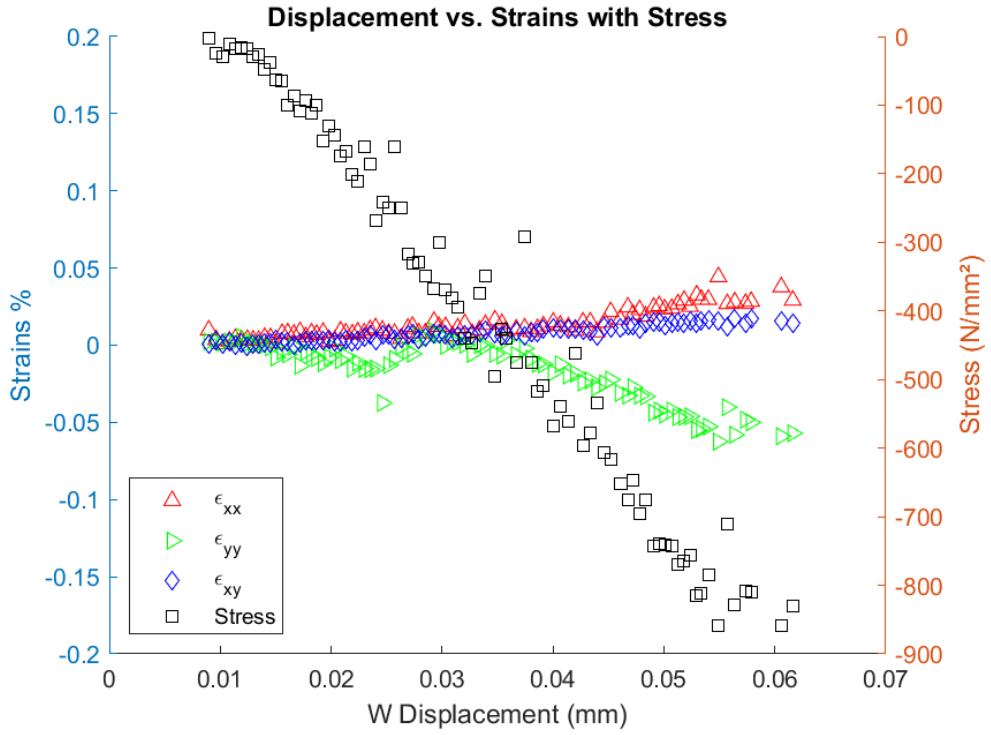

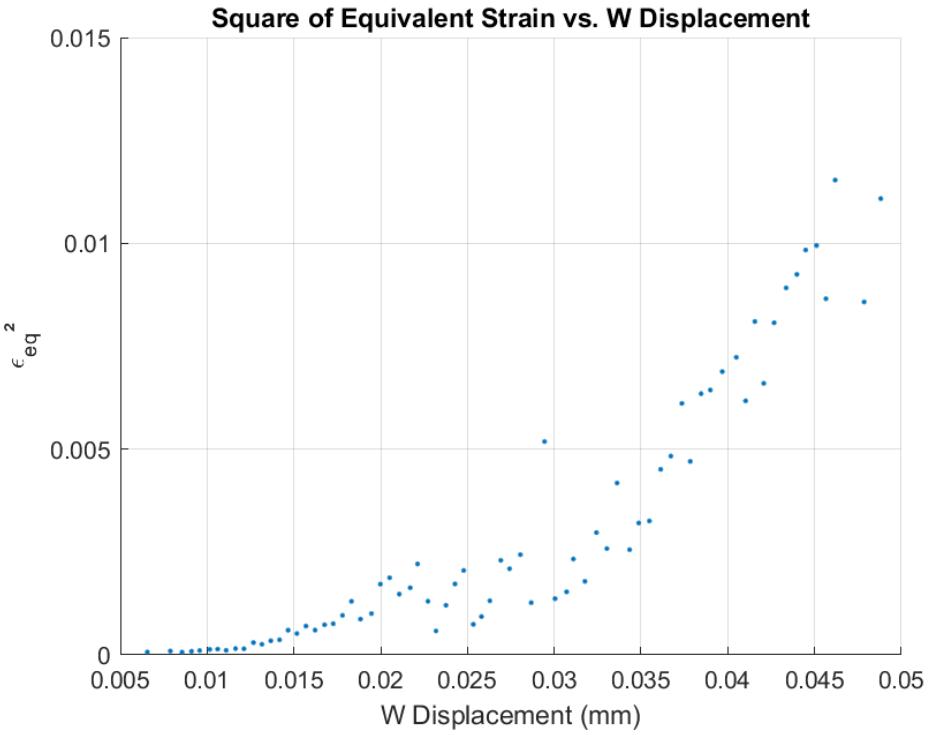

Impact Energy Level: 5 J

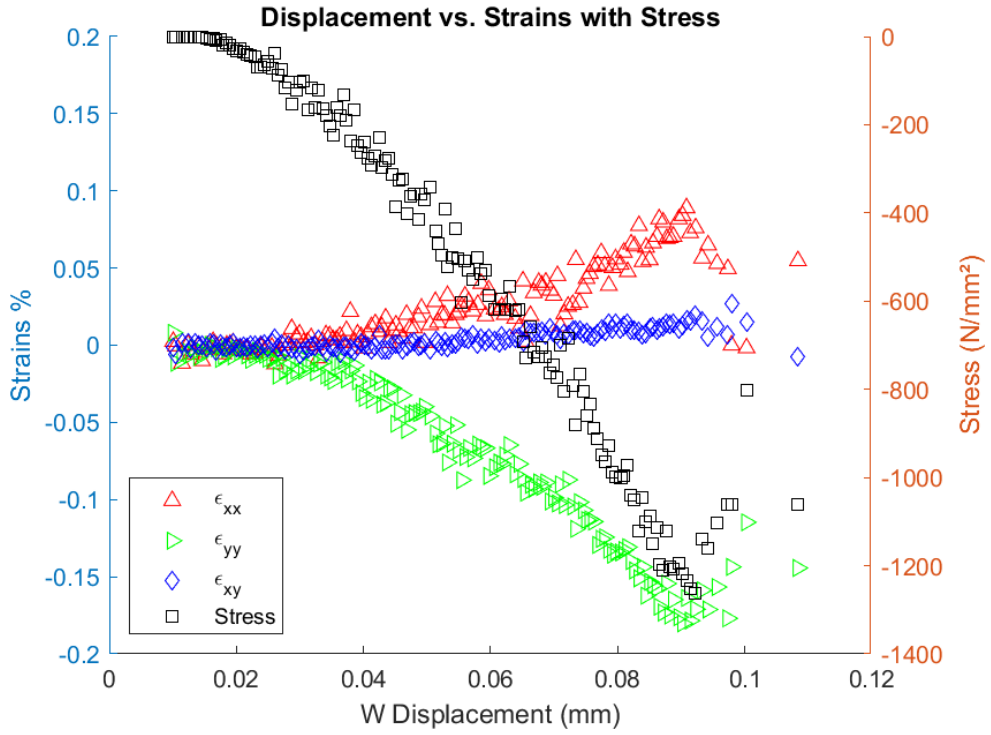

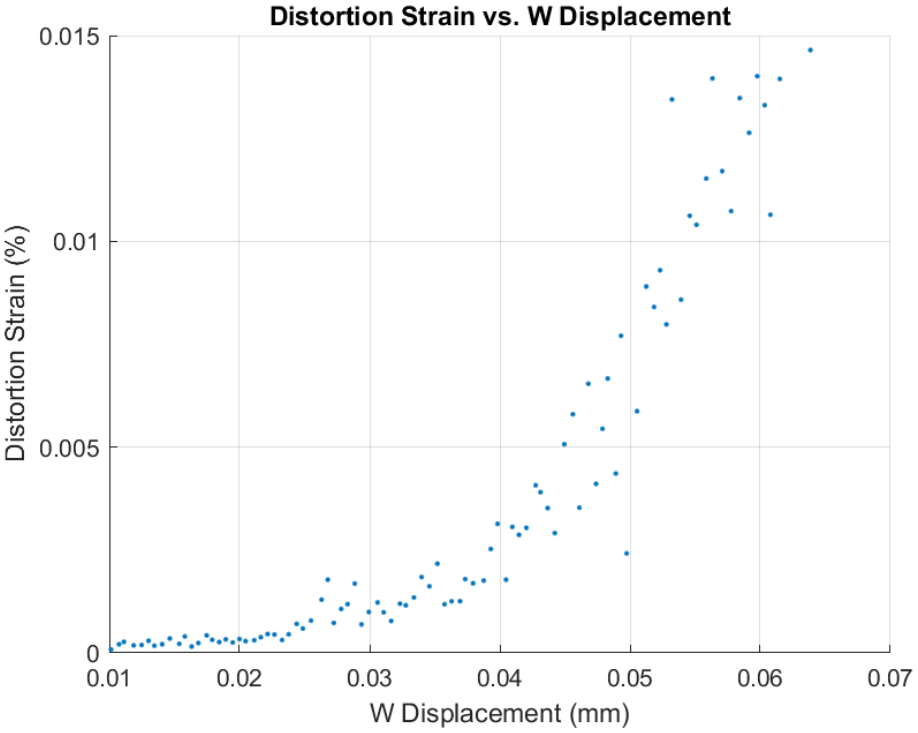

Impact Energy Level: 7.5 J

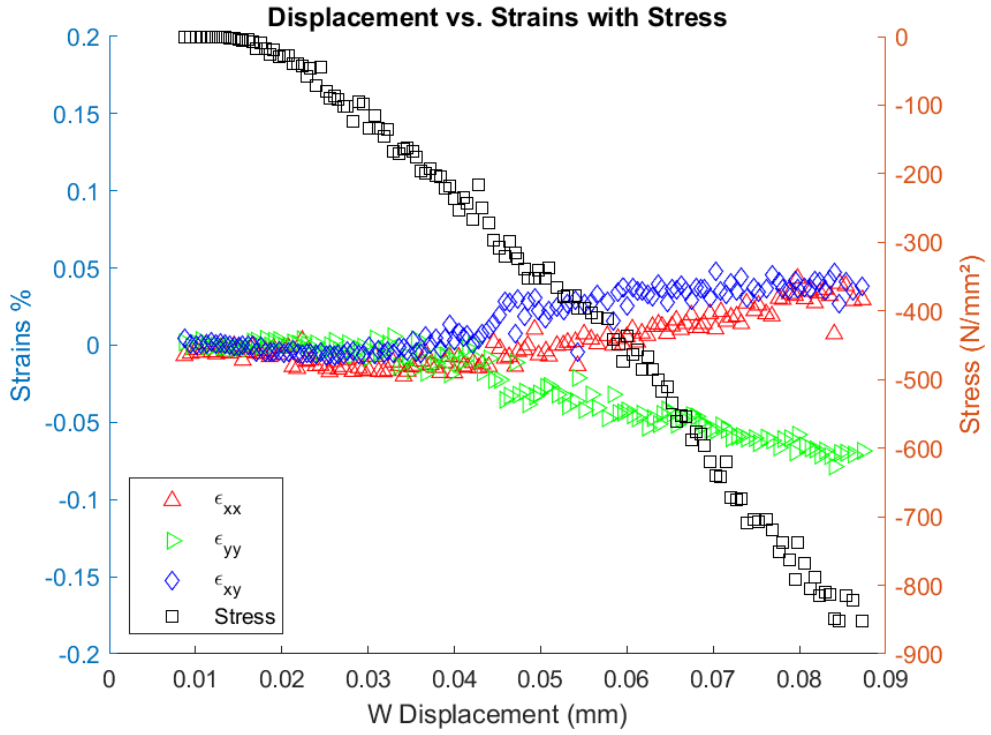

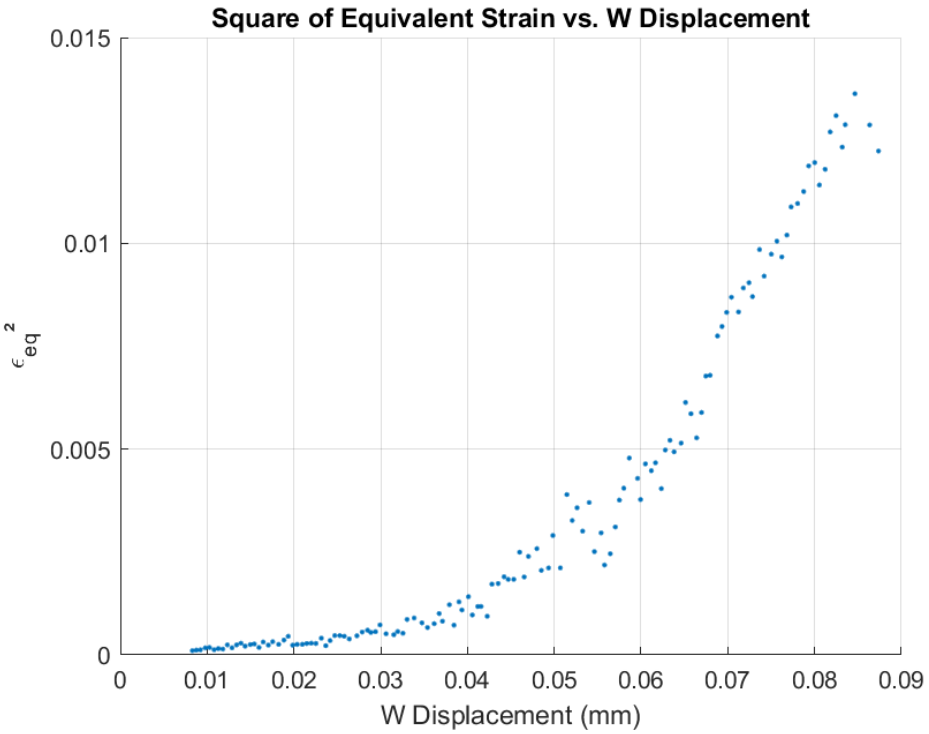

Impact Energy Level: 7.5 J

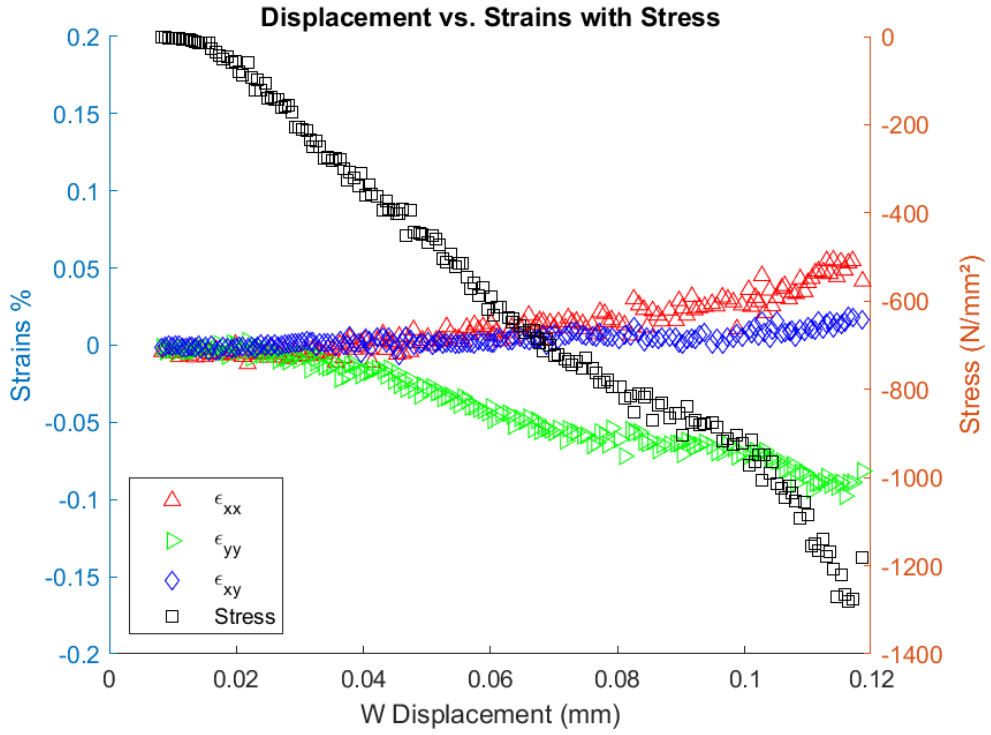

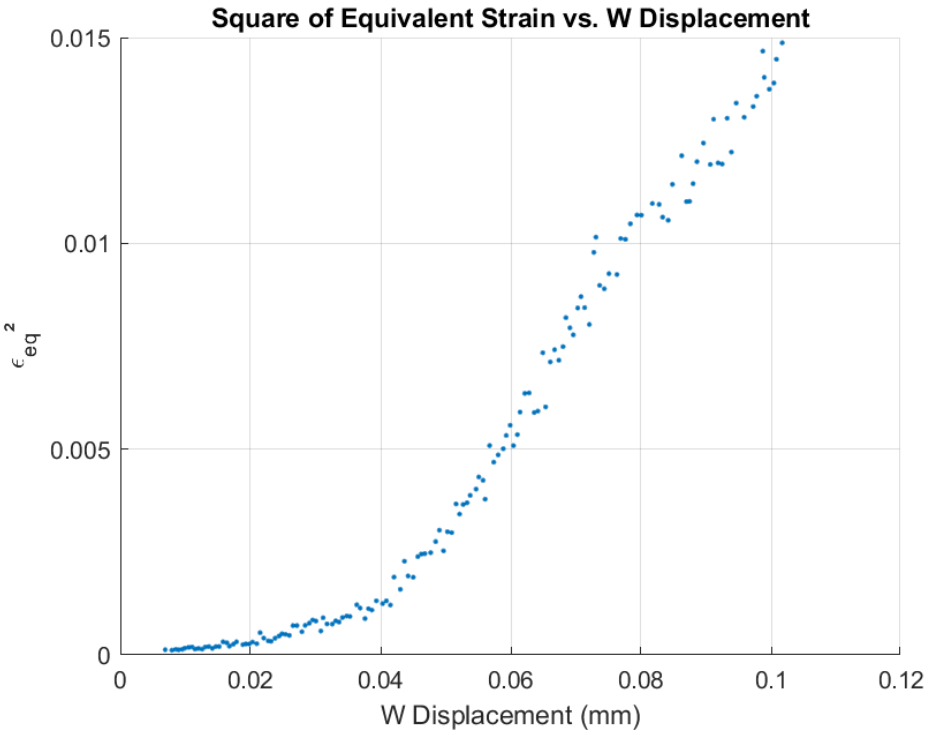

Impact Energy Level: 7.5 J

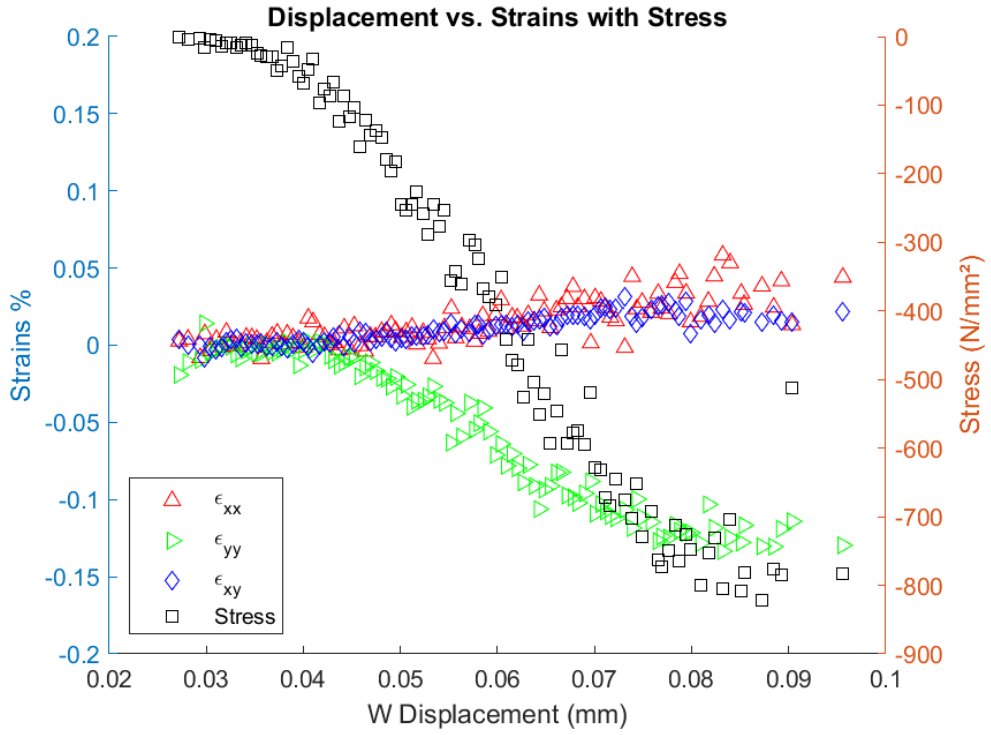

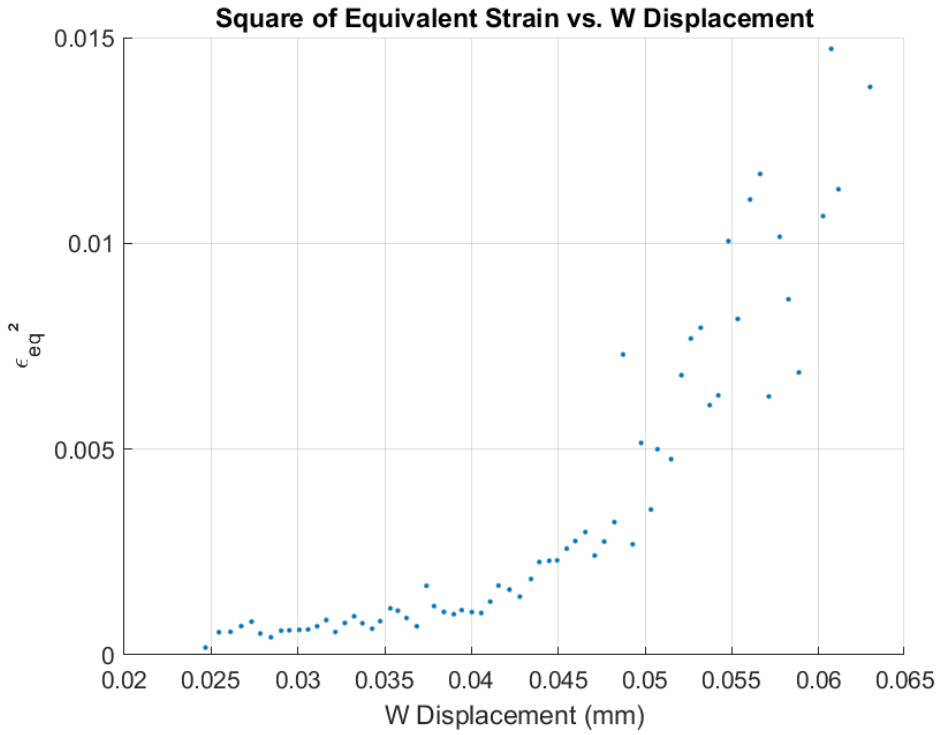

Impact Energy Level: 7.5 J

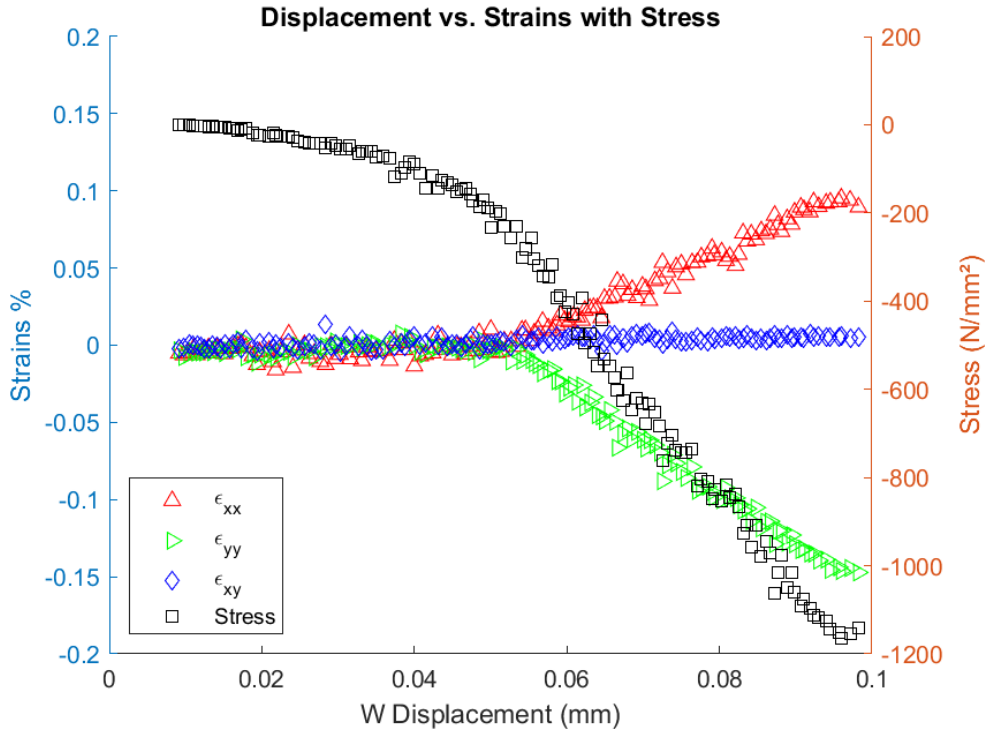

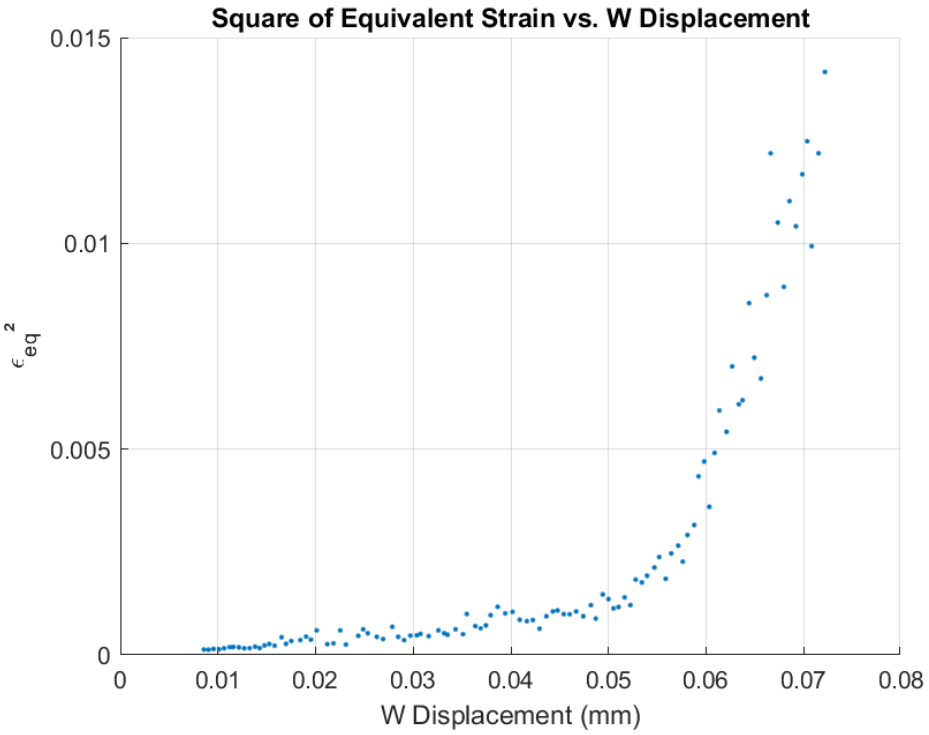

Impact Energy Level: 7.5 J

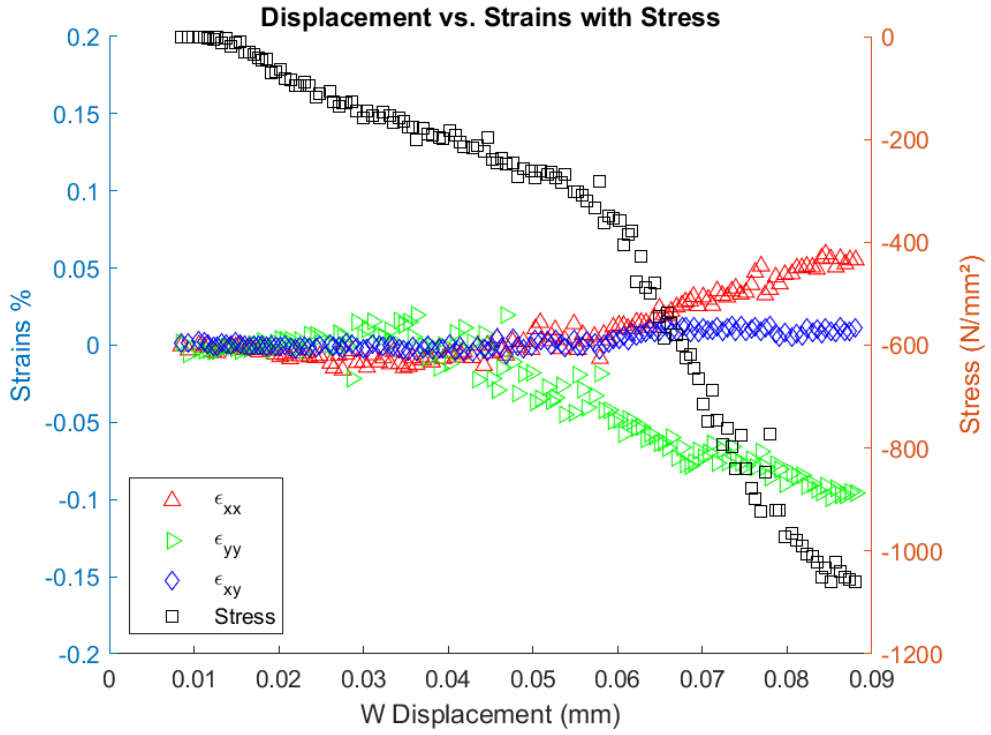

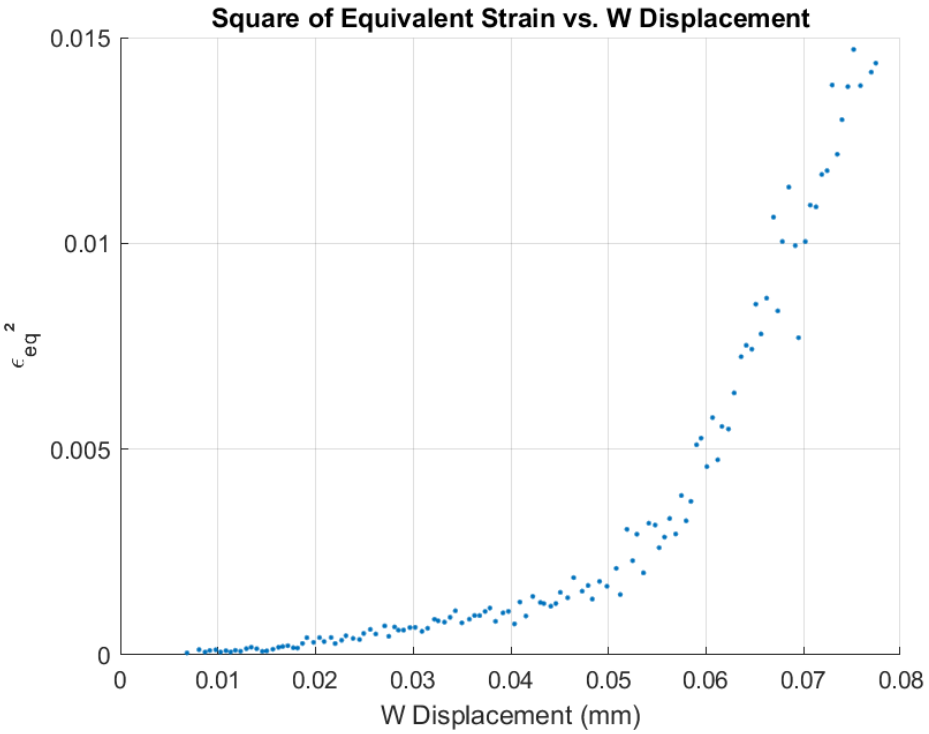

Impact Energy Level: 10 J

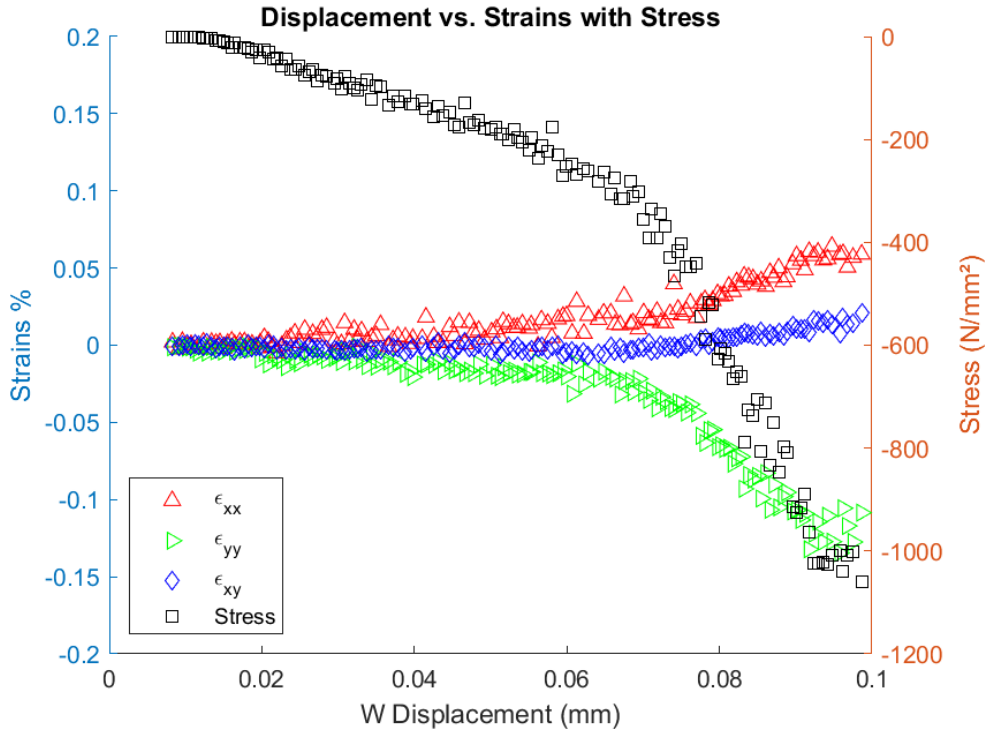

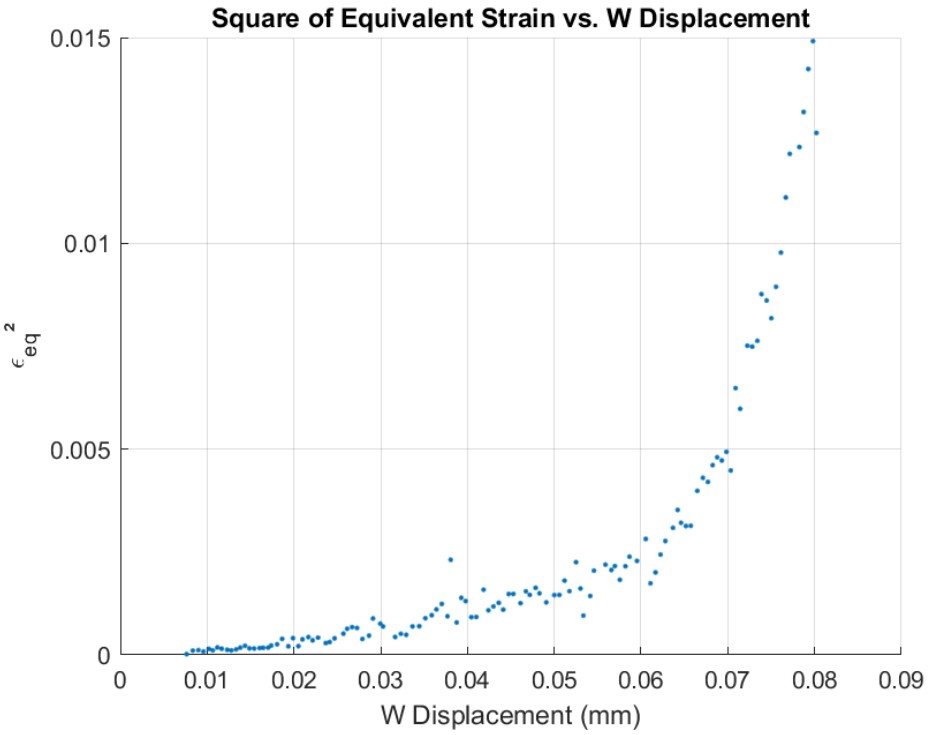

Impact Energy Level: 10 J

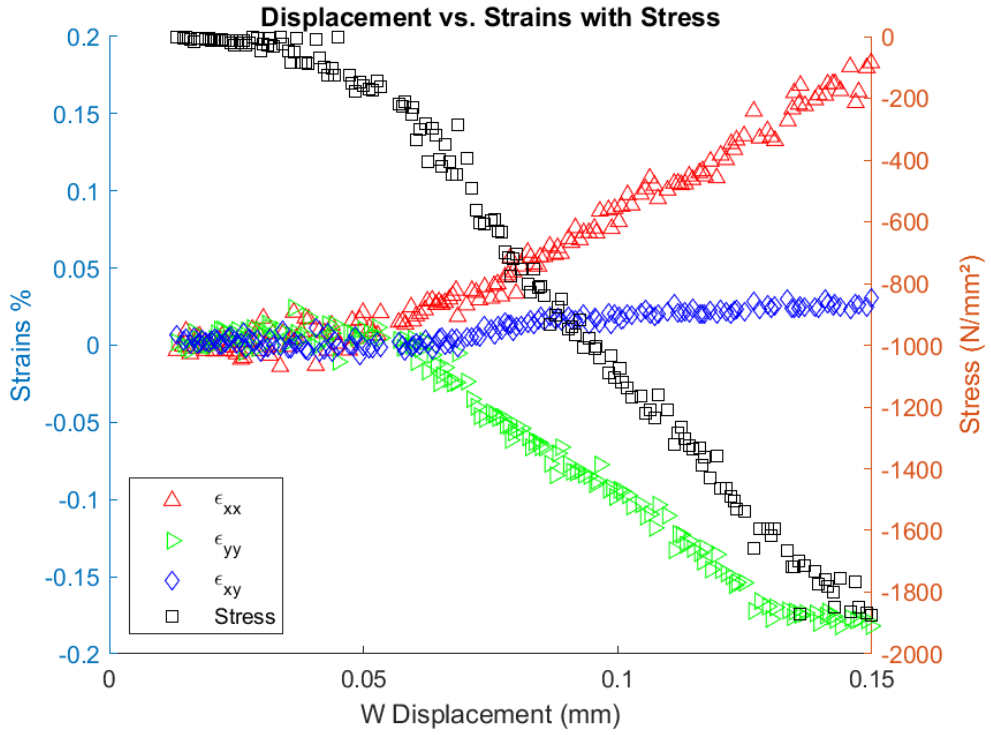

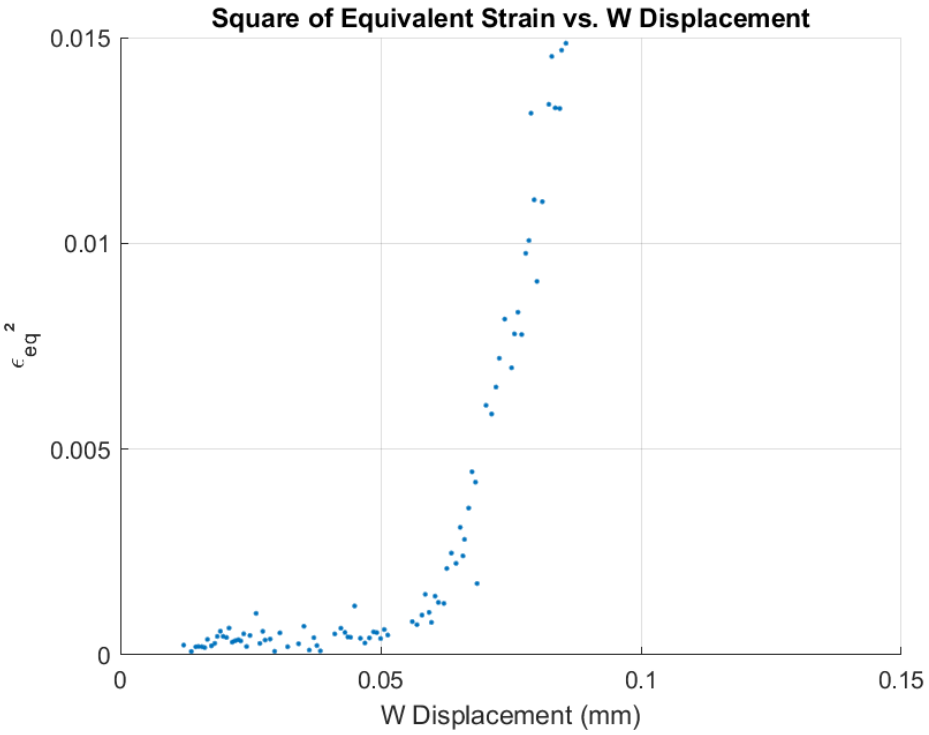

Impact Energy Level: 10 J

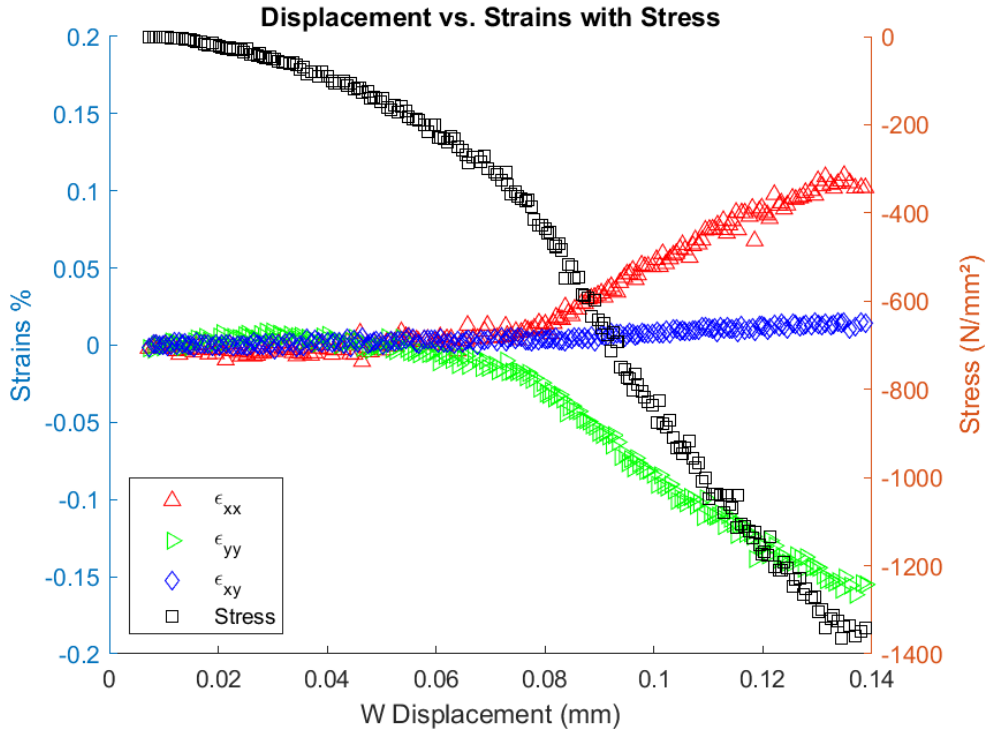

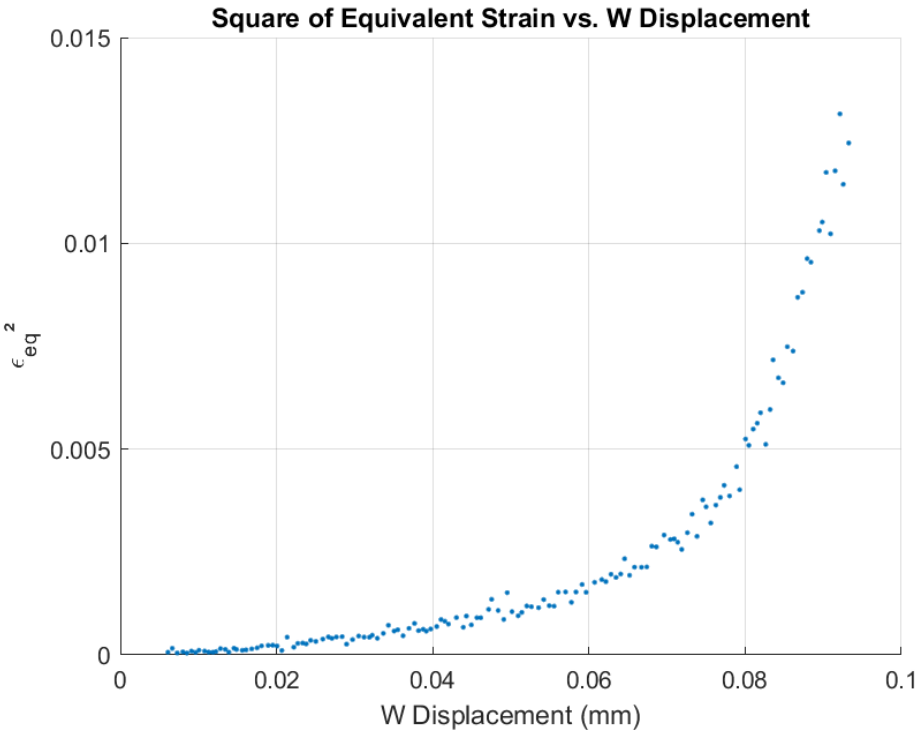

Impact Energy Level: 10 J

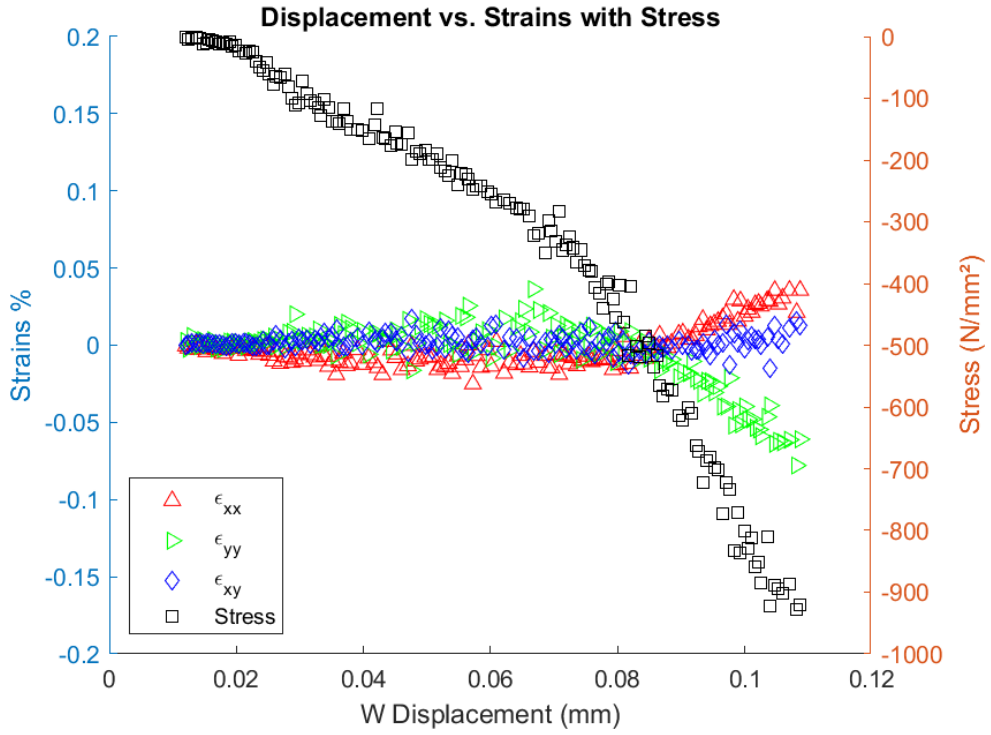

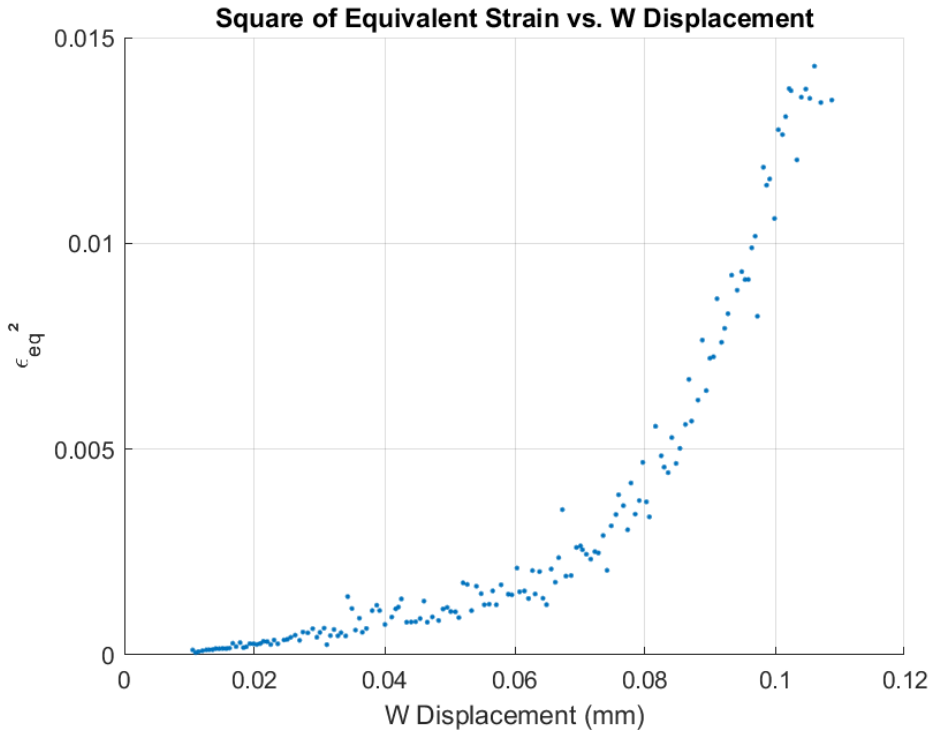

Impact Energy Level: 10 J

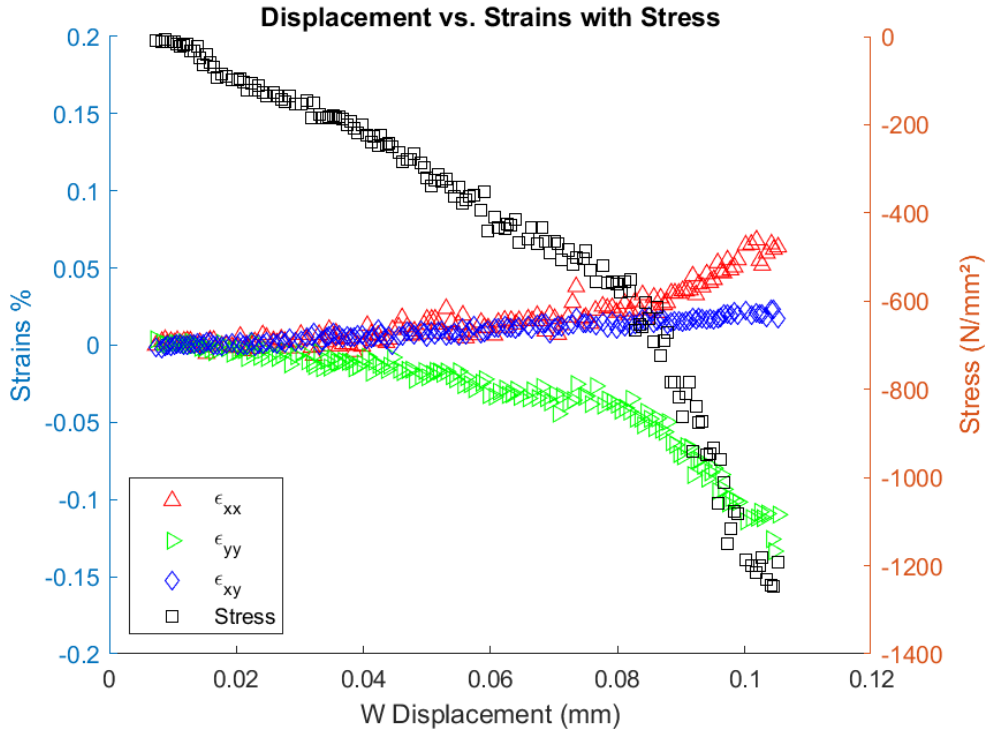

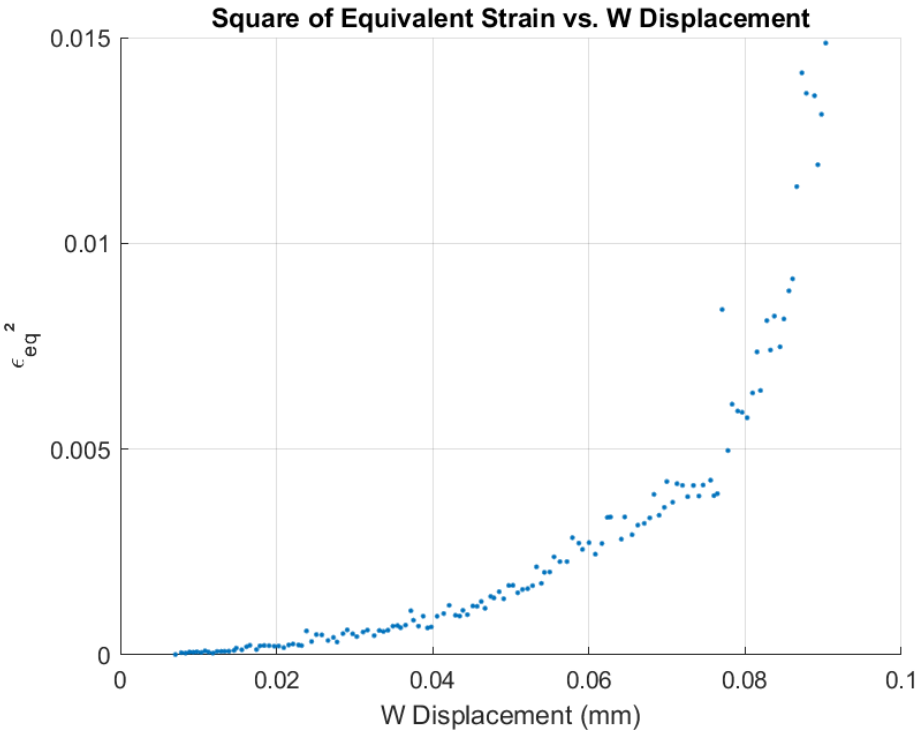

Impact Energy Level: 12.5 J

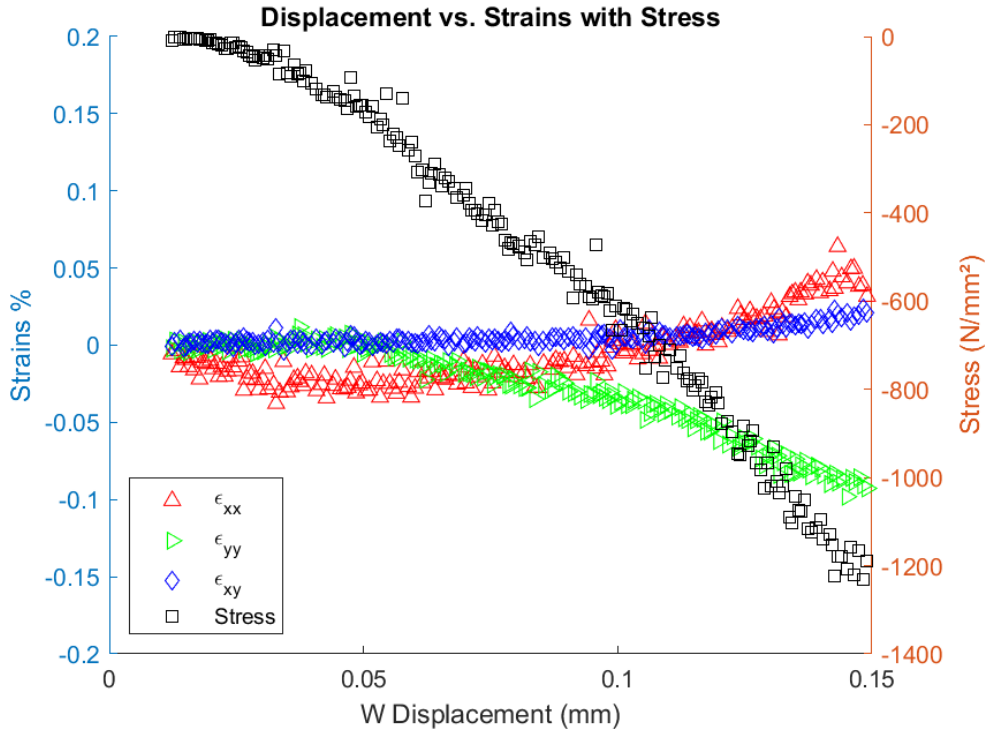

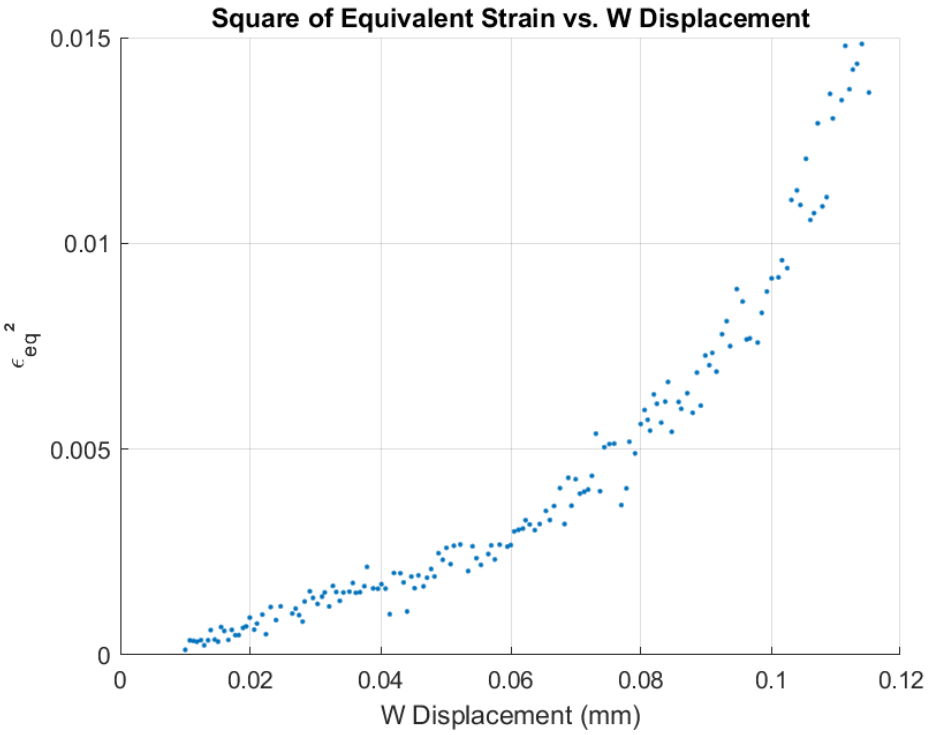

Impact Energy Level: 12.5 J

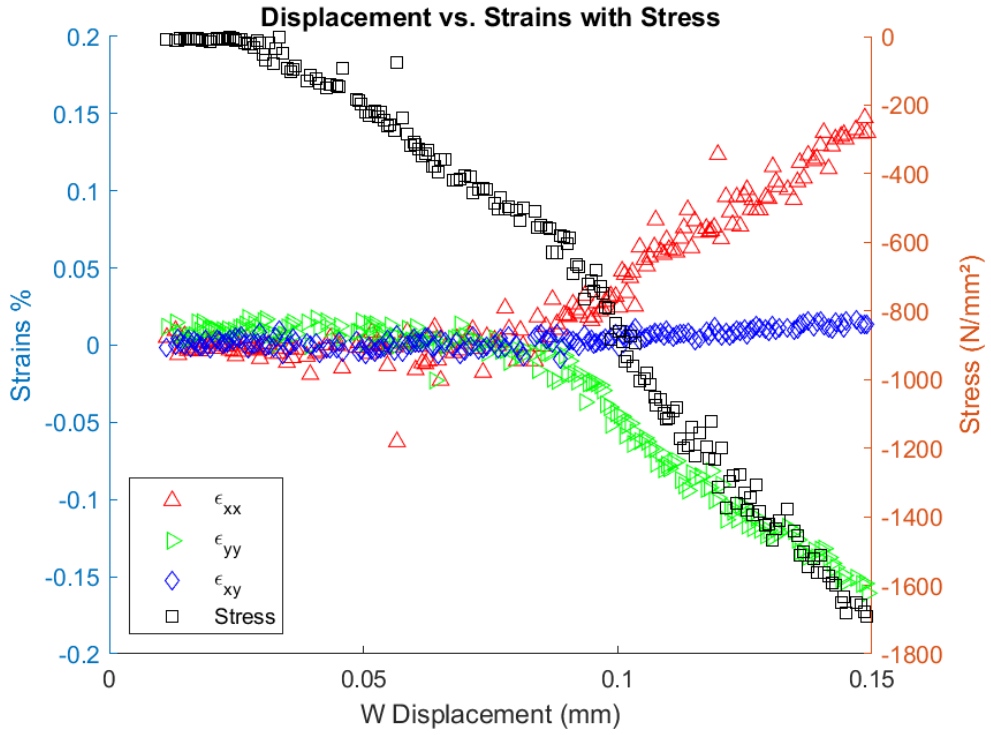

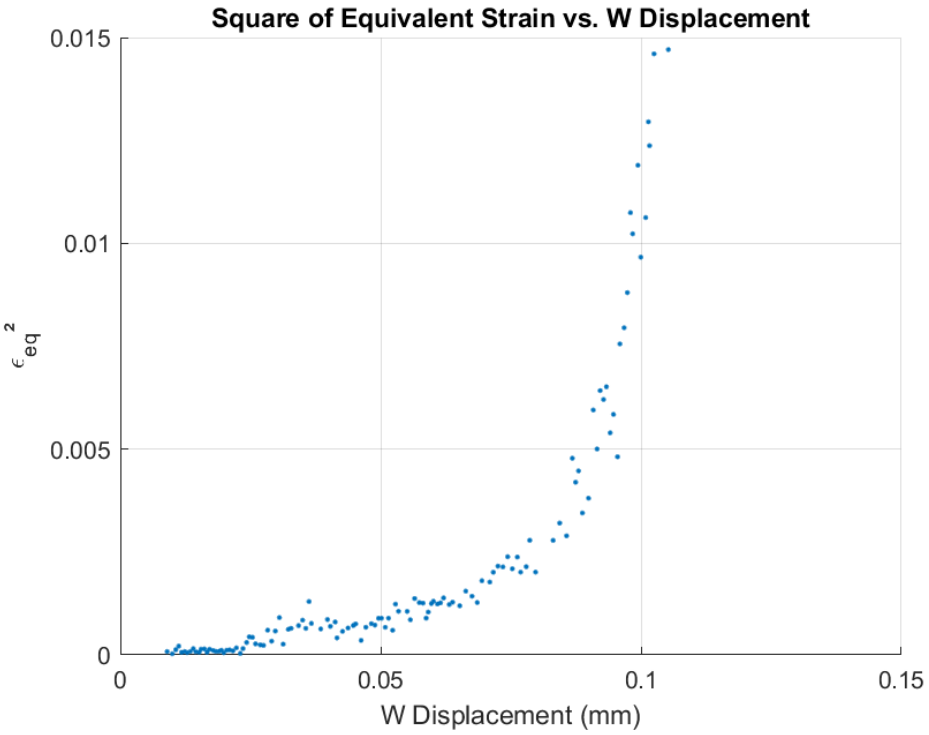

Impact Energy Level: 12.5 J

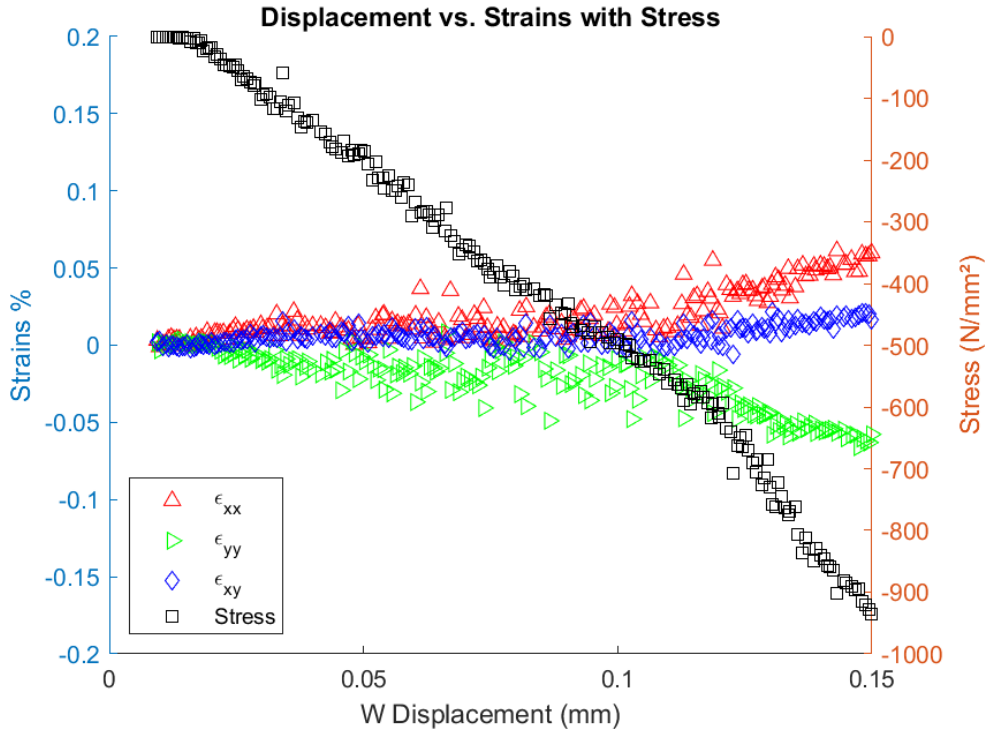

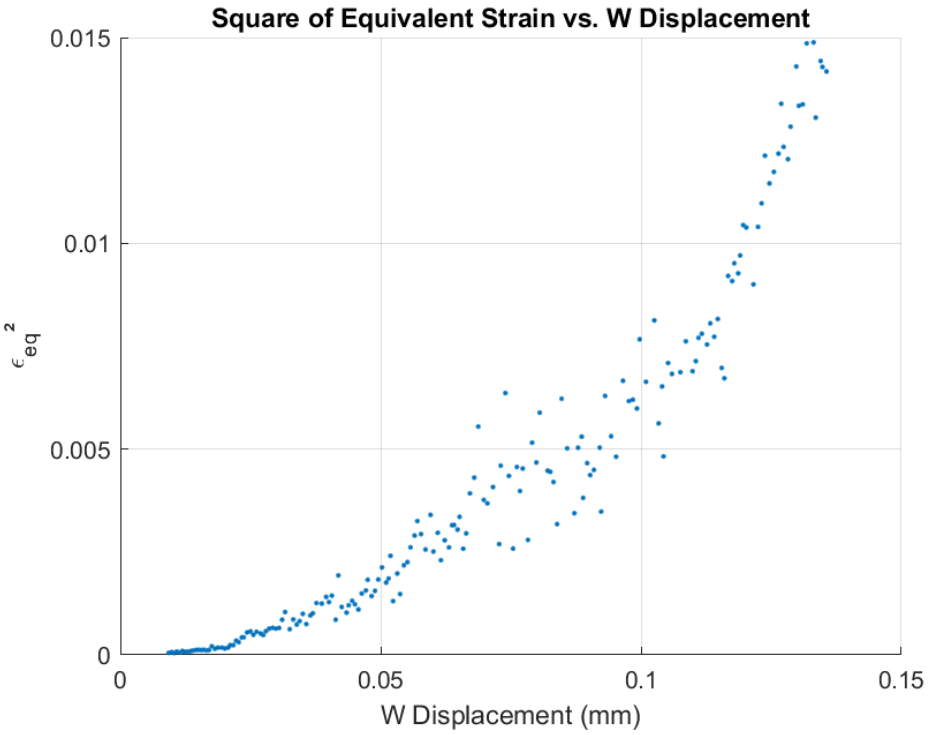

18 APPENDIX – I

Samples with the corresponding determinant plot for critical displacement "S" $[45/0/-45/90]_{3s}$

Impact Energy Level: 2.5 J

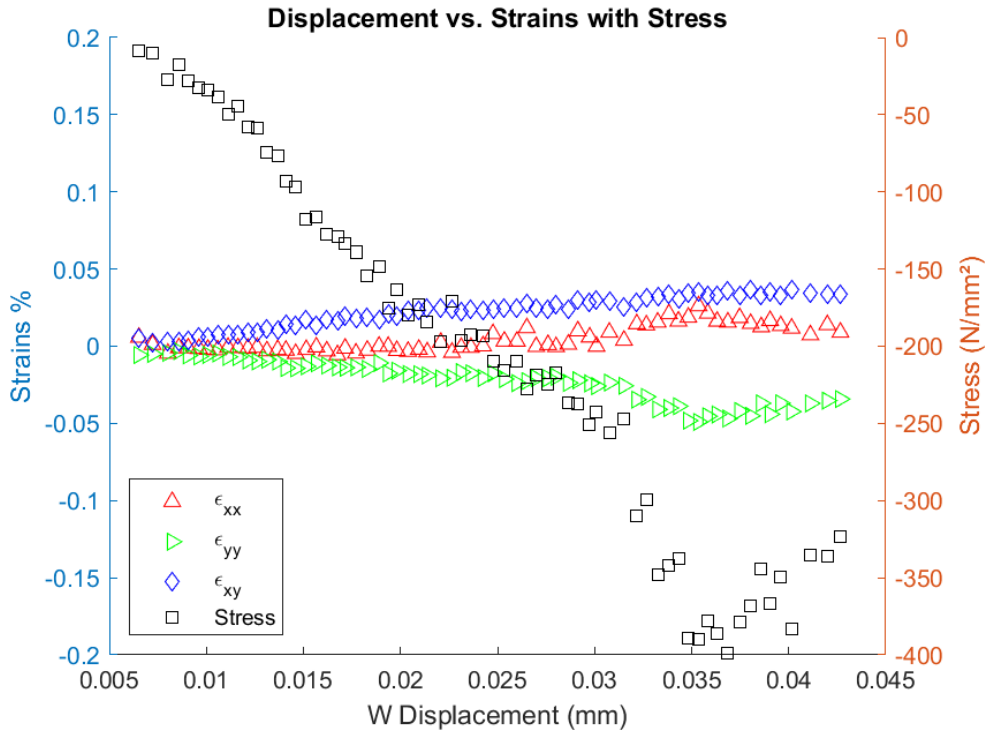

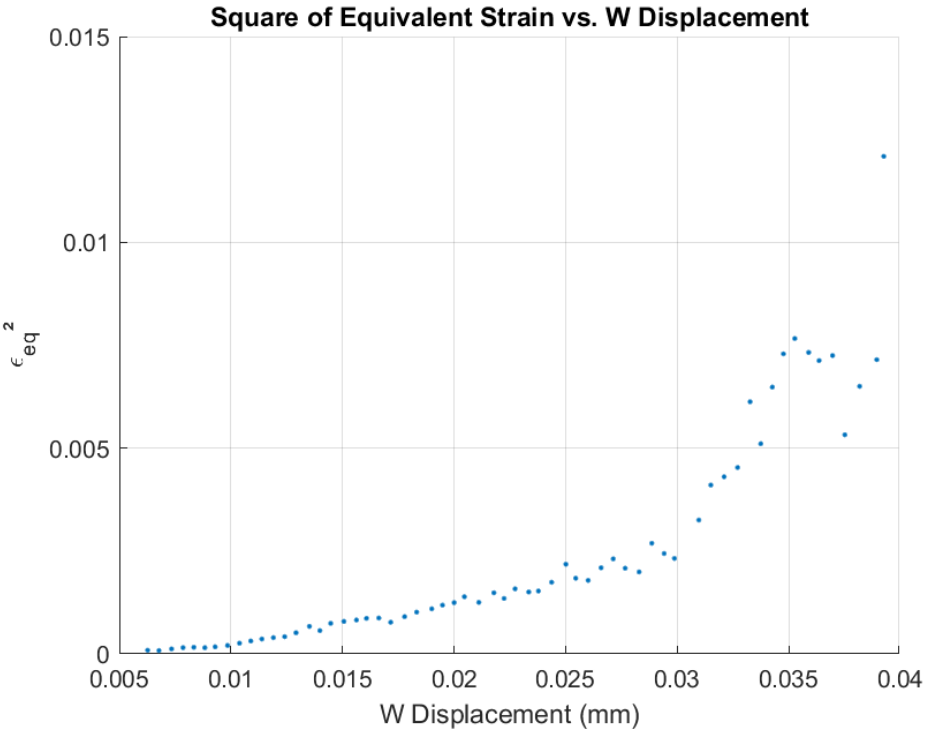

Impact Energy Level: 2.5 J

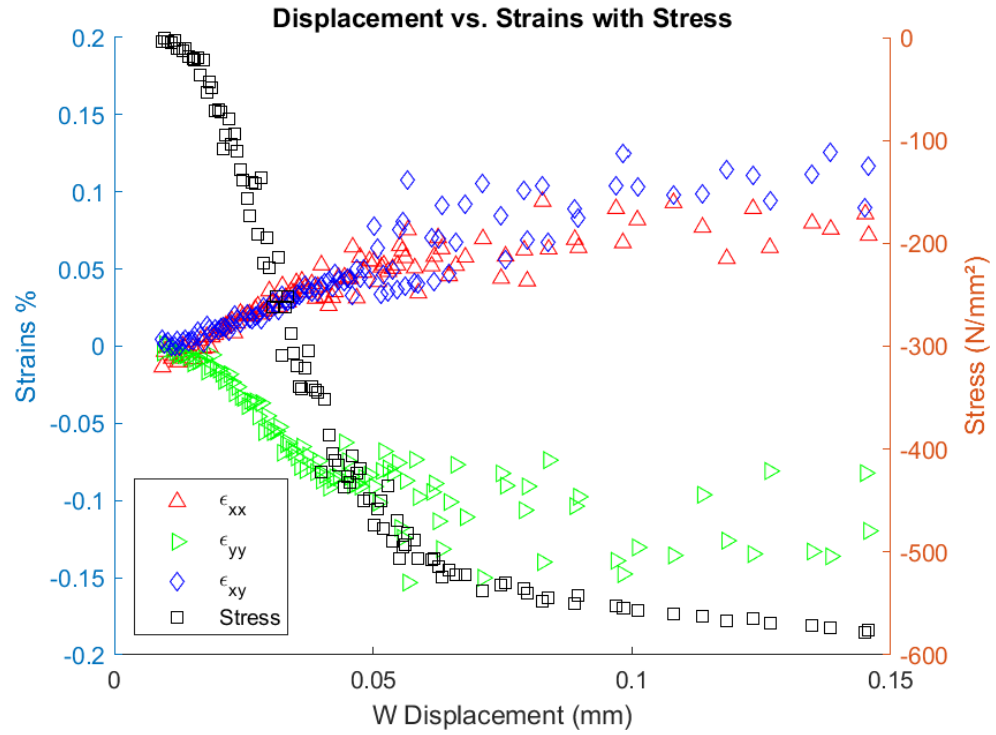

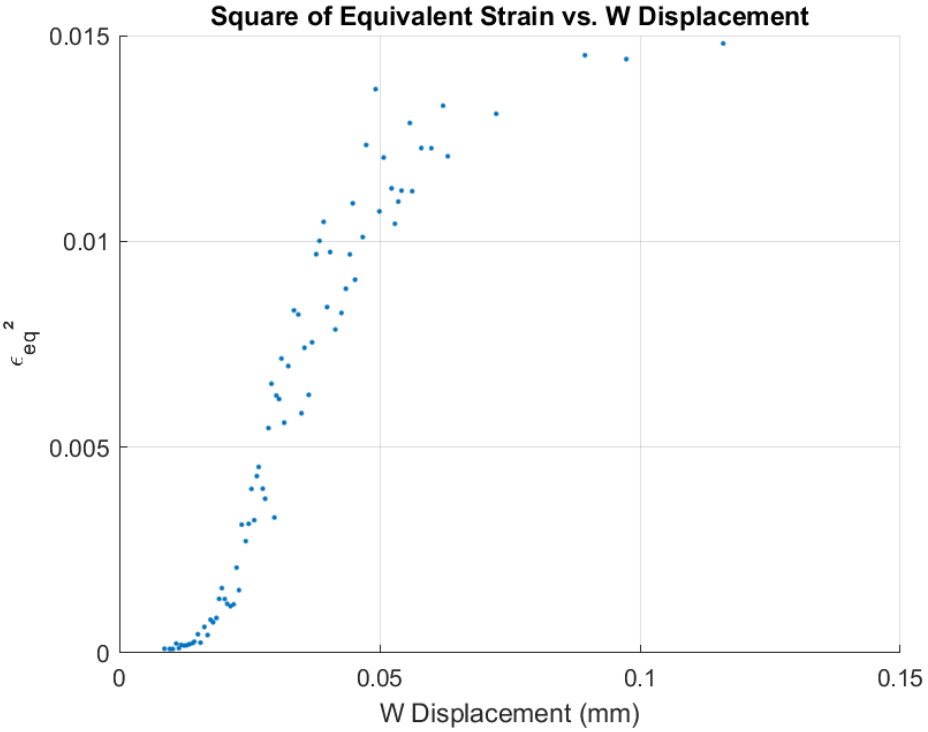

Impact Energy Level: 2.5 J

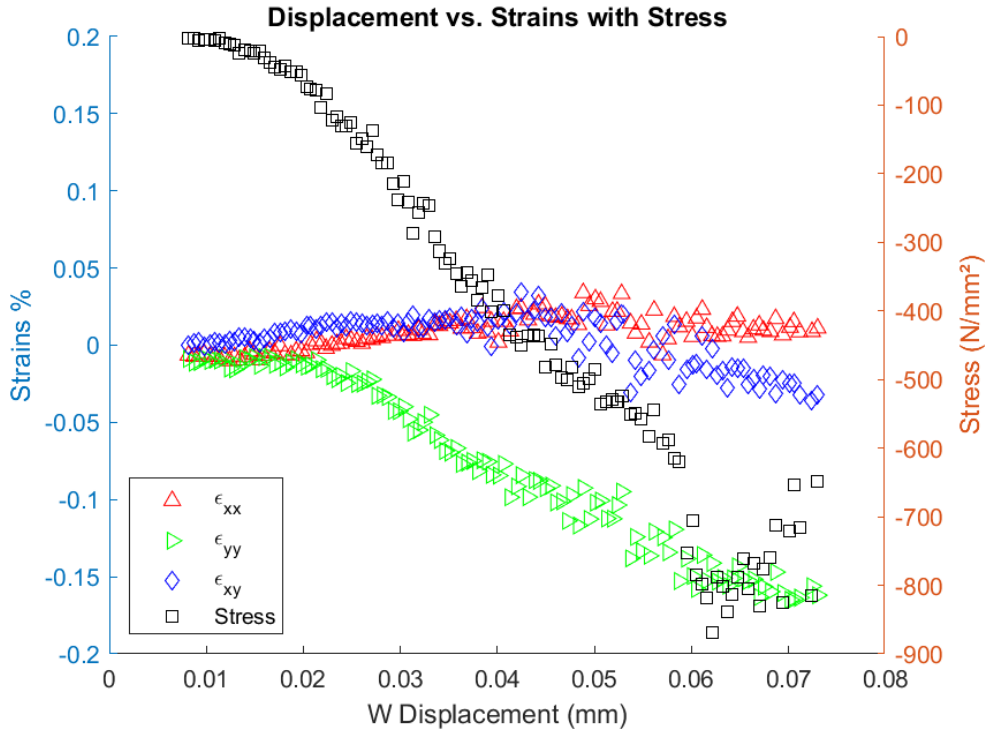

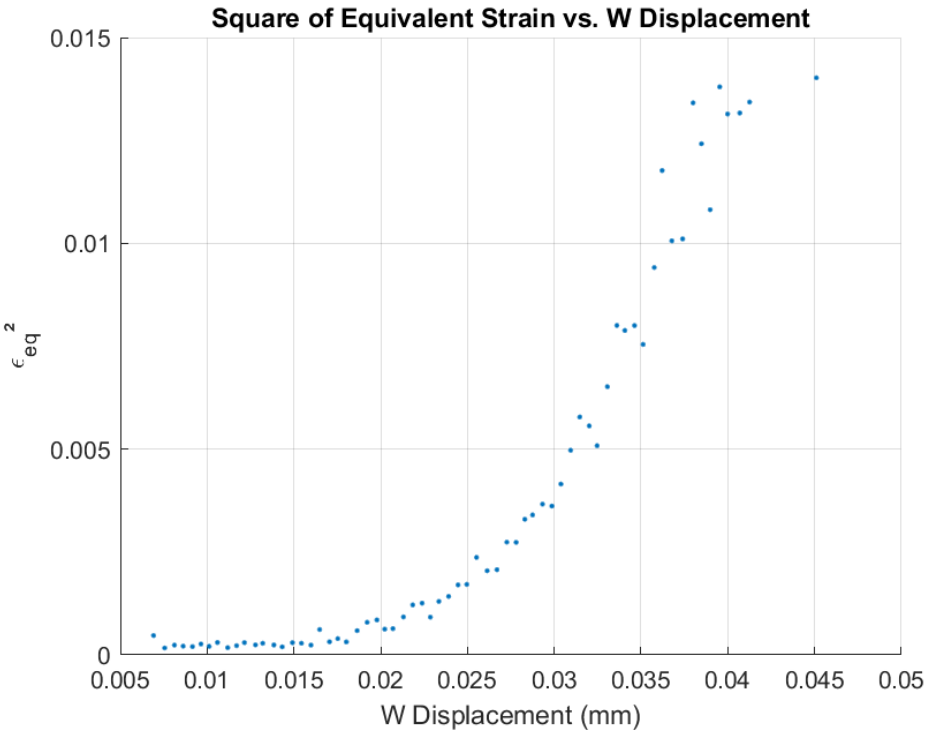

Impact Energy Level: 5 J

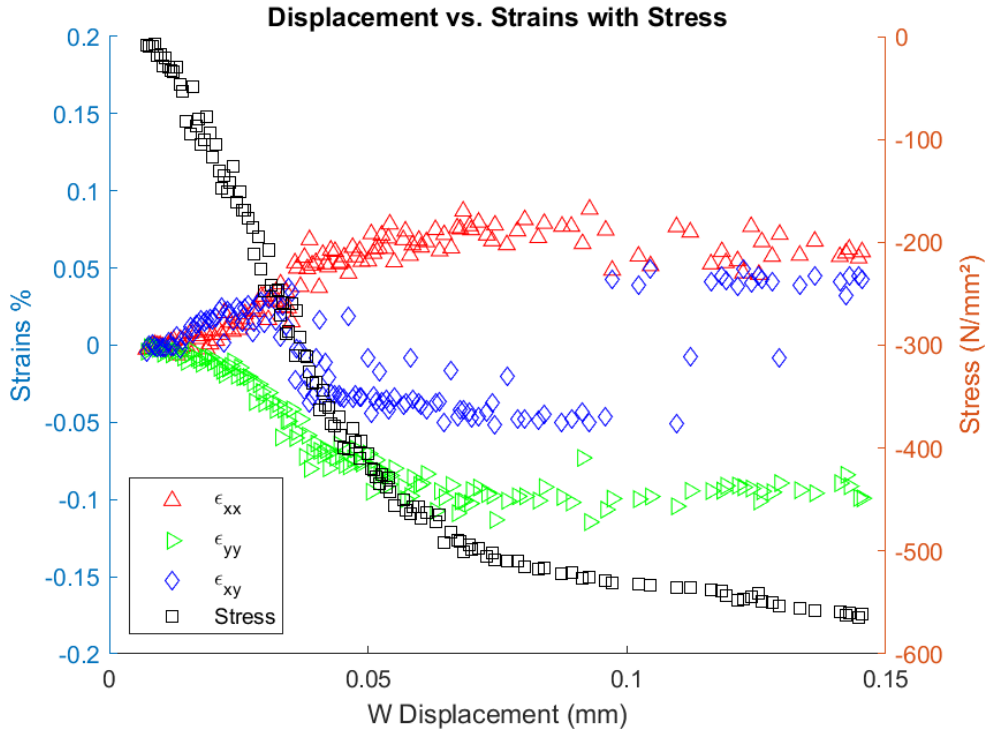

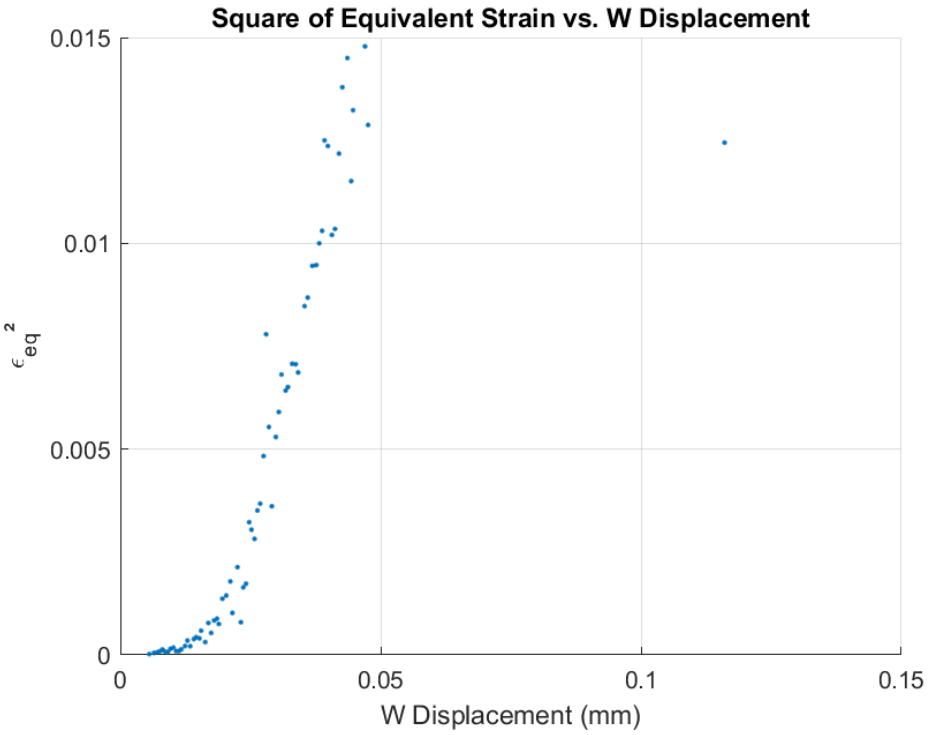

Impact Energy Level: 5 J

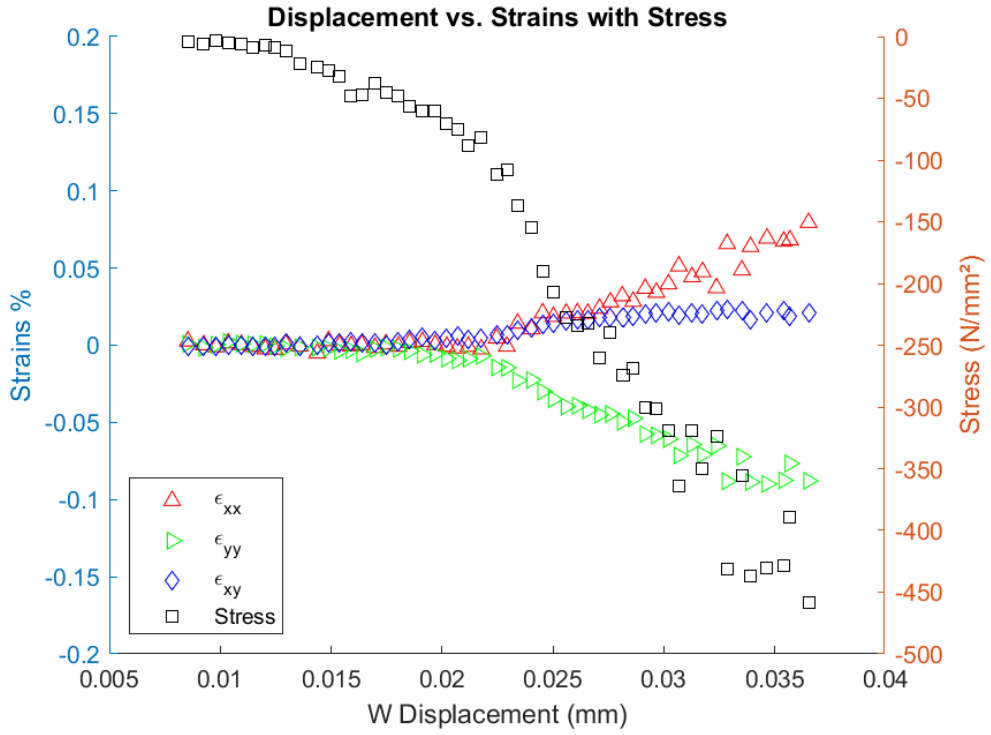

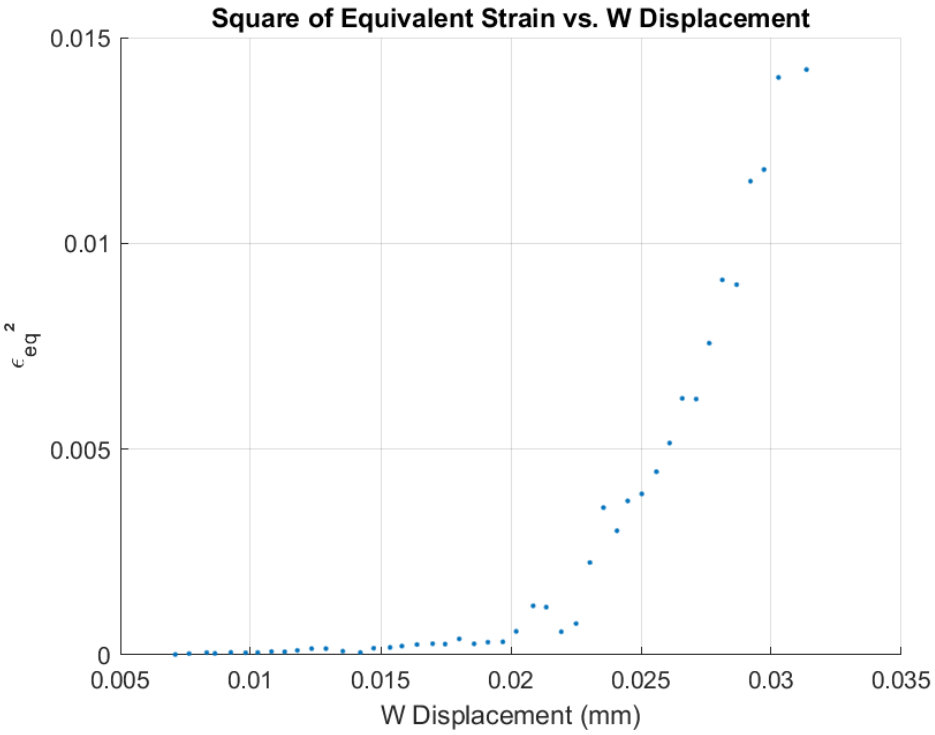

Impact Energy Level: 5 J

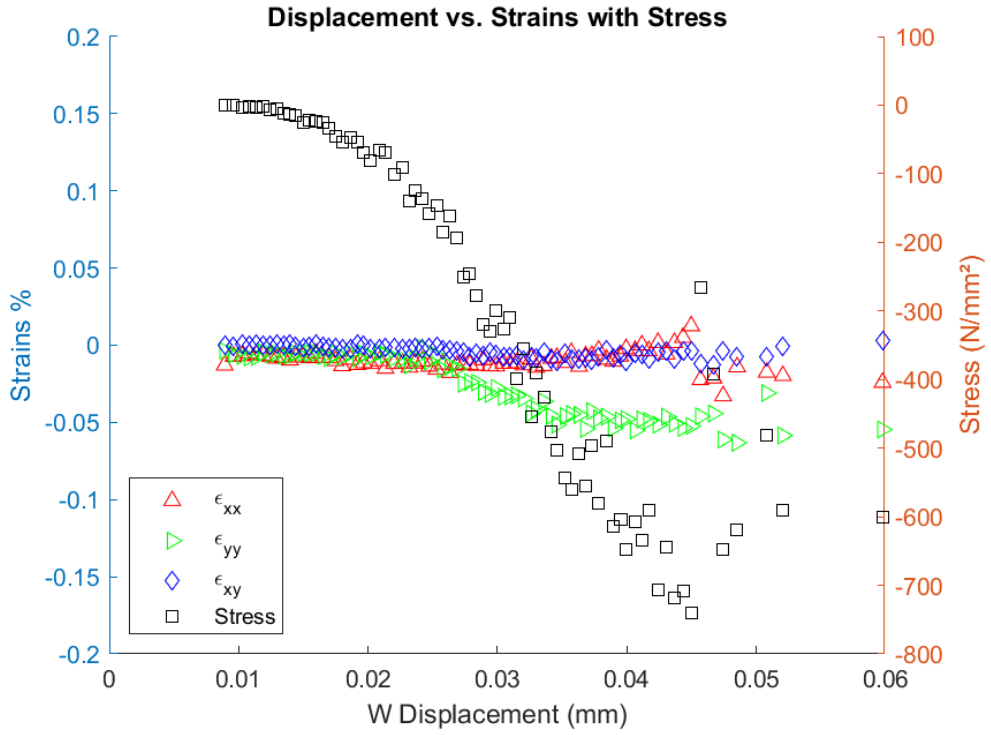

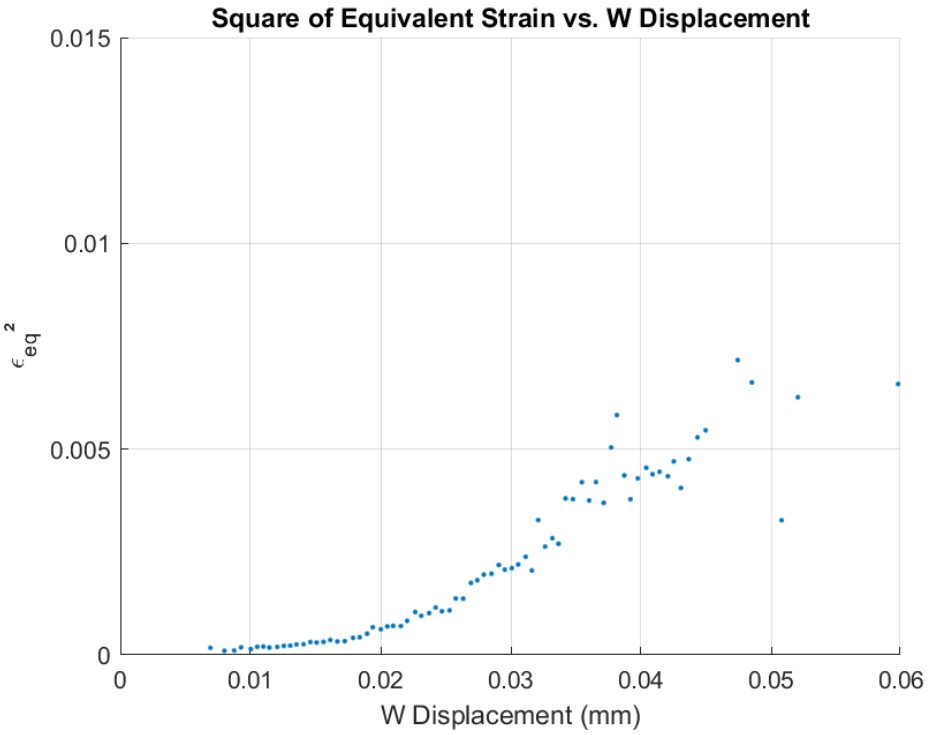

Impact Energy Level: 5 J

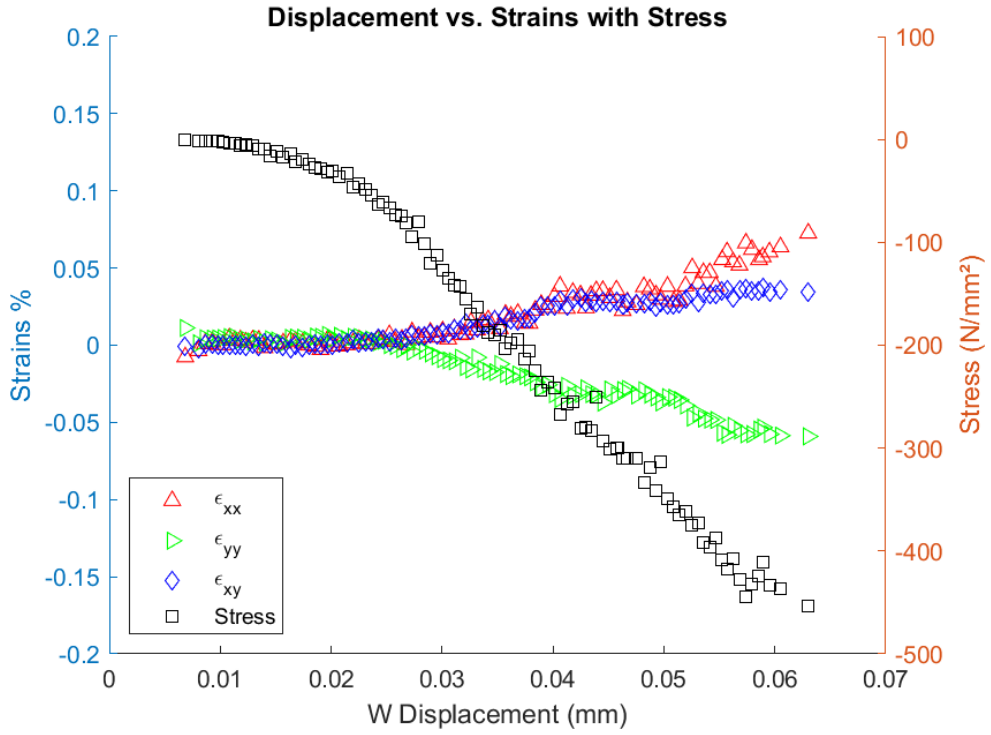

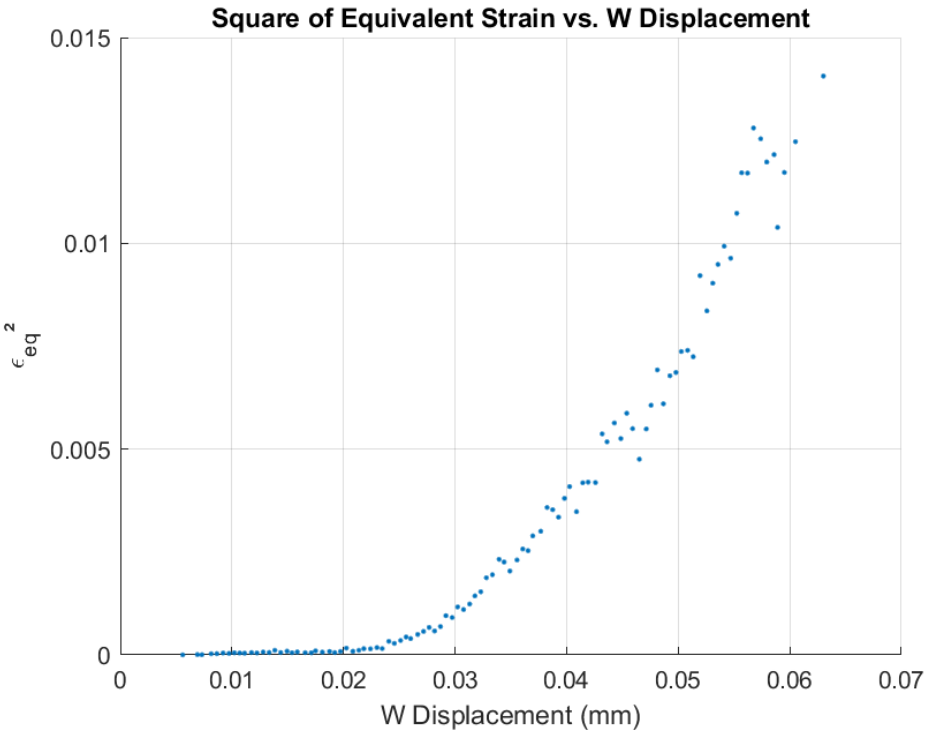

Impact Energy Level: 7.5 J

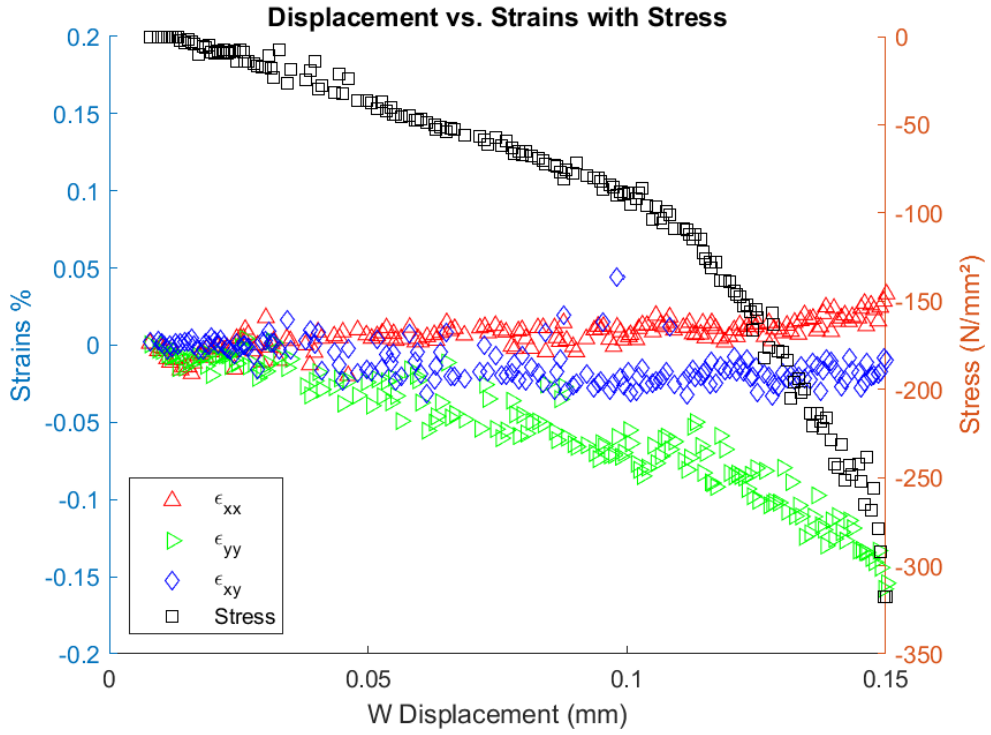

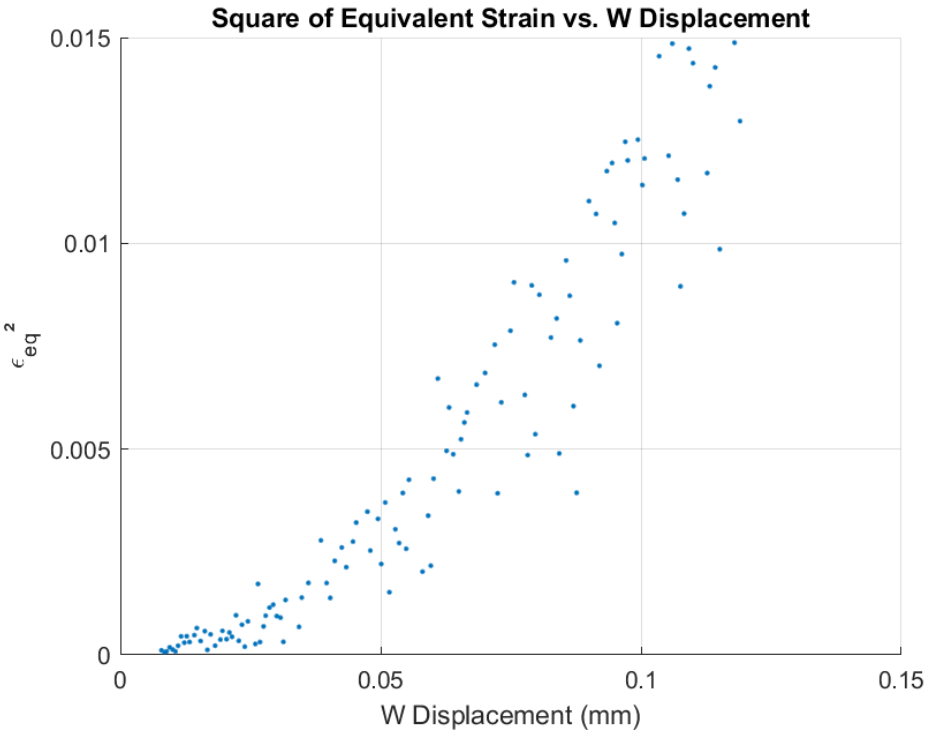

Impact Energy Level: 7.5 J

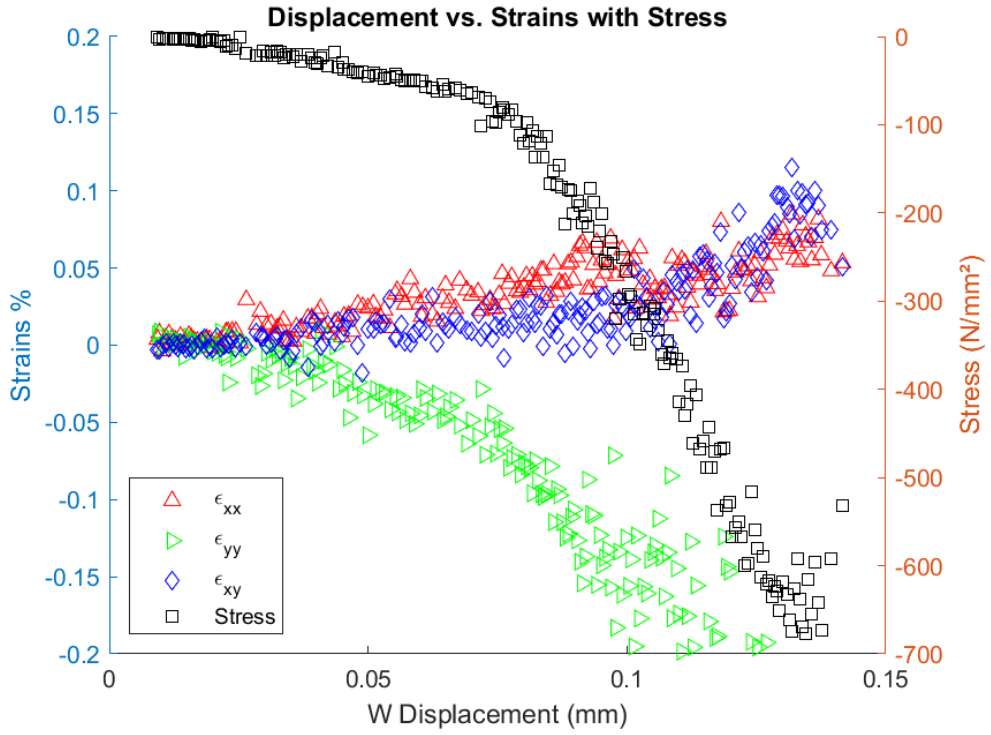

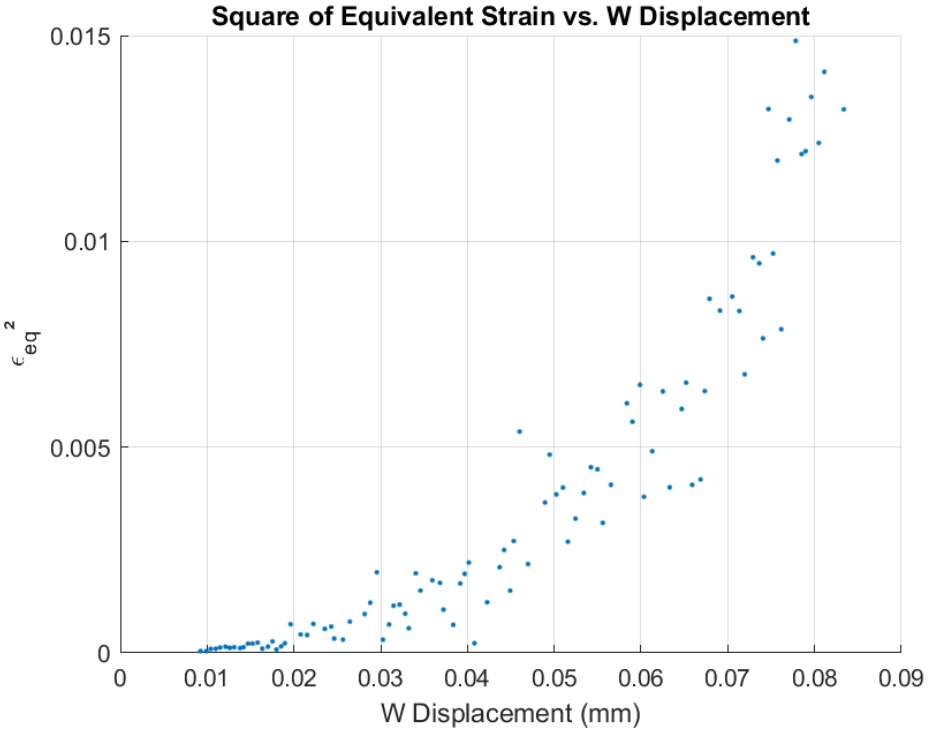

Impact Energy Level: 7.5 J

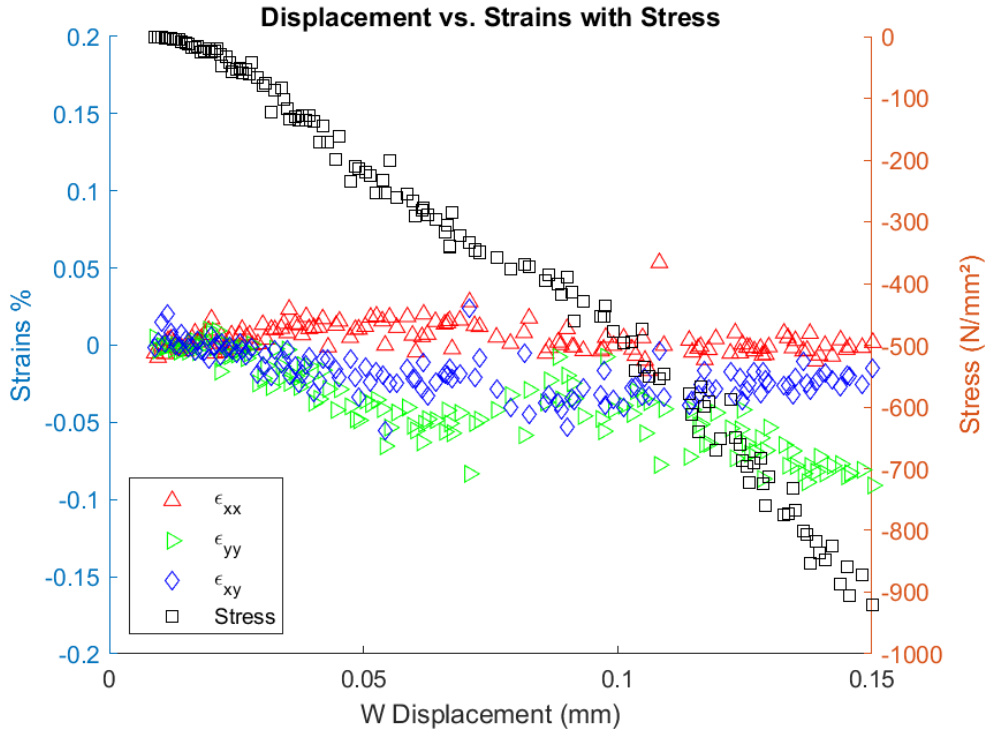

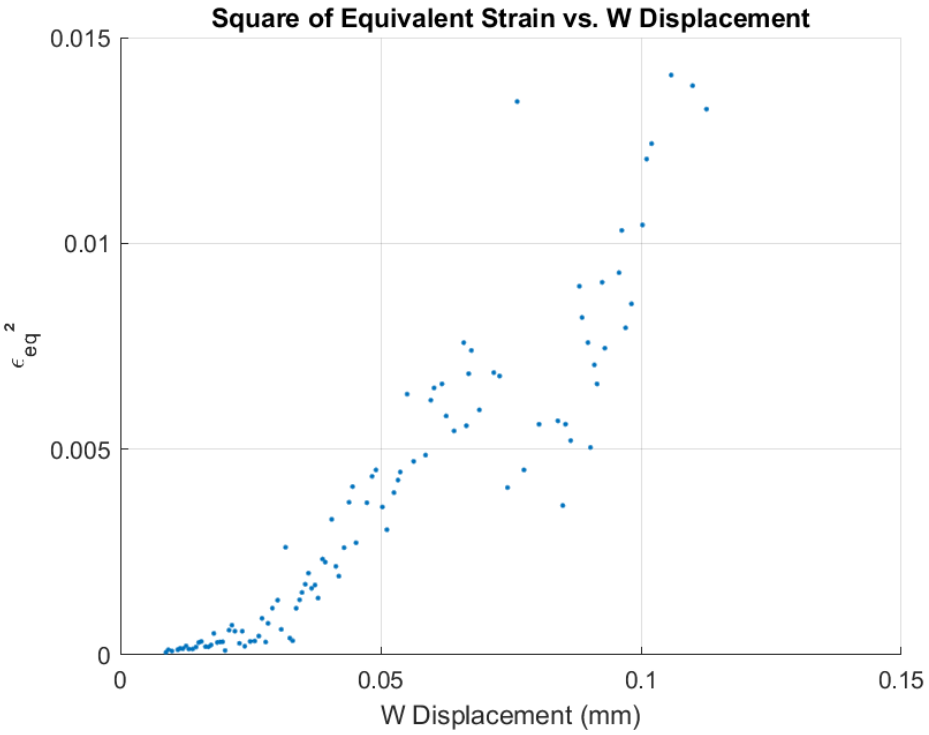

Impact Energy Level: 7.5 J

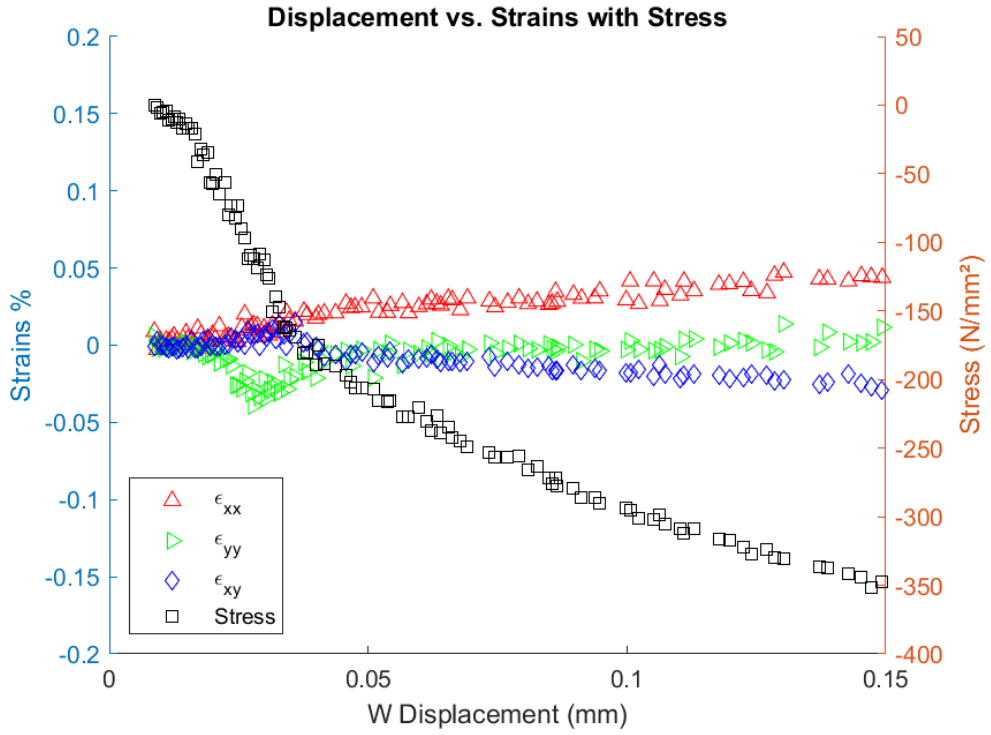

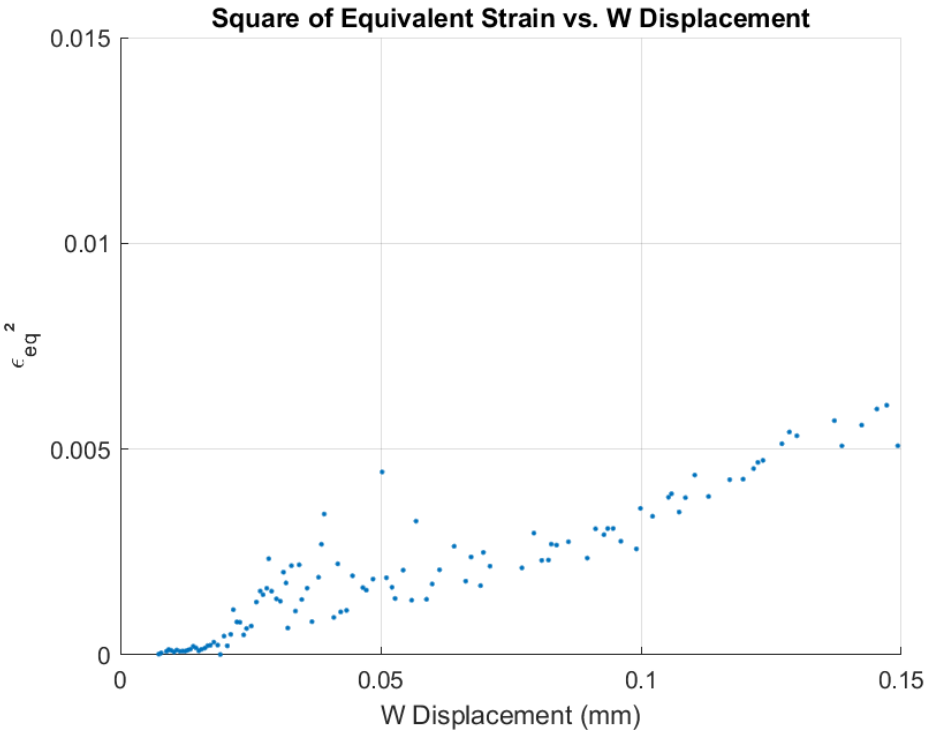

Impact Energy Level: 7.5 J

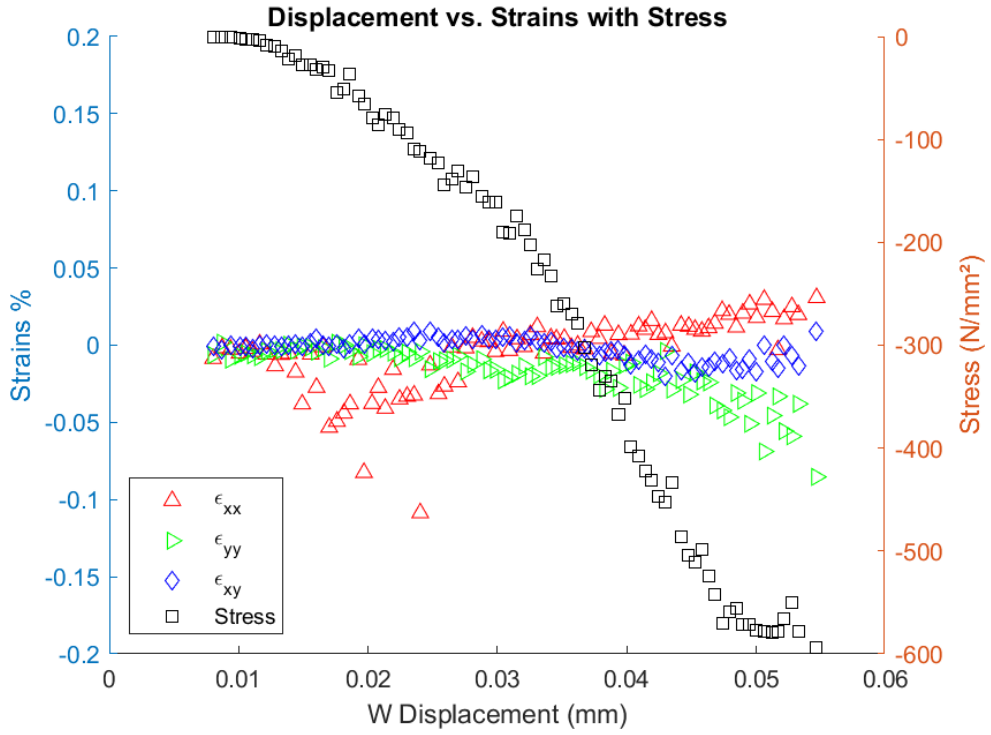

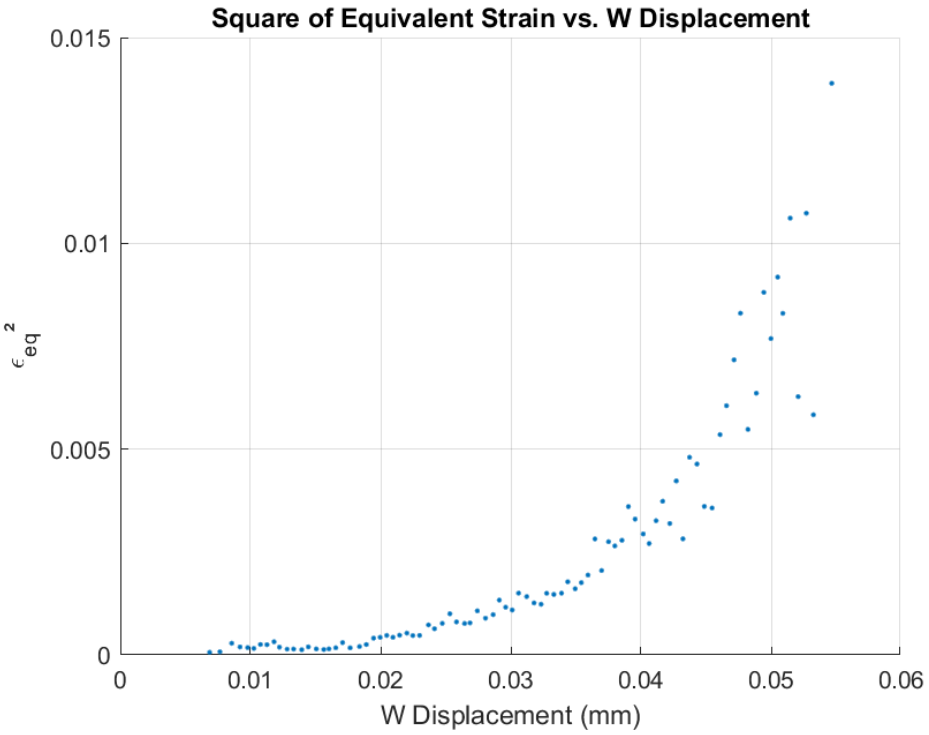

Impact Energy Level: 10 J

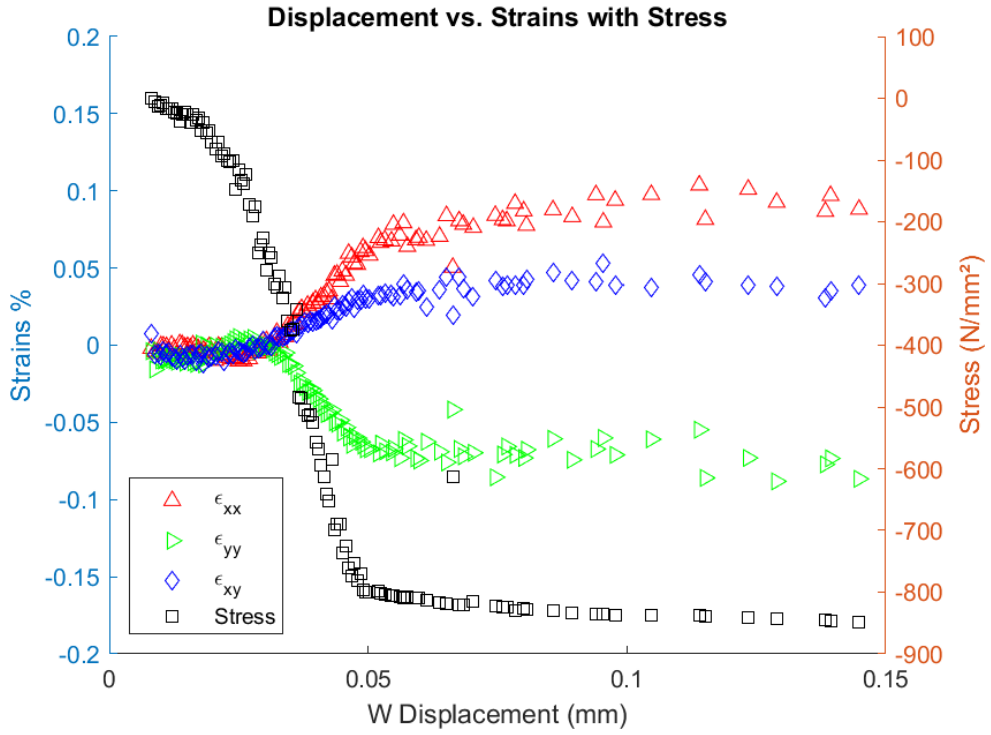

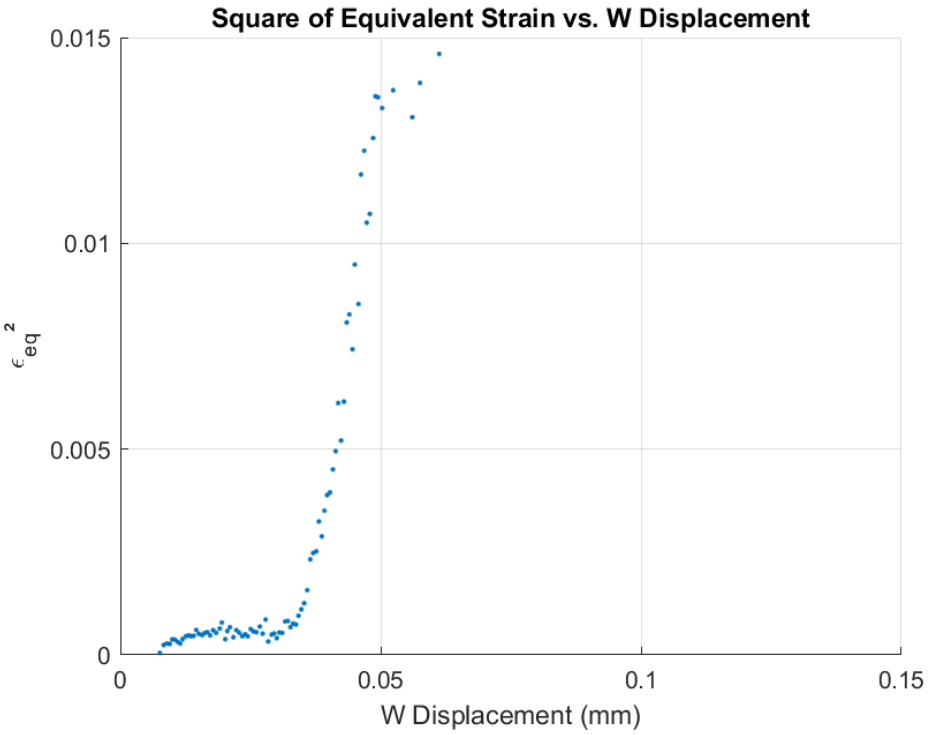

Impact Energy Level: 10 J

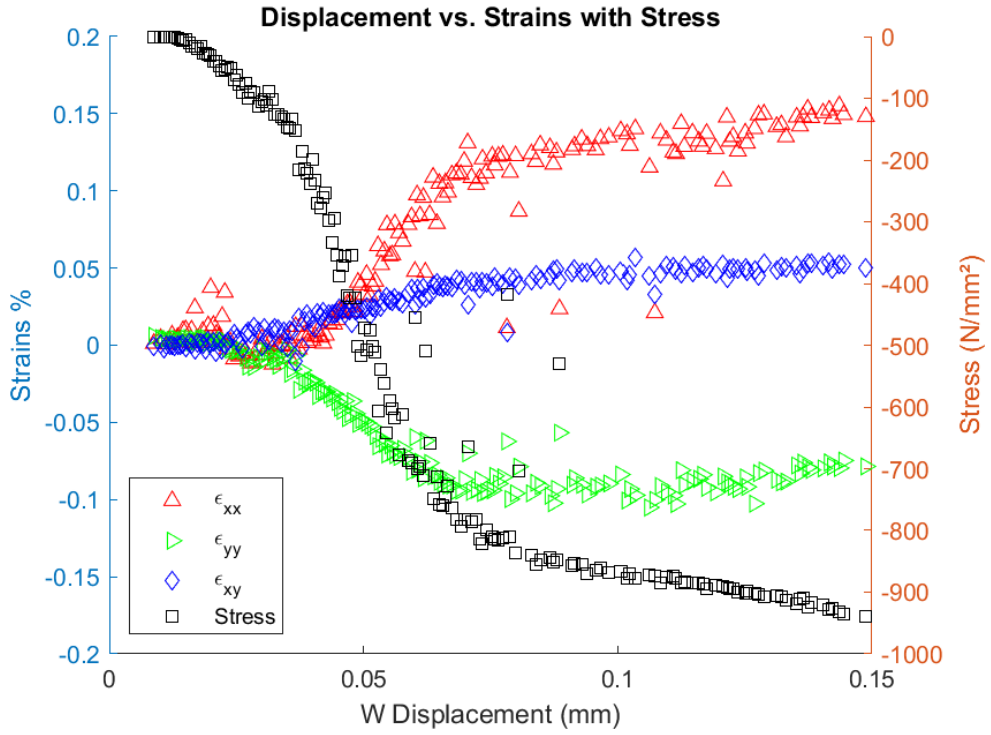

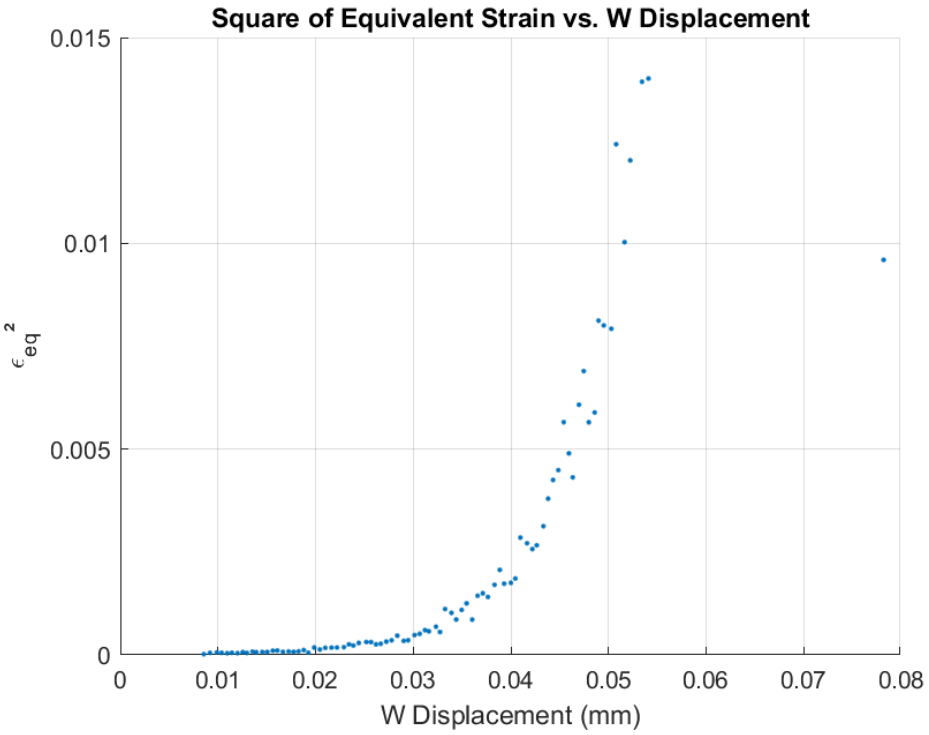

Impact Energy Level: 10 J

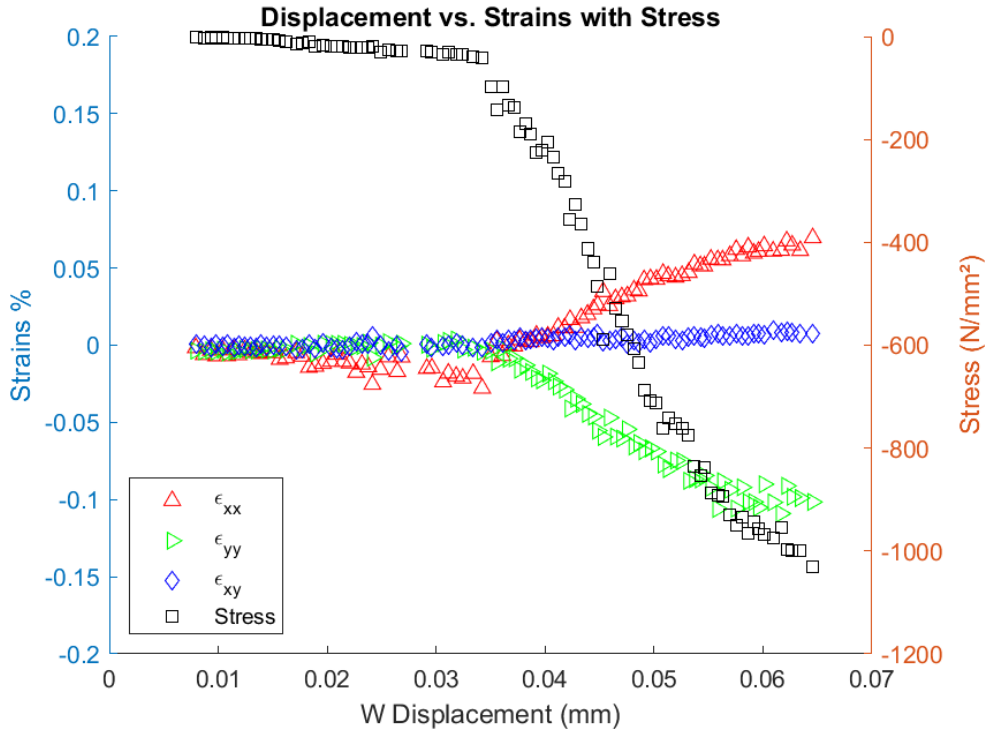

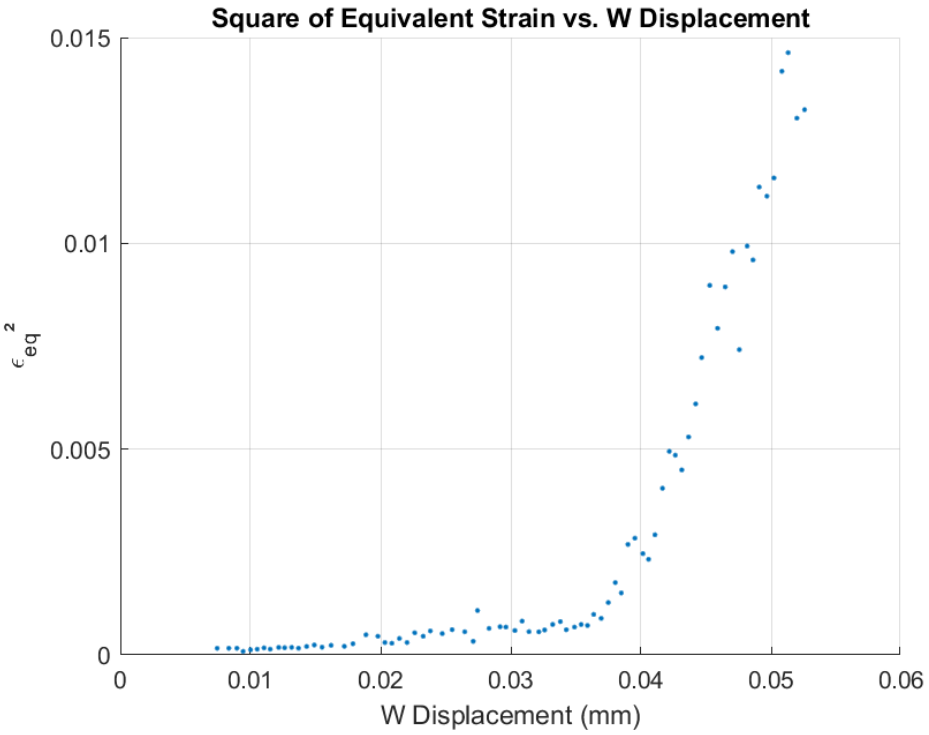

Impact Energy Level: 10 J

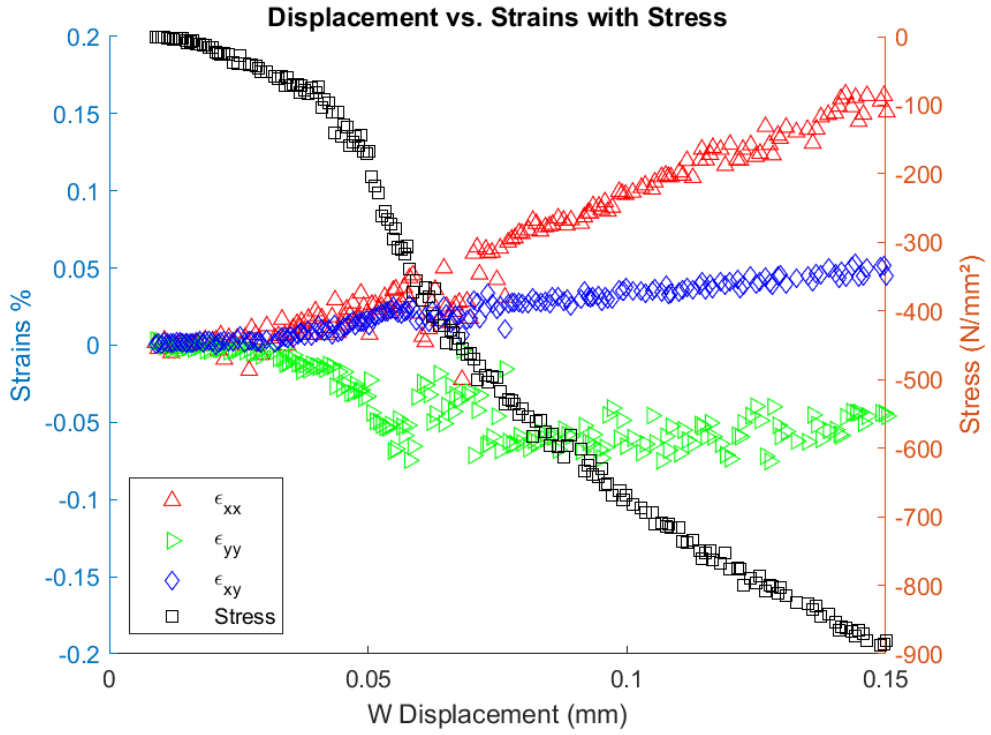

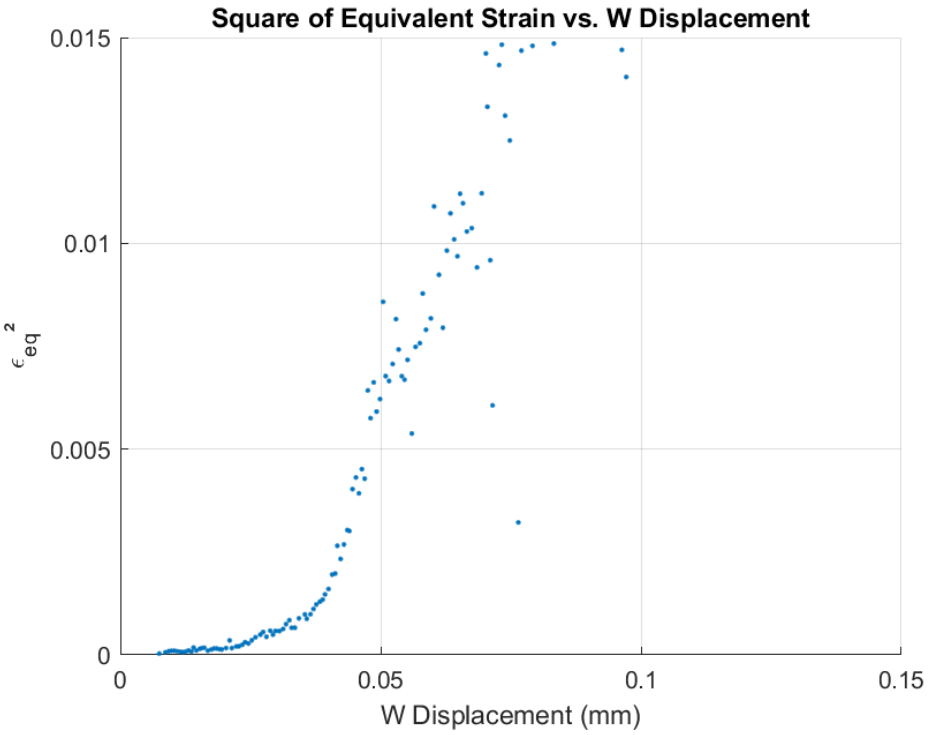

Impact Energy Level: 10 J

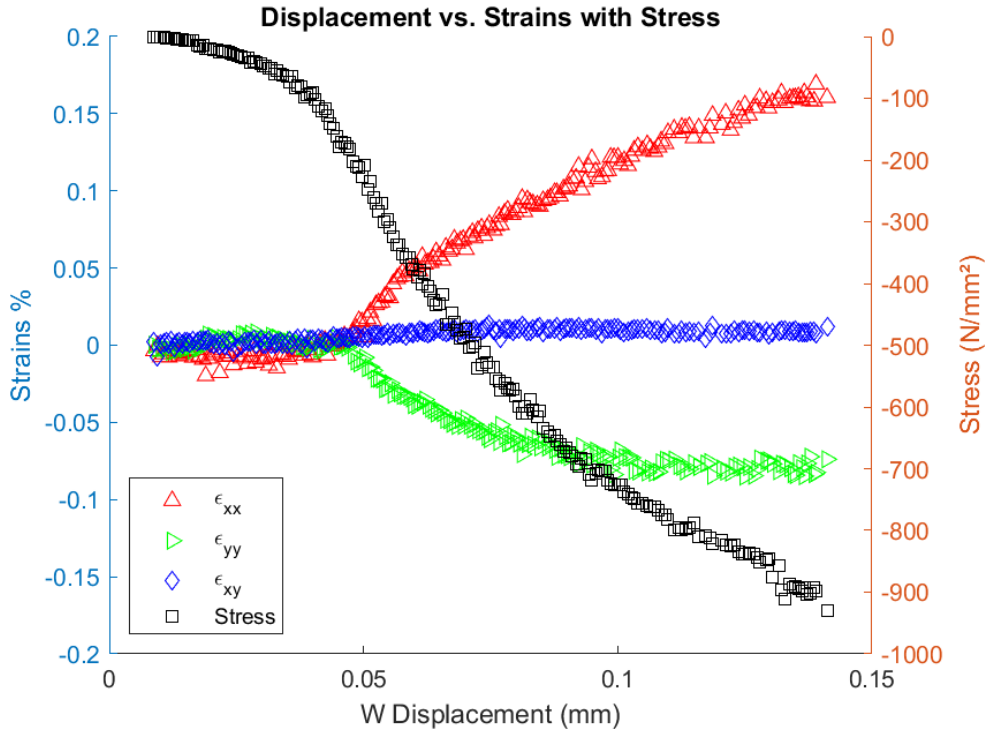

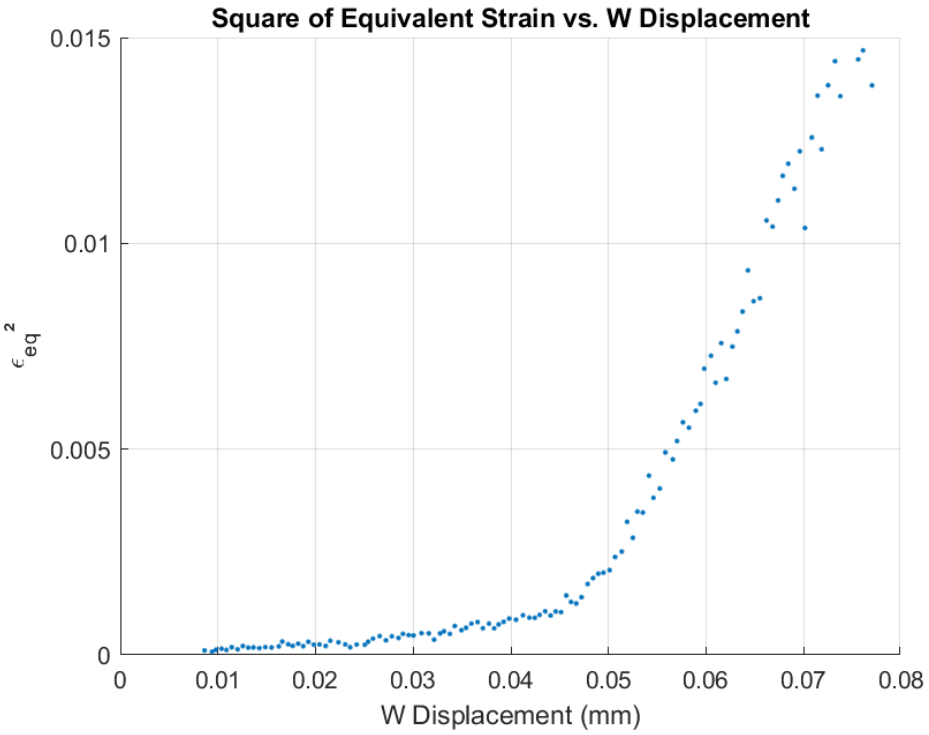

Impact Energy Level: 12.5 J

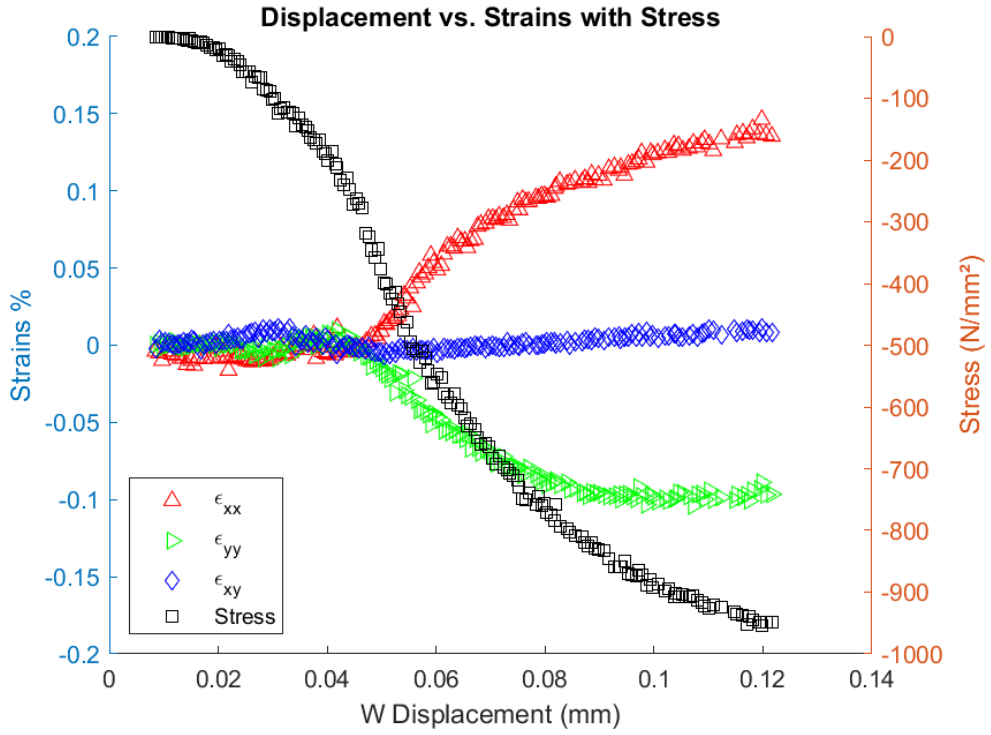

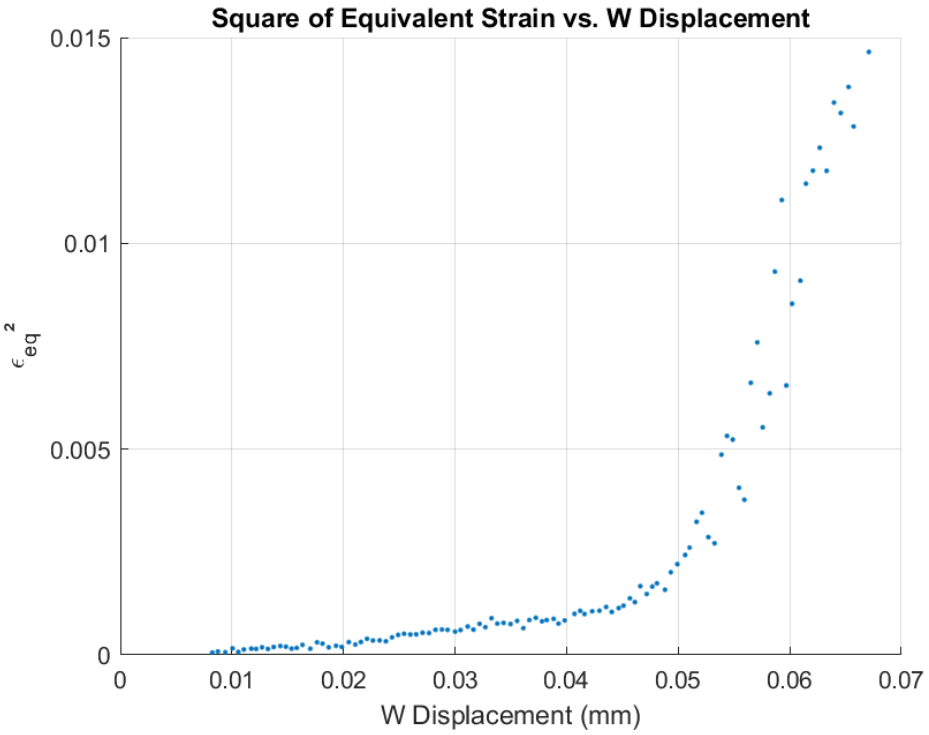

Impact Energy Level: 12.5 J

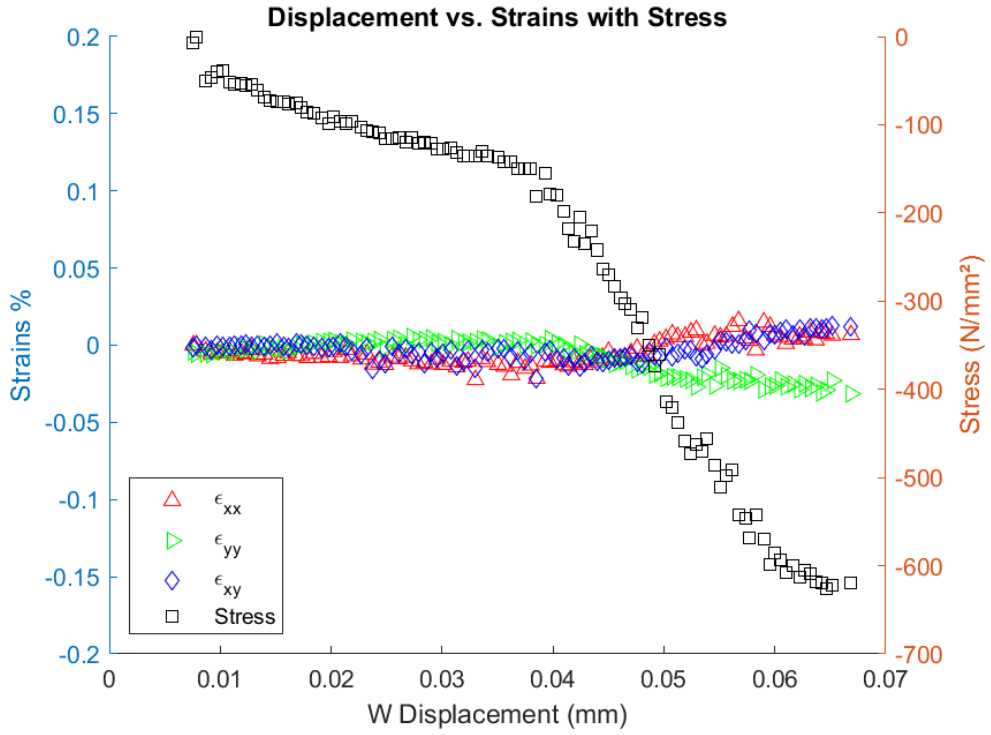

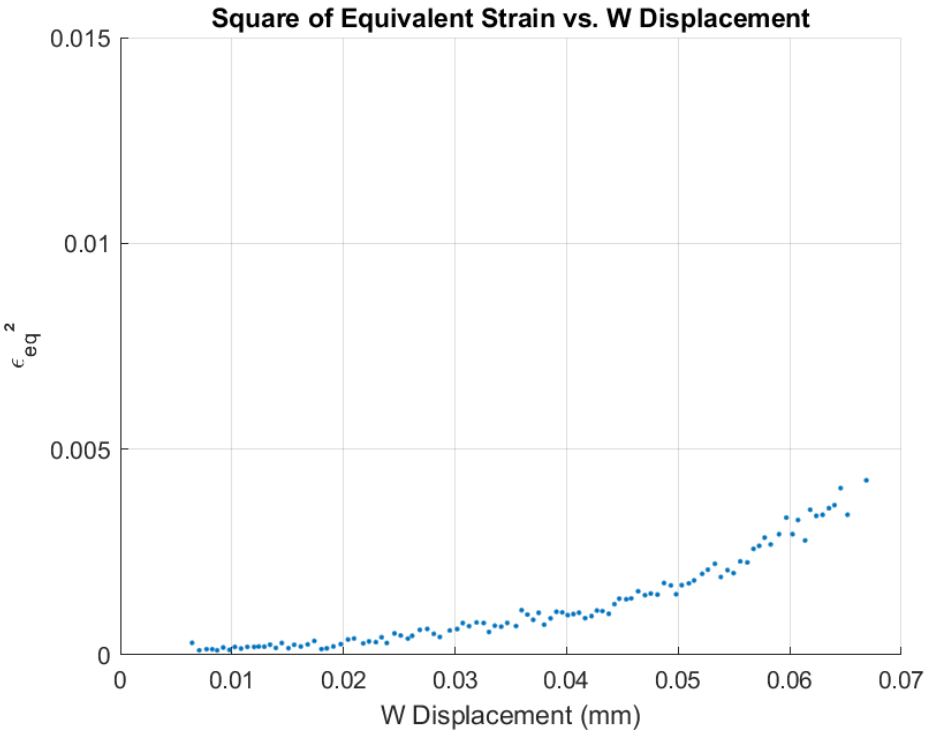

Impact Energy Level: 12.5 J

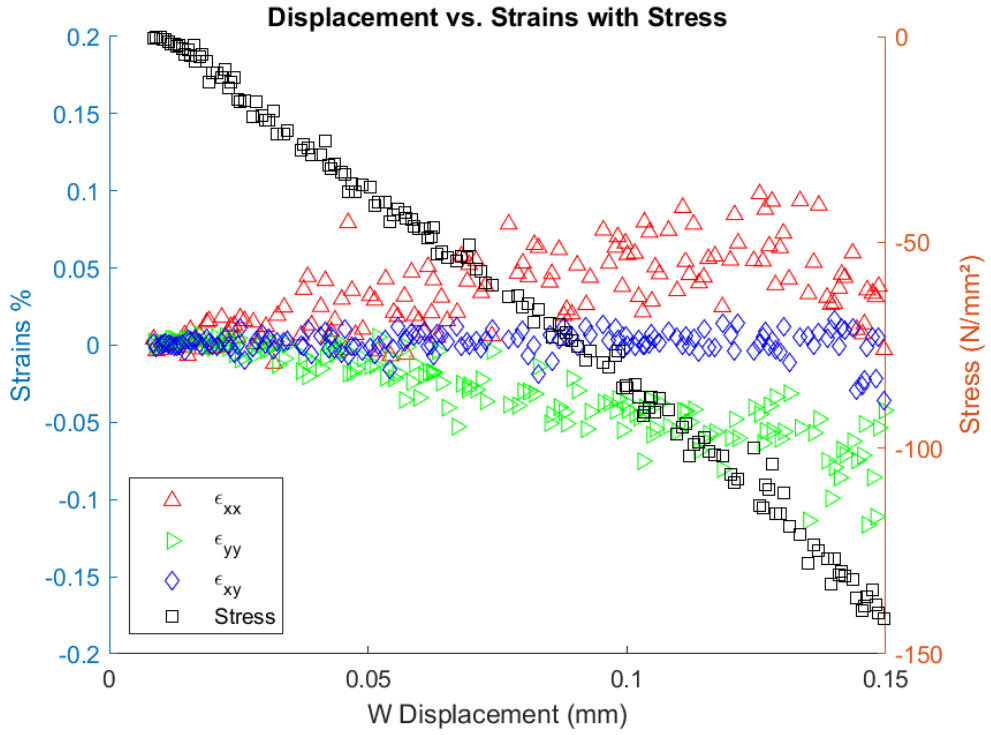

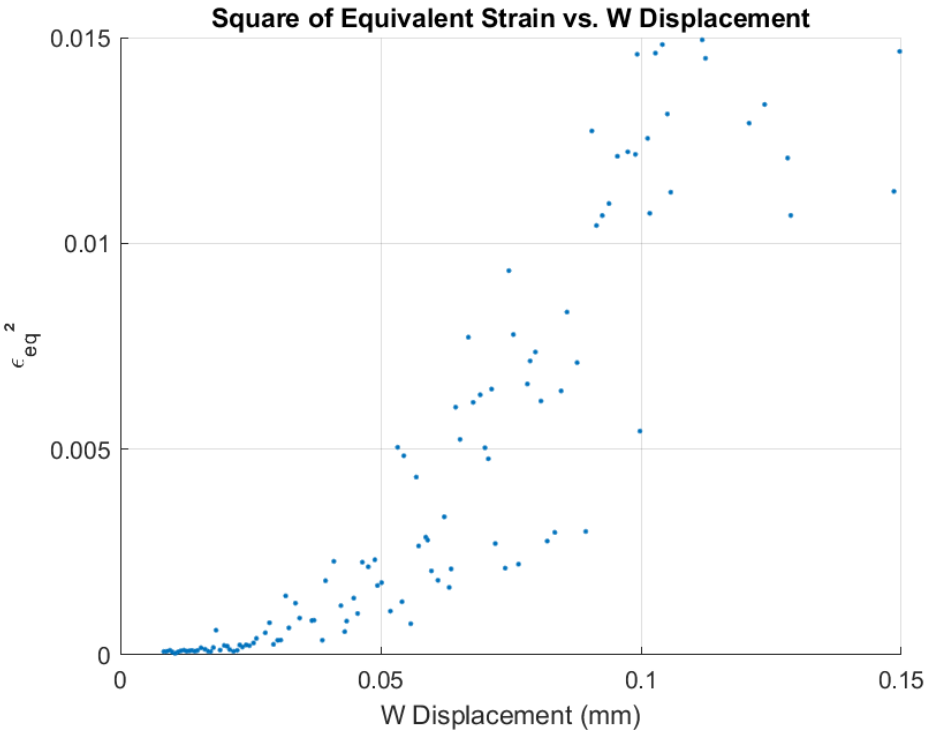

Impact Energy Level: 12.5 J

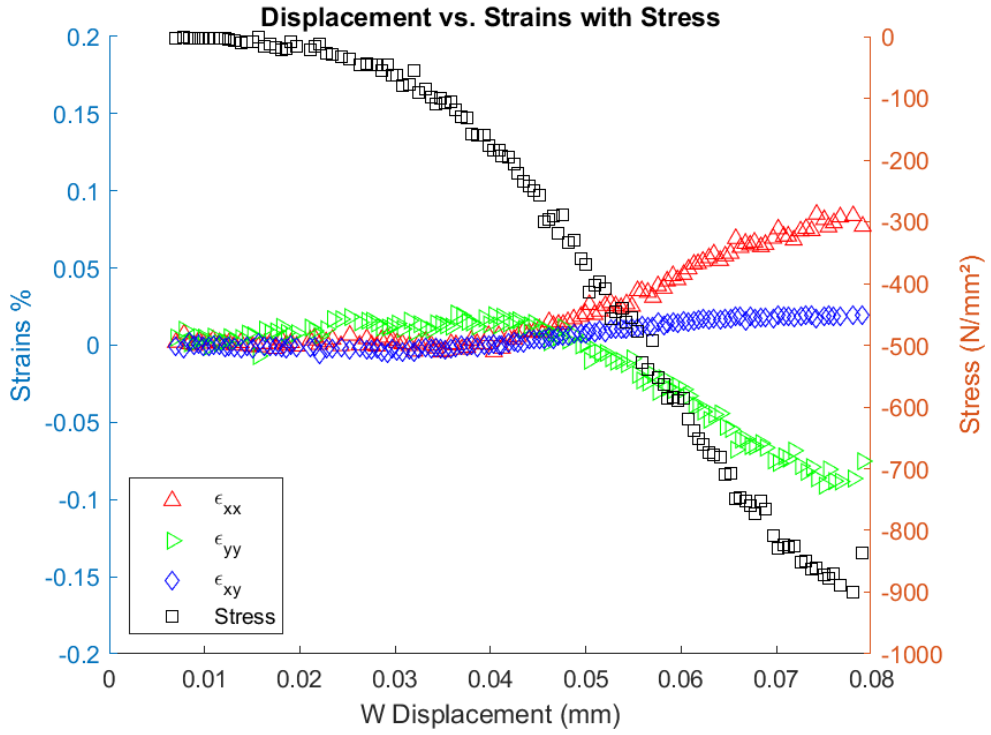

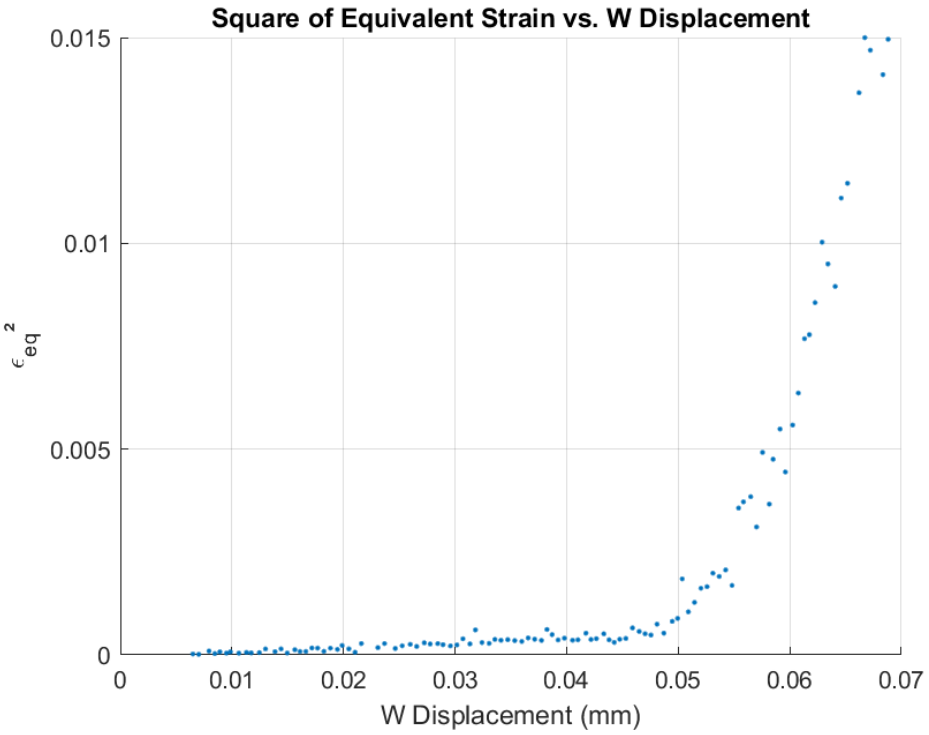

Impact Energy Level: 12.5 J